Magnetic fields in the Local Universe

Sebastian Hutschenreuter

SIGILL · UNIVERSITAT · LUDOVIC · MAXIM ·

München 2020

Magnetic fields in the Local Universe

Sebastian Hutschenreuter

Dissertation
an der Fakultät für Physik
der Ludwig–Maximilians–Universität
München

vorgelegt von
Sebastian Hutschenreuter
aus Heidelberg

München, den 23.4.2020

Erstgutachter: PD Dr. Torsten Enßlin
Zweitgutachter: Prof. Dr. Andreas Burkert
Tag der mündlichen Prüfung: 17.6.2020

Contents

1 Introduction 1

2 The primordial magnetic field in our cosmic backyard 5
- 2.1 Introduction . . . 5
- 2.2 Theory . . . 7
  - 2.2.1 Basics . . . 7
  - 2.2.2 Implementation . . . 10
  - 2.2.3 Simplifications . . . 11
- 2.3 Data . . . 12
- 2.4 MHD simulations . . . 14
- 2.5 Reconstructing primordial magnetic fields . . . 15
  - 2.5.1 Recombination . . . 15
  - 2.5.2 Today . . . 17
- 2.6 Summary and Discussion . . . 19

3 The Galactic Faraday sky revisited 31
- 3.1 Introduction . . . 31
- 3.2 Improving the Inference of the Faraday sky . . . 32
  - 3.2.1 The physics . . . 32
  - 3.2.2 The data . . . 35
  - 3.2.3 The model . . . 36
  - 3.2.4 The inference . . . 39
  - 3.2.5 The results . . . 40
- 3.3 Including the Free-Free emission . . . 43
  - 3.3.1 The physics . . . 43
  - 3.3.2 The data . . . 48
  - 3.3.3 The free free model . . . 49
  - 3.3.4 The Results . . . 54
- 3.4 Summary and conclusion . . . 61

4 The Galactic Faraday depth sky 2020 63
- 4.1 Introduction . . . 63
- 4.2 Modeling the Faraday depth sky . . . 64

4.2.1 Physics 64
4.2.2 Sky model 70
4.2.3 Catalog 72
4.3 The results 73
4.4 Conclusion 75

5 Disentangling the Faraday sky 79
5.1 Introduction 79
5.2 Observables 80
5.2.1 Faraday rotation measures 80
5.2.2 Pulsar dispersion measures 81
5.2.3 The electron emission measure 83
5.3 The models 85
5.3.1 Revisiting the Faraday sky model 85
5.3.2 Model 1 - Adding pulsar DM data 87
5.3.3 Model 2 - Adding the EM data 89
5.4 The results 90
5.4.1 Magnetic field sky 90
5.4.2 Dispersion measure sky 92
5.4.3 The filling factor 92
5.4.4 Faraday sky 97
5.5 Discussions 97

6 Circular polarization in the radio sky 99
6.1 Introduction 99
6.1.1 Testing the charge composition of the emitters 100
6.1.2 Circularly polarized synchrotron emission 101
6.2 The Galaxy in circular polarization: all-sky radio prediction and the charge of leptonic cosmic rays 103
6.2.1 Circular polarization in the Milky Way 103
6.2.2 Model 104
6.2.3 Estimator 110
6.2.4 Prediction 112
6.3 Determining the composition of radio plasma via circular polarization: the prospects of the Cygnus A hot spots 116
6.3.1 Previous studies on the composition of hot spots 116
6.3.2 Estimation 119
6.3.3 Conclusions 121

List of Figures

2.1 An illustration of the implemented algorithm. The ellipses indicate relevant redshifts. The labels near the arrows refer to the following steps: (a) Dark matter inference from galaxy data via `BORG`, (b) Linear dark matter transfer functions (Eq. 2.12), (c) translation of dark matter density to potential φ (Eq. 2.16), (d) time evolution of the potential via Eq. 2.13, (e) calculation of the magnetic field (Eq. 2.8), (f) induction equation (Eq. 2.17), (g) full MHD solver (see section 2.4) 13
2.2 A slice through the gas density distribution of the innermost region of the box averaged over 6 voxels in x direction at redshift $z = 0$ as a result of the `ENZO` simulation. The plane is about $1\,\mathrm{Mpc}\,h^{-1}$ thick. The red crosses indicate the positions of galaxies found by the 2M++ survey in the same volume. 21
2.3 The posterior mean (left) and uncertainty standard deviation field of the dark matter overdensities (right) at redshift $z = 1000$. This is the mean of the input data for our calculation averaged over 351 posterior samples of the matter field as generated by `BORG`. Our galaxy is centered in the middle. Areas close to the center a very pronounced in the mean, while areas further away are blurred out during the averaging. This reflects the Bayesian nature of the `BORG` algorithm, as the closer areas are very constrained by data, which leads to a relatively narrow posterior distribution in each pixel as reflected by the uncertainty variance. Therefore each sample looks similar there. The outer regions are barely constrained by data, leading to high uncertainties in the posterior. 22
2.4 The posterior mean (left) and uncertainty standard deviation (right) field of the absolute value of the Harrison magnetic field at redshift $z = 1088$. Just as in the case of the initial data in Fig. 2.3, we note a very similar pattern in the mean and variance plots for regions closer and further away from Earth. The uncertainties of the density fields translate into uncertainties of the magnetic field. 22
2.5 The matter power spectrum at $z = 10^3$. This is the spectrum of the input data. The red line is the mean averaged over the 351 samples. The grey area gives the uncertainty in the spectrum. 23

2.6 The power spectrum of the primordial scalar perturbations at redshift $z = 10^7$ as extracted from the cosmic structure reconstruction by Jasche et al. (2015). The dashed blue line indicates the scale invariant spectrum normalized with the Planck amplitude parameter $\mathcal{A}_s$, see Tab. 2.2. 23

2.7 The power spectrum of the scalar perturbations at redshift $z = 3402$ at the end of the radiation dominated epoch. The oscillations in the spectrum are the Baryon-Accoustic Osclillations (BAO). 23

2.8 The power spectrum of the magnetic field at redshift $z = 1088$ just before recombination. The spectrum is defined of a vector field is defined in Eq. (2.20) and Eq. (2.21). The spectrum peaks at approximately $\approx 3 \cdot 10^{-1}\,\mathrm{Mpc}^{-1}\,h$. 23

2.9 Scale averaged magnetic field at recombination. This is the result of Eq. (2.22). 24

2.11 The magnetic field and gas matter density in a slice trough the Virgo (above) and the Perseus-Pisces (below) cluster. The plots shows the gas matter density overplotted with the $y - z$ components of the magnetic field vectors. All colorbars have a logarithmic scaling. The coordinates are defined via the equatorial plane with reference to the galactic centre. The choice of the slice is purely for artistic reasons. 26

2.12 The magnetic field and gas matter density in an underdense region (above) and around the galactic center in the $x - y$ plane. The plots shows the gas matter density overplotted with the $x - y$ components of the magnetic field vectors. All colorbars have a logarithmic scaling. The coordinates are defined via the equatorial plane with reference to the galactic centre. . . . 27

2.13 The magnetic field strength averaged over line of sights in units of Gauss for sources within a distance of 60 Mpc/h from Earth. The plot is in galactic coordinates. The two dominant clusters in this image are Perseus Pisces in the middle left of the image and Virgo close to the North pole. Close ups of both structures are provided in Fig. 2.11. 28

2.14 A polarization-like plot visualizing the magnetic field morphology perpendicular to the LOS. This plot was generated using the 'Alice' module of the HEALPix software and the linear integral convolution algorithm (Cabral & Leedom 1993). The plot is in galactic coordinates. 28

2.15 The primordial magnetic field Faraday rotation measure for polarized sources located within a distance of 60 Mpch^{-1} from earth in units of radians per square metre. The plot is in galactic coordinates. The colormap is logarithmic on both the negative and the positve regime with a linear scaling between -10^{-29} and 10^{-29} rad$\cdot$m^{-2}, connecting both parts of the scale. We used the rescaled gas mass density as an estimate for the electron number density. 29

2.16 The electron dispersion measure in units of parsecs per cubic centimetre for sources within a distance of 60 Mpc/h from Earth. The plot is in galactic coordinates. We used the rescaled gas mass density as an estimate for the electron number density. The two dominant clusters in this image are Persues Pisces in the middle left of the image and Virgo close to the North pole. Close ups of both structures are provided in Fig. 2.11. 29

3.1 Reconstructions of the Faraday sky. Fig. (a) shows our main result, the posterior mean of reconstruction I. This map uses the free-free EM map as a proxy for the Faraday amplitude. The model furthermore contains fields that translate the free-free map into a Faraday amplitude, thereby balancing effects that support and those that disturb a direct relation of these two quantities. Fig. (b) contains the posterior mean of reconstruction II. Here we did not use the additional free-free data. Fig. (c) shows the posterior mean of the (NO15) reconstruction. We show the differences of the three maps in Fig. 3.2. These maps and all maps following in this paper are presented in Galactic coordinates centered at $(l, b) = (0°, 0°)$. 33

3.2 Differences of the reconstructions of the Faraday sky shown in Fig. 3.1. Figure (a) shows the difference between the NO15 map and reconstruction I. Figure (b) shows the difference between the NO15 map and reconstruction II. Figure (c) shows the difference between the Faraday depth skies resulting from reconstruction I and reconstruction II. 34

3.3 Sky map of the Faraday data set and its errors. Figure (a) shows the Faraday catalog used in this work projected on the sky. Figure (b) shows the corresponding uncertainties. We note that the region corresponding to the terrestrial south pole is only weakly constrained by data, except for the Galactic disk. 37

3.4 Logarithmic posterior uncertainties of the different reconstructions. Fig. (a) is the posterior uncertainty in ϕ of reconstruction I (the mean of which is shown in Fig. 3.1a). Fig. (b) shows the posterior uncertainty corresponding to reconstruction II (shown in Fig. 3.1b). Fig. (c) shows the posterior uncertainty corresponding to the NO15 reconstruction shown in Fig. 3.1c. . 41

3.5 Comparison of the power spectrum inferred by NO15 (dashed black) to the spectrum of the Faraday map including the free-free EM data (reconstruction I, red) and the results of reconstruction II in Sec. 3.2 (blue). The latter two inference algorithms also produce uncertainties in the power spectrum, which are depicted as shaded areas in the respective colors. 42

3.6 These figures show the estimated noise standard deviations $\widetilde{\sigma}$ compared to the σ values given by the Oppermann catalog and for the subset of analyzed by Vernstrom et al. (2019). To counteract the visual impression which is dominated by the outliers, we overlaid contour lines from the underlying log probability density function estimated via Gaussian kernels. Equality between the two quantities is marked by the red dashed line. The red crosses indicate the data points identified by Ma et al. (2019) as nπ-ambigious. . . 44

3.7 Sign fields of the different reconstructions. Their primary purpose is to capture the sign variations of the Faraday sky. Fig. (a) shows the field χ of reconstruction I as defined by the model in Eq. (3.20). Fig. (b) shows the field χ of reconstruction II as defined by the model in Eq. (3.8). Fig. (c) shows field s of the previous reconstruction by NO15, which served a similar purpose. Note that the difference in the scales of these fields is compensated by corresponding differences in the respective Faraday amplitude fields. . . 45

3.8 Fig. (a) shows the Galactic free-free EM map as obtained by the *Planck* Collaboration (Planck Collaboration 2016a). The further figures show the amplitude fields of the different reconstructions, which where supposed to capture the amplitude variations of the Faraday sky. Fig. (b) shows the exponentiated amplitude field ρ of the reconstruction II as defined by the model in Eq. (3.8). This field is not constrained by free-free data. Fig. (c) shows the exponentiated ϵ field defined in Eq. (3.18). This field is part of the revised Faraday map resulting from reconstruction I as well as the denoised free-free sky. A logarithmic version of this plot is shown in Fig. 3.9a. Fig. (d) shows the full Faraday amplitude field of reconstruction I as defined by the model in Eq. (3.20). This field is part of the result of the model in Eq. (3.20). A logarithmic version of this plot is shown in Fig. 3.9d. 46

3.9 These figures shows the logarithmic amplitude field of reconstruction I as defined by the model in Eq. (3.20) as well as its components. Fig. (a) shows the field ϵ defined in Eqs. (3.20) and (3.18), constrained by free-free and Faraday data. This is also the reconstructed log free-free map. Fig. (b) shows the second amplitude field δ defined in Eq. (3.20). The red crosses indicate the approximate angular positions of the Orion arm, as given by Vázquez et al. (2008) and Xu et al. (2009). Fig. (c) shows the logarithmic amplitude of the Faraday sky as defined in Eq. (3.19) without the additional δ contribution, while it is included in Fig. (d). 50

3.10 Figure (a) shows the Faraday sky containing only the amplitude contribution stemming from the field δ as defined in (3.21). This map is a rough estimate for the enhancement of the Faraday signal by the Orion arm. Figure (b) shows the faraday sky resulting from the complementary amplitude contributions (see also Fig. 3.9b). 51

3.11 Linear Polarization fraction $p = \frac{\sqrt{Q^2+U^2}}{I}$ of dust calculated from the *Planck* polarization data. 52

3.12 Hierarchical Bayesian model for reconstruction II. We decompose the Faraday depth ϕ into the fields χ and ρ, which are supposed to capture the sign and the overall amplitude of the signal, respectively (see Eq. (3.8)). The Faraday depth field ϕ together with the measurement noise n_ϕ determine the observed data d_ϕ via Eq. (3.4). The noise n_ϕ of every measurement i is assumed to be drawn from a Gaussian with variance $\eta_i \sigma_i^2$, where σ_i is the reported uncertainty and η_i a unknown uncertainty correction factor. . . . 54

3.13 Hierarchical tree model for the free free EM sky. We model $\mathrm{EM}_{\mathrm{ff}}$ via the exponentiated field ϵ (see Eq. (3.18)). The field $\mathrm{EM}_{\mathrm{ff}}$ is together with the noise n_{ff} connected to the observed data via Eq. (3.16) 55

3.14 The full hierarchical model excluding the power spectrum hyper priors for the fields. The lowest layer contains the data sets d_{ff} and d_ϕ. These are connected by the Eqs. (3.4) and (3.16) to the sky maps $\mathrm{EM}_{\mathrm{ff}}$ and ϕ. The sky maps in turn are connected to the Gaussian fields in the uppermost layer via the respective models defined in Eqs. (3.18) and (3.20). From there on, the higher branches for the respective correlation structure inference follow. These are not depicted here, but are shown and explained in the Appendix. 55

3.15 Fig. a) shows the difference between the field ϵ (as defined in Eq. (3.18)), inferred only by free-free data and the same field resulting from the joint inference with Faraday data (reconstruction I). Fig. b) shows the uncertainty of the ϵ field in reconstruction I. This demonstrates that the ϵ field is predominately determined by the free-free data irrespective of the simultanous inference of Faraday sky. There exist considerable deviations between the reconstructions near the Galactic poles. Figure (b) demonstrates thet the reconstruction is also rather uncertain in these regions. 57

3.16 Excerpt of the free-free reconstruction in the first slice, its uncertainty, followed by the same excerpt in the *Planck* free free EM data. The residual is shown in the last row. 58

4.1 Sky projections of the van Eck catalog and corresponding uncertainties. Fig. (a) shows the RMs, Fig. (b) the observed standard deviations These maps and all maps following in this paper are presented in Galactic coordinates centered at $(l, b) = (0^\circ, 0^\circ)$. 65

4.2 Inference results for the Galactic Faraday sky. Fig. (a) shows the posterior mean using the updated catalog, Fig. (b) the corresponding inferred standard deviations. The color scale is saturated at $\pm 250\,\frac{\mathrm{rad}}{\mathrm{m}^2}$ in the mean and $\pm 80\,\frac{\mathrm{rad}}{\mathrm{m}^2}$ in the uncertainties to highlight mid latitude features of the Galactic Faraday depth sky. 66

4.3 Inference results for the Galactic Faraday sky. Fig. (a) shows the posterior mean using the updated catalog, Fig. (b) the corresponding inferred standard deviations. In contrast to Fig. 4.2, the color scale is saturated at $\pm 1500\,\frac{\mathrm{rad}}{\mathrm{m}^2}$ in the mean and $\pm 400\,\frac{\mathrm{rad}}{\mathrm{m}^2}$ in the uncertainties to highlight disc features of the Galactic Faraday depth sky. 67

4.4 Figures (a) and (b) show the mean and uncertainty of the Galactic Faraday depth sky as inferred by HE19. 68
4.5 Slices through the inner part around the Galactic disc. Figs. (a) and (b) show excerpts of the galactic Faraday sky, including RM data points in the respective areas indicated by black pluses. The variance along the Galactic latitude is made visible by color coding the latitude for the 2 degree width of the strip. Figs. (c) and (d) show the same excerpts in the amplitude field e^{ρ}. The approximate locations of spiral arms (Hou et al. 2009; Vallée 2017) are indicated as black filled circles. The slice in Fig. (a) is also partly shown in Shanahan et al. (2019a), where the strong excess in Faraday depth in tangential direction to the Sagitarrius arm was first noted. 69
4.6 Power spectrum for the Faraday depth sky derived in this work, compared with results from HE19 and Oppermann et al. (2012a). 71
4.7 Histogram illustrating the correlation between the log amplitude field ρ and the logarithmic DM (Fig (a)) and logarithmic square root EM (Fig. (b)) skies, respectively. The former is calculated from a Galactic thermal electron model (Yao et al. 2017), while the latter was inferred by the *Planck* survey from microwave data (Planck Collaboration 2016a). 74
4.8 Posterior means of the components defined in Eq. (4.5). Fig. (a) shows the amplitude field e^{ρ} and Fig. (b) shows the sign field χ. 76
4.9 The Magellanic Clouds as seen with different observables. Figs. (a) and (b) show the Faraday depth and the underlying amplitude field as inferred in this work. Figs. (c) and (d) show emission measure (EM) as obtained by the *Planck* satellite (Planck Collaboration 2016a) and in H_{α} emission (Finkbeiner 2003; Gaustad et al. 2001). 77

5.1 Sky projections of the RMs coming from the van Eck catalog (Fig. (a)). Fig. (b) shows the corresponding the estimated standard deviations from HE20. These and all maps following are presented in Galactic coordinates centered at $(l, b) = (0°, 0°)$. 82
5.2 Positions of the pulsars that are collected in data-set $d_{\mathrm{DM,edge}}$ because they can be assumed to lie at the Galactic edge. The horizontal cut through the Galaxy in Fig. (a) contains only pulsars with a distance to the Galactic plane of $|z| < 3$ kpc, while Fig (b) shows all pulsars in the data-set. The background images are an artist impression (NASA/JPL-Caltech,R. Hurt (SSC/Caltech), Fig. (a)) or adapted from Gaia Collaboration et al. (2018) (Fig. (b)). 84
5.3 Sky projections of the *Planck* data and corresponding uncertainties. Fig. (a) shows the EM, Fig. (b) the corresponding standard deviations. 86
5.4 Graph illustrating the hierarchical Bayesian model used for the Faraday sky inference by HE19 and HE20. This is the base model that all further models derive from. 91
5.5 Graph illustrating the hierarchical Bayesian model described in Eqs. (5.17). 91

5.6 Graph illustrating the hierarchical Bayesian model described in Eqs. (5.20). 91

5.7 The LOS parallel and LOS averaged magnetic field, Fig. (a) shows the posterior mean of Model 1, Fig. (b) the corresponding results of Model 2. In both cases the color scale is saturated at $\pm 1.5\,\mu$G. 93

5.8 Inference results for the logarithmic Galactic DM sky. Fig. (a) shows the posterior mean of Model 1, Fig. (b) the corresponding results of Model 2. . 94

5.9 Slices through the Galactic DM sky. Fig. (a) shows the posterior mean resulting from Model 1 (5.5), while Fig. (b) shows the posterior mean resulting from Model 2 (5.6). The black dots indicate the corresponding results of Yao et al. (2017). 95

5.10 The logarithmic integrated electron density profile of Yao et al. (2017) in log dispersion measure units. 95

5.11 Inference results for the EM-DM filling factor (see Eq. (5.21)). Fig. (a) shows the posterior mean of the *psi* field from Model 2 (5.5), while Fig. (b) shows the log integrated dust density as derived by (Leike & Enßlin 2019). It should be noted that the colorbars are reversed in the two plots to highlight the anti-correlation of the two fields. 96

5.12 Inference results for the Galactic Faraday depth sky. Fig. (a) shows the posterior mean resulting from Model 1 (5.5), while Fig. (b) shows the posterior mean resulting from Model 2 (5.6). 98

6.1 Left: Synchrotron intensity at 408 MHz as provided by (Remazeilles et al. 2015a). Right: Faraday rotation map as constructed by (Oppermann et al. 2012b). Red indicates magnetic fields predominantly pointing towards the observer and clockwise rotation of the received linear polarisation. This is according to the IAU convention for measuring angles and is therefore opposite to the mathematical convention. 109

6.2 Left: Synchrotron emission intensity at 408 MHz of the simplistic 3D model. Right: Map of the resulting conversion factor $\alpha\sigma$, which translates the Faraday rotation map ϕ into the fractional CP map V/I at 408 MHz. For both the relativistic electron profile of Eq. 6.33 and $\beta = (0, 1)$ were assumed. . 109

6.3 Predicted circular polarisation intensity at 408 MHz for $\beta = (0, 1)$ (left) and $\beta = (1, 0)$. Red indicates clockwise rotation, according to the IAU convention for measuring angles that is opposite to the mathematical convention. 113

6.4 Predicted V/I ratio at 408 MHz for $\beta = (0, 1)$ (left) and the difference of the $\beta = (0, 1)$ and $\beta = (1, 0)$ ratios (right) 113

6.5 Profiles of the thermal and relativistic electron density used in this work in terms of the dimensionless quantities x_{th} and x_{rel} as defined in the context of Eq. 6.17. 115

List of Tables

2.1 Table of cosmological parameters used in this work (Planck Collaboration et al. 2016a). 7
2.2 Comparison of inflation parameters provided by the Planck collaboration (Planck Collaboration et al. 2016) and as inferred from the samples used in this work. 16

Zusammenfassung

Diese Doktorarbeit enthält die Resultate mehrerer Forschungsprojekte mit Fokus auf kosmologischen und astrophysikalischen Magnetfeldern. In der folgenden Zusammenfassung wird der Inhalt dieser Projekte kurz wiedergegeben. Referenzen und Würdigungen bezüglich bereits publizierter Arbeiten werden den Kapiteln vorangestellt.

Das erste Kapitel enthält die erste Vorhersage der Stärke und dreidimensionalen Struktur des heutigen Überbleibsels eines primordialen Magnetfeldes innerhalb eines sich mitbewegenden Volumens mit einer Kantenlänge von $600\,\mathrm{Mpc}/h$. Die grobe Idee ist hier das Materiedichtefeld, inferiert aus der heutigen, großräumigen Struktur des Universums, bis zu dem Punkt in die strahlungsdominierte Epoche zu übersetzen, an dem der kosmische Horizont wesentlich kleiner als die kleinste durch die Daten auflösbare Skala ist. Das so erhaltene primordiale Dichtefeld kann als Startwert für den sogenannten Harrisoneffekt genutzt werden, durch welchen Magnetfelder bis zur Rekombination generiert werden. Von da an werden die Magnetfeld- und Materiedichteentwicklung mit einer magnetohydrodynamischen Simulation zu Rotverscheibung $z = 0$ gebracht, wo die Magnetfeldstruktur im heutigen Universum offenbart wird.

In den Kapiteln zwei bis vier werden mehrere Analysen des galaktischen Faradaytiefenhimmels präsentiert. In einem ersten einfachen Inferenzmodell wird eine erste Abschätzung des Faradayhimmels aus den verstreuten Datenpunkten gegeben. Eine Komponente der Inferenz, welche die Amplitude des Effekts am Himmels erklären soll, zeigt große Ähnlichkeit mit dem galaktischen Emissionsmaß der Bremstrahlung freier Elektronen und Protonen. Darauf aufbauend werden zusätzliche Daten verwendet um den Faradayhimmel in seine Komponenten aufzulösen. In einem ersten phänomenologischen Model wird die Signatur des lokalen galaktischen Arms mit Hilfe der Bremstrahlungsdaten entdeckt. In weiteren Ansätzen werden zusätzlich Dispersionmaße galaktischer Pulsare verwendet um eine quantitative Vorhersage des sichtliniengemittelten Magnetfeldes zu machen.

Im letzten Kapitel werden zwei Projekte bezüglich Zirkularpolarisation im Radiobereich zusammengefasst. In der ersten Arbeit werden der Faradayhimmel und Synchrotronemissionsdaten verwendet um eine Vorhersage über den galaktischen Zirkularpolarisationshimmel zu geben. Durch die Sensitivität der Synchrotronstrahlung auf die Ladung des emittierenden Mediums können Aussagen über den Ladungsinhalt der Milchstraße gemacht werden. Dieselbe Eigenschaft wird in der zweiten Arbeit dazu verwendet zu zeigen, dass Beobachtungen von Stokes V dabei helfen könnten zu entscheiden, ob der Inhalt von Radiojets hadronischer oder leptonischer Natur ist.

Summary

This thesis comprises several research efforts centering around cosmological and astrophysical magnetic fields. In the following summary, these are shortly outlined. References and acknowledgments to the respective works are put in front of each chapter.

The first chapter entails the first prediction of today's remnants of a primordial large scale magnetic field both in strength and in three dimensional morphology within a co-moving box with edge length of $600\,\mathrm{Mpc}/h$. The general idea here is to translate the matter density field inferred from large scale structure data into the radiation dominated epoch up to the point where the horizon scale is much smaller than the smallest scale resolvable by the data. The density field obtained this way is used as initial conditions for the so called Harrison effect, which results in a magnetic field being generated up to recombination. From there on, magnetic field and matter evolution are simulated via a Magnetohydrodynamics solver up to red-shift $z = 0$, revealing the magnetic field structure today.

In chapters two to four several analyses of the Galactic Faraday depth sky are presented. Here, rotation measures of extra-Galactic point sources are used to constrain the Galactic component of the Faraday rotation sky. In a first simple inference model a full sky estimate is build from the scattered data points. A component of the inference, which is intended to model the sky amplitude, is found to have strong resemblance with the Galactic free-free emission measure sky. Hence, building on the simple model, additional data is used to disentangle the Faraday sky into its components. In a first phenomenological model, the signature of the local Galactic arm is discovered with the help of emission measure data. In further attempts, dispersion measure data from Galactic pulsars is additionally used to give a quantitative prediction of the line-of-sight averaged Galactic magnetic field sky.

In the last chapter, two research projects revolving around circular polarization in the radio regime are summarized. In the first work, the Faraday depth sky and synchrotron intensity data are used to give a prediction on the Galactic synchrotron circular polarization sky. Due to the sensitivity of circular polarization to the charge of the synchrotron light emitting medium, statements on the leptonic content of the Milky Way can be made. The very same property of circular polarization is used in the second paper in order to show that observations of Stokes V may help to decide whether the content of radio jets is hadronic or leptonic.

Chapter 1

Introduction

> The beauty of electricity or of any other force is not that the power is mysterious, and unexpected, touching every sense at unawares in turn, but that it is under law, and that the taught intellect can even now govern it largely.[1]
>
> *Michael Faraday*

Since the profound discoveries of Faraday and Maxwell in the 19th century, electromagnetic forces are a fundamental fragment of our understanding of nature. Beginning on the smallest scales with description of atoms, the interaction of molecules up to the scales of human interaction with the world, magnetism is ubiquitous and, usually, well described by Maxwell's laws that allow us to govern it.

Yet on the other end of the spectrum of scales, on distances which are necessary to describe the Milky Way and beyond, the observable Universe, the mere existence of magnetic fields, let alone their influence on the formation of structures are very often still mysterious and unexpected. The reason for this is of course not that they would be subject to different laws than their smaller relatives, but that their origin and evolution is hidden in the mysteries of the early Universe. Hence, if we understand the word law in the above quotation as being equivalent to a statement resulting in predictions and explanations of unexpected phenomena, it is surely uncontroversial to say that we have not yet been able to fully embed cosmological and astrophysical magnetic fields into a picture which Michael Faraday might have called beautiful. Consequently, the overall ambition of this thesis is to shed a small amount of light on what is potentially one of the most fruitful sources of information in cosmology and astrophysics.

In the course of this text, I will touch on several manifestations of magnetic fields in the observable Universe, both on cosmological scales and for the case of the Milky Way. The usual goal is to either reconstruct the magnetic field itself or a observable associated to it from available data sets. Irrespective of whether we are interested in three dimensional volumes or projections on the sphere, this reliance on real observational data implies that we naturally will always be dominated by structures close to us. This makes all of the reconstructions presented here ‘ocal’ relative to the scale of the object of interest. In order to to set the stage for the upcoming chapters, in the rest of the introduction contains a short description of both the cosmological and the Galactic environment shall be given.

---

[1] Jones (1870)

In most comprehensive descriptions of the Universe, its state and evolution are, somewhat unsurprisingly, described in terms of its dominant components. In case of the prevalent ΛCDM model these are radiation and matter, temporally encompassed by scalar fields necessary to explain the exponential expansion during inflation and in today’s epoch. Compared to these, large scale magnetic fields lead a somewhat shadowy existence under the reign of the dominating players, as they never reach the energy densities necessary to directly influence the large scale evolution of the Universe. However, they have the attractive property of being extremely stable and resilient in contrast to e.g. large scale electric fields (Grasso & Rubinstein 2001), which allows them to potentially preserve information on the early Universe. In partially motivation by this, several possible mechanisms of primordial magnetogenesis during inflation and the reheating epoch have been conceived, the remnants of which could provide us with important information on these still very poorly constrained ages. Unfortunately, as very often these are based on non standard-model physics, neither of these processes are forced by theoretical necessity or required by observational evidence. This reflects a general problem of primordial magnetic fields, as no unambiguous empirical proof demonstrates their existence. Our best probe of the early Universe, the cosmic microwave background (CMB), excludes magnetic fields with a strength above several nG (Planck Collaboration et al. 2016b). The mere presence of magnetic fields in galaxies and galaxy clusters may be a hint, as the dynamo mechanisms present there need seed fields to be amplified. Unfortunately, these seeds can alternatively be provided by magnetic outflows of galaxies and stars, respectively (Subramanian 2019). Some further indirect hints are given by inspection of the photon energy spectrum of blazars, which lack significant flux in the GeV regime (Neronov & Vovk 2010). The flux would be expected as a result from pair production and annihilation ensuing from TeV photons interacting with the CMB in cosmic voids. Magnetic fields would then lead to a deflection of electrons and positrons, thereby reducing the observed photon flux. But yet again, this claim has been disputed and alternative mechanisms can explain the phenomenon without invoking the existence of magnetic fields (Pfrommer et al. 2013). Even if magnetic fields are the culprit in this case, Langer & Durrive (2018) have shown that these can be generated during the epoch of reionization as well, both in sufficient magnitude and volume filling. However, regardless the somewhat shaky observational status of primordial magnetic fields, the fact that they may contain profound information on the early Universe has sparked continuous interest of cosmologists.

Intriguingly, the existence of a small primordial magnetic field is almost forced by conditions in the radiation dominated epoch of the Universe. As demonstrated by Harrison (1970), the small under-densities present in the matter and radiation fields in the primordial plasma generate vorticity structures, which together with different behavior of the still relativistic electrons and non-relativistic protons, result in a battery effect suitable for magnetic field generation. In the first chapter of this thesis, a three dimensional reconstruction the primordial magnetic field remnant as induced by the Harrison mechanism is presented, constrained by data of today's large scale structure of the Universe. This is first time such a prediction was made for the local Universe. Under the conservative assumptions made here the resulting fields strengths are to low to explain the missing link to today's magnetic fields in galaxy clusters or voids. The work nonetheless opens up a path to make testable predictions for alternative mechanisms of magnetogenesis.

Just as in the case of the evolution of our Universe, magnetic fields lead a somewhat passive existence in the formation of galaxies and clusters, which is dominated by gravitational collapse. Yet this time, this superficial statement does not hold up to closer inspection. Magnetic pressure is comparable to gas and cosmic ray pressure in the late stages of galaxy evolution, which at least makes some relevant influence debatable. Even more importantly, magnetic fields directly impact the distribution of cosmic rays as these diffuse easier along field lines. These highly relativistic particles heavily influence key properties of the interstellar medium such star formation. This makes magnetic fields indirectly an potential major player in shaping their host galaxies (Naab & Ostriker 2017).

The most notable contrast to primordial magnetic fields, however, is the far better observational situation. Magnetic fields have been observed in both galaxy clusters and filaments (Govoni et al. 2019). In galaxies, they have been observed up to red-shift $z \approx 0.5$ with the help of strong gravitational lensing (Mao et al. 2017). Indeed, it seems to be almost impossible to find compact structures in the Universe with no magnetic field associated to them.

Consequently, the problem here is not so much proving the existence of magnetic fields, but to unambiguously determine role in the dynamics of their hosting structures . In order to achieve this, their strength and morphology need to be determined, a task, that is hindered by the fact that all observables to our disposal couple the magnetic field with other quantities in often very non-trivial ways. This means that its usually necessary to additionally constrain e.g. the thermal or relativistic electron density, dust properties or stellar density. In addition to that projections effects further complicate the problem. This is especially severe in our home Galaxy the Milky Way, which although naturally resolvable to unprecedented scale compared to all other galaxies, has the severe disadvantage of being only observable from our position within the Galactic disc. Hence, reconstruction efforts of the Galactic magnetic field have to rely on a variety of sources in order to overcome these problems. In this work, the focus lies on the Faraday effect as such a source of information. Within a magnetized ionized medium, this effect leads to the rotation of linearly polarized light. In this work, the most up to date version of the Galactic sky projection of this effect is given, both in methodology and data. Building on that, additional data sets are used to bypass the problems mentioned earlier. This has enabled the discovery of hidden magnetic structures in the sky and resulted in a first time prediction of the line-of-sight averaged magnetic field strength of the Milky Way.

Chapter 2

The primordial magnetic field in our cosmic backyard

References and Acknowledgment

The work presented in this chapter was previously published in Hutschenreuter et al. (2018). I was the lead author of the paper under the supervision of Torsten Enßlin. I performed the calculation of the initial conditions from today matter density distribution, calculated the magnetic fields up to recombination and wrote the paper apart from the data section (Sect. 2.3). Sebastian Dorn performed preliminary work in his PhD thesis. Franco Vazza implemented the late time simulation and wrote the technical overview over it. Jens Jasche and Guilhem Lavaux provided the large scale structure density distribution, wrote the data section and helped out with bug tracing in the simulation. Daniela Paoletti contributed assistance in the calculation of the cosmological transfer functions. All co-authors helped proofreading the manuscript.

2.1 Introduction

Inference of primordial magnetic fields opens a unique window into the Early Universe between inflation and recombination. Although a variety of different astrophysical processes may generate magnetic fields, the primordial magnetic seed may very well be the origin of observed magnetic fields in galaxies and clusters. Primordial magnetic fields are a viable candidate for the 10^{-16} G to $\approx 10^{-15}$ G (Neronov & Vovk 2010; Neronov & Semikoz 2009; Tavecchio et al. 2010; Dolag et al. 2011) fields expected in cosmic voids due to the non-observation of GeV emission from TeV blazars among other explanations (Pfrommer et al. 2013). In any case, they represent by definition the minimal amount of magnetic fields present in the Universe. Literature provides a variety of very diverse effects for the generation of primordial magnetic fields coherent on a large range of scales. A incomplete list of possible magnetogenesis effects may include mechanisms at the end of inflation (e.g. during the reheating phase or exploiting the electroweak phase transitions), during QCD phase transitions or effects that make use of speculative non-standard model physics such as gravitational coupling of the gauge potential or string theory effects. Very often these mechanisms struggle with producing the necessary field strengths and/or, especially the post inflationary models, the necessary coherence lengths for large-scale magnetic fields. The scale problem might be solved, at least for helical magnetic fields, via an inverse cascade which transfers magnetic power to larger scales (Saveliev et al. 2012, 2013). Recent works have shown that a similar mechanism exists for non-helical fields (Brandenburg et al. 2015), although the process is still poorly understood (Reppin & Banerjee 2017). For a further discussion on different magnetogenesis models, we refer the reader to comprehensive review articles (Kandus et al. 2011; Subramanian 2016; Yamazaki et al. 2012; Durrer & Neronov 2013).

A more conservative Ansatz solely relying on the assumption of a ΛCDM Universe and conventional plasma physics was proposed by Matarrese et al. (2005). This approach is based on a mechanism initially proposed by Harrison (1970). During the later phases of the radiation dominated epoch of the Universe a two fluid battery effect occurred between the proton fluid and the tightly coupled electron-photon fluid. The densities $\rho_{(\alpha)}$, with $\alpha \in \{m, \gamma\}$ for baryons and the electron-photon fluid respectively, of the two components scale with the scale factor $a(t)$ as $\rho_{(\mathrm{m})} \sim a(t)^{-3}$ and $\rho_{(\gamma)} \sim a(t)^{-4}$, respectively. Therefore, the separately conserved angular momenta $L_{(\alpha)} \sim \rho_{(\alpha)}\, \omega_{(\alpha)}\, r^5$ in a rotational setup with radius $r(t) \sim a(t)$ requires the angular velocities $\omega_{(\alpha)}$ to depend on $a(t)$ with $\omega_{(\mathrm{m})} \sim a^{-2}$ and $\omega_{(\gamma)} \sim a^{-1}$, respectively. In other words, protons spin down faster than electrons, as the latter are carried by the still dominant photons. This difference in rotation then leads to currents that induce magnetic fields (Harrison 1970). The necessary vortical motion of both proton and radiation fluid are caused by effects that can be expressed as second order perturbations of the fluid equation (Matarrese et al. 2005).

The recent progress on the inference of the actual 3D realization of the large-scale dark matter structure and its formation history in the Local Universe and the fact that the Harrison mechanism is solely founded on well established plasma physics allows us to calculate the seed magnetic fields that had to be generated by this effect as well as their present day morphology and strength. Since these fields have to exist today in combination with fields of other sources, we are therefore able to provide credible lower bounds on the primordial magnetic field strength in the Nearby Universe. We structure this article as following:

Section 2.2 first summarizes the outcome of Matarrese et al. (2005) and then presents the computational steps that take us from dark matter over densities to magnetic fields. Section 2.3 gives a short overview on the dark matter density reconstruction used in this work. Section 2.4 provides the intermediate results on magnetic field configuration and power spectrum at radiation matter equality. Section 2.5 shows the results of the subsequent MHD simulation. Section 2.6 contains a summary and an outlook on potential improvements.

Parameter	Value
H_0	$67.74\ \mathrm{km\,Mpc^{-1}s^{-1}}$
h	0.6774
Ω_Λ	0.6911
Ω_m	0.3089
Ω_r	$5.389 \cdot 10^{-5}$
Ω_k	0.0
z_{eq}	3371

Table 2.1: Table of cosmological parameters used in this work (Planck Collaboration et al. 2016a).

2.2 Theory

This paper strongly relies on the theoretical framework outlined by Matarrese et al. (2005). This approach describes primordial density perturbations in the Early Universe before the recombination epoch as sources of magnetic fields via the Harrison mechanism (Harrison 1970). In the first part of this section we will summarize their assumptions and results. The second part describes the implemented reconstruction approach to translate our knowledge on dark matter over-densities into magnetic field estimates, first described by Dorn (2016).

2.2.1 Basics

All calculations here are performed using the standard ΛCDM model assuming the cosmological parameters described in Tab.2.1 following the 2015 results of the Planck mission (Planck Collaboration et al. 2016a). Following Matarrese et al. (2005) we further assume that the dominant constituents of the Universe in the relevant time frame behave as perfect fluids of dark matter, electrons, protons and photons. All equations and calculations are performed in Poisson gauge with the following line element:

$$\begin{aligned} ds^2 = \;& a^2(\eta)\,(-(1+2\phi)\,d\eta^2 + 2\chi_i\,d\eta\,dx^i \\ & + ((1-2\psi)\,\delta_{ij} + \chi_{ij})\,dx^i dx^j) \end{aligned} \tag{2.1}$$

a is the scale factor depending on conformal time η. ϕ and ψ are the Bardeen potentials, χ_i and χ_{ij} are vector and tensor perturbations, respectively.
The perfect fluid assumption results in a vanishing anisotropic stress tensor, which yields $\phi = \psi \equiv \varphi$ to first order in perturbation theory.

As perfect fluids are assumed, the energy momentum tensor simplifies to

$$T^{(\alpha)\mu}_{\nu} = (P^{(\alpha)} + \rho^{(\alpha)})\,u^{(\alpha)\mu}u_{(\alpha)\nu} + P^{(\alpha)}\delta^{\mu}_{\nu} \ . \tag{2.2}$$

with $P^{(\alpha)}$ the pressure, ρ_α the density and u^μ_α the bulk velocity for each component α. Pressure and density of a component are related via an equation of state

$$P^{(\alpha)} = w^{(\alpha)}\,\rho^{(\alpha)} \ . \tag{2.3}$$

We define the energy over-density with respect to the mean energy density $\overline{\rho^{(\alpha)}}$ (which is the same quantity as $\rho_0^{(\alpha)}$ in Matarrese et al. (2005)) of a component as

$$\delta^{(\alpha)} = \frac{\rho^{(\alpha)}}{\overline{\rho^{(\alpha)}}} - 1\ . \tag{2.4}$$

All quantities ($\delta^{(\alpha)}, u^{(\alpha)}, \varphi, \chi_i, \chi_{ij}$) can now be perturbed up to second order and related via their respective momentum equations including source terms to describe interactions. The coupling between the baryonic and radiation components is assessed by a tight coupling approximation to zeroth order which implies $v_i^{(p)} \approx v_i^{(e)} \approx v_i^{(\gamma)}$. This sets Thomson and Coulomb interaction terms to zero in this order. The curl of the momentum equations for the proton and photon components of the fluid gives evolution equations for the respective vorticities. The magnetic fields will be generated by vortical structures in the conductive non-relativistic baryonic component. To understand this, however, we turn our eye to the dominating photon component in that fluid. If a fluid component α was considered separately, its vorticity $\omega^{(\alpha)}$ is a conserved quantity as stated by Kelvin's circulation theorem. This holds for each order of perturbation theory separately, in particular for the dominating photons:

$$\omega'^{(\gamma)} = 0. \tag{2.5}$$

Given that we expect no vorticity in the initial conditions, external sources are absent and we have an ideal fluid where pressure and density gradients are aligned, photon vorticity should always be zero. There is however a subtelty that that comes into play due to the fact that photons experience pressure. The photon vorticity equation in second order is (Matarrese et al. 2005)

$$\begin{aligned}\omega_{i\,(2)}^{(\gamma)} = \; & -\tfrac{1}{2a^2}\epsilon_{ijk}\left[a v_{(2)}^{j,k\,(\gamma)} + a\chi_{(2)}^{j,k}\right. \\ & \left. + v_{(1)}^{j\,(\gamma)}\varphi_{(1)}^{,k} + v_{(1)}'^{j\,(\gamma)} v_{(1)}^{k\,(\gamma)}\right]\end{aligned} \tag{2.6}$$

The vorticity of photons in second order perturbation is not equal to the curl of the second order perturbed velocity field, but includes coupled first order terms. Since we need to obeye the conservation law in Eq. (2.5) and these first order terms are non-zero, a curl in the photon velocity field needs to be induced. If we now turn our eye to the proton vorticity equation these squared first order terms are absent due to the vanishing pressure:

$$\omega_{i\,(2)}^{(\mathrm{p})} = -\frac{1}{2a}\epsilon_{ijk}\left[v_{(2)}^{j,k\,(\mathrm{p})} + \chi_{(2)}^{j,k}\right] \tag{2.7}$$

The crucial connection is now that the tight coupling of the fluid components does not couple the vorticities of protons and photons but their velocities. Therefore the right part in Eq. (2.7) is non-zero and acts as a external source term for vorticity. Connecting this with Maxwells equations, we get an equation for the generation of magnetic fields.

In other words the arising proton vorticity needs to be offset by an external (magnetic) force, in order to keep angular momentum conserved. The tight coupling approximation is discussed in more detail in 2.2.3.

Matarrese et al. (2005) expressed the evolution equation for the magnetic field in terms of the first order scalar perturbations of the metric $\varphi_{(1)}$ which in the Newtonian limit gives the gravitational potential. By assuming negligible resistivity and therefore omitting magnetic diffusion terms and performing (at least partially) an analytic integration, they get (Matarrese et al. 2005; Dorn 2016)

$$\begin{aligned} B = \; & -\tfrac{m_p}{e\,a\mathcal{H}^2} \left[2\nabla\varphi' \times \nabla\varphi - \tfrac{1}{12\mathcal{H}}\nabla\left(\Delta\varphi\right) \times \nabla\varphi \right. \\ & \qquad \left. - \tfrac{1}{12\mathcal{H}^2}\nabla\left(\Delta\varphi'\right) \times \nabla\varphi\right] \\ & -\tfrac{1}{a^2}\int_{\eta_I}^{\eta} d\tilde{\eta}\,\tfrac{a}{\mathcal{H}}\,\nabla\varphi' \times \nabla\varphi + \tfrac{a_I^2}{a^2}B_I \end{aligned} \tag{2.8}$$

for the magnetic field at time η, assuming some initial field B_I at time η_I. A prime denotes derivation by conformal time. m_p is the proton mass, e the elementary charge, a the scale factor and $\mathcal{H} = a'/a$ the comoving Hubble constant. In the formulation above, the generation of magnetic fields is the result of a coupling between first order temporal and spatial gradients of the scalar perturbations. In other words, the generation of magnetic fields is the result of dynamics in the gravitational potential, which in turn are a result of the gravitational pull on infalling matter through the horizon and the counteracting radiation pressure. This close connection to the Baryo Accoustic Oscillations (BAOs) will be evident in the power spectra of our results at recombination. Even for $\varphi' = 0$, which is true in the matter dominated era, this terms is not zero, as the second term only depends on spatial gradients. The formulation above is very convenient, as the sole dependence on the scalar perturbations makes the connection to initial conditions and the corresponding state of the Universe today very easy, as will be demonstrated in the next section. The integral term was omitted by Matarrese et al. (2005) in their analysis on the correlation structure of the field. The initial field B_I can safely be set to zero due to the a_I^2/a^2 factor. The assumption of small resistivity can be justified via considering the diffusion timescale

$$\tau_{\text{diff}} = 4\pi\sigma L^2, \tag{2.9}$$

where L typical scale of magnetic structures and σ is the electron conductivity. Electron momentum transfer is dominated via Thomson scattering, we can therefore write $\sigma = \frac{n_e e^2}{n_\gamma m_e \sigma_T}$. Plugging everything in, using the cosmological parameters from the Planck mission (Planck Collaboration et al. 2016a) e.g. at recombination and $L \approx 1\,\text{Mpc}$, yields

$$\tau_{\text{diff}} \approx 10^{42}\,\text{s}, \tag{2.10}$$

which is orders of magnitude higher than the age of the Universe at $t_{\text{U}} \approx 4.4 \cdot 10^{17}\text{s}$. Therefore once generated magnetic structures survive for a very long time and ignoring the diffusion term is justified. In general, this is true throughout the history of the Universe, at least after inflation and on large scales (Turner & Widrow 1988). High conductivity also implies flux freezing, which will lead to magnetic field amplification during structure formation in the late time evolution of the magnetic field as we will see in our results.

In the following we discuss the implementation of equation (2.8).

2.2.2 Implementation

We now need to calculate φ and its spatial and temporal derivatives with respect to conformal time. We begin our calculation by translating the CDM density perturbations measured[1] shortly before the last scattering surface $\delta_{\mathrm{cdm}}(z \approx 1000)$ into primordial initial conditions deep inside the radiation epoch at z_{p}. Magnetogenesis can only take place on scales which have entered the cosmic horizon at the corresponding epoch. Therefore it makes sense to make this the criterion for z_{p}. We know that the horizon condition can be roughly written as

$$k_{\mathrm{h}} \cdot \eta_{\mathrm{h}} \approx 1 \tag{2.11}$$

with the conformal time measured in units of one over length, the speed of light set to one and with η indicating conformal time. Knowing that the smallest scales of the grid correspond to $k_{256} \approx 2.39\, h\,\mathrm{Mpc}^{-1}$ and $k_{512} \approx 4.78\, h\,\mathrm{Mpc}^{-1}$ with respective grid sizes of 256 and 512 points respectively, we know that the initial times must be on the order of the grid resolution $\eta_{256} \approx 0.42\,\mathrm{Mpc}\, h^{-1}$ and $\eta_{512} \approx 0.21\,\mathrm{Mpc}\, h^{-1}$ with the speed of light set to one. The equivalent redshifts are $z_{256} \approx 9.7 \cdot 10^5$ and $z_{512} \approx 1.9 \cdot 10^6$. Finally, $z_{\mathrm{p}} = 10^7$ was adopted in this work, as it safely satisfies the aforementioned condition. We obtain $\delta_{\mathrm{cdm}}(z_{\mathrm{p}})$ by using linear cosmological transfer functions and calculate the total energy over-densities $\delta_{\mathrm{tot}}(z_{\mathrm{p}})$ from it,

$$\delta_{\mathrm{tot}}(z_{\mathrm{p}}) = \frac{4}{3}\delta_{\mathrm{cdm}}(z_{\mathrm{p}}) = \frac{4}{3}T(k, z_{\mathrm{p}}, z_{\mathrm{rec}})\, \delta_{\mathrm{cdm}}(z_{\mathrm{rec}}) \tag{2.12}$$

The 4/3 factor comes from the adiabatic super-horizon solutions for the density perturbations (see e.g. Ma & Bertschinger (1995)). The transfer functions $T(k, z_{\mathrm{p}}, z_{\mathrm{rec}})$ in Poissonian gauge were calculated by the CLASS code (Blas et al. 2011). They contain all relevant physics at linear order.

The peculiar gravitational potential $\varphi(k, \eta)$ in the radiation epoch (implying $w^{(\gamma)} \approx 1/3$) evolves as (see, e.g., Matarrese et al. (2005))

$$\varphi(k, \eta) = \frac{3\, j_1(x)}{x}\varphi_0(k) \tag{2.13}$$

in Fourier space with initial conditions φ_0 at redshift $z = 10^7$, j_1 is the spherical Bessel function of first order and

$$x = \frac{k\,\eta}{\sqrt{3}}. \tag{2.14}$$

Furthermore, the linearised Einstein equations relate the total energy perturbations to the potential by

$$\delta_{\mathrm{tot}} = \frac{2}{3\mathcal{H}^2}\left(\Delta\varphi - 3\mathcal{H}\left[\varphi' + \mathcal{H}\varphi\right]\right). \tag{2.15}$$

---

[1] For further comments on the data see section 2.3 and (Jasche et al. 2015)

With this equation we can calculate the initial φ_0 in Fourier representation as

$$\varphi_0(k) = \frac{3\,\mathcal{H}^2}{2k^2\,\frac{j_1(x)}{x} - 6\mathcal{H}\left[\frac{\partial}{\partial\eta}\left(\frac{j_1(x)}{x}\right) + \mathcal{H}\frac{j_1(x)}{x}\right]}\,\delta_{\text{tot}}. \tag{2.16}$$

From there on we can use Eq. (2.13) again to calculate the potential and its derivatives at any time up to z_{eq}.

The potential φ will tend to a constant after radiation-matter equality, as pressure becomes negligible. This means that the first and third term in Eq. (2.8) do not contribute to magnetogenesis from the epoch of radiation-matter equality to recombination. We therefore evaluate these terms at radiation matter equality ($z \approx 3371$). From there on, these magnetic field terms are then propagated to recombination at redshift $z = 1088$ via the induction equation of magneto-hydrodynamics (MHD) (assuming again perfect conductivity):

$$\frac{\partial B}{\partial\eta} = \nabla \times (v \times B) \tag{2.17}$$

The fluid velocity v is also calculated in first order perturbation theory. The second term of equation (2.8) contains no time derivative of the potential and is therefore evaluated at recombination ($z = 1088$).

We illustrate the steps of the calculation in Fig. 2.1.

2.2.3 Simplifications

This calculation contains simplifying assumptions to keep the evolution equation for the magnetic field anaytically solvable. For completeness, those shall be discussed here.

The evolution of the potential via Eq. (2.13) is performed for a radiation dominated Universe with an equation of state given in Eq. (2.3). The transition to the matter dominated era is modelled in an abrupt way with $w = \frac{1}{3}$ before equality and $w = 0$ afterwards. As the real transition is smooth, scales in the order of the equality horizon maybe affected by the modelling and magnetogenesis may even take place even after recombination. A heuristic modelling via e.g. hyperbolic functions was not performed as the additional time dependence makes the evolution equations for the potential not analytically solvable. This could be incorporated in the model if needed for the price of more contrieved calculations. Related to that, the coupling between electrons and photons is modelled via the tight coupling approximation as mentioned earlier. Thomson scattering is very efficient for scales larger than the mean free path of the photons, which at recombination can be estimated via

$$d_{\text{Thomson}} = \frac{1}{n_e a \sigma_T} \approx 2\,\text{Mpc}\,h^{-1} \tag{2.18}$$

in comoving scales. As we will see in the next section, our calculation is performed on a $\approx 1.3\text{Mpc}\,h^{-1}$ grid. Therefore the tight coupling should ideally be expanded to higher order in case of the Thomson coupling.

The above mentioned shortcomings where overcome by more detailed studies on the the generation of primordial magnetic fields via the Harrison mechanism, which have been conducted by several authors in the past 15 years. Gopal & Sethi (2005) showed that differences between electron and photon velocities lead to source terms for magnetic field generation. Saga et al. (2015) and Fenu et al. (2011) have refined this calculation by including anisotropic stresses stemming from the imperfect Thomson coupling. A similar calculation was done by Christopherson et al. (2011) first on the generation of vorticity in second order and later on the subsequent magnetic field generation (Nalson et al. 2014) via the introduction of non-adiabatic pressure terms.

All of these approaches give source terms on which the Harrison mechanism can operate. The corresponding equations can in principle all be solved given suitable initial conditions. Only the approach shown above, however, gives an analytically integrable expression. All other models require the iterative solution of the respective magnetic field evolution equation in combination with all relevant quantities throughout the whole plasma era of the Universe up until recombination. This requires considerable computational effort to be implemented on the 512^3 voxel grid used in this work. For this reason, and as the field strengths which were found in (Gopal & Sethi 2005; Saga et al. 2015; Nalson et al. 2014; Fenu et al. 2011; Fidler et al. 2016) are comparable to the ones found by Matarrese et al. (2005), we find the above mentioned simplifications acceptable. Fidler et al. (2016) show that the exact treatment of the Thomson coupling gives rise to significant magnetogenesis even after last scattering, which highlights that a better modelling around recombination would be desirable, given that one can shoulder the resulting computational complications.

2.3 Data

This work builds upon three dimensional dark matter density fields previously inferred from the 2M++ galaxy compilation (Lavaux & Hudson 2011) via the BORG algorithm (Lavaux & Jasche 2016). The `BORG` algorithm is a full scale Bayesian inference framework aiming at the analysis of the linear and mildly-non-linear regime of the cosmic large scale structure (LSS) (Jasche & Wandelt 2013; Jasche et al. 2015). In particular it performs dynamical LSS inference from galaxy redshift surveys employing a second order Lagrangian perturbation model. As such the `BORG` algorithm naturally accounts for the filamentary structure of the cosmic web typically associated to higher order statistics as induced by non-linear gravitational structure formation processes. A particular feature, relevant to this work, is the ability of the `BORG` algorithm to infer Lagrangian initial conditions from present observations of the galaxy distribution (Jasche & Wandelt 2013; Jasche et al. 2015; Lavaux & Jasche 2016). More specifically the algorithm explores a LSS posterior distribution consisting of a Gaussian prior for the initial density field at a initial scale factor of a = 0.001 linked to a Poissonian likelihood model of galaxy formation at redshift z = 0 via a second order Lagrangian perturbation theory (2LPT) model [for details see (Jasche & Wandelt 2013; Jasche et al. 2015; Lavaux & Jasche 2016)], that is conditioned to the 2M++ galaxy compilation (Lavaux & Jasche 2016). Besides typical observational sys-

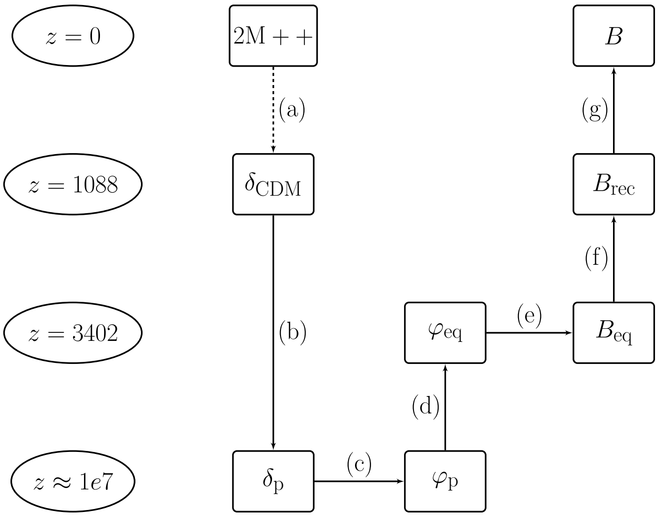
$z = 0$
$2M++$
B
(a)
(g)
$z = 1088$
δ_{CDM}
B_{rec}
(f)
$z = 3402$
(b)
φ_{eq}
(e)
B_{eq}
(d)
$z \approx 1e7$
δ_{p}
(c)
φ_{p}

Figure 2.1: An illustration of the implemented algorithm. The ellipses indicate relevant redshifts. The labels near the arrows refer to the following steps: (a) Dark matter inference from galaxy data via `BORG`, (b) Linear dark matter transfer functions (Eq. 2.12), (c) translation of dark matter density to potential φ (Eq. 2.16), (d) time evolution of the potential via Eq. 2.13, (e) calculation of the magnetic field (Eq. 2.8), (f) induction equation (Eq. 2.17), (g) full MHD solver (see section 2.4)

tematics and uncertainties, such as survey geometries, selection functions and noise this algorithm further accounts for luminosity dependent galaxy bias and performs automatic noise calibration (Lavaux & Jasche 2016). The `BORG` algorithm accounts for all joint and correlated uncertainties in inferred quantities by performing a Markov Monte Carlo chain in multi-million dimensional parameter spaces via an efficient implementation of a Hamiltonian Monte Carlo sampler (Jasche & Wandelt 2013). As a result the algorithm provides a numerical representation of the LSS posterior in the form of data constrained realizations of the present three dimensional dark matter distribution and corresponding initial conditions from which it formed. It is important to remark that each individual Markov sample qualifies for a plausible realisation of the LSS. Each sample of the dark matter distribution consists of a box with 256^3 grid points and $677.7\,\mathrm{Mpc}\,h^{-1}$ edge length, resulting in a resolution of approximately $2.5\,\mathrm{Mpc}\,h^{-1}$. For one sample of `BORG` we increase the resolution of the grid to 512^3 by augmenting the large scale modes with random fluctuations consistent with the known dark matter power spectrum. This sample is then propagated into todays configuration via a MHD simulation as explained in the following section. As described above we now apply the Harrison mechanism on data constrained initial conditions of the Nearby Universe.

2.4 MHD simulations

The MHD computation is started from the magnetic field generated at $z = 1088$ and is evolved to $z = 0$ using the cosmological code `ENZO` (Bryan et al. 2014). `ENZO` is a grid based code that follows the dynamics of dark matter with a particle-mesh N-body method, and a combination of several possible shock-capturing Riemann solvers to evolve the gas component (Bryan et al. 2014). The MHD method employed in this paper is the Dedner "cleaning" method (Dedner et al. 2002), which makes use of hyperbolic divergence cleaning to keep the (spurious) divergence of the magnetic field as low as possible during the computation. The magnetic fluxes across the cells are computed with a piecewise linear interpolation method and the fluxes are combined with a Lax-Friedrichs Riemann solver, with a time integration based on the total variation diminishing second order Runge-Kutta scheme (Wang & Abel 2009). Thanks to the capabilities of `ENZO` of selectively refining interesting patches in the domain at higher resolution, we used adaptive mesh refinement (AMR) to selectively increase the dynamical resolution in the formation region of galaxy clusters and groups, which is necessary to properly resolve structure formation and overcome the effect of magnetic field dissipation in converging flows at low resolution (Vazza et al. 2014).

In detail, we apply AMR only in the innermost $(120\,\mathrm{Mpc}\,h^{-1})^3$ region of the simulation, centred on the Milky Way location, and allowed for 5 levels of refinement (by increasing the resolution of a factor 2 at each level, therefore up to a $2^5 = 32$ refinement) whenever the local gas/dark matter density exceeded the mean density of surrounding cells by a factor of 3; the procedure is recursively repeated at each AMR level. This ensures that the magnetic field evolution in the innermost clusters regions is typically followed with a spatial resolution of $61 - 122\,\mathrm{kpc}\,h^{-1}$ (comoving) within the innermost AMR region of our volume. To confirm the consistency of our result, we show a slice through the gas density resulting from the simulation in Fig. 2.2. This plot indicates that we reproduce the large scale structure consistently with observations.

2.5 Reconstructing primordial magnetic fields

We will present the results of our work in two steps. First we focus on the statistical properties of the field at recombination. By applying the procedure described in the previous sections to an ensemble of data constrained initial conditions we can propagate observational uncertainties of the matter distribution as traced by the 2M++ survey to the derived magnetic fields. In doing so we arrive at an ensemble of initial magnetic fields which constitutes a numerical description of the magnetic field posterior distribution at redshift $z = 1088$ conditional on 2M++ galaxy data. The goal here is to show how these uncertainties translate onto the calculated primordial magnetic field and to give scale dependent estimates on correlations and field strengths at this epoch.

The second part will show the results after the MHD run at redshift $z = 0$. Here we will also turn our face on one particular realisation of the primordial magnetic field. We will show the large scale primordial magnetic field of some clusters of galaxies as well as the field in the close proximity to Earth. The resulting fields are available for download at [2].

2.5.1 Recombination

Means and Variances

To illustrate the uncertainties we show slice plots of the input data and the resulting magnetic field strength at recombination in Figs. 2.3 and 2.4. All plots are slices through the $(677.7\,\mathrm{Mpc}\,h^{-1})^3$ cube. The first plot shows the field resulting from one particular sample of the BORG algorithm. The comoving root mean square (rms) field strength is around $10^{-23}\,\mathrm{G}$. The uncertainties are rather large compared to the mean. This is a consequence of the sparse data, which is more constraining on the large scales than the small ones. Structures in the field appear to be rather small, typically with Mpc-scale (see Section 2.5.1).

Figs. 2.3 and 2.4 give an impression of the Bayesian properties of the BORG algorithm, which is translated onto our magnetic field realisations. They show the posterior mean and variance field of the magnetic field strength generated from 351 samples from the BORG posterior distributions. Areas which are highly constrained by data have well distinguishable structures in the mean, and have low uncertainty variance. The outer regions are less

---

[2] `https://wwwmpa.mpa-garching.mpg.de/~ensslin/research/data/data.html` or doi:10.5281/zenodo.1190925

	Planck(2015)	This work
$\ln(10^{10}\mathcal{A}_s)$	3.064 ± 0.023	≈ 3.1
n_s	0.9667 ± 0.0040	≈ 1

Table 2.2: Comparison of inflation parameters provided by the Planck collaboration (Planck Collaboration et al. 2016) and as inferred from the samples used in this work.

constrained, structures which are well visible in one particular sample are averaged out in the mean, and the variance is high.

Power spectra

Information on the correlation structure of a scalar field $s(x)$ can be gained from the corresponding scalar power spectrum defined as:

$$\langle s(k)s^*(k')\rangle_{P(s)} = (2\pi)^3\,\delta(k-k')\,P_s(k) \tag{2.19}$$

where the asterisk denotes the complex conjugate. In case of a magnetic field B, the statistically isotropic and homogeneous correlation tensor is defined as

$$\langle B_i(k)B_j^*(k')\rangle_{P(B)} = (2\pi)^3\,\delta(k-k')\,M_{ij}(k), \tag{2.20}$$

where the tensor M_{ij} is defined as (see e.g. (Durrer & Caprini 2003)):

$$M_{ij} = \frac{1}{2}\left(\delta_{ij} - \hat{k}_i\hat{k}_j\right)P_{\mathrm{B}}(k) + i\epsilon_{ijk}\hat{k}_k P_{\mathrm{H}}(k). \tag{2.21}$$

The helical part $P_{\mathrm{H}}(k)$ is assumed to be zero in this work. The magnetic field power spectra are therefore just the trace component of the magnetic field power spectrum tensor.

As a consistency check we first show the power spectrum of the initial CDM field and the scalar perturbations φ through some of the time steps of the algorithm in Figs. 2.5, 2.6 and 2.7. These plots show the averaged spectra from 351 samples from `BORG` together with the corresponding uncertainties. We also show the magnetic field power spectrum in Fig. 2.8.

Despite some deviations on very large scales reflecting the uncertainties mentioned in the previous section, the spectra agree to a very good level with our expectations. These deviations can be noted in our intitial matter fields coming from the `BORG` algorithm (Fig. 2.5) and further on in all the other averaged power spectra. We note a clear k^{-3} dependence in the primordial potential and matter power spectrum corresponding to an approximately unity spectral index as expected for uncorrelated and scale invariant structures (Harrison 1970; Zeldovich 1972). We can compare the spectrum with the Planck results as a consistency check, see Tab. 2.2 and the dashed line in Fig. 2.6.

The potential power spectrum at matter-radiation equality drops shortly above $k = 0.1\,\mathrm{Mpc}^{-1}\,h$, indicating the size of the horizon at that time. At small scales, the spectrum shows oscillations in Fourier space, which stem from the functional form of the potential evolution equation in Eq. (2.13). Physically speaking, these are the Baryon-accoustic oscillations (BAO's) induced by horizon crossing during the radiation epoch. The uncertainties again agree with the initial dark matter spectrum. The resulting power spectrum of the magnetic field is plotted in Fig. 2.8. It rises for small k-values with approximately $k^{3.5}$ as expected for a uncorrelated source-free vector field (Durrer & Caprini 2003) and peaks at $k_{\text{peak}} \approx 2 \cdot 10^{-1}\,\text{Mpc}^{-1}\,h$. The plot shows little 'bumps' on small scales, which are remnants of the oscillating potential in the radiation epoch. At this point it shall also be noted that in the time frame of our calculation any turbulence due to primordial velocity perturbations is not relevant. In Wagstaff et al. (2014) the authors show that given these perturbations the very Early Universe has Reynolds numbers in the range of 10^3. This then gives the perfect framework for a small-scale dynamo to amplify the magnetic seed fields originating from the Harrison effect to fields with strengths of approximately $10^{-15}\,\text{G}$, but with typical correlation lengths of the order of parsecs. Given the Mpc resolution of our grid, this is not relevant for this work.

Scale dependent mean field

To give a more intuitive picture of the expected magnetic field strengths, we convolve the magnetic field power spectrum with a Gaussian kernel in position space to get an estimate for B given a scale of reference λ.

$$B_\lambda^2 = \frac{1}{(2\pi)^3} \int P_B(k)\, e^{-\frac{k^2\lambda^2}{2}} d^3k \tag{2.22}$$

The result of this operation is shown in Fig. 2.9. For scales reaching from $2.65\,\text{Mpc}\,h^{-1}$ to $\approx 10\,\text{Mpc}\,h^{-1}$ the magnetic field strength weakly declines and has a typical strength of approximately $10^{-23}\,\text{G}$. For scales larger than $10\,\text{Mpc}\,h^{-1}$, B_λ roughly scales as

$$B_\lambda \sim \lambda^{-2.5}. \tag{2.23}$$

The field strength reaches from $10^{-23}\,\text{G}$ at the smallest scales just over $1\,\text{Mpc}\,h^{-1}$ to less than $10^{-27}\,\text{G}$ at scales over a $100\,\text{Mpc}\,h^{-1}$. This information is of course closely related to the magnetic field power spectrum.

2.5.2 Today

Field strength and correlation structure

In Figs. 2.10a we depict the power spectrum of the magnetic field today for one sample of the `BORG` posterior. We show the complete spectrum as well as the void power spectrum inferred via negleting dens voxels with gas density $\rho > 3 \cdot \overline{\rho}$ and the critical filter technique (Knollmüller et al. 2017a), which assumes that the unmasked regions are typical for the whole volume. The BAO signature and most small structures have been destroyed during structure formation, leading to a mostly red spectrum. For the complete spectrum and the voids, most power still lies on scales of about $k_{\text{peak}} \approx 10^{-1}\,\text{Mpc}^{-1}\,h$. The morphology of the complete power spectrum is rather similar to the void power spectrum, which is expected, as they compromise the largest volume share of the Universe and calculating a power spectrum is effectively a volume averaging procedure. The decrease at large scales again reflects the solenoidality of magnetic fields ($\nabla \cdot B = 0$) for uncorrelated signals (Durrer & Caprini 2003), as the large scale structure has a characteristic size and therefore larger scales are not strongly causally connected via gravity.

In Fig. 2.10b we show the joint probability function of matter density and magnetic field strength. Most of the probability mass lies on rather small densities, with varying magnetic field strengths. Large densities tend to be associated with large magnetic field strength. The lower bound of this plot follows a $B \propto \rho^{\frac{2}{3}}$ proportionality, which was already found in previous simulations, e.g. Vazza et al. (2017). All in all this leads to the picture that the magnetic field in the low density areas which are relatively little affected by structure formation mostly retain their correlation structure and morphology. After recombination, the field is frozen into the plasma. Therefore the field strength scales with $a(t)^{-2}$, explaining the field strengths somewhere around 10^{-29} G. Within dense structures the field is at least amplified up to $10^{-26.5}$ G. We underline this view with specific examples in the next chapter.

Field realisations

In Figs. 2.11 and 2.12 we show structures in the magnetic field and the density field which belong to different morphological features of the Local Universe. We find that the magnetic field strength strongly correlates with the gas density in all of these structures, consistent with a frozen-in behaviour of magnetic fields. In very dense clusters such as Virgo and Perseus-Pisces in Fig. 2.11, the magnetic field morphology seems to be driven by the infall of matter on the cluster. Of course the simulation is too coarse to correctly cover the structure formation and magnetic field behaviour on small scales within these structures, for this reason any small scale structures in these plots are highly uncertain. Also the maximum magnetic field strength maybe higher, as we cannot resolve any potential dynamo mechanism during structure formation. In underdense regions as depicted in the upper image in Fig. 2.12, we observe a morphology similar to the initial conditions, with a characteristic scale of a few Mpc/h. Apart from the aforementioned $a(t)^{-2}$ dependence of the field strength, the morphology seems to relatively unaffected, which is consistent with our view of a 'frozen' magnetic field. In the lower image of Fig. 2.12 we show the magnetic field in a slice around our galaxy. The field here is slightly amplified up to field strengths of 10^{-28} G, as a slight overdense structure seems to have formed in the region, which may correspond to the Local Group. The Local Group has a typical scale of about 2 Mpc, which is slightly below the smallest data constraint scale in our calculation, making the association difficult.

Full sky maps

We can use the results of the `ENZO` simulation to estimate the expected Faraday rotation of linear polarized light under the influence of a magnetic field. Faraday rotation measure (RM) is calculated via

$$\mathrm{RM} = \frac{e^3}{2\pi m_e^2 c^4} \int_0^{R_{\max}} n_{\mathrm{th}}\, B\, dr \tag{2.24}$$

in cgs units (see e.g. Oppermann et al. (2012c)). It is essentially a line of sight (LOS) integration up to a distance $R_{\max}$ over the magnetic field B weighted with the electron number density n_{th}. This can be computed using the publicly available Hammurabi Software (Waelkens et al. 2009a), which performs the necessary LOS integration over a sphere around the Earth[3]. The result can be seen in Fig. 2.15. The same software is also able to calculate the dispersion measure of electrons (DM)

$$\mathrm{DM} = \int_0^{R_{\max}} n_{\mathrm{th}}\, dr \tag{2.25}$$

and the LOS averaged absolute magnetic field strength, shown in Figs. 2.16 and 2.13. These maps nicely trace dense structures in the sphere over which we integrated. We also used the output of Hammurabi for the LOS perpendicular components of the magnetic to generate a polarization like plot in Fig. 2.14, which traces the magnetic field morphology in the sphere. Comparing the plots we see that areas of large RM correspond to large electron densities, as we expect given the linear n_{th} dependence of RM. We also note again that the magnetic field strength and morphology correlates with the density.

Of course the expected signal is beyond any chance of measurability, and in the realistic case we expect that the memory of any such tiny seed field within clusters is entirely lost due to the dynamo amplification process (Beresnyak & Miniati 2016), which is expected to be much more efficient on scales smaller than what is resolved at our resolution here. The void signal, however, although a few order of magnitudes smaller, may be relatively undisturbed by such processes, at least away from other possible sources of magnetisation, like dwarf galaxies (Beck et al. 2013).

2.6 Summary and Discussion

We calculated the large scale primordial magnetic field originating from the Harrison effect (Harrison 1970) and second order vorticity generation in the radiation dominated era. This is the first time a data constraint reconstruction of the remnant of a primordial magnetic field was achieved.

For that, we used our knowledge about the large scale structure in the Universe coming from the 2M++ galaxy survey and the `BORG` algorithm to infer the corresponding density distributions deep in the radiation epoch. Using an existing formalism for the magnetic field generation from these initial conditions, we then found at recombination a field coherent on comoving scales in the $10\,\mathrm{Mpc}\,h^{-1}$ regime, with a maximum field strength of about $10^{-23}\,\mathrm{G}$ at these scales. By means of a MHD simulation we evolved the magnetic field through structure formation and came up with field strengths higher than $\approx 10^{-27}\,\mathrm{G}$ and $\approx 10^{-29}\,\mathrm{G}$ in clusters of galaxies and voids, respectively. We specifically showed the structure of the field around well known structures in the Local Universe, such as the Virgo and Perseus Pisces cluster.

---

[3] We used a reimplementation of Hammurabi [Wang et al., in prep.]; https://bitbucket.org/hammurabicode/hamx

The above results, including the statistical properties of the magnetic fields, the morphology of the field on above Mpc scales and the expected observables shown in Figs. 2.15 and 2.16 rely only on the assumption of a ΛCDM cosmology and conventional plasma physics. We introduced further simplifications such as the tight coupling approximation and the simplified modelling around the radiation matter equality due to computational constraints. In Fenu et al. (2011) and Saga et al. (2015), the authors calculated the correct evolution equations without these simplifications, leading to slightly different spectra, but comparable magnetic field strengths. Large scale magnetic fields can also be produced by more speculative mechanisms for primordial magnetogenesis, by transferring magnetic energy of small scaled magnetic fields to larger scales via an inverse cascade and by magnetogenesis driven by radiation pressure during reionisation. For this reason, we view our results as a lower limit on the magnetic field strength in the Local Universe. This is especially true for clusters, as for once small scales are not strongly constraint by our data and moreover we where not able to resolve the relevant scales for magnetic field amplification via turbulence, as predicted by e.g. Subramanian et al. (2006). We did arrive at magnetic field strengths which could act as a seed field for the galactic dynamo (Davis et al. 1999), however given the fact that we cannot adequately resolve sub-Mpc scales and galactic magnetic fields maybe explained without a primordial seed, we refrain from giving an estimate to which extent the Harrison magnetic field could have influenced galactic magnetic fields. If the non-observation of TeV-photons from blazars is caused by void magnetic fields of strength 10^{-15} G (Neronov & Vovk 2010; Neronov & Semikoz 2009), our prediction is not sufficient to explain these. However, these (non-) observations can also be explained by other processes as shown by Pfrommer et al. (2013).

Considering the rather conservative assumptions made in our calculations, we can provide a credible lower bound on the strength of the large scale magnetic field today and an impression of its expected morphology. The logical next step building up on this work would be a refinement of the calculation via the implementation of more sophisticated formalisms for the generation of primordial magnetic fields, especially including a more accurate baryon photon interaction treatment.

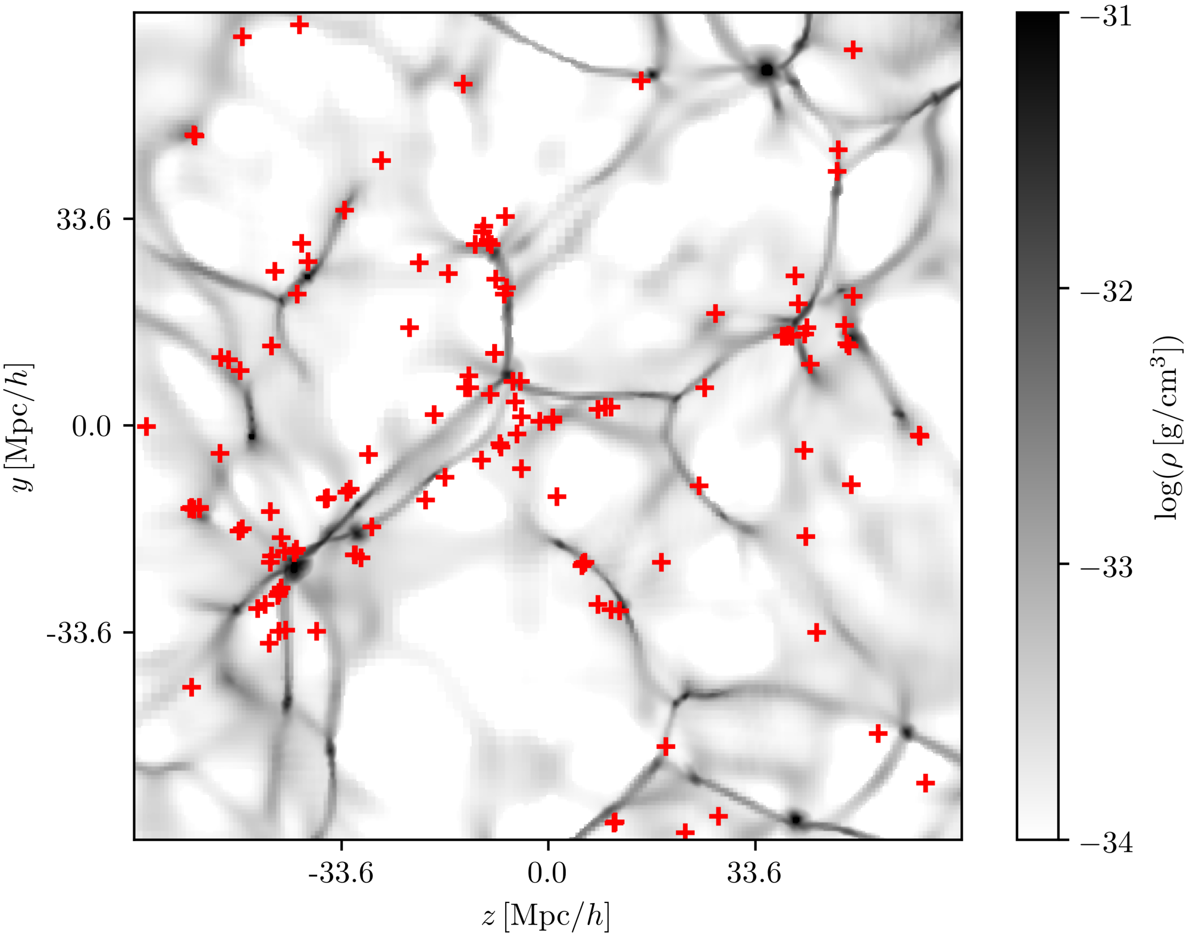

Figure 2.2: A slice through the gas density distribution of the innermost region of the box averaged over 6 voxels in x direction at redshift $z = 0$ as a result of the `ENZO` simulation. The plane is about $1\,\mathrm{Mpc}\,h^{-1}$ thick. The red crosses indicate the positions of galaxies found by the 2M++ survey in the same volume.

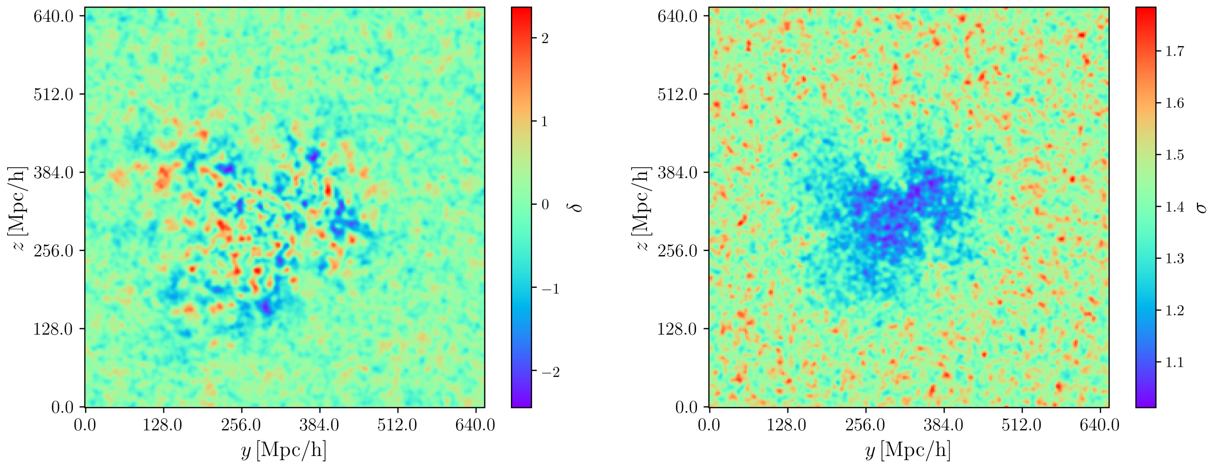

Figure 2.3: The posterior mean (left) and uncertainty standard deviation field of the dark matter overdensities (right) at redshift $z = 1000$. This is the mean of the input data for our calculation averaged over 351 posterior samples of the matter field as generated by `BORG`. Our galaxy is centered in the middle. Areas close to the center a very pronounced in the mean, while areas further away are blurred out during the averaging. This reflects the Bayesian nature of the `BORG` algorithm, as the closer areas are very constrained by data, which leads to a relatively narrow posterior distribution in each pixel as reflected by the uncertainty variance. Therefore each sample looks similar there. The outer regions are barely constrained by data, leading to high uncertainties in the posterior.

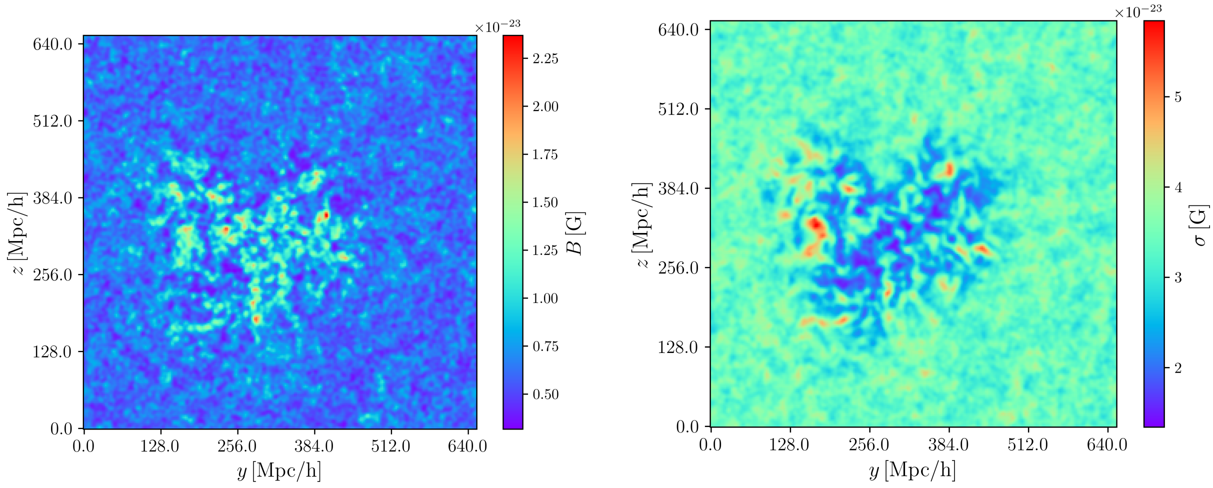

Figure 2.4: The posterior mean (left) and uncertainty standard deviation (right) field of the absolute value of the Harrison magnetic field at redshift $z = 1088$. Just as in the case of the initial data in Fig. 2.3, we note a very similar pattern in the mean and variance plots for regions closer and further away from Earth. The uncertainties of the density fields translate into uncertainties of the magnetic field.

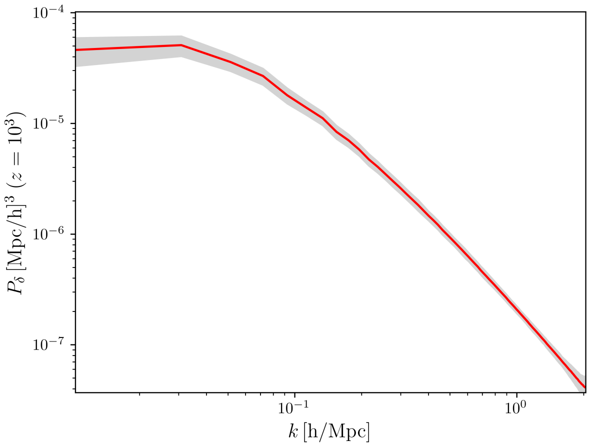

Figure 2.5: The matter power spectrum at $z = 10^3$. This is the spectrum of the input data. The red line is the mean averaged over the 351 samples. The grey area gives the uncertainty in the spectrum.

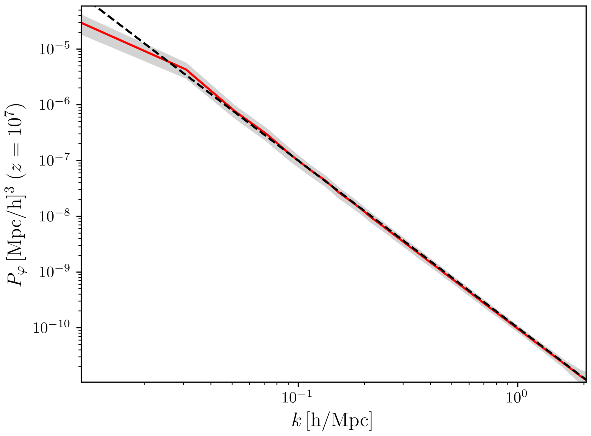

Figure 2.6: The power spectrum of the primordial scalar perturbations at redshift $z = 10^7$ as extracted from the cosmic structure reconstruction by Jasche et al. (2015). The dashed blue line indicates the scale invariant spectrum normalized with the Planck amplitude parameter $\mathcal{A}_s$, see Tab. 2.2.

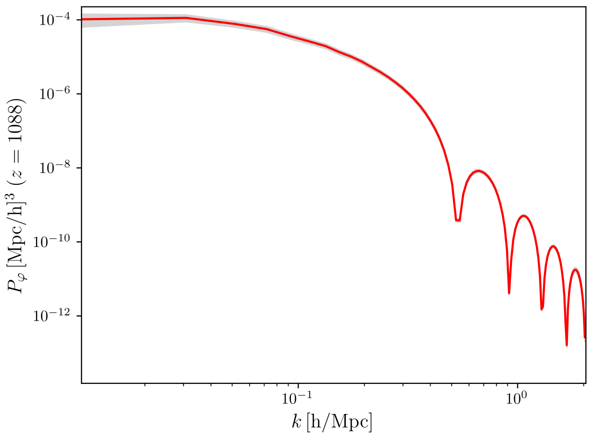

Figure 2.7: The power spectrum of the scalar perturbations at redshift $z = 3402$ at the end of the radiation dominated epoch. The oscillations in the spectrum are the Baryon-Accoustic Osclillations (BAO).

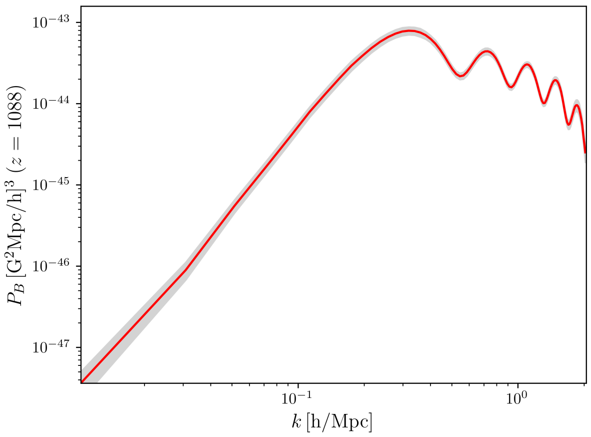

Figure 2.8: The power spectrum of the magnetic field at redshift $z = 1088$ just before recombination. The spectrum is defined of a vector field is defined in Eq. (2.20) and Eq. (2.21). The spectrum peaks at approximately $\approx 3 \cdot 10^{-1}\,\mathrm{Mpc}^{-1}\,h$.

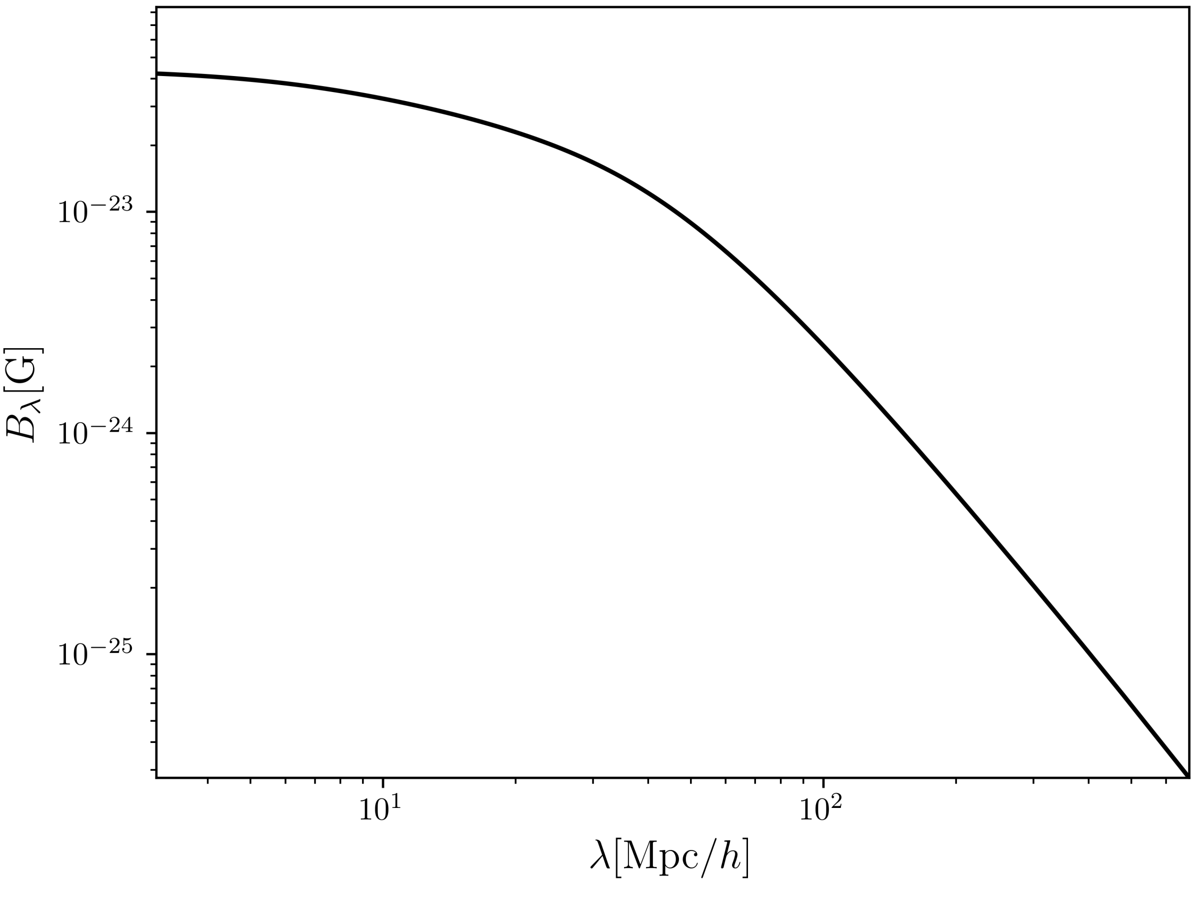

Figure 2.9: Scale averaged magnetic field at recombination. This is the result of Eq. (2.22).

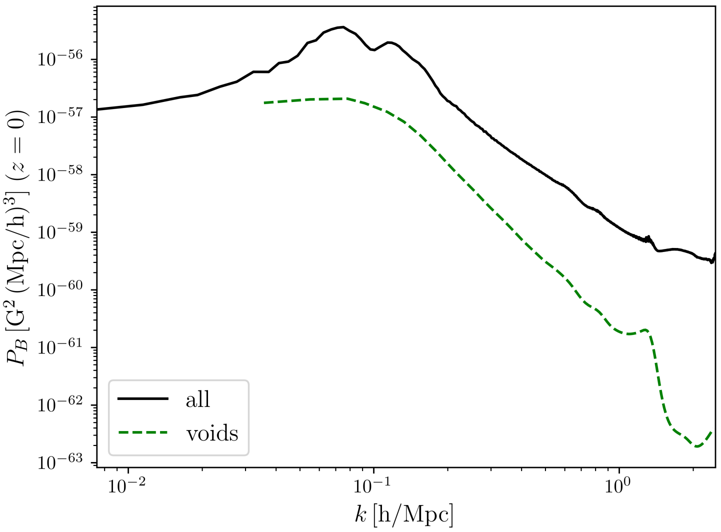

(a) The magnetic power spectrum at $z = 0$, defined according to Eq. (2.20). The black line indicates the spectrum for the complete magnetic field in the box. The green dashed line indicates the void power spectrum, computed only from a part of the box. Here we considered voxels with gas density $\rho < 3 \cdot \overline{\rho}$ as void voxels. The void power spectrum was inferred using the critical filter technique (Knollmüller et al. 2017a), which assumes that the unmasked regions are typical for the whole volume.

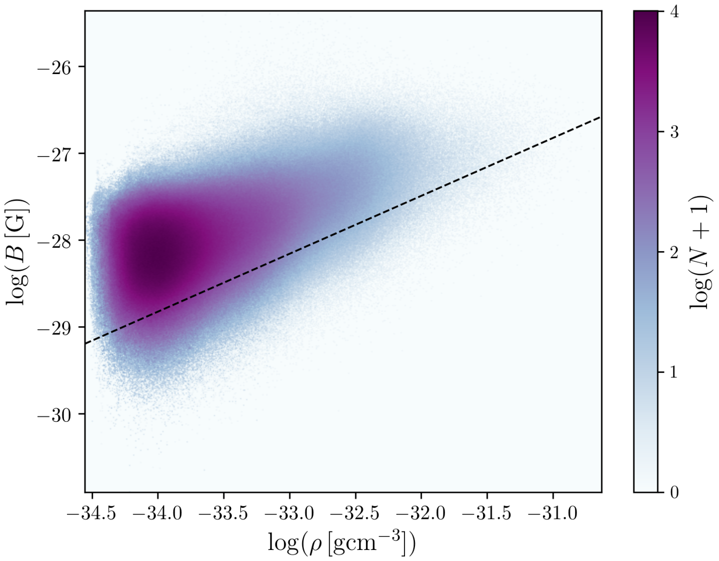

(b) Joint histogramn of the magnetic field and matter density at redshift $z = 0$ with 512^2 bins. The dashed line indicates the $B \propto \rho^{2/3}$ relation resulting from the flux freezing of the magnetic field lines. This relation is also observed in simulations starting with unconstrained magnetic field conditions, see e.g.Vazza et al. (2017).

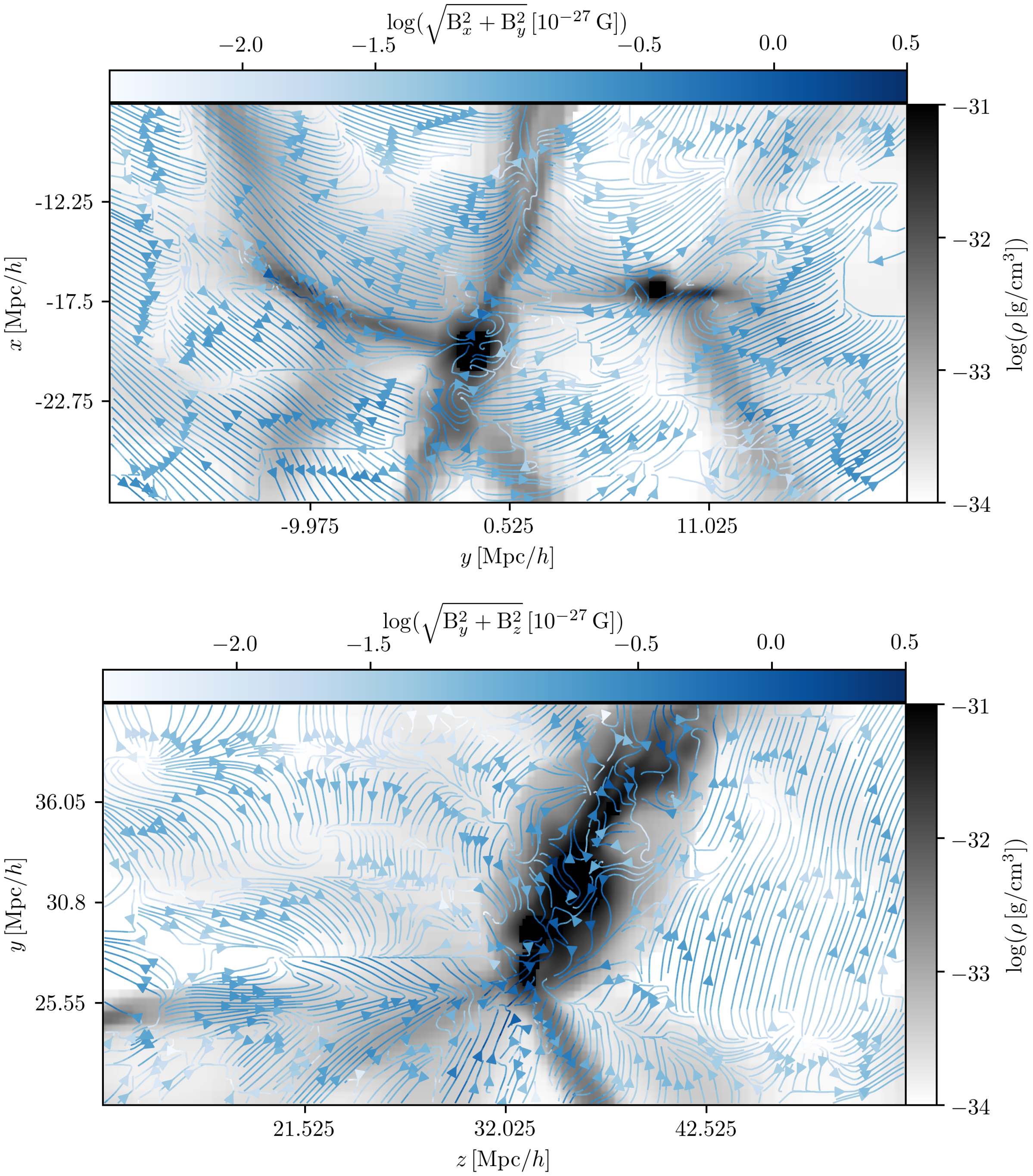

Figure 2.11: The magnetic field and gas matter density in a slice trough the Virgo (above) and the Perseus-Pisces (below) cluster. The plots shows the gas matter density overplotted with the $y - z$ components of the magnetic field vectors. All colorbars have a logarithmic scaling. The coordinates are defined via the equatorial plane with reference to the galactic centre. The choice of the slice is purely for artistic reasons.

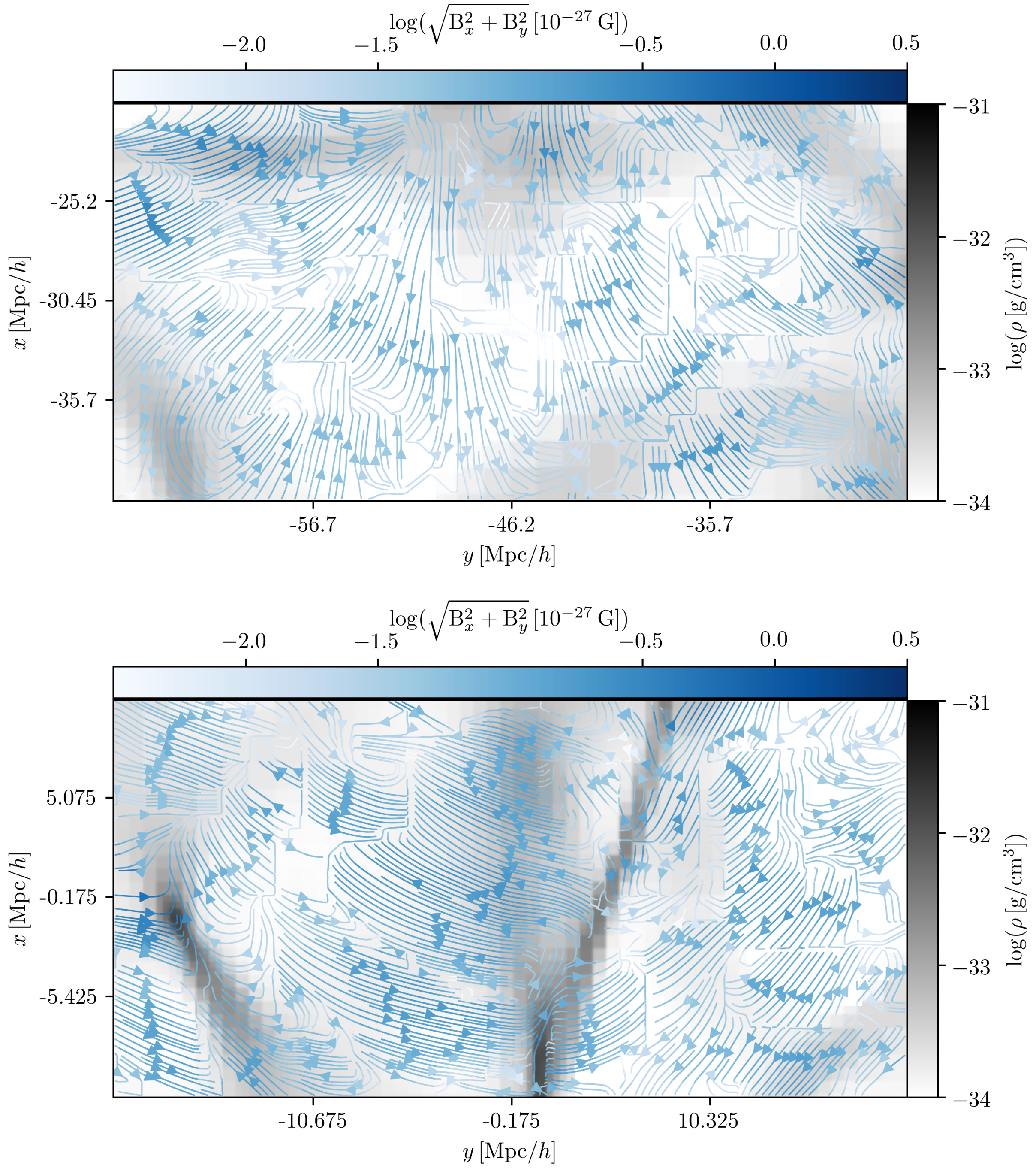

Figure 2.12: The magnetic field and gas matter density in an underdense region (above) and around the galactic center in the $x - y$ plane. The plots shows the gas matter density overplotted with the $x - y$ components of the magnetic field vectors. All colorbars have a logarithmic scaling. The coordinates are defined via the equatorial plane with reference to the galactic centre.

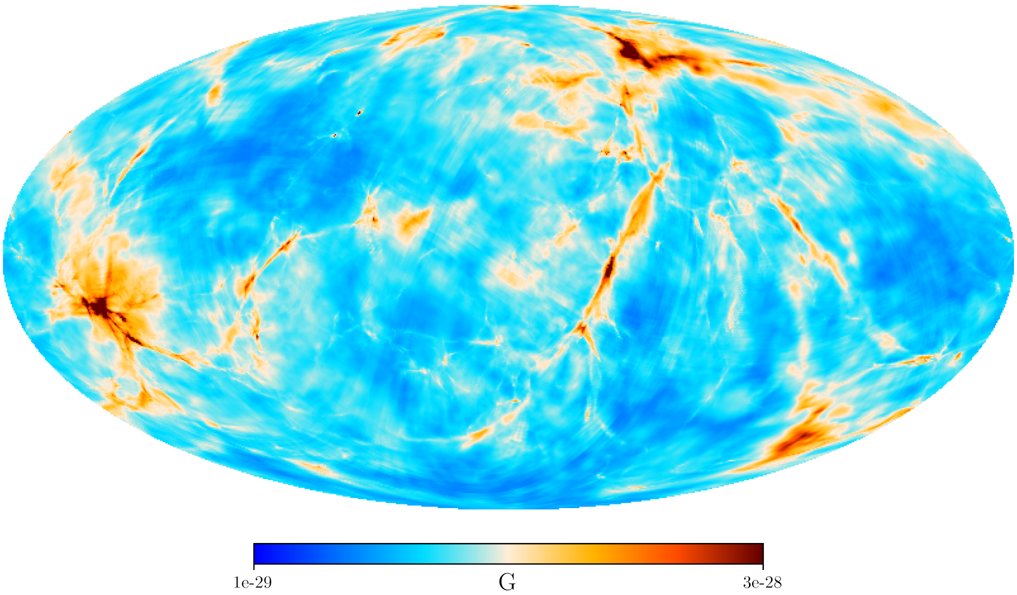

Figure 2.13: The magnetic field strength averaged over line of sights in units of Gauss for sources within a distance of 60 Mpc/h from Earth. The plot is in galactic coordinates. The two dominant clusters in this image are Perseus Pisces in the middle left of the image and Virgo close to the North pole. Close ups of both structures are provided in Fig. 2.11.

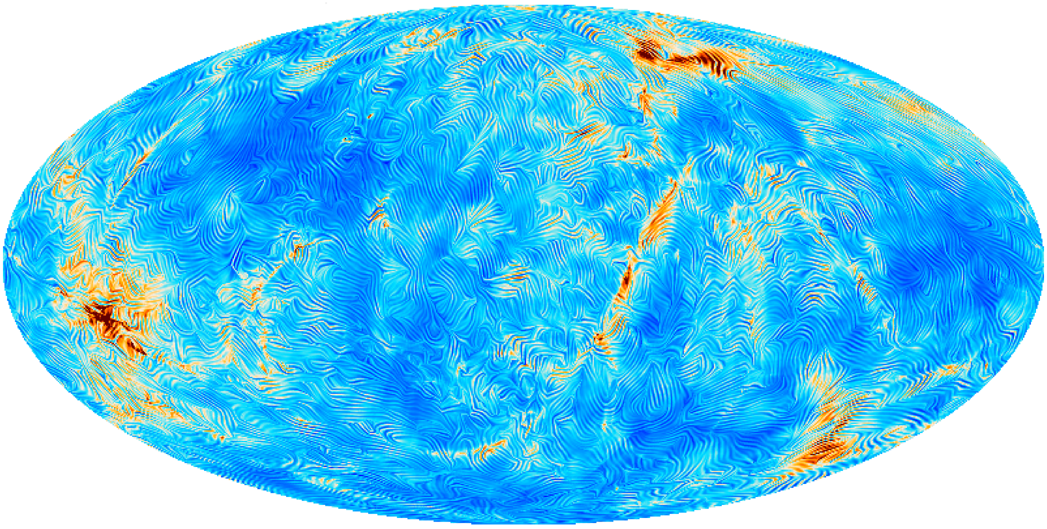

Figure 2.14: A polarization-like plot visualizing the magnetic field morphology perpendicular to the LOS. This plot was generated using the 'Alice' module of the HEALPix software and the linear integral convolution algorithm (Cabral & Leedom 1993). The plot is in galactic coordinates.

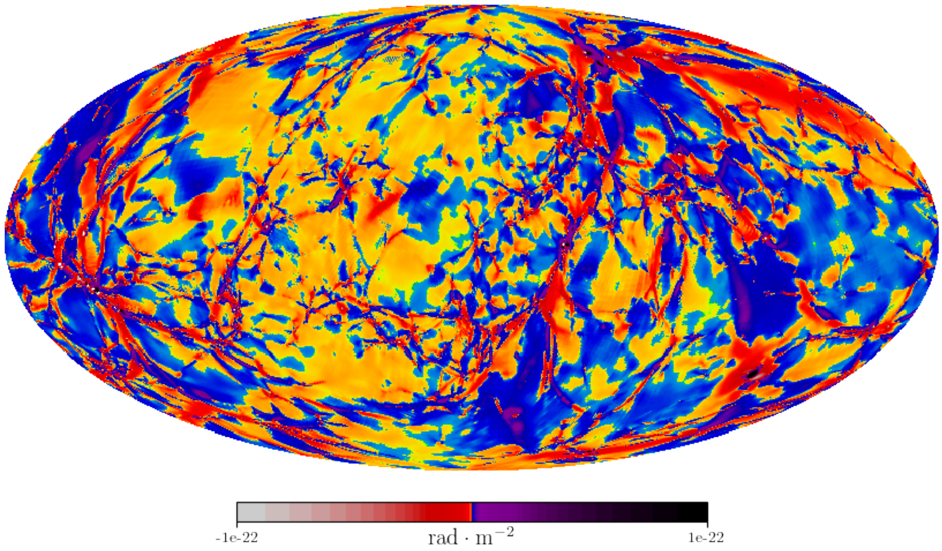

Figure 2.15: The primordial magnetic field Faraday rotation measure for polarized sources located within a distance of 60 Mpch^{-1} from earth in units of radians per square metre. The plot is in galactic coordinates. The colormap is logarithmic on both the negative and the positve regime with a linear scaling between -10^{-29} and 10^{-29} rad$\cdot$m^{-2}, connecting both parts of the scale. We used the rescaled gas mass density as an estimate for the electron number density.

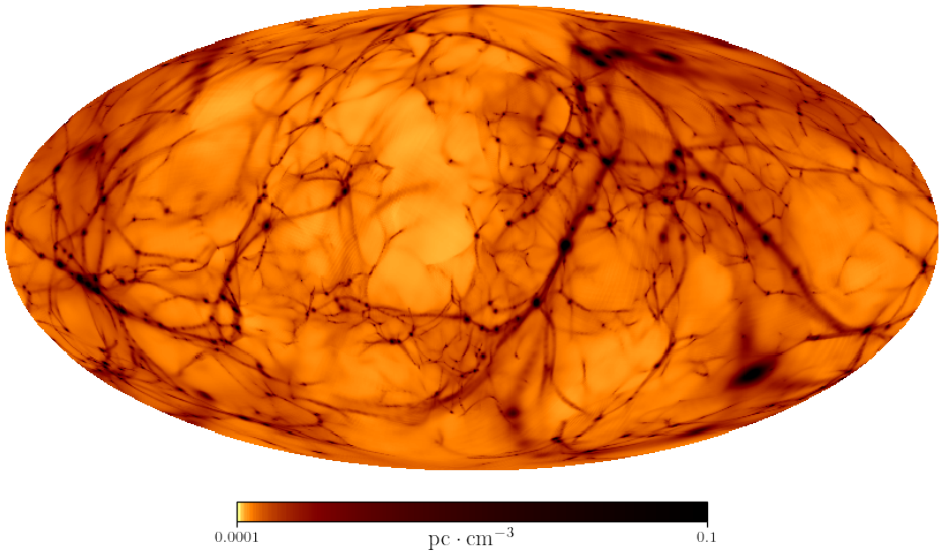

Figure 2.16: The electron dispersion measure in units of parsecs per cubic centimetre for sources within a distance of 60 Mpc/h from Earth. The plot is in galactic coordinates. We used the rescaled gas mass density as an estimate for the electron number density. The two dominant clusters in this image are Persues Pisces in the middle left of the image and Virgo close to the North pole. Close ups of both structures are provided in Fig. 2.11.

Chapter 3

The Galactic Faraday sky revisited

References and Acknowledgment

The work presented in this chapter was previously published in Hutschenreuter & Enßlin (2020b). I was the lead author of the paper under the supervision of Torsten Enßlin. The numerical calculations and all chapters were implemented and written by me, respectively.

3.1 Introduction

The Faraday rotation effect is one of the primary sources of information on astrophysical and cosmological magnetic fields. This includes the fields of planets (Boudjada & Lecacheux 1991), stars (Kooi et al. 2017), other galaxies (Gießübel et al. 2013) and galaxy clusters (Dreher et al. 1987b), as well as more curious objects such as radio jets, lobes, and relics (e.g. Bonafede et al. (2013)). In particular, the study of the Faraday rotation induced by the Milky Way magnetic field is of twofold importance. First of all it is an interesting research topic on its own, due its connection to the formation and structure of our home galaxy, but furthermore it also constitutes a non-negligible foreground component. All polarized light stemming from cosmological sources passes through the Galaxy and interacts with the Galactic magnetic field, which affects its polarization direction. Accurate and highly resolved Galactic foreground templates are therefore a necessary condition for any precision measurement of extra-galactic magnetic fields via Faraday rotation.

Multiple efforts have been made to to map the Galactic Faraday sky, quite a few of them already to remarkable accuracy (e.g. in Frick et al. (2001); Johnston-Hollitt et al. (2004); Dineen & Coles (2005); Xu et al. (2006); Oppermann et al. (2012a); Xu & Han (2014), and Oppermann et al. (2015)). The approach in Oppermann et al. (2012a) is especially important to us, as we will rely on the same theoretical framework for our inference algorithms. We will refer to this paper as NO12 and to its successor paper Oppermann et al. (2015) as NO15 from here on.

Our goal in this work is to further sharpen our knowledge on the Faraday sky by exploiting correlations to the electron emission measure (EM) as traced by bremsstrahlung measured from electron proton interaction in the interstellar medium, commonly known as the Galactic free-free emission. This is well motivated by observation as well as physical considerations, as we will outline later on. In a more general context, we hope to demonstrate an interesting test case of multi-wavelength astronomy, and show that the synthesis of long existing data sets still can yield undiscovered information, under the condition that our a priori physical knowledge is employed and the data is treated in a consistent way. Our main result, the revised Faraday sky including the free-free data (from here on "reconstruction I") is shown in Fig. 3.1a and the revised map without free-free data in Fig. 3.1b (from here on "reconstruction II") .

The paper is structured as follows. In Sec. 3.2 we develop our updated reconstruction method. This involves an amplitude field aiming at representing the overall Galactic structure and a sign field representing magnetic reversals and smaller scaled structures. It turns out that the reconstructed amplitude field resembles the free-free EM of the Galaxy, which is physically plausible. In order to take advantage of this, we extend the method to fold in the measurements of the free-free EM sky in Sec. 3.3. We conclude in Sec. 3.4.

3.2 Improving the Inference of the Faraday sky

3.2.1 The physics

The rotation angle Δ_λ of the polarization plane of linearly polarized light due to Faraday rotation can be written in most astrophysical settings as (Burn 1966)

$$\Delta_\lambda = \phi\left(n_{\mathrm{th}}, B_{\mathrm{LOS}}\right)\lambda^2, \tag{3.1}$$

where λ is the wavelength at which the light is observed. The Faraday depth ϕ depends on the thermal electron density n_{th} and the line of sight (LOS) component of the magnetic field B_{LOS}. More specifically for a polarized extra-galactic source shining through the interstellar medium, the Galactic part of the Faraday depth ϕ_{gal} can be written as (Brentjens & de Bruyn 2005a)

$$\phi_{\mathrm{gal}} = \frac{e^3}{2\pi m_e^2 c^4}\int_{\mathrm{LOS}} dl\, n_{\mathrm{th}} B_{\mathrm{gal,LOS}}, \tag{3.2}$$

where B_{gal} is the galactic magnetic field, e is the electron charge, m_e is the electron mass and c the speed of light. Contributions to the observed rotation angle not only come from the Galactic magnetic field but also contain extra-galactic, potentially source internal contributions. The Faraday rotation measure (RM) is commonly obtained by fitting the rotation angle defined in Eq. (3.1) over λ^2 and calculating the slope. Only in cases with negligible foreground emission this slope is equal to ϕ. Otherwise, the resulting observed curve in λ^2 space will not be linear and ϕ must be obtained via a spectral analysis technique commonly known as RM-synthesis (Brentjens & de Bruyn 2005a). In this work we will use data points from both techniques and will therefore use the term 'Faraday data' for

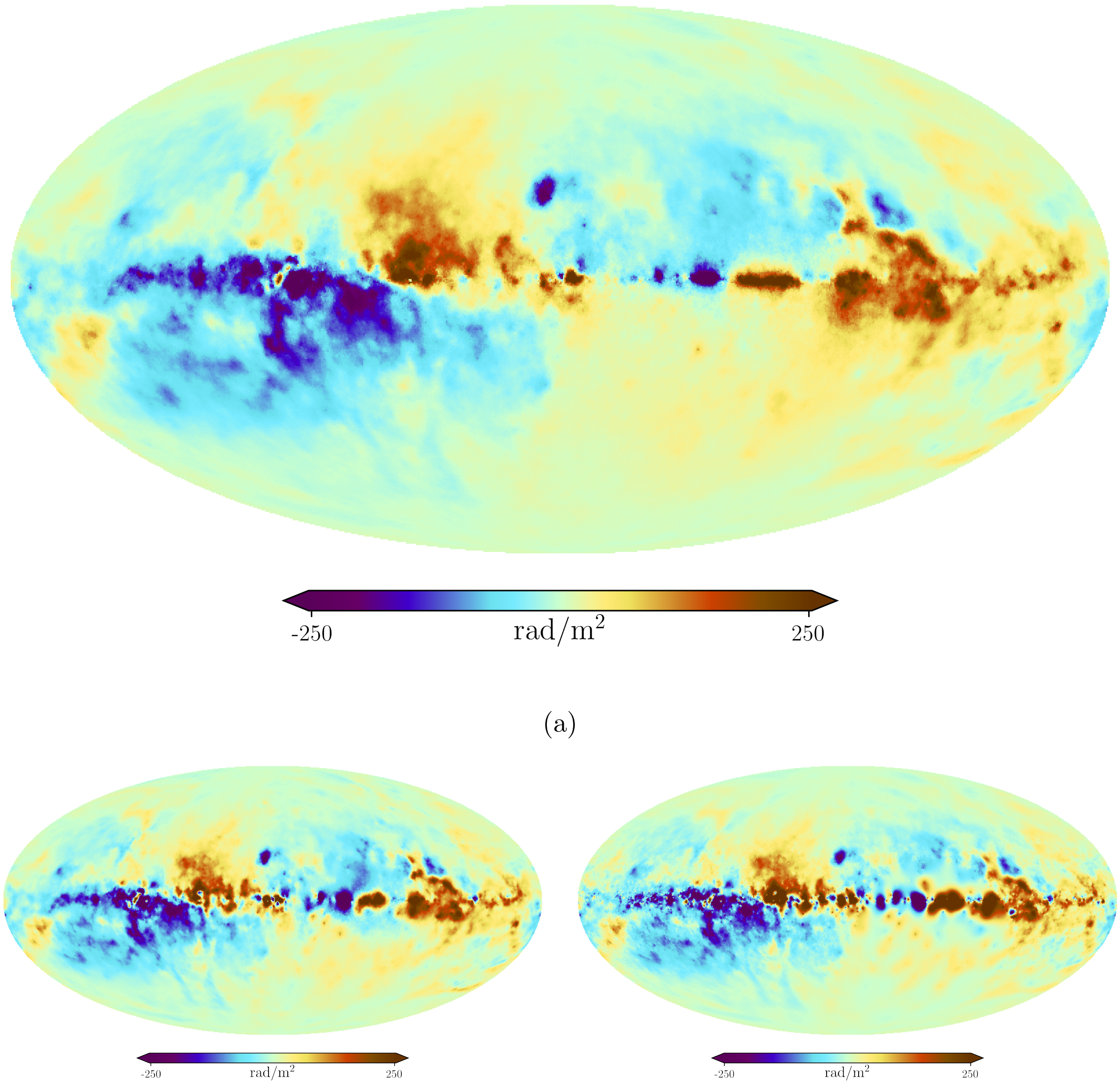

(a)

(b)

(c)

Figure 3.1: Reconstructions of the Faraday sky. Fig. (a) shows our main result, the posterior mean of reconstruction I. This map uses the free-free EM map as a proxy for the Faraday amplitude. The model furthermore contains fields that translate the free-free map into a Faraday amplitude, thereby balancing effects that support and those that disturb a direct relation of these two quantities. Fig. (b) contains the posterior mean of reconstruction II. Here we did not use the additional free-free data. Fig. (c) shows the posterior mean of the (NO15) reconstruction. We show the differences of the three maps in Fig. 3.2. These maps and all maps following in this paper are presented in Galactic coordinates centered at $(l, b) = (0°, 0°)$.

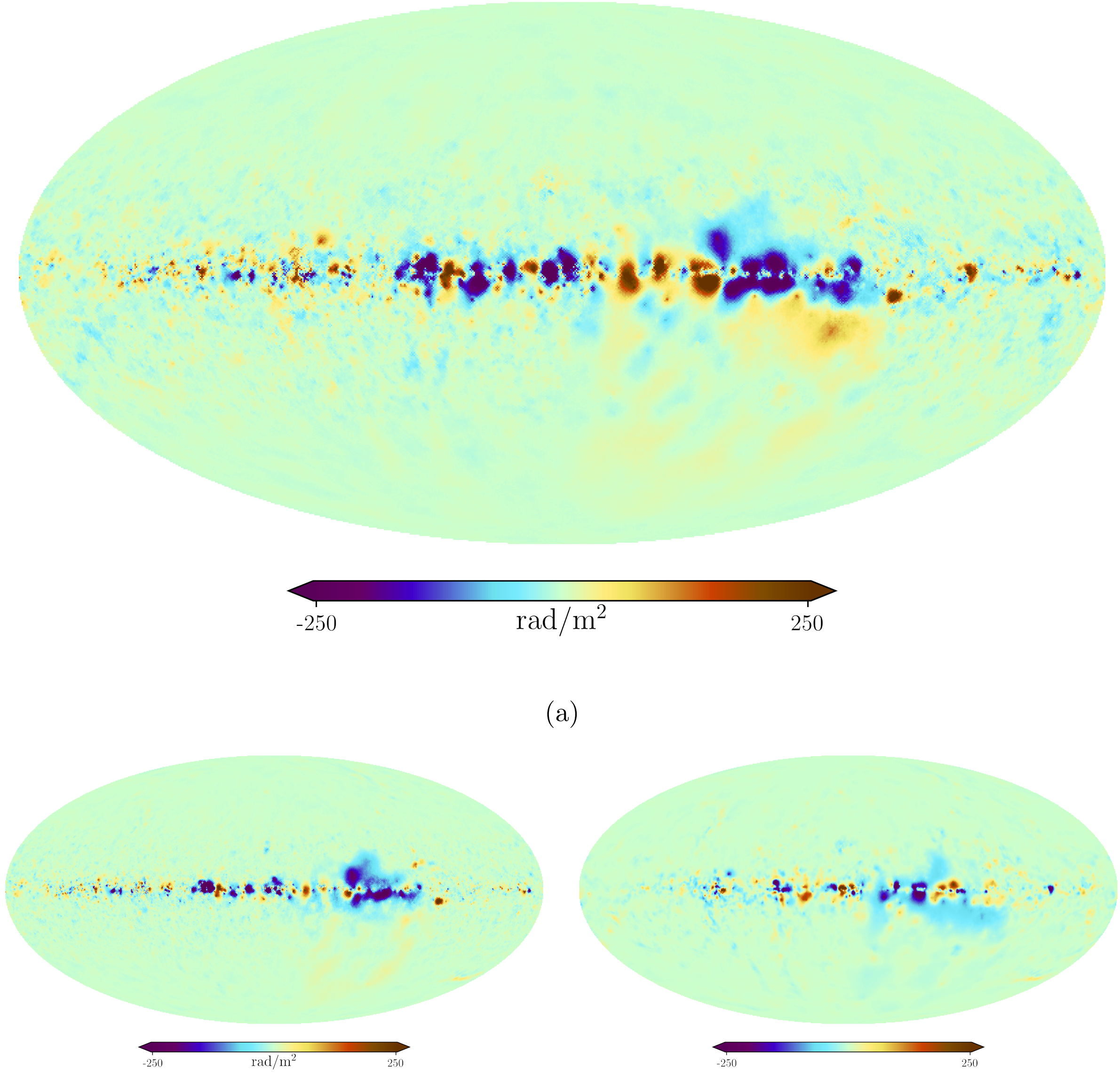

(a)

(b)

(c)

Figure 3.2: Differences of the reconstructions of the Faraday sky shown in Fig. 3.1. Figure (a) shows the difference between the NO15 map and reconstruction I. Figure (b) shows the difference between the NO15 map and reconstruction II. Figure (c) shows the difference between the Faraday depth skies resulting from reconstruction I and reconstruction II.

both RM and RM-synthesis data, in the spirit of NO12. Similar to the approach taken by NO12, it will be helpful to separate the Faraday depth signal into

$$\phi = \phi_{\text{gal}} + \phi_{\text{etc}}. \tag{3.3}$$

The terms ϕ_{gal} and ϕ_{etc} describe the aforementioned Galactic and other e.g. extragalactic, source intrinsic, or ionospheric contributions, respectively. Our goal in this work will be the estimation of ϕ_{gal} as a correlated field on the sky. This implies the necessity for an at least stochastic estimation of the other contributions. The connection of ϕ to the observed data d_ϕ is the topic of the next section.

3.2.2 The data

A measurement of the Galactic Faraday depth can be modeled via

$$d_\phi = \mathcal{R}_\phi \phi + n_\phi, \tag{3.4}$$

where we ignore for the moment the potential non-galactic contributions mentioned in Eq. (3.3). The quantity n_ϕ in Eq. (3.4) is the measurement noise. The operator $\mathcal{R}_\phi$ is called the response and describes the noiseless measurement process translating the signal into data space. In this case, the evaluation of the response at the location of source i is sufficiently described via

$$[\mathcal{R}\phi]_i = \int_{S^2} d\widehat{e}\; \phi\left(\widehat{e}\right) \delta(\widehat{e} - \widehat{e}_i), \tag{3.5}$$

with $\widehat{e}$ being the radial unit vector on the 2-sphere. The measurement noise can be assumed to be independent and Gaussian distributed according to

$$\mathcal{P}\left(n_\phi\right) = \mathcal{G}\left(n_\phi, N_\phi\right) = \frac{1}{\sqrt{|2\pi N_\phi|}} e^{-\frac{1}{2} n_\phi N_\phi^{-1} n_\phi^\dagger}, \tag{3.6}$$

with zero mean and known noise covariance N_ϕ. The noise will play an important role for our estimation of non-galactic contributions to ϕ, which will be discussed in more detail in Sec. 3.2.3. For the moment we assume N_ϕ to be simply given by the observational measurement uncertainties, therefore being a diagonal matrix in data space.

As we are conducting a Bayesian inference, our main task is the evaluation of the posterior probability distribution. An integral part of this distribution is the likelihood, which in our case is best described by the following Gaussian:

$$\mathcal{P}\left(d_\phi | \phi\right) = \mathcal{G}\left(d_\phi - \mathcal{R}_\phi \phi, N_\phi\right) \tag{3.7}$$

The likelihood will be further determined by the the specific modeling of ϕ, which we will present in Sec. 3.12. There we will also specify the different prior terms.

The data set used in this work is exactly the same compilation of Faraday rotation measures as used in NO12 and is mostly publicly accessible [1]. This compilation contains rotation measures, corresponding standard deviations and source positions for 41632 sources [2]. Similar to NO15 we multiply the uncertainties of the Taylor et al. (sub-)data set (Taylor et al. 2009) with 1.22 according to Stil et al. (2011). We note that Vernstrom et al. (2019) argue against this generic increase of the uncertainties and in contrast favor a decrease at least for a subset of the Taylor catalog. Furthermore it was found by Ma et al. (2019) that some of the data points of the same catalog suffer from nπ-ambiguities, which means that the reported RM's can be offset by multiples of $\pm 652.9\,\mathrm{rad\,m^{-2}}$. We will discuss in the model section how we deal with such systematic effects in the data.

---

[1] `https://wwwmpa.mpa-garching.mpg.de/~ensslin/research/data/faraday_revisited.html`

No additional polarimetric information, such as e.g. Faraday spectra, was used in this work. The data and the corresponding standard deviations are shown in Figs. 3.3a and 3.3b.

Next, we specify the modeling of ϕ in Eq. (3.4). We will furthermore explain the treatment of the non-galactic components of d_ϕ.

3.2.3 The model

The sky model

The results of the previous reconstruction (NO15) indicates that the Faraday sky has two characteristics that necessarily need to be modeled for an optimal inference. Firstly, the sign of the sky field changes rapidly, which reflects the rather abrupt directional changes of the LOS magnetic field component. Secondly, the absolute value of the signal varies over two orders of magnitude, most notably the Galactic disk will have a much stronger signal than the Galactic poles. For these reasons, we chose to parameterize $\phi : S^2 \to \mathbb{R}$ as a point-wise product between two fields living on the sky, or explicitly

$$\phi \equiv \chi e^{\rho} \, \frac{\mathrm{rad}}{\mathrm{m}^2}, \tag{3.8}$$

where $\chi : S^2 \to \mathbb{R}$ will be called the sign field, as it is able to capture the information on the sign of the Faraday depth, and $\rho : S^2 \to \mathbb{R}$ will be called the amplitude field, as e^{ρ} is strictly positive after the exponentiation and is able to model the large amplitude variations of the Faraday sky over orders of magnitude. Both fields are unitless. This is a more generic approach than in NO12 where, instead of an amplitude field, a profile function was used to capture the latitudinal dependence of the overall Galactic Faraday dispersion profile. Note that the sign field is in no way constrained to only contain information on the sign of the

---

[2] Bonafede et al. (2010a); Broten et al. (1988); Brown et al. (2003); Taylor et al. (2003); Brown et al. (2007); Haverkorn et al. (2006); McClure-Griffiths et al. (2005); Clarke et al. (2001); Clarke (2004); Clegg et al. (1992); Feain et al. (2009, 2011); Gaensler et al. (2001a); Hammond (2011); Heald et al. (2009); Braun et al. (2007); Hennessy et al. (1989); Johnston-Hollitt (2011, 2003); Johnston-Hollitt & Ekers (2004); Kato et al. (1987); Kim et al. (1991); Klein et al. (2003); Gregorini et al. (1998); Vigotti et al. (1999); Lawler & Dennison (1982); Dennison (1979); Mao et al. (2010, 2012a); Gaensler et al. (2005); Mao et al. (2008); Minter & Spangler (1996); Oren & Wolfe (1995); O'Sullivan (2011); Roy et al. (2005); Rudnick & Jones (1983); Schnitzeler (2011); Simard-Normandin et al. (1981); Tabara & Inoue (1980a); Taylor et al. (2009); Condon et al. (1998); Van Eck et al. (2011); Wrobel (1993)

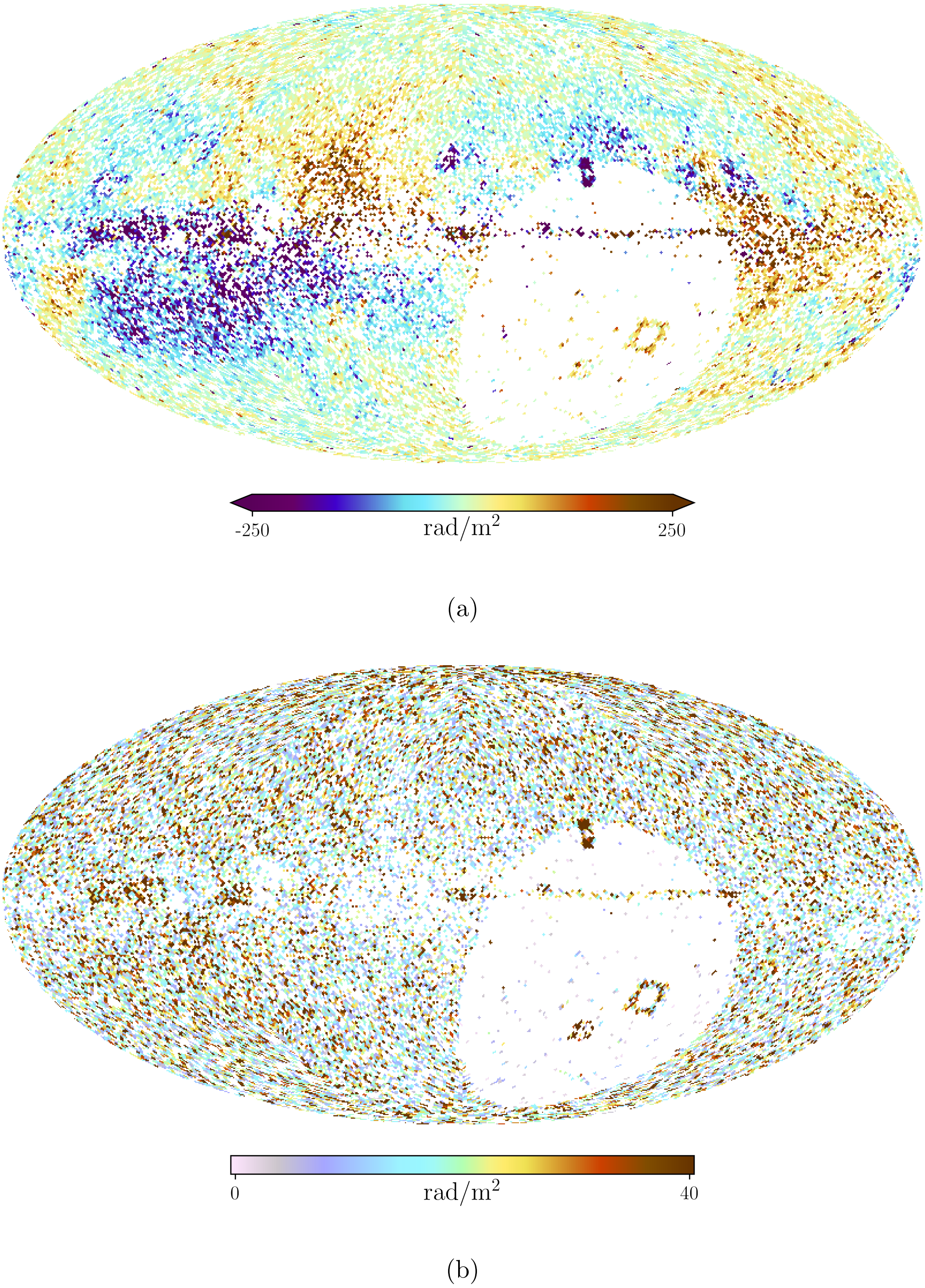

(a)

(b)

Figure 3.3: Sky map of the Faraday data set and its errors. Figure (a) shows the Faraday catalog used in this work projected on the sky. Figure (b) shows the corresponding uncertainties. We note that the region corresponding to the terrestrial south pole is only weakly constrained by data, except for the Galactic disk.

signal, but also can capture morphological features, leading to a degeneracy between the two fields. This could be broken by either imposing constraints on the correlation structure for one, or both, of the fields, or by introducing new data that informs the algorithm on one of the two fields. However, it turns out that the symmetry is sufficiently broken by the Gaussian process priors we impose on both fields separately, in combination with the specific functional form of ϕ as given by Eq. (3.8). Sign variations can only be captured by the sign field, ensuring that it is structured. The overall amplitudes of these fluctuations, which change as a function of position on the sky, are more easily represented by the amplitude field, which therefore preferentially absorbs them. Both fields are assumed to have independent and Gaussian isotropic statistics. Their joint prior probability function is

$$\mathcal{P}\left(\chi, \rho | S_\chi, S_\rho\right) = \mathcal{G}\left(\chi, S_\chi\right) \mathcal{G}\left(\rho, S_\rho\right). \tag{3.9}$$

In contrast to the distribution in Eq. (3.6), the covariances S_χ and S_ρ are unknown. If this were not the case, the above model in a Bayesian setting would directly lead to a specific application of the well known (non-linear) Wiener filter (Wiener 1966; Enßlin et al. 2009). This is not the case unfortunately, as in our case we have little a priori knowledge on the correlation structure. Similar inference problems have been solved in the past in the previous reconstruction of the Faraday sky by NO12 and elsewhere (e.g. in Selig et al. (2015); Pumpe et al. (2018); Leike & Enßlin (2019)).

All of these inferences relied on a framework laid out by information field theory (IFT) (Enßlin et al. 2009; Enßlin 2019). IFT connects Bayesian statistics with methods from statistical and quantum field theory, joining them into a inference scheme that connects noisy, incomplete data with the underlying continuous field(s). Considering the problem mentioned above, the requirement of simultaneously inferring the map and the correlation structure of a field leads to the critical filter formalism, which was first formulated in IFT by Enßlin & Weig (2010) and Enßlin & Frommert (2011). We will follow the most modern formulation, as outlined in Knollmüller et al. (2017b).

The noise model

We also need to find an estimate for the non-galactic contributions to the Faraday rotation. In this part of the inference, we follow the approach in NO12 very closely. We will start by inserting Eq. (3.3) into the measurement equation (3.4) and define an effective noise term $\tilde{n}_\phi$:

$$d_\phi = \mathcal{R}_\phi(\phi_{\text{gal}} + \phi_{\text{etc}}) + n_\phi \equiv R_\phi \phi_{\text{gal}} + \tilde{n}_\phi \tag{3.10}$$

We have no reason to drop the assumption of Gaussianity for the new noise term $\tilde{n}_\phi$, but have to adapt the covariance to include the increase in uncertainty. As we have no a priori guesses on the specific systematics of the different sources, we will infer this increase (or decrease) in uncertainty as well. This is implemented by introducing the following model

$$\widetilde{N}_\phi = \text{diag}\left(\eta_\phi \sigma_\phi^2\right), \tag{3.11}$$

for the new noise covariance $\widetilde{N}$, where η_ϕ are the parameters that need to be inferred and σ_ϕ^2 is the reported measurement uncertainty. We will assume η_ϕ to follow an inverse gamma distribution:

$$\mathcal{P}\left(\eta_\phi|\alpha_\phi,\beta_\phi\right)=\frac{\beta_\phi^{\alpha_\phi}}{\Gamma(\alpha_\phi)}\eta_\phi^{-\alpha_\phi-1}\exp\left(-\frac{\beta_\phi}{\eta_\phi}\right) \tag{3.12}$$

The hyper-parameters α_ϕ and β_ϕ need to be specified for the inference. Conveniently, this model should also take care of sources suffering from nπ ambiguities, as an increased noise term down-weights the respective data points in the inference.

We choose the slope parameter for the power law to be $\alpha_\phi = 2.5$. Furthermore we demand the prior expectation value of η_ϕ to be unity, which results in $\beta_\phi = 1.5$. Note that this is a different choice of parameters as in NO12 and NO15, where the authors chose $\alpha_\phi = 1$ and β_ϕ such that the prior expectation value of $\ln(\eta_\phi)$ is zero. This implies that we are more restrictive for the noise correction parameters and make it harder for the algorithm to classify data points as noise. This choice is motivated by the fact that we are now also inferring the profile field. In the old algorithm of NO12 the Faraday profile was fixed during the inference and only determined after the inference of the sign field was performed. This made it easy for the algorithm to identify outliers, as for example cases where $|d_\phi| \gg |\phi|$ are only explainable by the noise correction if the signal field is already sufficiently determined at the location of the data point d_ϕ. In our case, the profile is a priori much more flexible and inferred simultaneously, making the identification of inconsistencies much more ambiguous. If we a priori want to have single data points to have a comparable impact as in NO12, we have to restrict the noise estimation to some degree. We chose α_ϕ and β_ϕ such that we are able to reproduce the previous results, as we have no reason to distrust the results of NO12 and NO15 and we have no better measure for the choice of hyper-parameters.

3.2.4 The inference

The hierarchical Bayesian model described in the previous sections can be symbolically depicted as a hierarchical tree, of which the lower branches are shown in Fig. 3.12. The higher branches of the tree contain the hyper-parameters and are discussed in the appendix together with the more explicit likelihood and prior functions.

The evaluation of the posterior is a non-trivial task in our case, as the non-linearities in the models lead to highly non-Gaussian distributions for which no analytical description is known to exist. Furthermore, the fact that we aim for an simultaneous inference of the fields determining the Faraday map, as well as their correlation structures, leads to a strong interdependence between all degrees of freedoms. Our desired resolution of ≈ 10 arcmin also leads to a high dimensionality. Together with the high dimensionality of the problem, on the order of 10^6 unknown parameters, this leads to considerable numerical complexity. IFT solves such problems by providing efficient and well-tested algorithms for posterior evaluation. We employ here the Metric Gaussian Variational Bayes method (MGVI), which is better suited for simultaneous map and correlation structure inference compared to the maximum a posteriori algorithm used in Oppermann et al. (2012a). We furthermore implement the aforementioned hierarchical tree as a forward model, which aims among other

things for a more efficient numerical coupling between different parts of the model and allows the employment of sampling methods.
On a technical side, the inference was conducted using version 5 of the NIFTy python package (Selig et al. 2013; Steininger et al. 2017; The NIFTy5 team et al. 2019) for numerical information field theory. NIFTy is specifically designed for IFT applications and provides libraries for implementing the above mentioned models as well as for inferring their parameters and the uncertainties of those.

3.2.5 The results

Comparison to older results

The posterior mean Faraday depth map of reconstruction II relying on Faraday data only and inferred according to the model depicted in Fig. 3.12 is shown in Fig. 3.1b, the previous one of NO15 in Fig. 3.1c, with corresponding standard deviations in Figs. 3.4b and 3.4c, respectively. The difference of both maps are shown in Fig. 3.2b. A visual comparison of the two maps reveals satisfying agreement. The difference map, however, shows that there are indeed significant small scaled deviations of the maps in the area of the Galactic disk. These may be a result of the different noise estimation parameters in the updated inference and/or the different treatment of the amplitude field (see the discussion in Sec. 3.2.3). One should note that reconstruction II was conducted with a doubled resolution, which may also be responsible for some of the very small scaled differences.
The uncertainty maps nicely demonstrate the impact of the sky modeling on the inference. Fig. 3.4c shows that the uncertainty of the previous reconstruction, which exhibits imprints of the longitudinal galactic profile used in the amplitude modeling. Our updated uncertainty map in Fig. 3.4b shows a decrease in uncertainty in certain regions, especially in the galactic disk. This simply reflects the fact that our updated inference scheme can use the correlation information encoded in the data much more efficiently.

A further quantity which needs to be inspected are the power spectra depicted in Fig. 3.5, as they have been inferred with different algorithms in NO15 and the approach chosen in reconstruction II. We note that we can confirm the slope of the spectrum. The revised map resulting from reconstruction II has significantly less power on small scales. Again, the parameter change in the noise estimation may be the reason for this difference, as we know that it can have a considerable impact on the smaller scales, as we change the ability of the algorithm to increase uncertainties to accommodate outliers in the data.
With respect to the error estimation, we show in Fig. 3.6 the comparison of the reported observational noise standard deviation σ and our estimate for the noise $\widetilde{\sigma}$ according to Eq. (3.10). The uncertainties of some sources have been multiplied by factors of up to 1000, indicating strong internal or extra-galactic contributions to these particular Faraday data points. Nonetheless, we confirm or even decrease the uncertainties for most measurements, as demonstrated by the contour lines shown in the figure, which represent a normalized density plot in the $\sigma - \widetilde{\sigma}$ plane. We furthermore highlighted the 9 data points which were identified by Ma et al. (2019) as nπ-ambigious. Our algorithm has down-weighted all of

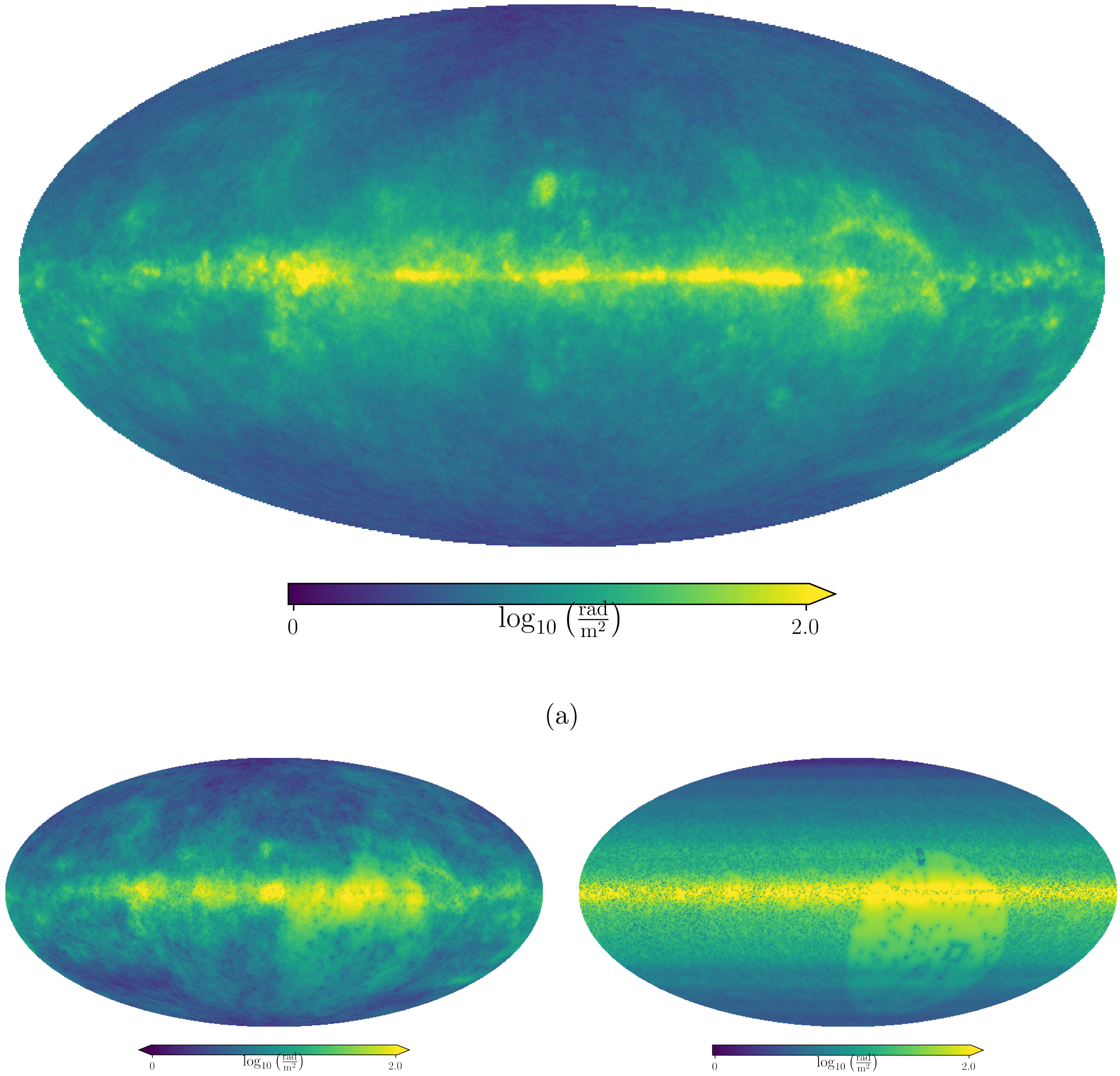
0
$\log_{10}\left(\frac{\mathrm{rad}}{\mathrm{m}^2}\right)$
2.0
0
$\log_{10}\left(\frac{\mathrm{rad}}{\mathrm{m}^2}\right)$
2.0
0
$\log_{10}\left(\frac{\mathrm{rad}}{\mathrm{m}^2}\right)$
2.0

(a)

(b)

(c)

Figure 3.4: Logarithmic posterior uncertainties of the different reconstructions. Fig. (a) is the posterior uncertainty in ϕ of reconstruction I (the mean of which is shown in Fig. 3.1a). Fig. (b) shows the posterior uncertainty corresponding to reconstruction II (shown in Fig. 3.1b). Fig. (c) shows the posterior uncertainty corresponding to the NO15 reconstruction shown in Fig. 3.1c.

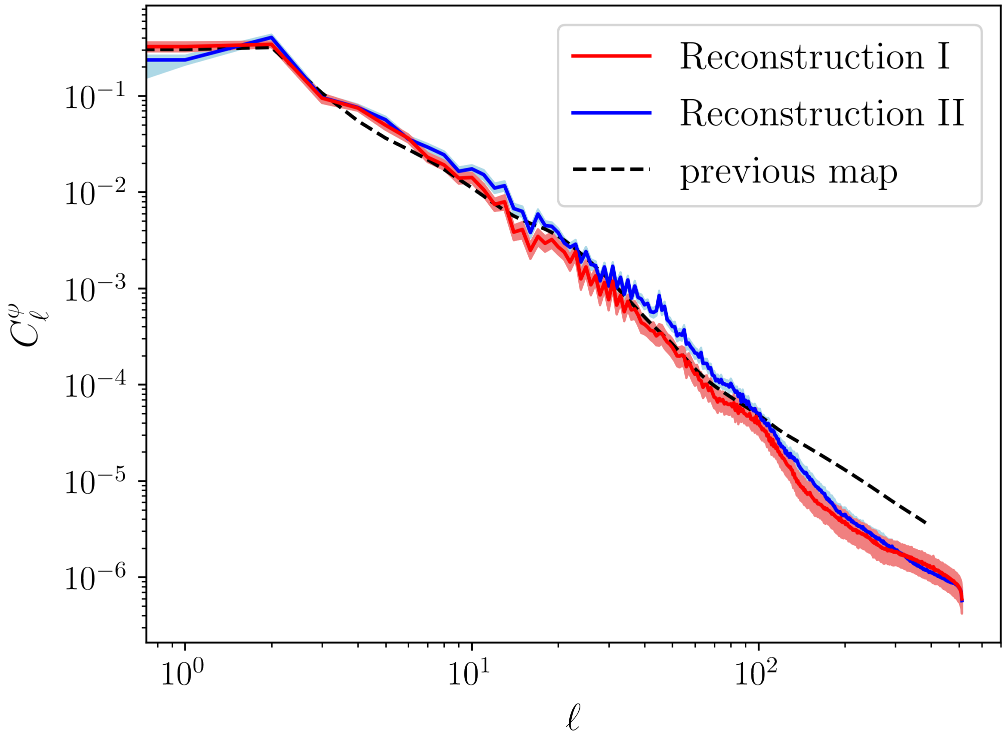

Figure 3.5: Comparison of the power spectrum inferred by NO15 (dashed black) to the spectrum of the Faraday map including the free-free EM data (reconstruction I, red) and the results of reconstruction II in Sec. 3.2 (blue). The latter two inference algorithms also produce uncertainties in the power spectrum, which are depicted as shaded areas in the respective colors.

them, indicating its capability to identify problematic data. The noise estimation results for the subset of the Taylor catalog analyzed by Vernstrom et al. (2019) is shown in Fig. 3.6b. A large fraction of the error bars of these data points were decreased, in accordance with Vernstrom et al. (2019), who draw their conclusions from a reanalysis of the original polarimetric data.
With this we conclude the comparison between the NO15 results and our reconstruction II and turn our face to the analysis of the underlying components of our sky model defined in Eq. (3.8).

The sign and amplitude fields

The sign and amplitude fields, χ and ρ, are shown in Figs. 3.7b and 3.8b, respectively. The sign field captured most of the small scale structure, but has more or less completely lost all information on the Galactic disc profile, which was absorbed by the amplitude field, as intended by our modeling. χ shows some similarity to the corresponding signal field inferred by NO15, which is shown in Fig. 3.7c. The exponentiated amplitude field appears to be relatively smooth with few distinguished features apart from the large scaled disk profile. These features, however, show remarkable similarity to galactic emission measure (EM) as traced by free-free emission, which was precisely mapped by missions investigating the Cosmic Microwave Background (CMB) such as *Planck* (Planck Collaboration 2016a), as it is a important foreground component in the microwave sky. We show the *Planck* free-free EM map in Fig. 3.8a. The color scales were chosen to highlight the structures in the maps of which we think that they originate from the same galactic structures. These apparent resemblances (which can already be seen by simply taking the absolute value of the NO15 map) between both maps have motivated us in including the free-free EM map in our inference. A investigation of the physical plausibility of this correlation (and its absence for some regions) is given in the next section.

3.3 Including the Free-Free emission

3.3.1 The physics

In addition to the visual similarities between the free-free EM map and our inferred amplitude field, we want to further motivate this apparent congruence by investigating the physics of the free-free emission and the Faraday rotation a bit more closely. The EM traced by the bremsstrahlung emitted by thermal electrons on protons in the warm interstellar medium can be quantified via (see e.g. Smoot (1998))

$$\mathrm{EM}_{\mathrm{ff}}\left(n_{\mathrm{th}}\right) = \int_{\mathrm{LOS}} dl\, n_{\mathrm{th}}^2 \equiv \int_{\mathrm{LOS}} dl\, \mathrm{em}_{\mathrm{ff}}, \tag{3.13}$$

where we defined $\mathrm{em}_{\mathrm{ff}} \equiv n_{\mathrm{th}}^2$ as a source term for $\mathrm{EM}_{\mathrm{ff}}$.
If we turn to the Faraday depth and want to study Eq. (3.2) with the intention of an comparison to $\mathrm{EM}_{\mathrm{ff}}$, we must quantify the dependence of B_{LOS} on the thermal electron density.

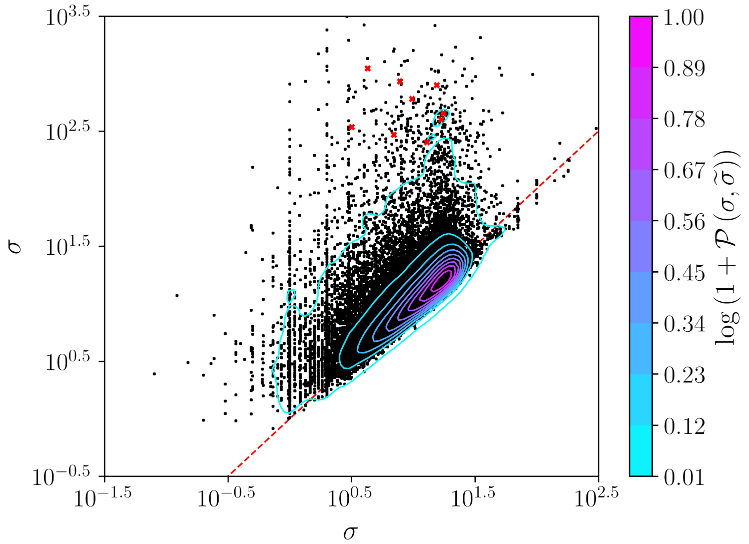

(a)

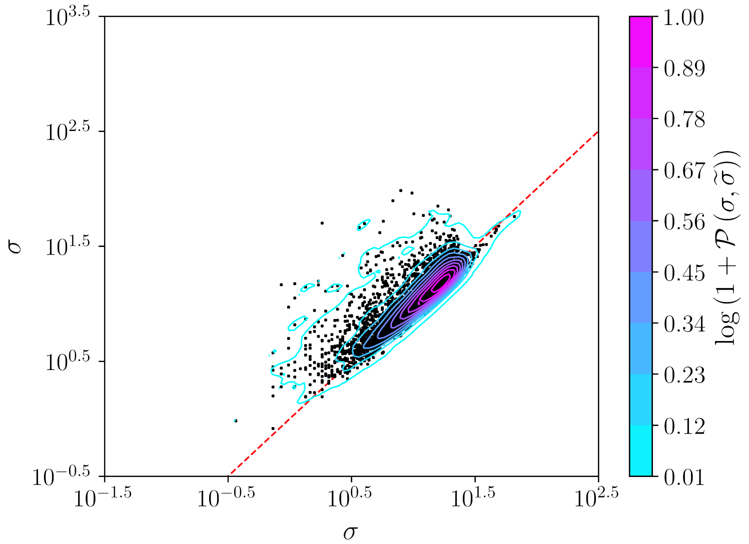

(b)

Figure 3.6: These figures show the estimated noise standard deviations $\widetilde{\sigma}$ compared to the σ values given by the Oppermann catalog and for the subset of analyzed by Vernstrom et al. (2019). To counteract the visual impression which is dominated by the outliers, we overlaid contour lines from the underlying log probability density function estimated via Gaussian kernels. Equality between the two quantities is marked by the red dashed line. The red crosses indicate the data points identified by Ma et al. (2019) as nπ-ambigious.

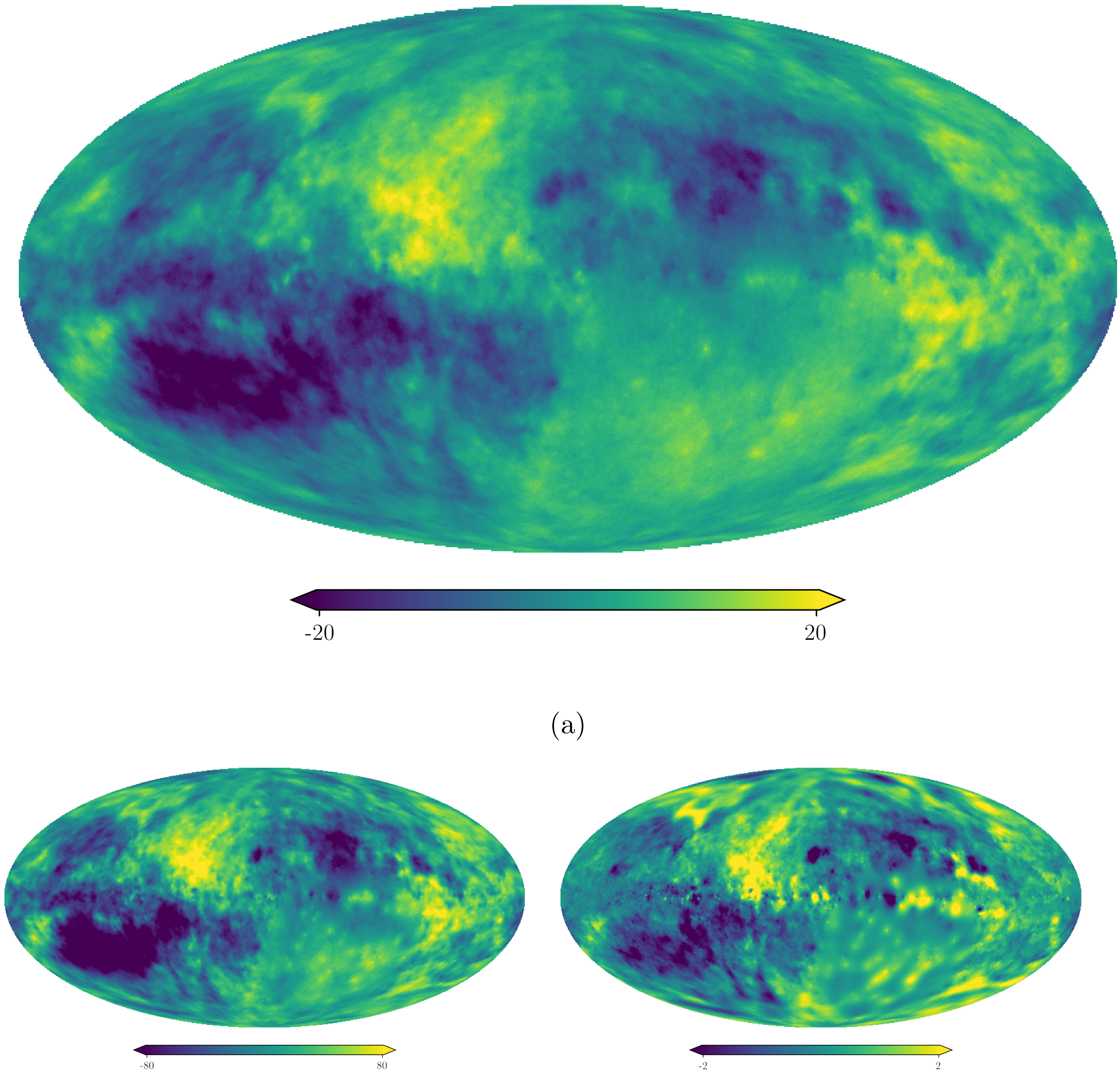

(a)

(b)

(c)

Figure 3.7: Sign fields of the different reconstructions. Their primary purpose is to capture the sign variations of the Faraday sky. Fig. (a) shows the field χ of reconstruction I as defined by the model in Eq. (3.20). Fig. (b) shows the field χ of reconstruction II as defined by the model in Eq. (3.8). Fig. (c) shows field s of the previous reconstruction by NO15, which served a similar purpose. Note that the difference in the scales of these fields is compensated by corresponding differences in the respective Faraday amplitude fields.

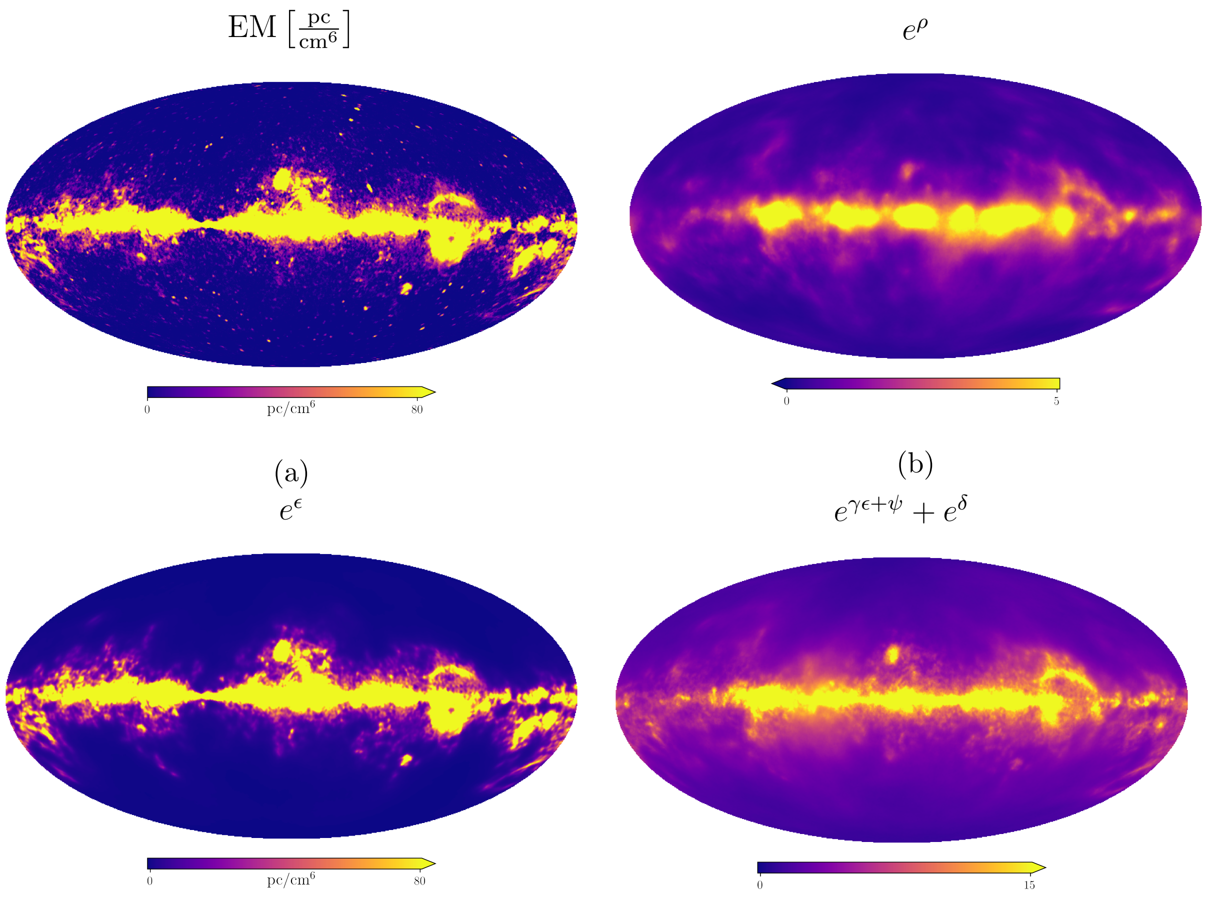
EM $\left[\frac{\mathrm{pc}}{\mathrm{cm}^6}\right]$
0
pc/cm^6
80
e^{ρ}
0
5
e^{ϵ}
0
pc/cm^6
80
$e^{\gamma\epsilon+\psi} + e^{\delta}$
0
15

(a) (b) (c) (d)

Figure 3.8: Fig. (a) shows the Galactic free-free EM map as obtained by the *Planck* Collaboration (Planck Collaboration 2016a). The further figures show the amplitude fields of the different reconstructions, which where supposed to capture the amplitude variations of the Faraday sky. Fig. (b) shows the exponentiated amplitude field ρ of the reconstruction II as defined by the model in Eq. (3.8). This field is not constrained by free-free data. Fig. (c) shows the exponentiated ϵ field defined in Eq. (3.18). This field is part of the revised Faraday map resulting from reconstruction I as well as the denoised free-free sky. A logarithmic version of this plot is shown in Fig. 3.9a. Fig. (d) shows the full Faraday amplitude field of reconstruction I as defined by the model in Eq. (3.20). This field is part of the result of the model in Eq. (3.20). A logarithmic version of this plot is shown in Fig. 3.9d.

In general, we can assume the magnetic flux to be frozen into the Galactic interstellar medium (ISM) (de Gouveia Dal Pino 2006). The exact nature of the $B - n_{\mathrm{th}}$ relationship, however, is complicated as it strongly depends on the morphology and dynamics of the plasma under consideration. In the simplest case of an isotropically collapsing structure, flux freezing leads to an $|B| \propto n_{\mathrm{th}}^{\frac{2}{3}}$ dependence (Mestel 1966). For a realistic description the ISM, however, one needs to consider non-linear magneto-hydrodynamics (MHD). Under certain simplifying assumptions as shown in Passot & Vázquez-Semadeni (2003) one may decompose the ISM flow into several wave types corresponding to different modes, leading to different density dependencies of the magnetic field strength. Most notably in the low density regime, the dominating mode approaches a constant in n_{th}, implying no correlation between $|B|$ and n_{th} in this regime. Furthermore, as waves corresponding to different modes may very well travel trough the same regions within a short time span, the $B - n_{\mathrm{th}}$ correlation may be subject to large variability in all regimes of measured electron density (Vázquez-Semadeni 2015). This pattern was confirmed for tracers of non-ionized hydrogen such as Zeeman splitting by e.g. Crutcher et al. (2010), who found no $B - n_{\mathrm{H}}$ correlation for particle density regimes $n < 300\mathrm{cm}^{-3}$, and strong variations in the regime above in molecular clouds, indicating a power law dependence of roughly $|B| \propto n_{\mathrm{H}}^{0.65}$. Furthermore, Harvey-Smith et al. (2011) found no correlation between n_{th} and $|B|$ in several known HII regions as did Purcell et al. (2015) specifically for the Gum nebula.
We therefore assume the dependence of the magnetic field strength on n_{th} to follow a power law with an unknown and spatially dependent coefficient $|B| \propto n_{\mathrm{th}}^{p_B}$, which could very well be zero. We can then rewrite the proportionality of the absolute value of integrand of the Faraday depth in Eq. (3.2) on n_{th}

$$\begin{aligned} B_{\mathrm{LOS}} n_{\mathrm{th}} = |B| \cos(\theta) n_{\mathrm{th}} \propto \\ \propto n_{\mathrm{th}}^{1+p_B} \cos(\theta) \propto \mathrm{em}_{\mathrm{ff}}^{\frac{1+p_B}{2}} \cos(\theta). \end{aligned} \tag{3.14}$$

Here we introduced the angle θ indicating the orientation of the magnetic field with respect to the LOS. Its impact will be discussed later on. If $p_B \approx 1$ for all locations along a line of sight, the absolute value of the Faraday integrand does strongly depend on the free-free emissivity and the additional electron density dependence has completely canceled. In the unrealistic case that $p_B = -1$, the absolute value of the Faraday integrand would be completely uncorrelated to the free-free source term. As discussed before, in some cases the electron density will not be a good tracer for the magnetic field strength and the LOS projection might partly mask the relation in the observables, which again limits the above relationship. Nonetheless, we think that the above considerations motivate the inclusion of the free-free map as a proxy for the Faraday amplitude field in our inference, as most realistic cases of the power law index p_B will result in a correlation between the free-free EM and the Faraday sky. On the other hand, this analysis also indicates that the effects of ISM dynamics on the magnetic field strength have to be considered for a reliable inference.
A second effect that needs to be taken into account are sign reversals of the magnetic field along the line of sight, which could strongly affect the value of ϕ in contrast to $\mathrm{EM}_{\mathrm{ff}}$. To

consider these, we approximate the line of sight integral via

$$\begin{aligned}\phi \propto \int_{\mathrm{LOS}} dl\,|B|\cos(\theta) n_{\mathrm{th}} &= L\langle |B| n_{\mathrm{th}} \cos(\theta)\rangle_L \approx \\ &\approx L^2 \langle |B| n_{\mathrm{th}}\rangle_L \langle \cos(\theta)\rangle_L,\end{aligned} \tag{3.15}$$

where L is the length of the line of sight and $\langle \ldots \rangle_L \equiv \frac{1}{L}\int_{\mathrm{LOS}} dl \ldots$ indicates an averaging process along the line of sight. The last approximation implies statistical independence between the magnetic field strength and θ. This shows that, to good approximation, the geometry of the magnetic field can lead to a multiplicative term, which is not constrained by the free-free data alone and has to be considered independently. In our setup, it can only be further determined by discrepancies between the Faraday and free-free data sets. Both effects, the unknown $B - n_{\mathrm{th}}$ correlation and the potential sign reversals might be responsible for discrepancies between the free-free data and the Faraday amplitudes resulting from our reconstruction II (see Fig. 3.8b).

Similar to the first part of this paper, we will first discuss properties of the EM data and then show the modeling of the respective sky maps in Sec. 3.3.3.

3.3.2 The data

In this work, we use the free-free EM map of the *Planck* 2015 release (Planck Collaboration 2016a). This map is a side product of a foreground subtraction process of the *Planck* team in their pursuit of the CMB sky reconstruction. The free-free sky is a dominant component of this foreground in the low frequency regime, along with synchrotron and spinning dust emission (Planck Collaboration 2016b). Most components in the microwave sky are hardly distinguishable, as they result from similar structures in the sky. *Planck* therefore employs a sophisticated component separation algorithm called `COMMANDER` (Eriksen et al. 2008), mostly exploiting the different energy spectra of the components. This algorithm uses the Gibbs sampling technique to approximate the posterior distribution for all components, also making use of the WMAP data (Bennett et al. 2013) and a 408 MHz survey map (Haslam et al. 1982a; Remazeilles et al. 2015b) for the separation. An updated version of `COMMANDER` employed in the 2018 release of *Planck* takes the correlation structure of the components into account. However, *Planck* has not released an updated free-free map in 2018.

Note that the measured free-free EM also contains a dependency on the thermal electron temperature T_{e}. The *Planck* team has modeled the free-free emission as a analytical combination of both EM and T_{e}, which allowed to produce separate maps for both quantities. This is a considerable advantage of the *Planck* data over other tracers of EM, such as e.g. H-α data, for which also full sky maps exist, but for which temperature and EM have not been separated. As we have no good model on the dependence of the magnetic field and consequently the Faraday depth on T_{e}, we prefer to use the pure EM data, as this minimized the physical systematics that have to be modeled.

As a side product of the estimation of the posterior via sampling, *Planck* provides us not only with the posterior mean of the free-free component, but also with uncertainties, which are a valuable source of information and lets us treat the free-free data as a slightly noisy measurement of the true free-free EM with known uncertainties. Unfortunately, upon inspecting the *Planck* data, we found some pixels to have extremely small and in case of the free-free temperatures even zero variances. As this is rather surprising given the large degeneracy between the components, we expect this to be a numerical artifact of the sampling procedure or of the marginalization process that results in the uncertainties for specific components. Our algorithm relies on accurate uncertainty measures for all pixels. In case of a severe underestimation of the errors in some specific area, this region is over-weighted by the algorithm in the inference of the correlation structure, thereby immediately affecting other parts of the sky and subsequently all other maps of the inference. This has to be accounted for if one is not completely sure that the noise values are free of systematics. We will therefore perform a similar noise estimation procedure as for the Faraday data.

With this in mind, we write the measurement equation for the free-free EM data as

$$d_{\mathrm{ff}} = \mathcal{R}_{\mathrm{ff}}\mathrm{EM}_{\mathrm{ff}} + n_{\mathrm{ff,obs}} + n_{\mathrm{ff,sys}} \equiv \mathcal{R}_{\mathrm{ff}}\mathrm{EM}_{\mathrm{ff}} + \widetilde{n}_{\mathrm{ff}}. \tag{3.16}$$

In case of *Planck*, the response $\mathcal{R}_{\mathrm{ff}}$ is just a unit matrix, as the data is already provided as a full sky map on the resolution we desire. Here, we decompose the noise n_{ff} into two components, namely an observed one obtained by `COMMANDER` and an unobserved one, which contains systematics. As we do not consider the correlation structure of the noise in for any data set, the procedure of noise estimation is the same from here on as in 3.2.3, apart from different hyper priors. In this case, we choose $\alpha_{\mathrm{ff}} = 1$ and β_{ff} such that the expectation value over $\ln(\eta_{\mathrm{ff}})$ is zero, as we a priori expect most of the noise values to be correct but the η_{ff} parameter to vary over orders of magnitude in cases they are not.

The lower branches of the free-free sky model are shown in Fig. 3.13. The full extended model for the hierarchical Bayesian model is shown in Fig. 3.14. Using the considerations above, the likelihood for the free-free sky is again Gaussian in analogy to Eq. (3.7)

$$\mathcal{P}\left(d_{\mathrm{ff}}\right) = \mathcal{G}\left(d_{\mathrm{ff}} - \mathcal{R}_{\mathrm{ff}}\mathrm{EM}_{\mathrm{ff}} | \widetilde{N}_{\mathrm{ff}}\right), \tag{3.17}$$

with the noise covariance $\widetilde{N}_{\mathrm{ff}}$ defined in analogy to Eq. (3.10). Again, we still need to explain the detailed model for $\mathrm{EM}_{\mathrm{ff}}$ and its priors. This is presented in the next section.

3.3.3 The free free model

The sky model

We now turn our head to the modeling of the free-free sky and its connection to the amplitude field of the Faraday sky under the constraint of the physical limitations considered in Sec. 3.3.1. We model $\mathrm{EM}_{\mathrm{ff}}$ with a log-normal approach, again to enforce positivity and to capture the expected large variability of $\mathrm{EM}_{\mathrm{ff}}$ on the sky:

$$\mathrm{EM}_{\mathrm{ff}} \equiv e^{\epsilon} \cdot \frac{\mathrm{pc}}{\mathrm{cm}^6}. \tag{3.18}$$

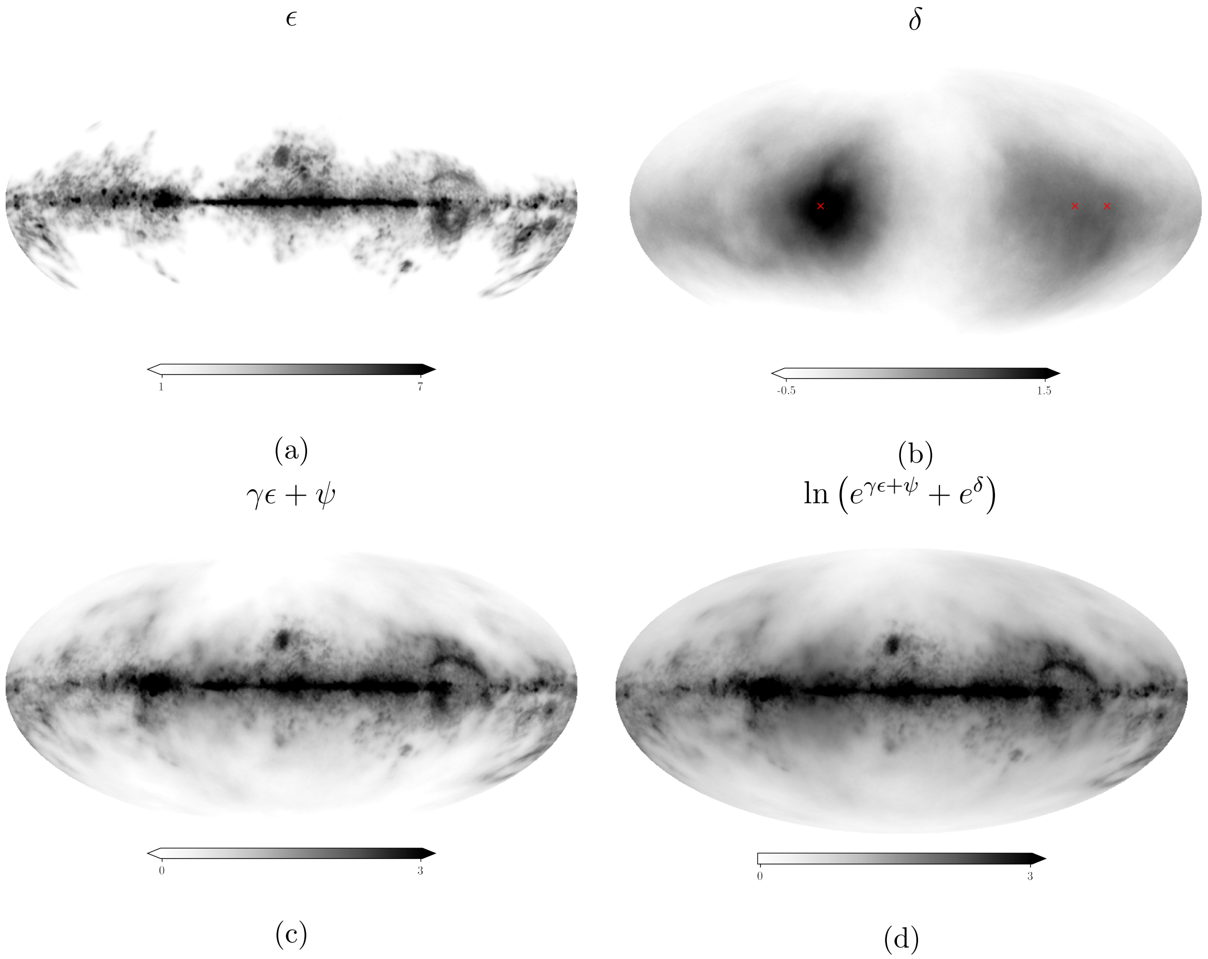
ϵ
δ
1
7
-0.5
1.5
(a)
(b)
$\gamma\epsilon + \psi$
$\ln\left(e^{\gamma\epsilon+\psi} + e^{\delta}\right)$
0
3
0
3
(c)
(d)

Figure 3.9: These figures shows the logarithmic amplitude field of reconstruction I as defined by the model in Eq. (3.20) as well as its components. Fig. (a) shows the field ϵ defined in Eqs. (3.20) and (3.18), constrained by free-free and Faraday data. This is also the reconstructed log free-free map. Fig. (b) shows the second amplitude field δ defined in Eq. (3.20). The red crosses indicate the approximate angular positions of the Orion arm, as given by Vázquez et al. (2008) and Xu et al. (2009). Fig. (c) shows the logarithmic amplitude of the Faraday sky as defined in Eq. (3.19) without the additional δ contribution, while it is included in Fig. (d).

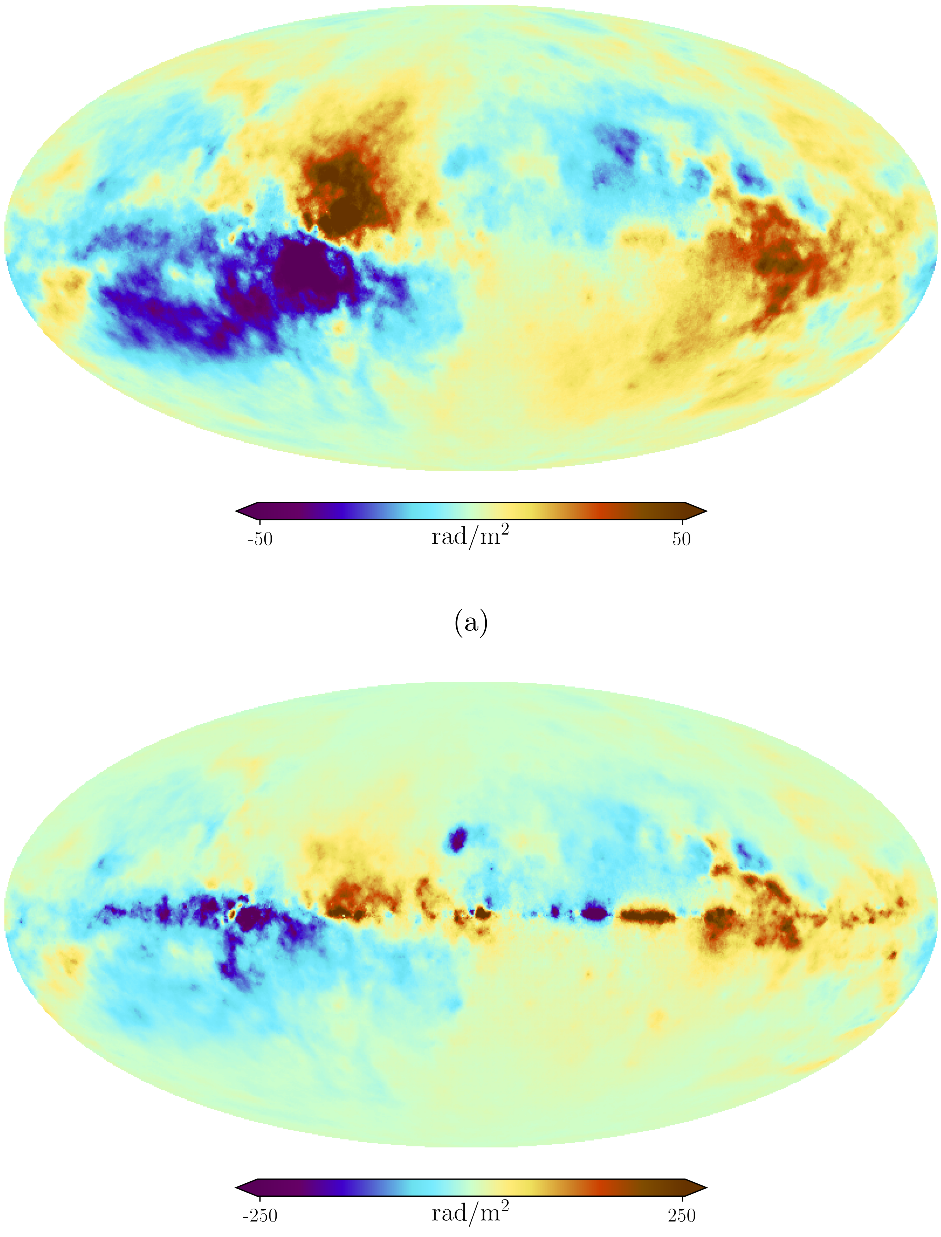

(a)

(b)

Figure 3.10: Figure (a) shows the Faraday sky containing only the amplitude contribution stemming from the field δ as defined in (3.21). This map is a rough estimate for the enhancement of the Faraday signal by the Orion arm. Figure (b) shows the faraday sky resulting from the complementary amplitude contributions (see also Fig. 3.9b).

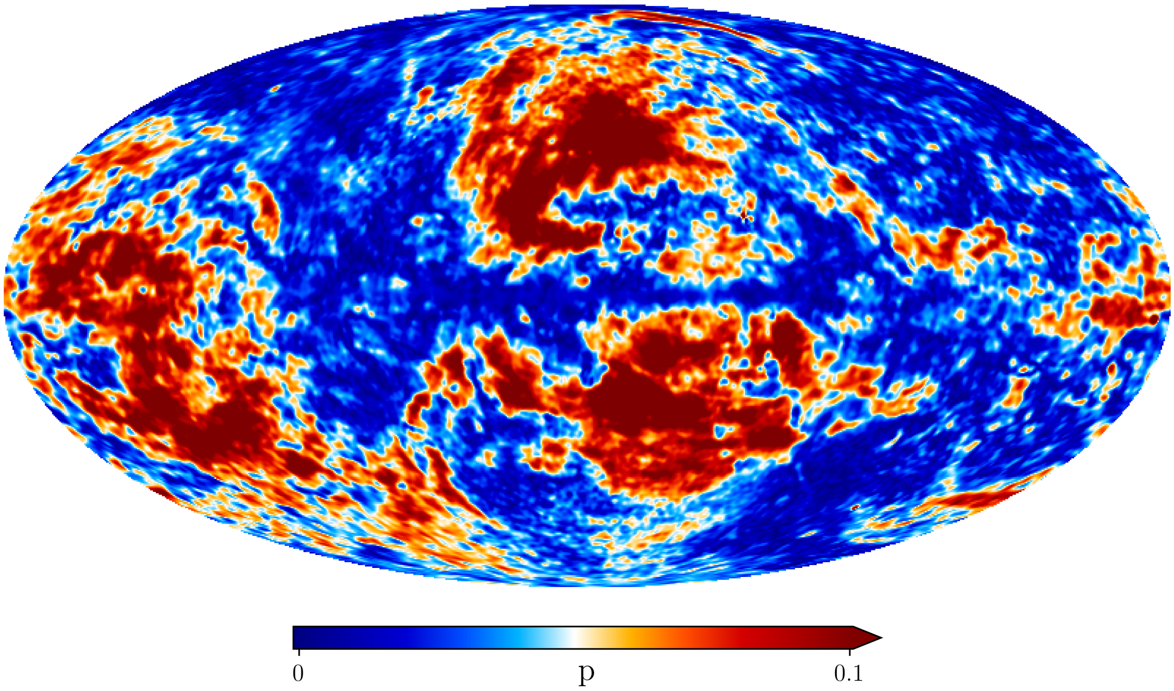

Figure 3.11: Linear Polarization fraction $p = \frac{\sqrt{Q^2+U^2}}{I}$ of dust calculated from the *Planck* polarization data.

If the true free-free EM sky were a perfect estimator for the amplitude field of the Faraday sky, we could simply replace ρ in Eq. (3.8) with ϵ to simultaneously infer both quantities from both data sets. However, as discussed in Section 3.3.1 a necessary condition for a combination of the information of free-free EM and Faraday rotation measures is to account for magnetic field reversals, different scalings with the thermal electron density and potential systematics in the data sets. All issues can be accounted for by introducing further terms to the model.

We start with our approach to model the differences in the electron density scaling and the geometry factor introduced by the sign reversals. As we can only work with the LOS integrated quantities, the most natural way of inferring the three dimensional effective scaling factor $\frac{1+p_B}{2}$ in Eq. (3.14) is not possible, as this would necessarily imply setting up the full 3D problem, for which we are lacking the necessary depth information. In the future, this information might be provided by a sufficient number of rotation and dispersion (DM) measures from pulsars, which was demonstrated with mock data for DM by (Greiner et al. 2016a). We therefore choose to introduce two scaling fields $\gamma : S^2 \to \mathbb{R}$ and $\psi : S^2 \to \mathbb{R}$ into the modeling according to Eq. (3.19). This essentially sets up a linear fit for the logarithm of the Faraday amplitude field in terms of the reconstructed logarithmic free-free sky:

$$\phi = \left(e^{\gamma\epsilon+\psi}\right)\chi. \tag{3.19}$$

This model somewhat mimics the approximation derived in Eq. (3.15), with γ approximating the role of the power law coefficients and e^{ψ} the geometry factor. Unfortunately, we loose the interpretation of the γ field in terms of $\frac{1+p_B}{2}$ in Eq.(3.14) due to the aforementioned lack of consistent 3D modeling. Furthermore, the large scale modes of the ψ and γ fields are to a degree degenerated, making a quantitative interpretation of the ψ field very hard, although the smaller scaled morphology may be informative. Altogether, these terms should be able to capture sign reversal effects as well as strong deviations from the proportionality of the magnetic field strength on the thermal electron density presented in Eq. (3.14).

We further have to consider the case where the Faraday sky contains amplitude structure not present in the $\mathrm{EM}_{\mathrm{ff}}$ sky. This is done by expanding the model according to

$$\phi = \left(e^{\gamma\epsilon+\psi} + e^{\delta}\right)\chi. \tag{3.20}$$

Here, the second amplitude field $\delta : S^2 \to \mathbb{R}$ is not connected to the free-free EM map, giving it the possibility to capture structures that are in the Faraday data but not in the free-free data. All newly introduced fields are assumed to follow Gaussian statistics, so their prior is similar to Eq. (3.9), again with unknown correlation structure. One should note at this point that the obvious a priori degeneracies between the newly introduced helper fields are usually broken during the inference, if sufficiently supported by data. This is possible due to the joint correlation structure inference, which constrains the respective fields just to the degree it is demanded by the inference problem.

Although there is motivation for each term, the above modeling might be viewed as ad hoc,

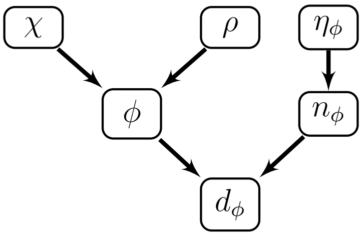

Figure 3.12: Hierarchical Bayesian model for reconstruction II. We decompose the Faraday depth ϕ into the fields χ and ρ, which are supposed to capture the sign and the overall amplitude of the signal, respectively (see Eq. (3.8)). The Faraday depth field ϕ together with the measurement noise n_ϕ determine the observed data d_ϕ via Eq. (3.4). The noise n_ϕ of every measurement i is assumed to be drawn from a Gaussian with variance $\eta_i \sigma_i^2$, where σ_i is the reported uncertainty and η_i a unknown uncertainty correction factor.

as one may certainly argue for the addition or omission of certain terms or a completely different modeling altogether. There are certain limitations for potential models, as they all have to be able to capture the physical characteristics (say e.g. the sign reversal of the Faraday map), and should be kept as simple as possible. Unfortunately these requirements already allow for a range of different parametrizations. We have varied the model during our analysis by e.g. adding or omitting further terms in Eq. (3.20). We found little variation in the overall morphology of the Faraday sky, apart form the disk, where e.g omission of the γ and ψ field lead to an extremely pronounced features, with Faraday depth values reaching regimes a magnitude higher than previous reconstructions. As we think that the above presented physical considerations are too important to be neglected, we deem the resulting maps in these cases as unrealistic. Given that all newly introduced helper fields have captured distinct structures as we will show in Sec. 3.3.4, we view the model in Eq. (3.20) as one of the simplest cases which can capture all relevant effects, but nonetheless we deem the systematic errors higher than the statistical ones in this inference. To gain some insights on the robustness of the obtained free-free EM map, we will further perform an inference just for the $\mathrm{EM}_{\mathrm{ff}}$ sky with the model in Eq. (3.18), unconstrained by Faraday data. The comparison of the result to the outcome of the joint Faraday and $\mathrm{EM}_{\mathrm{ff}}$ inference will be presented in the results section. We can implement this extended model numerically with similar algorithms as described in Sec. 3.2.4.

3.3.4 The Results

The revised Faraday map

In the following we show the results of the model depicted in Fig. 3.14. We show the mean, the differences to the results of NO15 and reconstruction II, and the power spectrum in Figs. 3.1a, 3.2a, 3.2c and 3.5, respectively. The inclusion of the free-free sky has lead to a notable difference in our newly revised estimate of the Faraday sky. Driven by the strong disc in the free-free data, the Faraday sky now has a similarly strongly pronounced

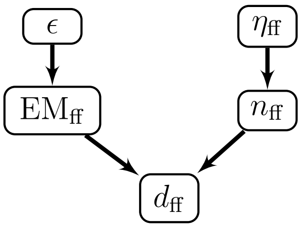
ϵ
η_{ff}
$\mathrm{EM}_{\mathrm{ff}}$
n_{ff}
d_{ff}

Figure 3.13: Hierarchical tree model for the free free EM sky. We model $\mathrm{EM}_{\mathrm{ff}}$ via the exponentiated field ϵ (see Eq. (3.18)). The field $\mathrm{EM}_{\mathrm{ff}}$ is together with the noise n_{ff} connected to the observed data via Eq. (3.16)

.

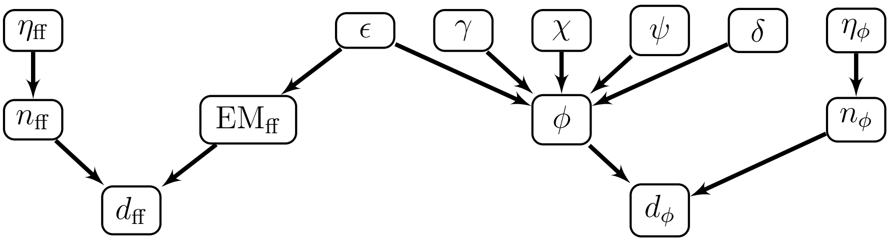
η_{ff}
ϵ
γ
χ
ψ
δ
η_ϕ
n_{ff}
$\mathrm{EM}_{\mathrm{ff}}$
ϕ
n_ϕ
d_{ff}
d_ϕ

Figure 3.14: The full hierarchical model excluding the power spectrum hyper priors for the fields. The lowest layer contains the data sets d_{ff} and d_ϕ. These are connected by the Eqs. (3.4) and (3.16) to the sky maps $\mathrm{EM}_{\mathrm{ff}}$ and ϕ. The sky maps in turn are connected to the Gaussian fields in the uppermost layer via the respective models defined in Eqs. (3.18) and (3.20). From there on, the higher branches for the respective correlation structure inference follow. These are not depicted here, but are shown and explained in the Appendix.

disc feature as well. Other features mostly farther away from the Galactic plane remained relatively stable, such as the northern arc of the Gum nebula, which is also strongly visible in the free-free data. In Fig. 3.4a, we show the updated uncertainties. These have again narrowed considerably compared to reconstruction II as shown in Fig. 3.4b. The innermost part of the disc, however, is still quite uncertain. Furthermore one should be aware that any model uncertainties are not considered in this plot. The region of increased uncertainty in the Southern sky is not discernible anymore. This effect can be attributed to the inclusion of the EM data, which now strongly constrains the profile field in this area. The new power spectrum of the Faraday map is shown as the red line in Fig. 3.5. It is very similar to that of reconstruction II, with a notable offset towards smaller scales, implying a slightly steeper power law.

The components

We now discuss some of the components of the Faraday model in Eq. (3.20), apart from the ϵ field in Fig. 3.9a, which will be more closely debated in the following section dedicated to the inference results of the free-free EM sky.

The revised Faraday amplitude is shown in Fig. 3.8d. The comparison to the amplitude field of reconstruction II in Fig. 3.8b and the free-free data in Fig. 3.8a demonstrate the influence of both the Faraday and the free-free data on the new field. The field is enhanced by roughly a factor of 4 compared to the old amplitude field. This may be a result of the symmetry breaking process described in Sec. 3.2.3, as now the amplitude field is partially constrained by the free-free sky. The comparison of the sign fields will demonstrate that this factor was mostly absorbed there.

The second amplitude field δ is shown in Fig. 3.9b, its influence on the total logarithmic Faraday amplitude is demonstrated by Figs. 3.9c and 3.9d. The field is dominated by two diffuse structures of enhanced δ, centered in the Galactic plane and separated by roughly 180° longitude. Remembering the discussion in Sec. 3.3.1, the δ field is supposed predominately capture amplitude variations between the free-free and the Faraday sky. Larger values of δ can be caused by systematic errors in either the EM or the Faraday data and/or a high alignment of the magnetic field with the LOS in this direction. The approximated longitudinal difference of the two δ enhancements of about 180° as well as their positions seem to correspond to the angular positions of the Orion arm on the sky, which are depicted in the plot as red crosses. In the first quadrant of the Milky Way, at about 60° longitude, this minor arm is known to extend over several kiloparsec up to the Sagittarius arm, with which it might merge (Xu et al. 2009). In the other direction towards the third quadrant of the Galaxy, the structure of the arm is much more complex. Even a bifurcation or a crossing with the Perseus arm seems possible (Vázquez et al. 2008). A overview over properties of the Local Arm is given by (Vallée 2018). Moreover, the local arm can also be localized in three dimensional reconstructions of the local dust distribution, see e.g. Lallement et al. (2018); Leike & Enßlin (2019). We have indicated possible continuations of the arm in the plot at 240° and 260° longitude, respectively. The δ field seems to reflect not only the position of the arm, but also its morphology, as the

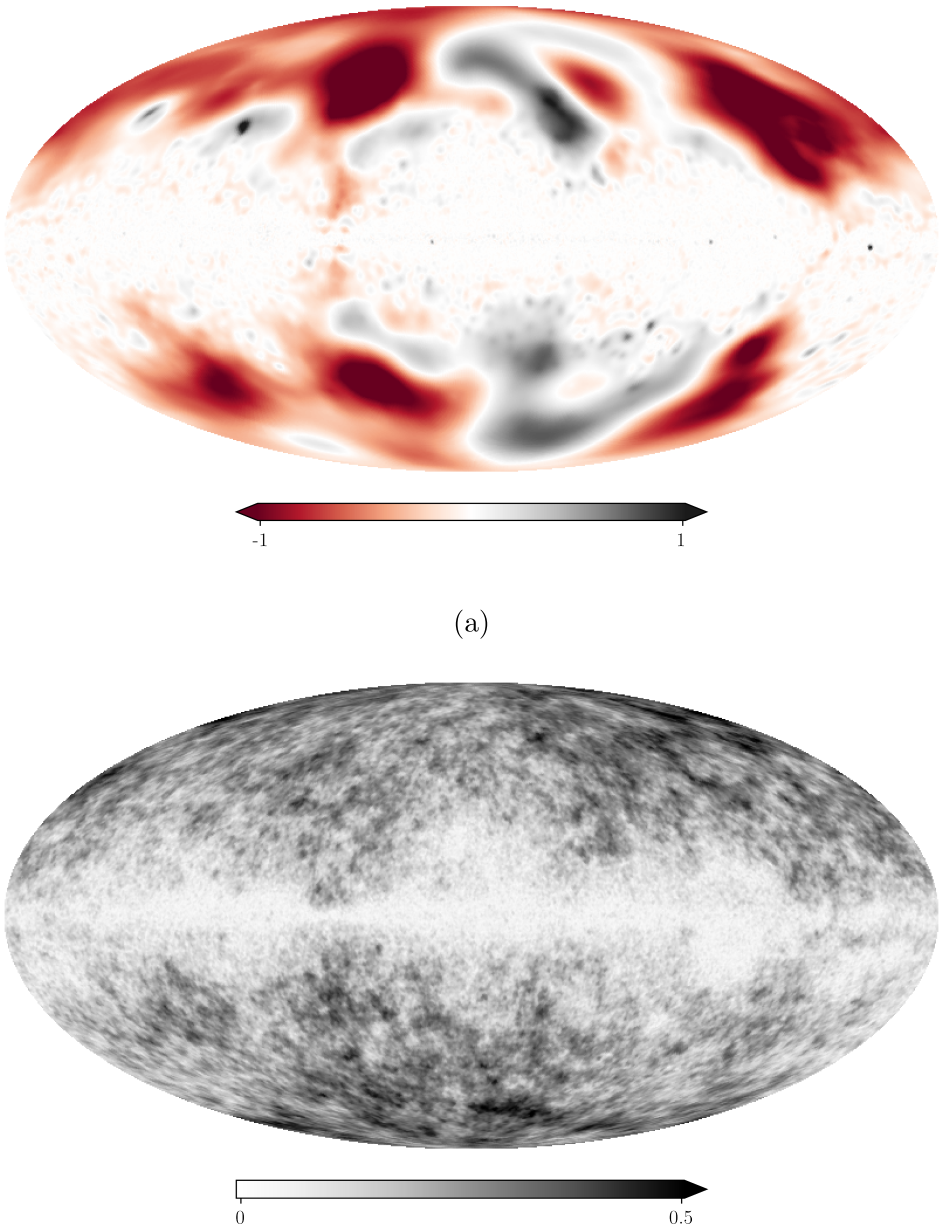

(a)

(b)

Figure 3.15: Fig. a) shows the difference between the field ϵ (as defined in Eq. (3.18)), inferred only by free-free data and the same field resulting from the joint inference with Faraday data (reconstruction I). Fig. b) shows the uncertainty of the ϵ field in reconstruction I. This demonstrates that the ϵ field is predominately determined by the free-free data irrespective of the simultanous inference of Faraday sky. There exist considerable deviations between the reconstructions near the Galactic poles. Figure (b) demonstrates thet the reconstruction is also rather uncertain in these regions.

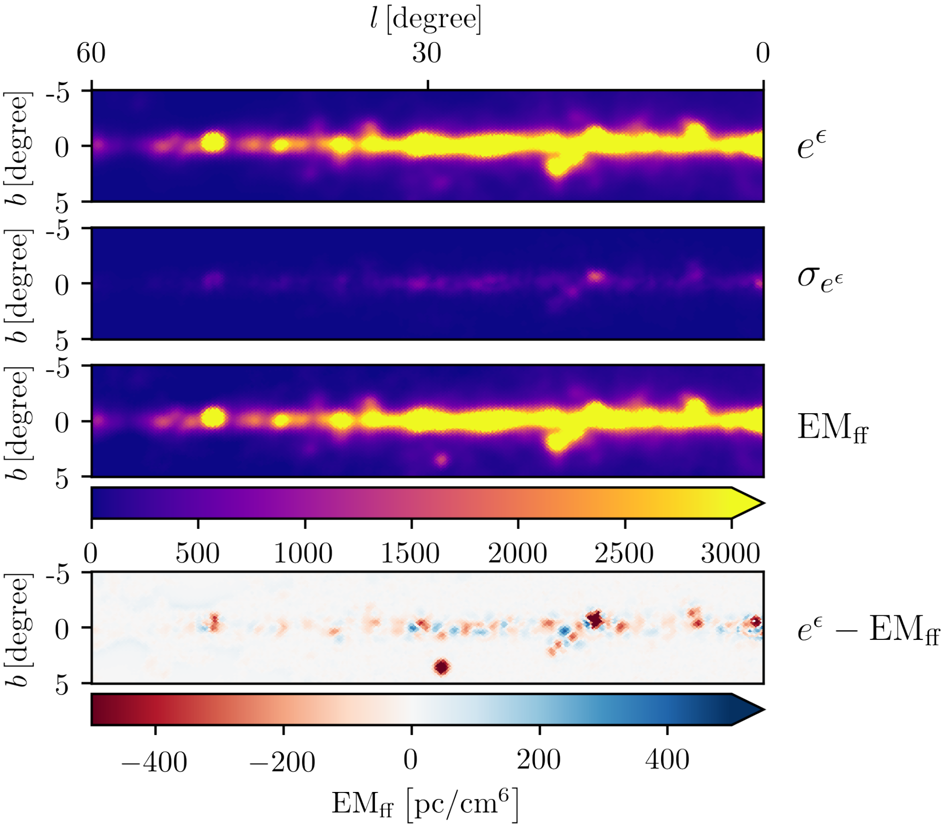

l [degree]
60
30
0
b [degree]
-5
0
5
e^{ϵ}
$\sigma_{e^{\epsilon}}$
$\mathrm{EM}_{\mathrm{ff}}$
0
500
1000
1500
2000
2500
3000
$e^{\epsilon} - \mathrm{EM}_{\mathrm{ff}}$
−400
−200
0
200
400
$\mathrm{EM}_{\mathrm{ff}}$ [pc/cm^6]

Figure 3.16: Excerpt of the free-free reconstruction in the first slice, its uncertainty, followed by the same excerpt in the *Planck* free free EM data. The residual is shown in the last row.

structure in the third quadrant is more diffuse, as opposed to the relatively pronounced structure at 60° longitude. All in all, this would argue for a high magnetic field alignment as a viable possibility for the interpretation of the second amplitude field. As the Sun is positioned directly in the Orion arm, we expect more coherent magnetic fields along the LOS directed pointed directly to the dominant direction of the arm. Remembering the discussion in Sec. 3.3.1, this then may lead to a disproportionate increase in the observed Faraday data as the free-free EM map would indicate at these positions. Furthermore, the Faraday sky in Fig. 3.1a indeed shows opposite magnetic field signs for those regions, as one would expect for a field traversing the solar location. We show the field

$$\phi_{\text{Orion}} = e^{\delta}\chi \tag{3.21}$$

in Fig. 3.10a, which corresponds to our estimate of the enhancement of the Orion Faraday depth, should the above considerations be true and if the χ field really only captured the sign. The complementary Faraday component (in terms of amplitude contributions) is shown in Fig. 3.10b. The considerable differences to Fig. 3.1a in the sky regions corresponding to the Orion arm reveal again the influence of the δ field there. Of course we can not rule out any of the other explanations for the observed δ enhancements, the plot in Fig. 3.10a should therefore be taken with care. On the other hand, we can find additional evidence for magnetic field LOS alignment in the Orion Arm and the adjacent sign revresal region as well as for a physical counterpart of the δ field in the literature. For example, the enhancement in the Orion Arm and its correlation to EM was also noted by Haverkorn et al. (2004), who compare EM and RM structure functions in the Southern sky and see evidence for two spatially distinct Faraday screens, one of which they attribute to the Local Arm. The region was also investigated by Brown et al. (2007), who again find evidences for distinct Galactic arms. The field reversal region between the Orion and the Sagittarius arm in the Northern sky is investigated by e.g. Ordog et al. (2017). They discuss a diagonal progression of the reversal region from $(l, b) = (67°, 4°)$ to $(l, b) = (56°, -2°)$, which is strongly visible in Fig. 3.10a- Especially interesting to us are the results of Bracco et al. (2019), who were able to produce a map on the linear dust polarization fraction using 3D analytical models of the magnetic field under the assumption of a helical magnetic field component. Their map shows strong morphological similarities to our δ field, with very little polarization in the regions of the Local Arm. As dust polarization probes the planar component of the magnetic field, this indicates that most of the magnetic field strength lies in the LOS component of the magnetic field. This can be confirmed by comparing to the *Planck* dust polarization fraction map calculated from the *Planck* Stokes parameter maps in Fig. 3.11, which also show similar features in the respective regions of the Local Arm.

The comparison of the amplitude field in Fig. 3.9c without the δ contributions with the ϵ field alone (see Fig. 3.9a) reveal the linear rescaling of the free-free contribution by to the γ and ψ fields according to Eq. (3.19). This mostly results in a much less pronounced disk, which seems to be disfavored by the Faraday data.

Finally we discuss the sign field χ in Fig. 3.7a. Little has changed in this component morphologically compared to Fig. 3.7b. The absolute value of the field has decreased by approximately a factor of 4. This factor was mostly absorbed into the new amplitude field, as discussed before. Interestingly enough, we can still discern the region of under-dense Faraday data in the southern sky in this plot, which has very little structure in it. This is further evidence that the decrease in uncertainty in Fig. 3.4a in this region is caused by the now strongly determined amplitude field, while the small-scaled structure of the sign of the Faraday depth is still only vaguely known. Apart from that, the field has again fully served its intended purpose, namely capturing the sign of the Faraday sky.

We now discuss the results of the inference of the free-free EM sky.

The revised free-free map

The revised free-free EM sky constrained by both the *Planck* and the Faraday data is shown in Fig. 3.8c, the logarithm of it is shown in Fig. 3.9a. We have also run a $\mathrm{EM}_{\mathrm{ff}}$ inference solely using the *Planck* data. The difference to Fig. 3.9a is shown in Fig. 3.15a. There is little difference between the maps, indicating that the systematic differences of the data sets were mostly absorbed by the second amplitude field δ and the rescaling fields γ and ϵ. Notable differences appear only towards the Galactic poles, where *Planck* has measured little to no free-free component, while considerable Faraday rotation exists. These regions are also subject to strong uncertainty in the reconstructed free-free EM, as indicated in Fig. 3.15b. The visual comparison of Fig. 3.8c to the data shown in Fig. 3.8a demonstrates good accordance. The main difference is the lack of small structures far away from the disc, which were mostly absorbed into the noise.

Closer inspection reveals some small scaled deviations in the disc, which we want to investigate by showing an excerpt of the disc ranging from 0° to 60° longitude in Fig. 3.16. This shows approximately the same region as the first plot of Fig. 7 in Planck Collaboration (2016b), where the *Planck* team compares their free-free temperature map with independent measurements via the radio recombination line survey (RRL). While our reconstruction reproduced the overall morphology, some peaks in the picture experience deviations around 20 %. In general our results seem to underestimate the amplitudes compared to *Planck*. It is noteworthy that the comparison between *Planck* and RRL resulted in a similar statement, as the *Planck* features were generally much more pronounced. We will refrain from drawing physical conclusions from these discrepancies as these can only be resolved by a detailed discussion of the *Planck* data analysis, which is beyond the scope of this work. Note again that the Faraday data has little influence on this result. The changes are mainly driven by the noise estimation and the full consideration of the correlation structure of the free-free EM sky. We think that this deems the inclusion of the correlation structure in the inference an important step for any component separation algorithm, as also shown in Knollmüller & Enßlin (2017).

3.4 Summary and conclusion

We infer the Galactic Faraday sky map using the same data as NO12 using an updated algorithm. This involves the separation of the Faraday sky into the point wise product of a sign and amplitude field, which both are supposed to mainly capture the sign and the Galactic profile of the Faraday sky, respectively. In the first part of the paper, we can largely confirm the old results in map and power spectrum. Smaller differences can be explained by the algorithmic advancements. The biggest improvement here is the updated uncertainty map, where we were able to significantly reduce the error bars over the whole sky, especially in some locations in the galactic disc.

In the further proceedings we notice that the amplitude field has notable similarities to the Galactic free-free EM map. In the second part of the paper we therefore incorporate free free EM data as a potential proxy for the Faraday amplitude field into our inference. This leads to a new Faraday map which now is notably different to previous results. The Galactic disc is much more pronounced and uncertainties are largely reduced. Since a pronounced Galactic disc is very sensible, as well as required by the data, which now is more satisfied as in any of the other approaches, we regard this map as the most reliable and therefore to be the main result of this work. Nonetheless, it has to be noted that our error maps cannot incorporate modeling uncertainties of our inference model. In addition, the component fields introduced in our model to resolve discrepancies between the two data sets reveal indicators for more LOS aligned magnetic field structures in the direction of the Orion arm. We also produce a denoised free-free EM map, which agrees with the *Planck* data on which it is based to large extent, but which is free of many of the point source like structures seen in the latter above the Galactic disc.

Of course any additional data will improve our work. Specifically for the Southern Sky new RM data is already available and the analysis with our framework is under way. Looking further into the future, the ongoing ASKAP-POSSUM survey (Gaensler et al. 2010) as well as the anticipated SKA polarization surveys will allow us to resolve the Faraday sky to unprecedented sharpness of detail.

Chapter 4

The Galactic Faraday depth sky 2020

This chapter contains work to be submitted to Astronomy&Astrophysics. I was the lead author of the paper under the supervision of Torsten Enßlin. The paper has a total of 28 additional co-authors, who contributed data to the catalog and to proofreading of the manuscript. The numerical calculations were implemented by me. Apart from Sect. 4.2.3 (which was contributed by Cameron van Eck), all chapters were written by me.

4.1 Introduction

The Faraday effect describes the rotation of linearly polarized light in a magnetized plasma and provides information on the line-of-sight (LOS) component of magnetic fields weighted by the thermal electron density. These quantities are key puzzle pieces for the characterization and modeling of many astrophysical objects, such as galaxies and galaxy clusters. A primary objective of research on cosmic magnetism has therefore been the investigation of the polarimetric properties of peculiar objects. Over the years, this has lead to a dense coverage of rotation measure (RM) data spreading over the whole sky. These not only depend on the properties of the objects in question but on that of all environments through which the light has passed upon arriving at the telescope. This leads to a potential intertwining of information of completely different astrophysical environments. Most notably, the plasma our home Galaxy is known to be largely magnetized and therefore responsible for a significant degree of Faraday rotation. In order to disentangle this information, reconstruction procedures have been developed. Specifically in the case of the Galactic Faraday depth sky, a useful measure for discerning Galactic and extra-Galactic components is the similarity of RM values of nearby sources on the sky. One expects that large angular correlations in RMs more likely result from local effects, implying that RMs resulting from extra-Galactic processes should be mostly uncorrelated on angular scales of arc-minutes or larger. First all-sky methods to reconstruct the Galactic Faraday sky where developed by e.g. Frick et al. (2001); Johnston-Hollitt et al. (2004); Dineen & Coles (2005); Xu et al. (2006); Oppermann et al. (2012a); Xu & Han (2014).

In this paper, we are continuing the work of Oppermann et al. (2012a), Oppermann et al.

(2015) and Hutschenreuter & Enßlin (2020a). In the latter reference, henceforth abbreviated with HE19, the authors introduce two inference models. The simpler one is a generalization of the model used in Oppermann et al. (2012a), while the more complicated one informs the amplitude of the Faraday sky with data on the emission measure (EM) of thermal electrons, as obtained from the *Planck* satellite.

These works use Bayesian inference schemes, that utilize the whole sky correlation structure of the Galactic part of the Faraday depth sky, in order to (a) perform the aforementioned component separation and (b) to interpolate between data points on the sky. As the precise form of the correlation structure is unknown, it is also inferred jointly with the sky map.

The aim of this paper is to provide the community with the most recent version of the Faraday depth sky with a minimal set of physical assumptions. The combination of the RM data set with other data sets as done in HE19 have also been performed and lead to a variety of results. However, discussing those, in particular in the light of the many options that exist for the inclusion of new data sets and modeling assumptions, exceeds the scope of this paper, which is to provide a methodologically clean update on the Faraday sky depth. Thus, we perform the same analysis as in HE19, but are restricting ourselves to the simpler model which uses rotation measure (RM) data only. It should be noted, that the Faraday depth maps of the simple analysis presented here and the more sophisticated to be presented in a separate publication largely agree. This publication should therefore be regarded as the primary reference for the Faraday depth sky 2020, whereas the other as providing a physical interpretation, which depends more on assumptions.

We structure the paper as following: Sect. 4.2 shortly summarizes the relevant physics, the modeling and the data used in this work. Sect. 4.3 then discusses the results and Sect. 4.4 gives a conclusive summary.

4.2 Modeling the Faraday depth sky

4.2.1 Physics

The angle of rotation Δ_λ of the polarization plane linearly polarized light experiences between emission and detection can be described by

$$\Delta_\lambda = \mathrm{RM}\,\lambda^2 \tag{4.1}$$

Burn (1966), where λ is the observational wavelength and RM is the rotation measure, defined by this equation. Determining RMs is usually done by observing Δ_λ at different wavelengths and fitting the result in λ^2 space. In the ideal case of a thin plasma screen being the only source for the rotation effect, the RM is equal to the Faraday depth ϕ, which is defined via

$$\phi = \frac{e^3}{2\pi m_e^2 c^4} \int_{\mathrm{LOS}} dl\, n_{\mathrm{th}} B_{\mathrm{LOS}}, \tag{4.2}$$

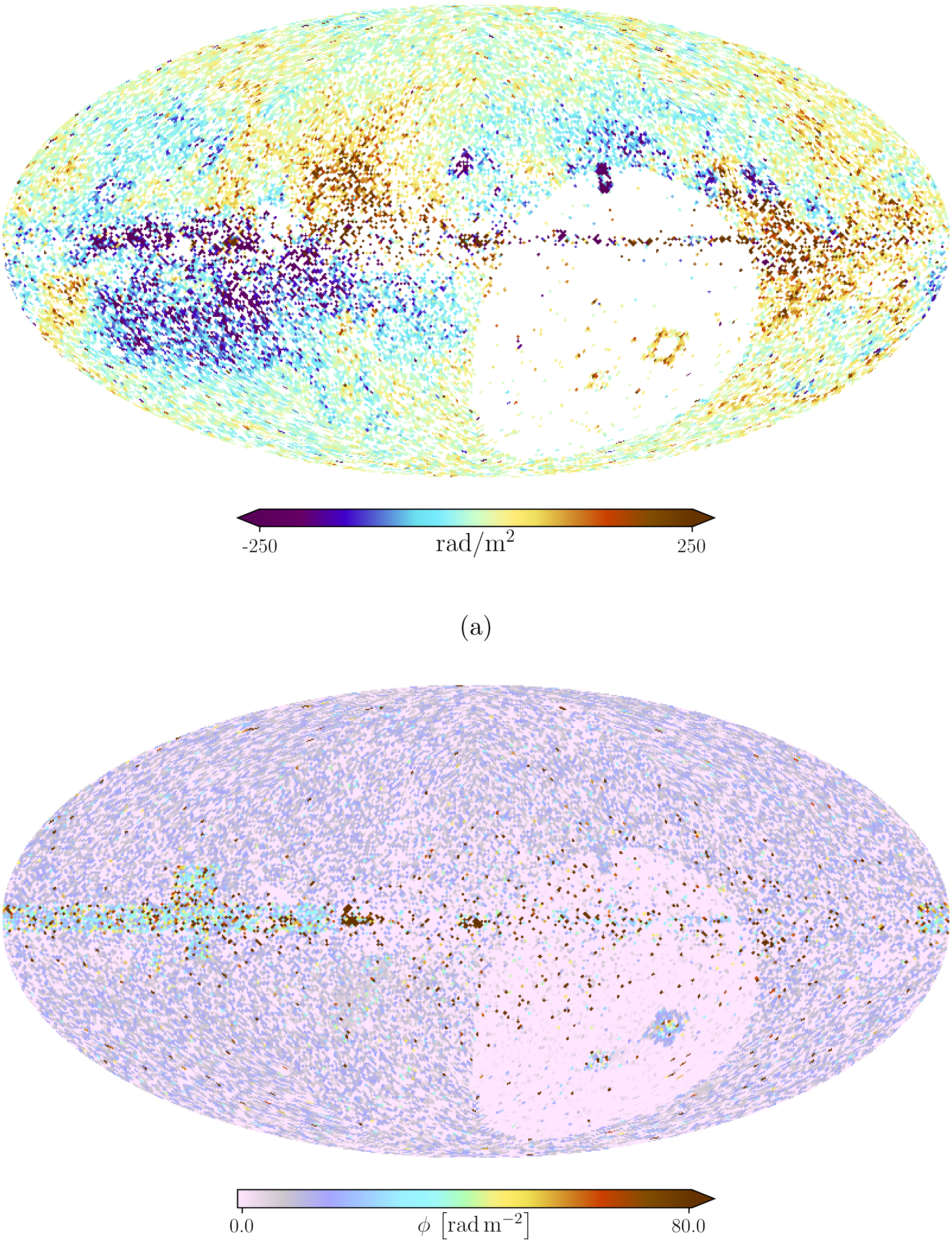

(a)

(b)

Figure 4.1: Sky projections of the van Eck catalog and corresponding uncertainties. Fig. (a) shows the RMs, Fig. (b) the observed standard deviations These maps and all maps following in this paper are presented in Galactic coordinates centered at $(l, b) = (0°, 0°)$.

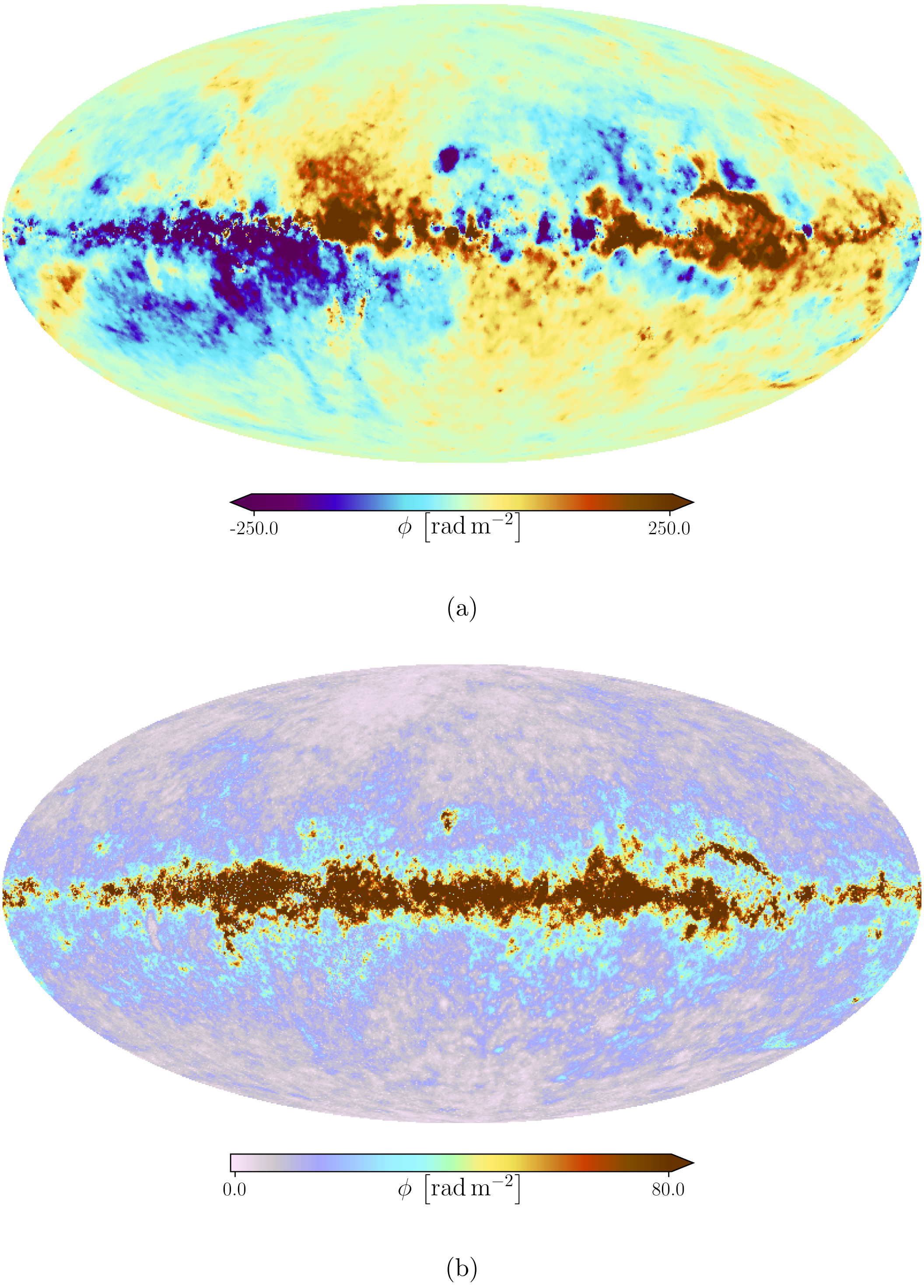

Figure 4.2: Inference results for the Galactic Faraday sky. Fig. (a) shows the posterior mean using the updated catalog, Fig. (b) the corresponding inferred standard deviations. The color scale is saturated at $\pm 250\,\frac{\text{rad}}{\text{m}^2}$ in the mean and $\pm 80\,\frac{\text{rad}}{\text{m}^2}$ in the uncertainties to highlight mid latitude features of the Galactic Faraday depth sky.

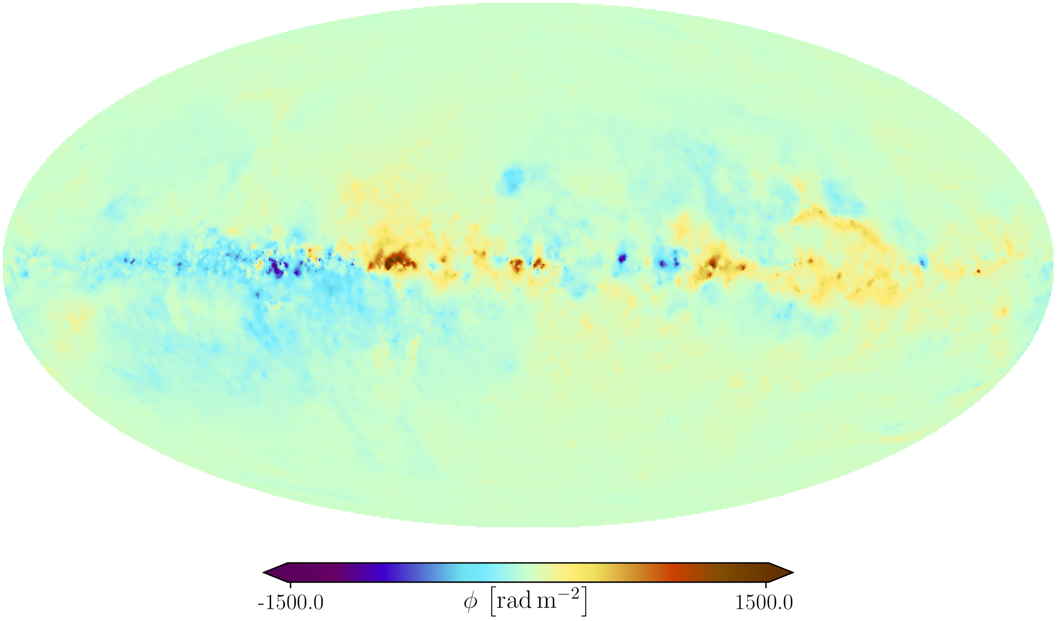

(a)

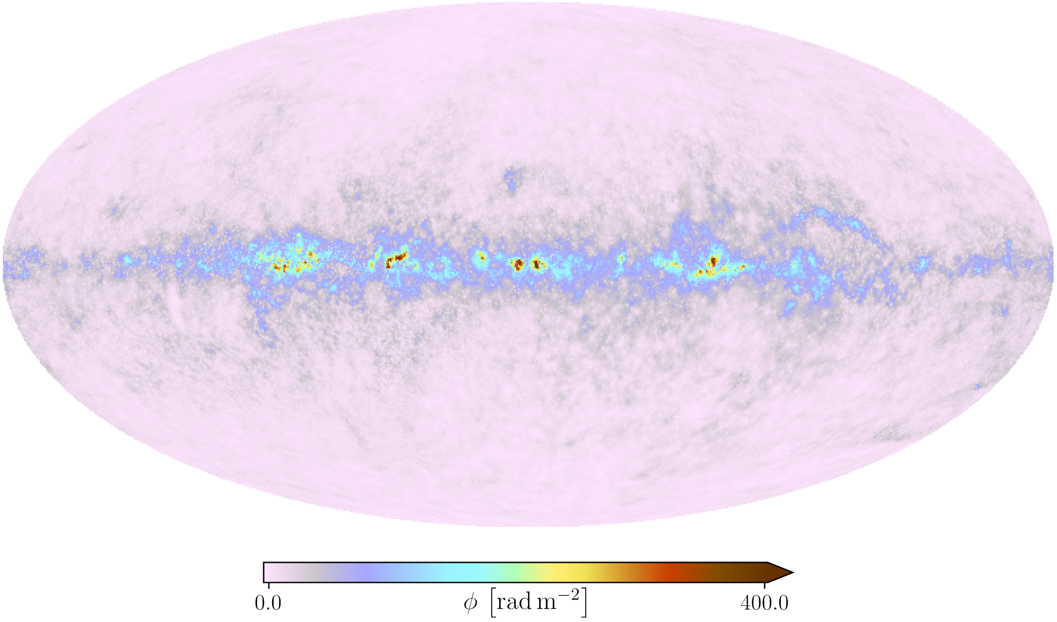

(b)

Figure 4.3: Inference results for the Galactic Faraday sky. Fig. (a) shows the posterior mean using the updated catalog, Fig. (b) the corresponding inferred standard deviations. In contrast to Fig. 4.2, the color scale is saturated at $\pm 1500\,\frac{\text{rad}}{\text{m}^2}$ in the mean and $\pm 400\,\frac{\text{rad}}{\text{m}^2}$ in the uncertainties to highlight disc features of the Galactic Faraday depth sky.

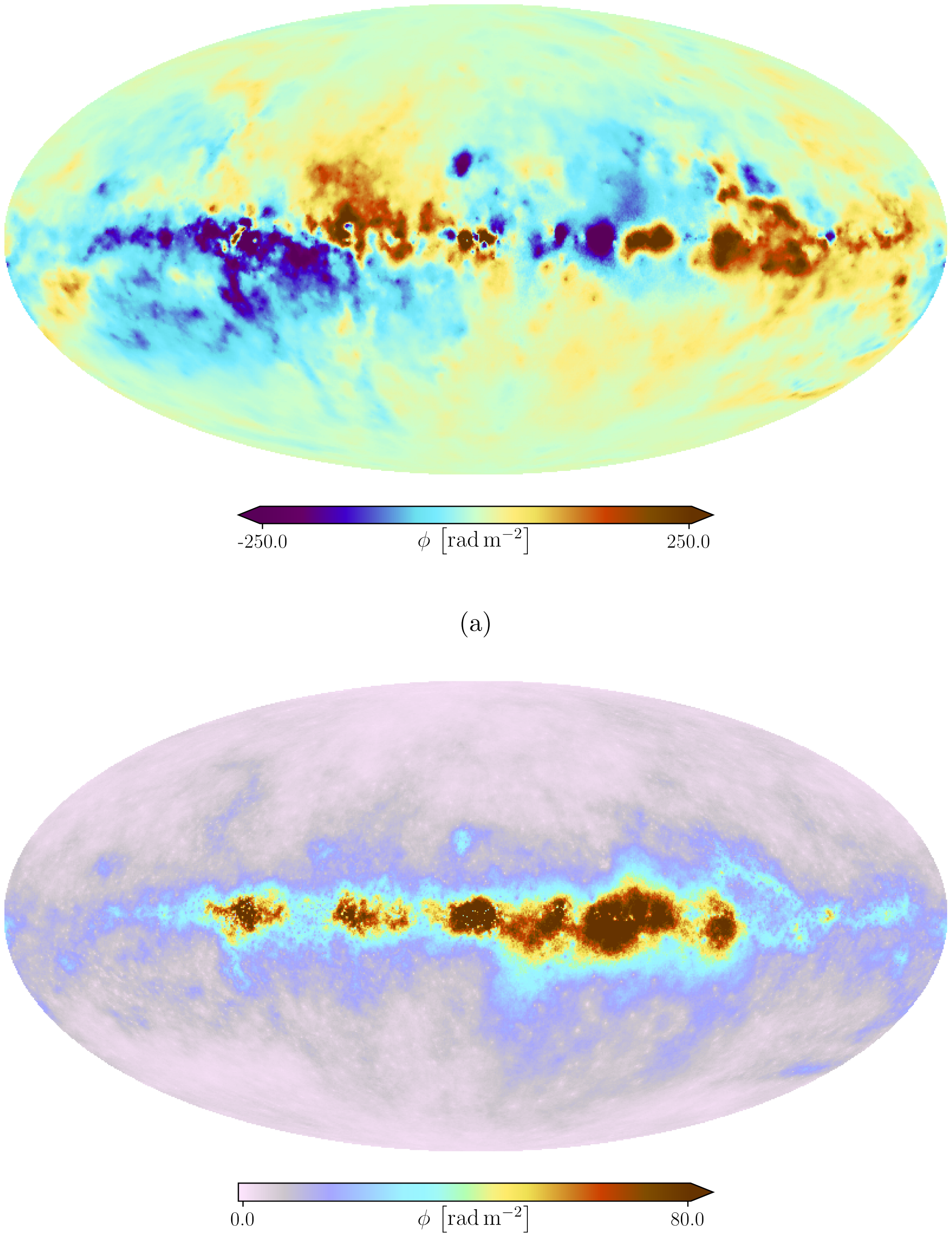
-250.0
ϕ [rad m^{-2}]
250.0
0.0
ϕ [rad m^{-2}]
80.0

(a)

(b)

Figure 4.4: Figures (a) and (b) show the mean and uncertainty of the Galactic Faraday depth sky as inferred by HE19.

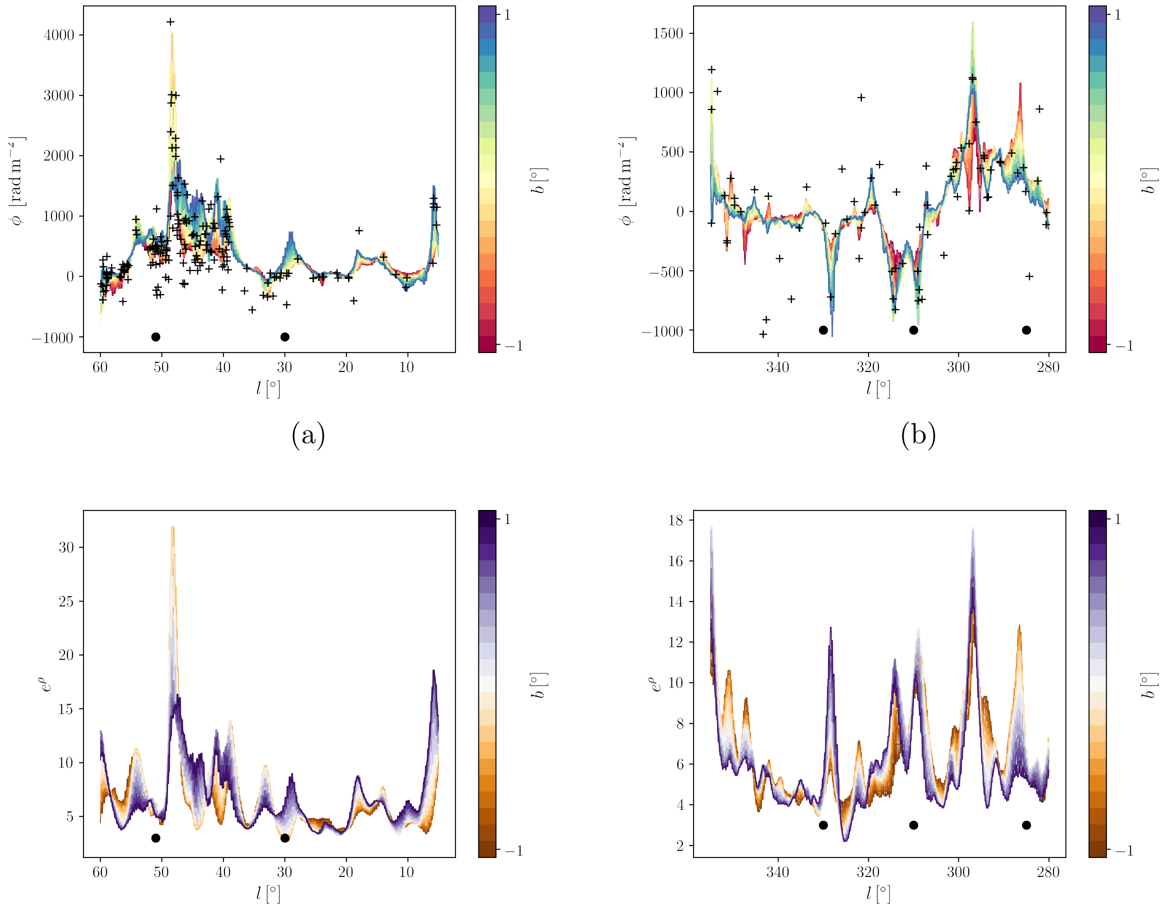

(a) (b)

(c) (d)

Figure 4.5: Slices through the inner part around the Galactic disc. Figs. (a) and (b) show excerpts of the galactic Faraday sky, including RM data points in the respective areas indicated by black pluses. The variance along the Galactic latitude is made visible by color coding the latitude for the 2 degree width of the strip. Figs. (c) and (d) show the same excerpts in the amplitude field e^{ρ}. The approximate locations of spiral arms (Hou et al. 2009; Vallée 2017) are indicated as black filled circles. The slice in Fig. (a) is also partly shown in Shanahan et al. (2019a), where the strong excess in Faraday depth in tangential direction to the Sagitarrius arm was first noted.

where n_{th} is the thermal electron density and B_{LOS} the line of sight (LOS) component of the magnetic field. The physicals constants e, m_e and c describe the elementary charge, the electron mass and the speed of light, respectively and the integral runs from the observer to the source. Unfortunately, the relation RM $= \phi$ is generally not correct. Measurements of ϕ are therefore very often obtained via more elaborate reconstruction techniques, such as RM synthesis Brentjens & de Bruyn (2005a); Bell & Enßlin (2012). In this work we will use data for ϕ which was determined either with a simple slope fit in λ^2 space or via RM synthesis. We will therefore refer to this data simply as 'Faraday data' in consistency with HE19. Especially the slope fitted data is prone to systematical errors, as demonstrated e.g. by Ma et al. (2019).

In this work, we are interested in the Galactic component of the Faraday depth sky ϕ_{gal}. Due to the additivity of ϕ one can rewrite the data equation for the Faraday depth as

$$d_\phi = R\phi + n_\phi = R\left(\phi_{\text{gal}} + \phi_{\text{etc}}\right) + n_\phi = R\phi_{\text{gal}} + \widetilde{n}_\phi, \tag{4.3}$$

where the R is a projection operator connecting the sky with data space and the (Gaussian) noise term n_ϕ contains the known observational error. The non-Galactic component ϕ_{etc} contains e.g. extra-Galactic ionospheric contributions and is absorbed together with the observational noise into an adapted noise term $\widetilde{n}_\phi$, which needs to be estimated. This is done using the same noise estimation technique as first described in Oppermann et al. (2012a) and by using the same hyper-parameters as used in HE19. This noise estimation procedure also takes care of the systematical errors discussed earlier e.g. due to slope misfitting.

4.2.2 Sky model

The sky model for ϕ_{gal} has been well motivated in HE19. Here, we would like to give a very short alternative motivation, which provides connection points for additional data sets, e.g. on the Galactic electron density. If one assumes no correlation between n_{th} and B_{LOS}, which is reasonable for the warm ionized medium of the Galaxy (Harvey-Smith et al. 2011; Passot & Vázquez-Semadeni 2003) , Eq. (4.2) can be written as (Draine 2011)

$$\phi \propto \text{DM} \left\langle B_{\text{LOS}} \right\rangle_{\text{LOS}}, \tag{4.4}$$

where we introduced the dispersion measure DM $= \int_{\text{LOS}} dl\, n_{\text{th}}$ and the LOS averaged magnetic field strength $\left\langle B_{\text{LOS}} \right\rangle_{\text{LOS}}$. This equation is used to motivate the simplest model for the Faraday sky,

$$\phi = e^{\rho} \chi \frac{\text{rad}}{\text{m}^2}, \tag{4.5}$$

implemented already in HE19. Here, ρ and χ are Gaussian fields living on the sky with unknown correlation structure that needs to be determined. The log-normal field e^{ρ} is supposed to take over the role of the DM, while χ models the magnetic field average. As

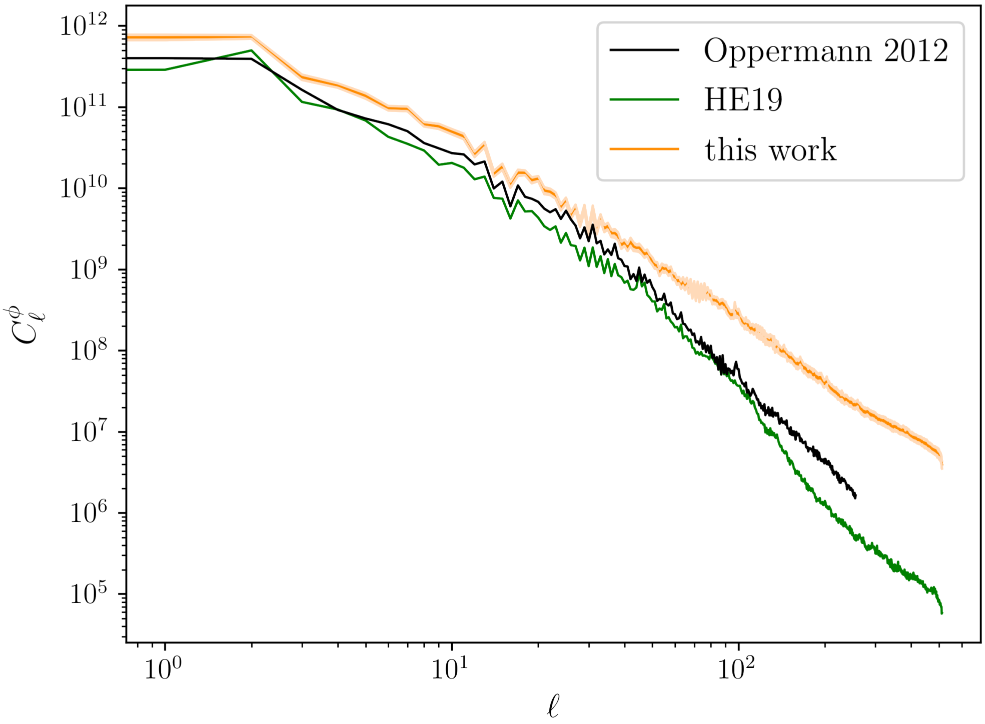

Figure 4.6: Power spectrum for the Faraday depth sky derived in this work, compared with results from HE19 and Oppermann et al. (2012a).

already noted in HE19, one cannot break the degeneracy of this model and relate the component fields to the respective physical quantities without further information and/or assumptions. This is attempted in the mentioned separate work.

The inference of the correlation functions has been updated in accordance with recent developments in numerical information field theory, for details see Arras et al. (2020). The new model is equally flexible in representing different power spectra, but has the advantage of more intuitive and better decoupled hyper-parameters. This inference was implemented in the newest version of the NIFTy package (The NIFTy5 team et al. 2019).

4.2.3 Catalog

We have used a newly compiled master catalog of published extra-galactic source RM data[1], to be published by van Eck et al. (in prep.)[2]. This catalog was assembled independently of the Oppermann et al. (2012a) catalog, but contains most of the same sources plus many published since then. A list of the individual catalogs included can be found online with the master catalog. This new master catalog is not yet complete, with papers being prioritized for inclusion based on combination of catalog size, recency, ease of data access (i.e., Vizier or machine readable tables were preferred to LaTeX or PDF tables, which were preferred to images of tables). The version of the catalog used here includes RMs from 44 papers, which encompasses nearly all of the catalogs published in the past 20 years with more than 30 RMs. Sources reported with multiple RM values (from RM synthesis or QU-fitting) had all components included as separate entries in the catalog. Catalogs of pulsar RMs were not included in the current version, but pulsars present in the individual catalogs were included and labeled as such where possible. The master catalog does not make any attempt to identify duplicate RMs; if a source appears in multiple catalogs, all measurements are kept. This results in a catalog of 52 413 RMs, which is a significant expansion on the 41 330 used by Oppermann et al. (2012a).

In this work, a a-priori noise level of 10% was a assumed for sources without error bars, which was then subject to the same noise estimation procedure as all other data points. We furthermore did not exclude duplicates or pulsars. In the case of duplicates, the noise estimation technique of Oppermann et al. (2012a) is strictly speaking not optimal, as the assumption of independence for the error estimates does not hold anymore. In our case the number of duplicates is small, we therefore deem this approximation acceptable. In future studies of the Faraday sky, this might have to be revised.

---

[1] Brown et al. (2003); Minter & Spangler (1996); Tabara & Inoue (1980a); Kim et al. (2016); Oren & Wolfe (1995); Betti et al. (2019); Van Eck et al. (2011); Bonafede et al. (2010a); Clarke et al. (2001); Johnston-Hollitt (2003a); Clegg et al. (1992); Gaensler et al. (2001b); Rudnick & Jones (1983); Wrobel (1993); Kim et al. (1991); Lawler & Dennison (1982); Hennessy et al. (1989); Kato et al. (1987); Van Eck et al. (2018); Costa & Spangler (2018); Taylor et al. (2009); Mao et al. (2010); O'Sullivan et al. (2017); Roy et al. (2005); Battye et al. (2011); Broten et al. (1988); Heald et al. (2009); Law et al. (2011); Mao et al. (2012a); Klein et al. (2003); Brown et al. (2007); Schnitzeler et al. (2019); Rossetti et al. (2008); Simard-Normandin et al. (1981); Mao et al. (2012b); Vernstrom et al. (2018); Mao et al. (2008); van Eck & Brown (in prep.); Anderson et al. (2015); Feain et al. (2009); Riseley et al. (2018); Costa et al. (2016); Shanahan et al. (2019b); Kaczmarek et al. (2017)

[2] This master catalog can be found online at https://github.com/Cameron-Van-Eck/RMTable; this paper used version 0.1.6 of this catalog.

4.3 The results

In the following we present the results of the model introduced in Sect. 4.2. We show the resulting Faraday sky and uncertainties in Figs. 4.2 and 4.3 on different color scales. For comparison, the previous results of HE19 are shown in Fig. 4.4. On large scales, the results are in good agreement with each other, while on smaller scales many more structures are discernible in the new reconstruction. Furthermore, Fig. 4.3a reveals a strong disc with absolute values often exceeding 1500 rad/m^2, with a maximum above 4000 rad/m^2, which stands in strong contrast to the previous inference results which had a maximum only shortly above 1000 rad/m^2. This is highlighted in the slice plots in Fig. 4.5, which cut the sky region in the inner Galactic plane in longitudinal direction. The excess to 4000 rad/m^2 in the Sagitarrius region in Fig. 4.5a has been first noted by Shanahan et al. (2019a). We note that excesses in Faraday depth are also notable towards the other known spiral arms, although not as pronounced. This does not necessarily indicate exceptionalism of the Sagitarrius region, but can also be explained by a lack of data coverage in other parts of the plane, as especially the longitude region $l \in (150, 360)$ still has a under-dense data coverage and many older surveys are limited to moderate RM values.

We attribute the emergence of both the stronger disc as well as the new smaller scaled structures mostly to the newly available data-points. A significant contribution to this improvement might also come from the new correlation structure modeling implemented in the newest version of NIFTy (Arras et al. 2020). A hint in this is given by the inferred power spectrum plotted in Fig. 4.6, compared to the previous spectra inferred by HE19 and Oppermann et al. (2012a). The plot shows a significant offset of the new spectrum compared to its predecessors. This indicates stronger fluctuations on all scales, which were captured in previous results. The new power spectrum furthermore shows close resemblance to a power-law on all scales, with a slope of $\approx$ 2. In contrast to that, the power spectra on small scales where at least somewhat suppressed in HE19 and Oppermann et al. (2012a), in the latter case to some degree due to the coarser resolution. This is consistent with the stronger small scaled structures visible in Fig. 4.2a as compared to Fig. 4.4a. The scatter plots in Fig. 4.7 investigate the correlation between the amplitude field (shown in Fig. 4.8a) and both the DM sky and the square root of the EM sky. The latter was inferred from cosmic microwave data by the *Planck* survey (Planck Collaboration 2016a), while the former is calculated from a parametric model of the Galactic thermal electron density (Yao et al. 2017) based on pulsar DM data. Visually, although the EM map of *Planck* is much more detailed and the DM map relies on very little data and strong modeling assumptions, we see a much better correlation of the amplitude field with DM sky than with the EM map, especially for small amplitude field values. This is confirmed by Pearson cross-correlation coefficients of 0.854 for the log DM map and 0.746 for the log square root EM map. In the case of the non-logarithmic maps, the contrast is not so strong as we calculate coefficients

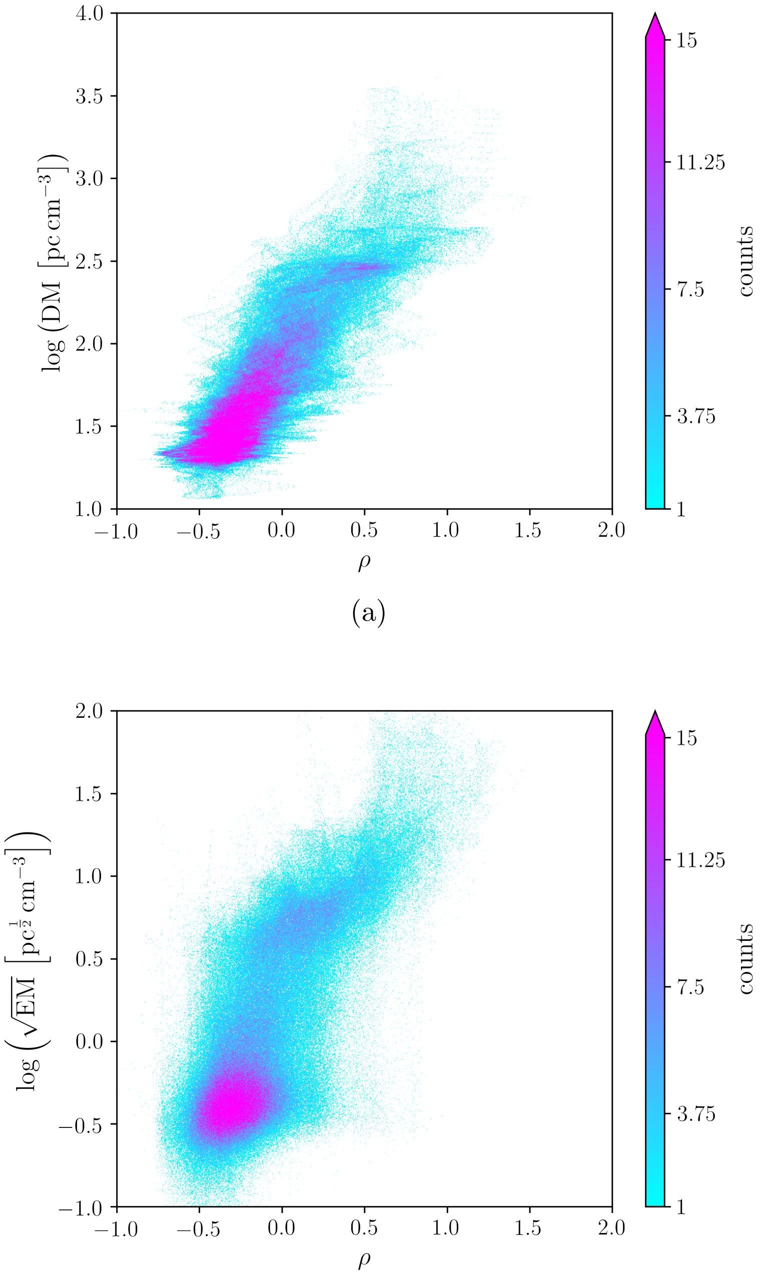

(a)

(b)

Figure 4.7: Histogram illustrating the correlation between the log amplitude field ρ and the logarithmic DM (Fig (a)) and logarithmic square root EM (Fig. (b)) skies, respectively. The former is calculated from a Galactic thermal electron model (Yao et al. 2017), while the latter was inferred by the *Planck* survey from microwave data (Planck Collaboration 2016a).

of 0.686 for the $e^\rho - \mathrm{DM}$ correlation and 0.711 for the $e^\rho - \sqrt{\mathrm{EM}}$ correlation. In the case of the DM map some of the missing correlation to the amplitude map can be explained by the fact that the Yao et al. (2017) electron model lacks small scale structure as it relies on very little data. The differences to the square root EM map are best explained by the missing volume filling factor that needs to be considered in order to equate the EM and DM skies. Gaensler et al. (2008) show that this factor is variable over the sky and ranges between 0.04 mid-plane to about 0.3 at higher latitudes. As demonstrated in HE19, the EM sky is nonetheless a valuable source of information on the Galactic electron density profile. It is however necessary to model these systematic volume effects by introducing additional degrees of freedom, as implemented phenomenologically in HE19. We further show the component fields e^ρ and χ in Figs. 4.8a and 4.8b. Both show strong similarity to the analog component fields found in HE19.

We show that the amplitude field is a good tracer of dense Galactic structures also on smaller scales in Fig. 4.9, where we show the Magellanic clouds in our Faraday depth and amplitude reconstructions and in the EM and H_α skies. The comparison to especially the EM sky shows good agreement on the morphology of the large Magellanic cloud. In case of the small Magellanic cloud, the profile seems to be slightly offset towards the known 'wing' feature, indicating somewhat enhanced magnetic field strengths in this region. Furthermore, the region between the clouds shows small negative values in contrast to the surrounding positive regions of Faraday depth. This is consistent with an additional coherent magnetic field structure between the clouds as first reported by Kaczmarek et al. (2017).

If the amplitude field is indeed a good tracer of the morphology of the DM, this implies that by Eq. (4.4) the sign field in 4.8b should trace the morphology of the averaged LOS component of the Galactic magnetic field to equal quality. This would indicate several large scale regions in the mid-latitude magnetic field sky with a relatively strong LOS component of the Galactic magnetic field coherently pointing in one direction.

4.4 Conclusion

We have reconstructed the Galactic Faraday depth sky using newly available RM data. We have found a significantly enhanced Galactic disc with Faraday depth values up to $4000\,\mathrm{rad/m^2}$ consistent with recent measurements of Faraday excesses in the Sagitarrius region and were able to improve our constraints on the small scaled structures in the sky map. These improvements indicates a strong potential of the upcoming RM surveys of ASKAP, Meerkat, LOFAR and SKA in increasing our knowledge on the Galactic magnetic field, as they will provide a vast catalog of new RM measurements. This information will in turn provide a pivotal role in constraining the Galactic magnetic field and is an important input for upcoming three dimensional reconstructions of the magnetized interstellar medium.

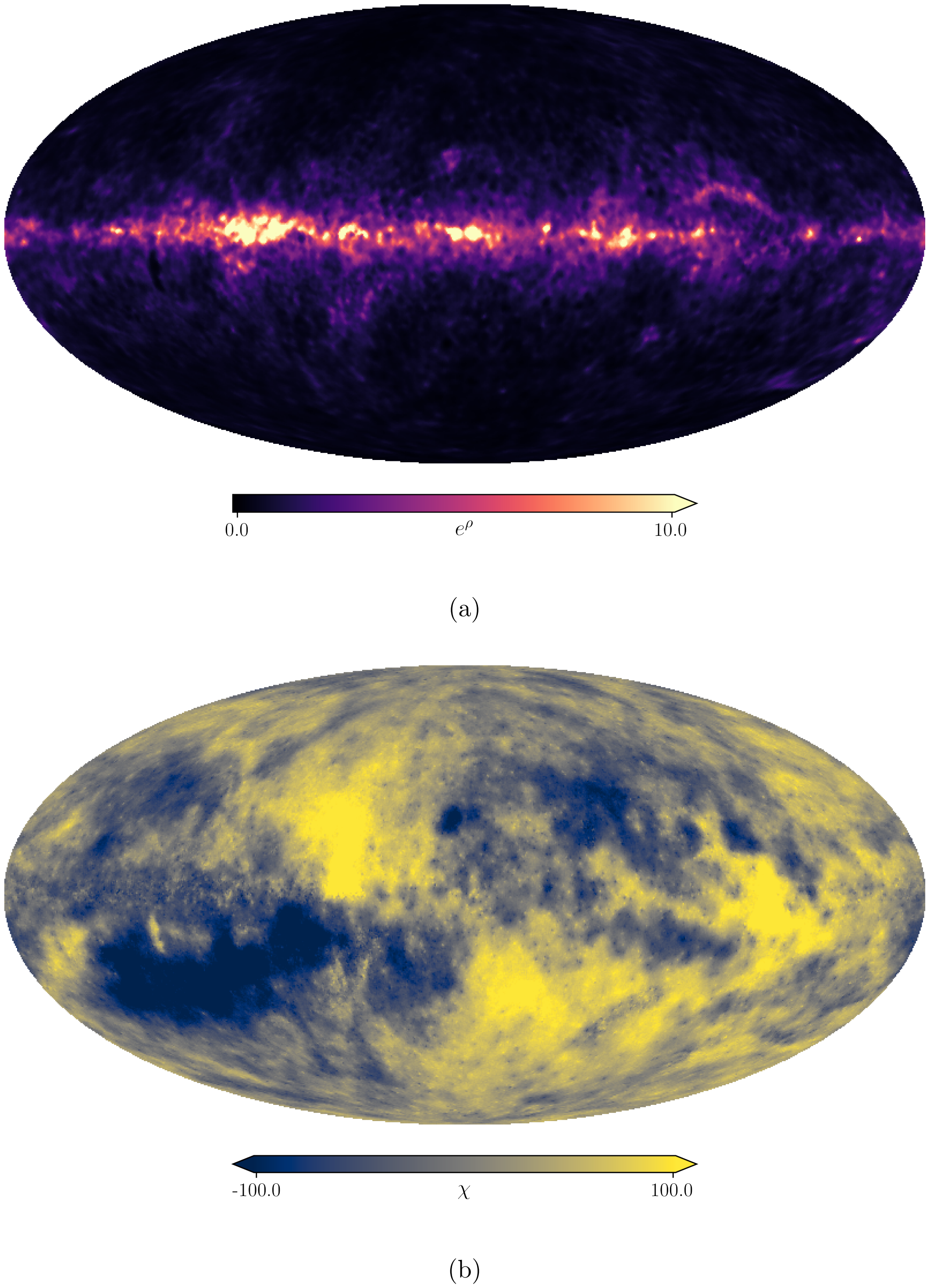
0.0
e^{ρ}
10.0
-100.0
χ
100.0

(a)

(b)

Figure 4.8: Posterior means of the components defined in Eq. (4.5). Fig. (a) shows the amplitude field e^{ρ} and Fig. (b) shows the sign field χ.

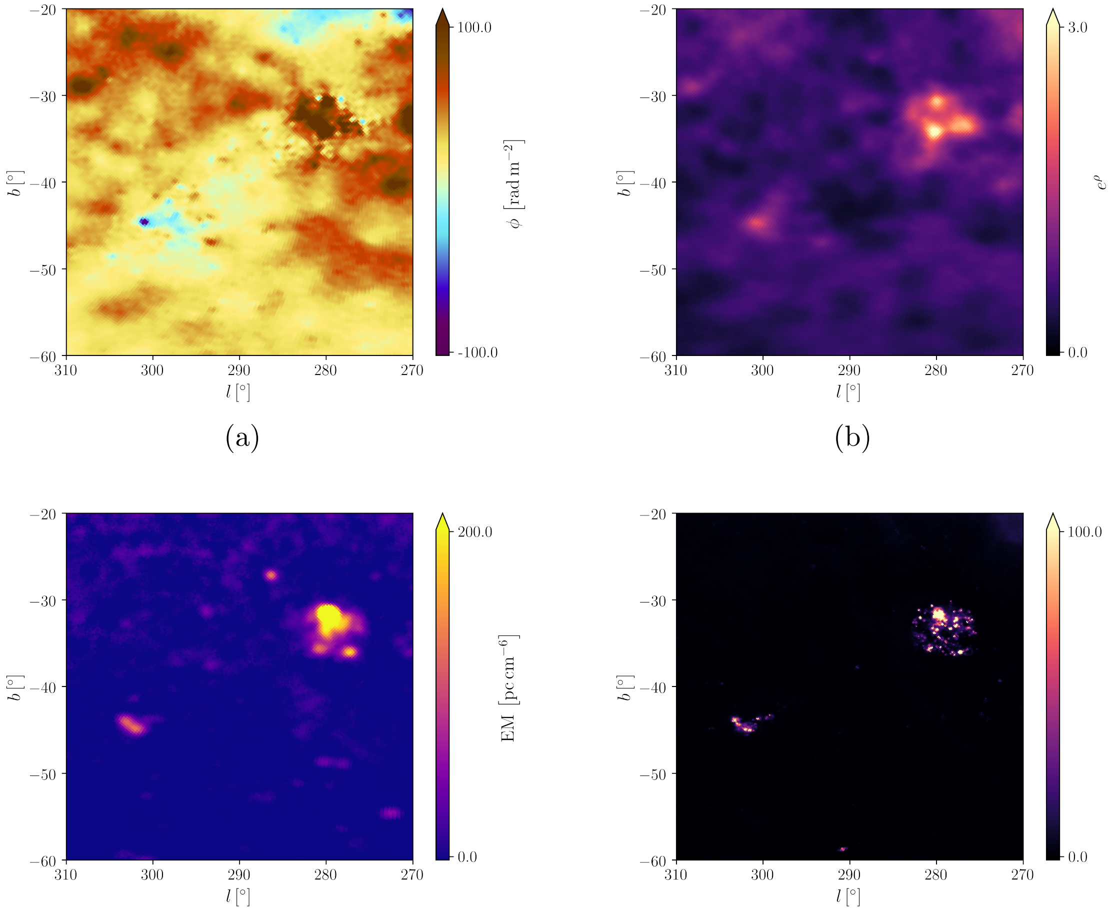
−20
−30
−40
−50
−60
$b\,[°]$
310
300
290
280
270
$l\,[°]$
100.0
-100.0
$\phi\ [\mathrm{rad\,m^{-2}}]$
3.0
0.0
e^{ρ}
200.0
0.0
$\mathrm{EM}\ [\mathrm{pc\,cm^{-6}}]$
100.0
0.0

(a) (b)

(c) (d)

Figure 4.9: The Magellanic Clouds as seen with different observables. Figs. (a) and (b) show the Faraday depth and the underlying amplitude field as inferred in this work. Figs. (c) and (d) show emission measure (EM) as obtained by the *Planck* satellite (Planck Collaboration 2016a) and in H_α emission (Finkbeiner 2003; Gaustad et al. 2001).

Chapter 5

Disentangling the Faraday sky

References and Acknowledgment

This chapter contains the results of a yet unpublished project lead by me under the supervision of Torsten Enßlin.

5.1 Introduction

The structure of the Milky Way is best expressed in terms gas and stellar density, velocities, and force fields, as these can be related to the dynamical laws that govern the formation of structure and the overall shape of galaxies today. To our fortune, these fundamental quantities can be determined by a variety of observables, which, to our misfortune, in general do not yield constraints for those individually, but are mixed and entangled in nontrivial and sometimes nonlinear ways.
Prominent examples of such observables intervening several Galactic constituents are e.g synchrotron radiation coupling the relativistic electron density n_{rel} with the squared perpendicular component of the Galactic magnetic field $B_{\perp}$, or stellar polarization in the optical regime, which gives information on the magnetic field direction and dust properties. The only route to disentangle these and similar observables and to map out the structure of the Galaxy is to cross-correlate them with each other and/or to compare with simulations. For some observables, this has been successfully performed, e.g Polderman et al. (2020) constrain the cosmic ray electron density and magnetic field strength from synchrotron radiation and free-free absorption or Leike & Enßlin (2019) reconstruct the local Galactic dust density from stellar absorptions and positions.

In this paper, we aim to disentangle the Galactic Faraday depth sky into its physical components. The Faraday effect couples the line-of-sight (LOS) component of the magnetic field $B_{\|}$ with the thermal electron number density n_{th}. It is the only observable that provides direct information on $B_{\|}$ for most regimes in the interstellar medium (ISM), apart from longitudinal Zeeman splitting, which may be observable in very dense regions such as molecular clouds (Beck & Wielebinski 2013) and circular polarization of synchrotron radiation, which will only be observable with next generation radio telescopes (Enßlin et al. 2017). The Faraday effect has long been used to constrain the magnetic field strength (Frick et al. 2001; Han et al. 2006). Such works often exploit the information of pulsars, which have the advantage of potentially providing RM and DM associated with a known distance. The disadvantage is that few pulsars are known with independent distance measurements (about X at the time of writing this paper) and hence, in case the large scale fields of the whole Milky Way are to be constrained, one has to appeal to strong modeling assumption on the magnetic field and/or the thermal electron density. Extra-Galactic RM sources have also been used to constrain the Galactic magnetic field in conjuncture with EM information stemming from free-free emission (Hutschenreuter & Enßlin 2020a).

In the latter reference, henceforth abbreviated with HE19, we included the free-free EM sky as a phenomenological proxy for the Faraday depth amplitude and were thereby able to make qualitative statements on the local structure of the Galactic magnetic field. In particular, the alignment of the magnetic field with the local Orion spiral arm was revealed thereby. In this work we will replace our phenomenological model used in HE19 with a more physical one, with the aim to turn qualitative predictions into quantitative ones. This will be attempted with the help of four different data sets, namely (mostly) extra-Galactic Faraday rotation measures (RMs) as compiled by van Eck et al. (in prep.), pulsar DM data (Manchester et al. 2005) and the emission measure (EM) map of the *Planck* survey. As byproducts, we obtain sky maps on the volume filling factor that translates the EM and DM skies and a cleaned EM sky field.

The statistical methodology of this work foots on the same grounds as previous inferences of the Galactic Faraday depth sky in Oppermann et al. (2012a), HE19 and HE20, namely Information Field Theory (IFT). IFT is information theory for fields and field-like quantities and can cope with large, incomplete, and noisy data sets. For references to IFT see Enßlin (2019) and for the accompanying python package NIFTy, in which the algorithm used in this work is implemented in, see The NIFTy5 team et al. (2019).

We structure the paper as following: Sect. 5.2 describes the physics relevant for this paper, putting special emphasis on effects that correlate the different relevant physical quantities. Sect. 5.3 then explains the different models the data is interpreted in. Sect. 5.4 discusses the results and finally Sect. 5.5 gives a conclusive summary.

5.2 Observables

5.2.1 Faraday rotation measures

The angle of rotation Δ_λ of the polarization plane of linearly polarized light travelling through a magneto-ionic plasma, can be described by the following formula Burn (1966)

$$\Delta_\lambda = \mathrm{RM}\,\lambda^2, \tag{5.1}$$

where λ is the observational wavelength and RM is the rotation measure, defined by this equation. Determining RMs is usually done by observing Δ_λ at different wavelengths and fitting the result in λ^2 space. In the ideal case of a thin plasma screen being the only source for the rotation effect, the RM is equal to the Faraday depth ϕ, which is defined via

$$\begin{aligned}\phi &= \frac{e^3}{2\pi m_e^2 c^4} \int_{\mathrm{LOS}} dl\, n_{\mathrm{th}} B_{\mathrm{LOS}} = \\ &= 0.812 \int_{\mathrm{LOS}} dl\,[\mathrm{pc}]\; n_{\mathrm{th}} \left[\mathrm{cm}^{-3}\right] B_{\mathrm{LOS}}\,[\mu\mathrm{G}]\,, \end{aligned} \tag{5.2}$$

where n_{th} is the thermal electron density and B_{LOS} the LOS component of the magnetic field. The physicals constants e, m_e and c describe the elementary charge, the electron mass and the speed of light, respectively, and the integral runs from the observer to the source. It should be noted that the Faraday effect is mostly a tracer of large scale magnetic fields. This implies that the LOS averaged magnetic field strength significantly underestimates the total magnetic field strength in strongly turbulent environments.

One can write down the measurement equation for the Faraday depth

$$d_\phi = R\phi + n_\phi, \tag{5.3}$$

where the R is a projection operator connecting the sky with data space and the (Gaussian) noise term n_ϕ contains the Gaussian statistical noise with known covariance. In this work, we are using a newly compiled data catalog of RM measures (van Eck et al. in prep.). We furthermore use the noise estimate provided by HE20 instead of the observational errors, as in these the potential extragalactic components and observational systematics from e.g. nπ-ambiguities (Ma et al. 2019) are already factored in.

5.2.2 Pulsar dispersion measures

Pulsars are magnetized and rapidly rotating neutron stars (Lorimer 2008), emitting beamed electromagnetic radiation. This results in periodic radio pulses. As light travels slower within interstellar plasma at lower frequencies, the arrival time t of the pulse varies with frequency ν, which can be expressed as (Draine 2011)

$$\frac{\partial \mathrm{t}}{\partial \nu} = -\frac{e^2}{\pi \nu^3 m_e c}\mathrm{DM_i}, \tag{5.4}$$

where the dispersion measure $\mathrm{DM_i}$ of pulsar i is defined as

$$\mathrm{DM_i} = \int_{\mathrm{LOS_i}} n_{\mathrm{th}}. \tag{5.5}$$

The LOS goes from Earth to the pulsating neutron star. Therefore, DMs obtained from pulsars provide a lower limit on the Galactic DM sky for the respective LOS they probe. These are the ones we require for this work, as they probe the DM practically over the same Galactic length as the background radio sources used to construct the Faraday rotation sky. Identifying the subset of the known pulsar population that is located beyond the boundary

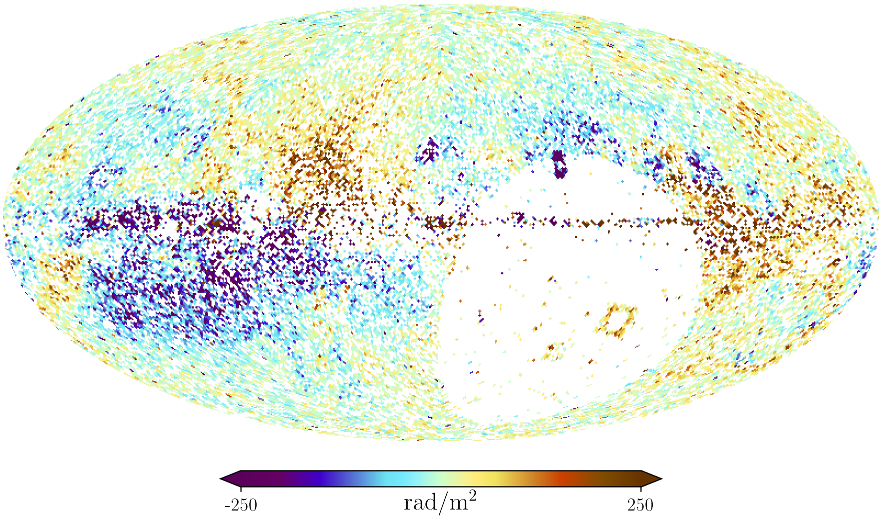

(a)

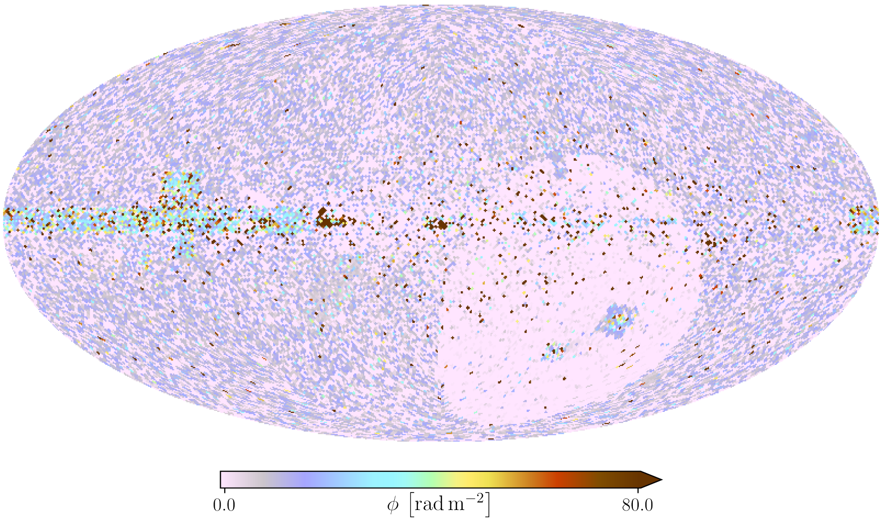

(b)

Figure 5.1: Sky projections of the RMs coming from the van Eck catalog (Fig. (a)). Fig. (b) shows the corresponding the estimated standard deviations from HE20. These and all maps following are presented in Galactic coordinates centered at $(l, b) = (0°, 0°)$.

region of the Milky Way is a non-trivial task. Distance measurements independent of n_{th} are only available for a minority of pulsars, mostly via parallaxes, associations with known structures or HI absorption. In this work we will use the Australia Telescope National Facility (Manchester et al. 2005) catalog of pulsars [1]. From this catalog, we identify pulsars satisfying the condition

$$\frac{x_{\mathrm{Gal}}^2}{(16\,\mathrm{kpc})^2} + \frac{y_{\mathrm{Gal}}^2}{(16\,\mathrm{kpc})^2} + \frac{z_{\mathrm{Gal}}^2}{(4\,\mathrm{kpc})^2} > 1, \tag{5.6}$$

where $x_{\mathrm{Gal}}, y_{\mathrm{Gal}}$ and z_{Gal} are the coordinates of the pulsar in a Galacto-centric coordinate system. The corresponding DMs are collected in a data set $d_{\mathrm{DM,edge}}$. This data set is illustrated in Fig. 5.2.

We explicitly exclude pulsars in the Magellanic Clouds, which on the one hand satisfy Eq. 5.6, but on the other hand show strong internal DM scatter, indicating internal DMs comparable to that of the Milky way in their direction. As we also have a large number or RMs for the Magellanic Clouds and they are sufficiently resolved given the resolution we would like to achieve, we treat them as a part of the Galactic sky. They and all other pulsars which do not fulfill the condition in Eq. (5.6) all provide a lower limit for the DM of their respective LOS and are therefore collected in a second data set $d_{\mathrm{DM,lower}}$.

5.2.3 The electron emission measure

In some of the reconstruction algorithms, we will constrain the amplitude of the Faraday rotation sky by using additional information on the projected thermal electron density. One of the – from a physical point of view – easiest obtainable measure on this quantity is the electron emission measure (EM), defined via

$$\mathrm{EM}_{\mathrm{P}} = \int_{\mathrm{LOS}_{\mathrm{P}}} n_{\mathrm{th}}^2. \tag{5.7}$$

The subscript P indicates the process that traces the EM. To give specific examples, the EM can be e.g. constrained by observing radiation stemming from free-free emission (the bremsstrahlung resulting from the interaction of free protons and electrons) or H-α emission tracing the hydrogen Balmer-α line. H-α emission as a tracer of EM has the disadvantage that both electron temperature and foreground dust absorption need to be considered, which is beyond the scope of this work. Free-free emission is an important Galactic foreground in the microwave sky, especially in the low-frequency regime around 30 GHz, and was therefore accurately determined by Cosmic Microwave Background (CMB) missions such as *Planck* (Planck Collaboration 2016a) or WMAP (Bennett et al. 2013). The observed free-free emission depends on two Galactic environmental variables, namely the thermal electron density n_{th} and the thermal electron temperature T_{e}. Under the assumption that the latter is constant along the LOS, the *Planck* team has produced both

---

[1] `http://www.atnf.csiro.au/research/pulsar/psrcat`

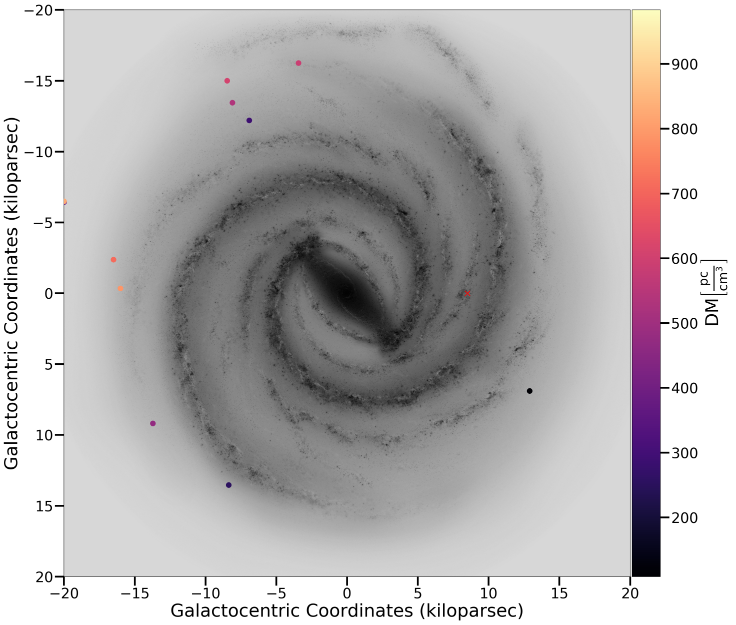

(a)

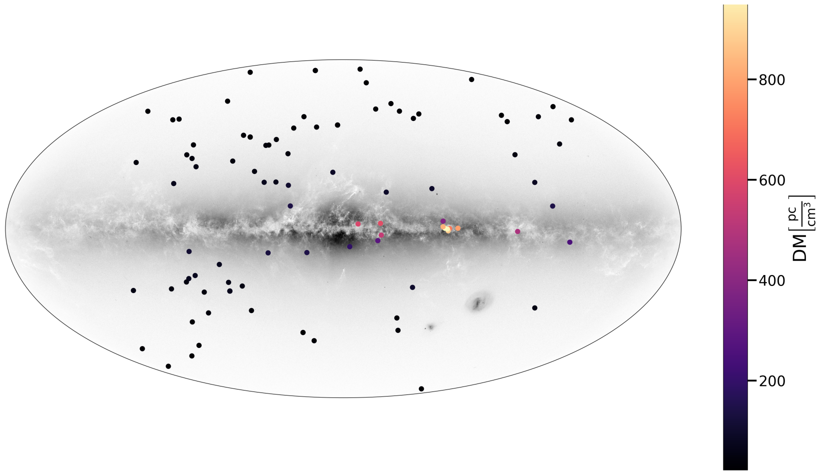

(b)

Figure 5.2: Positions of the pulsars that are collected in data-set $d_{\mathrm{DM,edge}}$ because they can be assumed to lie at the Galactic edge. The horizontal cut through the Galaxy in Fig. (a) contains only pulsars with a distance to the Galactic plane of $|z| < 3$ kpc, while Fig (b) shows all pulsars in the data-set. The background images are an artist impression (NASA/JPL-Caltech,R. Hurt (SSC/Caltech), Fig. (a)) or adapted from Gaia Collaboration et al. (2018) (Fig. (b)).

T_e and EM maps (Planck Collaboration 2016a). The T_e map is barely constrained by the *Planck* data and therefore is of limited use here. In HE19, we used the $\mathrm{EM}_{\mathrm{ff}}$ map to construct a proxy for the amplitude of the Galactic Faraday depth sky. This will also be the case here, albeit with updated models. It was furthermore discussed in HE19 that the uncertainties given by the *Planck* team seem not to capture the full uncertainty (Planck Collaboration 2016a). In this work, we will therefore rely on the same noise estimation technique as in HE19.

5.3 The models

In general, we non-parametrically model the quantities that need to be inferred as a non-linear combination of Gaussian fields defined over the sky, each characterized by a unknown correlation structure, that needs to be inferred simultaneously with the field it characterizes. The inference of the respective correlation functions is modeled slightly differently in accordance with recent developments in numerical information field theory, for reference see (Arras et al. 2020). As an example, to infer a flux density on the sky, we assume it to be an exponentiated Gaussian process, as the resulting field is positive and large variations in flux are easily representable this way.

In the following, we introduce the LOS-average over a quantity x

$$\langle x \rangle_{\mathrm{L_P}} \equiv \frac{1}{\mathrm{L_P}} \int_0^{\mathrm{L_P}} dl\, x, \tag{5.8}$$

with $\mathrm{L_P}$ indicating the length of the LOS traced by a physical process P. This notation allows an interpretation of the observables as expectation values or higher order moments of the statistical distribution of x. This enables a calculus in which we can make physically interpretable statements in order to justify the models we use. The integrals in Eqs. (5.2) and (5.7) will typically receive their most significant contributions from the Milky Way and in case of Eq. (5.2) maybe from the direct vicinity of the source. In some cases, the observational tracers might be blocked, e.g. due to absorption, making it important to distinguish averages stemming from different observables.

5.3.1 Revisiting the Faraday sky model

In order to motivate our modeling and later on interpret our results, we will further investigate the dependencies of ϕ_{gal}. We write according to Eq. (5.8):

$$\phi_{\mathrm{gal}} = 0.812\, \mathrm{L}_\phi\ [\mathrm{pc}] \left\langle n_{\mathrm{th}} \left[\mathrm{cm}^{-3}\right] B_{\mathrm{LOS}}\, [\mu\mathrm{G}] \right\rangle_{\mathrm{L}_\phi} \tag{5.9}$$

In order to further constrain ϕ (apart from further RM measurements), one needs information on either B_{LOS} or n_{th} or both. Observationally, the two quantities are generally decoupled in the warm inter-stellar medium (ISM) (Crutcher et al. 2010), but maybe correlated in denser regions such as molecular clouds (Harvey-Smith et al. 2011; Purcell et al.

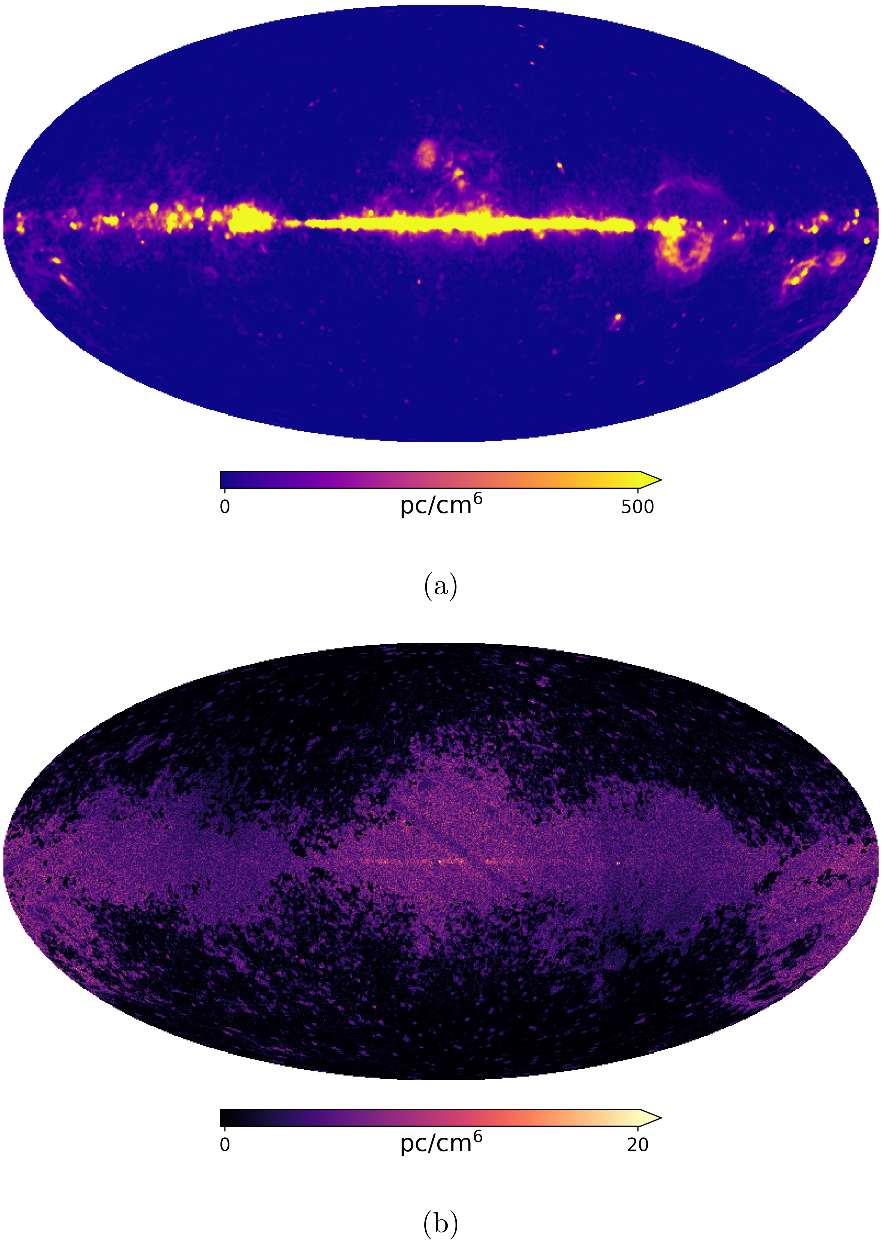
0
pc/cm^6
500
0
pc/cm^6
20

(a)

(b)

Figure 5.3: Sky projections of the *Planck* data and corresponding uncertainties. Fig. (a) shows the EM, Fig. (b) the corresponding standard deviations.

2015) which may dominate the average for certain LOS. (see also discussion in HE19). From a theoretical perspective, both anti - correlation (due to magnetic pressure compensating lacking gas pressure in conditions close to pressure equilibrium (Beck et al. 2003)) or correlation (due to compression in shock fronts or gravitationally collapsing structures) is reasonable. Either way, if such a correlation is to be assumed, one of the simplest model assumptions to make is that the magnetic field strength scales with some power law of the electron density or more explicitly

$$B = \frac{n_{\mathrm{th}}^{p}}{n_{\mathrm{th},0}^{p}} B_{\mathrm{corr}}. \tag{5.10}$$

Here, the amplitude corrected magnetic field B_{corr} is now assumed to be uncorrelated to the electron density. If the amplitude of the magnetic field is completely determined by the electron density apart from a constant factor, $B_{\mathrm{LOS,corr}}$ would only be proportional to a geometry factor $\cos(\theta)$, where θ is the angle between the LOS and the magnetic field vector. Inserting this into Eq. (5.9) and exploiting the assumed independence of $B_{\mathrm{LOS,corr}}$ and n_{th}, we get

$$\phi = 0.812 \, \frac{\mathrm{L}_{\phi}}{n_{\mathrm{L}_{\phi}\mathrm{th},0}^{p}} \left\langle n_{\mathrm{th}}^{p+1} \right\rangle_{\mathrm{L}_{\phi}} \left\langle B_{\mathrm{corr}} \cos(\theta) \right\rangle_{\mathrm{L}_{\phi}} , \tag{5.11}$$

If we assume no correlation between n_{th} and and B_{LOS} by setting $p = 0$, this simplifies to

$$\phi = 0.812 \, \mathrm{L}_{\phi} \left\langle n_{\mathrm{th}} \right\rangle_{\mathrm{L}_{\phi}} \left\langle B_{\mathrm{LOS}} \right\rangle_{\mathrm{L}_{\phi}} = \mathrm{DM}_{\phi} \left\langle B \cos(\theta) \right\rangle_{\mathrm{L}_{\phi}} , \tag{5.12}$$

where we introduced the dispersion measure $\mathrm{DM}_{\phi} = \int_{\mathrm{LOS}} dl \, n_{\mathrm{th}}$. Regardless of the value of p, on can use Eqs. (5.11) and (5.12) to motivate the simplest model for the Faraday sky, used already by HE19 and HE20:

$$\phi = e^{\rho} \chi \frac{\mathrm{rad}}{\mathrm{m}^2} \tag{5.13}$$

In both HE19 and HE20, the log-normal field e^{ρ} is phenomenologically models large variations in Faraday rotation amplitude, while χ is supposed to represent the sign of the Faraday rotation sky and small ampliutude variations. In this work, e^{ρ} models the p-th moment of the electron density (or the DM if $p = 0$), while χ models the magnetic field average, making this the base model for this work. The model is illustrated in Fig. 5.4. Both fields have an unknown correlation structure that needs to be determined. As noted in HE20, one cannot relate the component fields to the respective physical quantities without further assumptions. To attempt this is the main ambition of this work.

5.3.2 Model 1 - Adding pulsar DM data

If we assume Eq. (5.12) to be correct for most part of the sky, we can use additional DM data in order to break the aforementioned degeneracy between the ρ and χ field. As discussed in Sec 5.2, most pulsars will only provide us with a lower limit on the Galactic DM sky, but a subset of distant, mostly high latitude pulsars may be used as noisy estimator of the true full Galactic DM at their respective location on the sky due to their conjectured location behind the Milky Way. The model for their associated true DMs is then

$$\mathrm{DM}_{\mathrm{edge}} = \mathcal{R}_{\mathrm{edge}} e^{\rho}, \tag{5.14}$$

with $\mathcal{R}_{\mathrm{edge}}$ being a projection operator from the sky onto data-space. The pulsar data $d_{\mathrm{DM,edge}}$ is assumed to contain Gaussian noise. Instead of using the observational uncertainties for its likelihood covariance, which are generally very small as timing information is usually very accurate, we assume errors of at least one $\frac{\mathrm{pc}}{\mathrm{cm}^{-3}}$. This is done to account for systematic uncertainties as e.g. unaccounted small scaled electron density structure in the vicinity of the pulsar which might lead to an overestimation of DM or, vice versa additional structure behind the pulsar which would lead to a local under estimation of the Galactic DM sky. For all other pulsars, which can not be assumed to probe the full LOS through the Galaxy, we need to account for the unobserved DM fraction behind the pulsar by multiplying the respective sky value with a fudge factor r, for which we assume a uniform prior between 0 and 1. This gives the following model for their associated true DMs:

$$\mathrm{DM}_{\mathrm{lower}} = r \mathcal{R}_{\mathrm{lower}} e^{\rho} \tag{5.15}$$

Again, $\mathcal{R}_{\mathrm{lower}}$ is a projection operator. In order to enforce our prior knowledge that the Galactic DM is strictly larger than the observed pulsar DM up to the observational error, we implement a logistic likelihood function

$$\mathcal{P}\left(\mathrm{DM}_{\mathrm{lower}} | d_{\mathrm{DM,lower}}\right) \propto \frac{1}{1 + e^{-\sigma^{-1}\left(\mathrm{DM}_{\mathrm{lower}} - d_{\mathrm{DM,lower}}\right)}}, \tag{5.16}$$

with σ being the observed DM error. This likelihood is close to zero for $\mathrm{DM}_{\mathrm{lower}} \ll d_{\mathrm{DM,lower}}$ and nearly 1 for $\mathrm{DM}_{\mathrm{lower}} \gg d_{\mathrm{DM,lower}}$. The steepness of the ascent in between is steered by σ^{-1}. This is an improper likelihood as it technically is not normalizable without a cutoff at high $\mathrm{DM}_{\mathrm{lower}}$. It is always possible to choose the cutoff high enough, such that we never have to evaluate the likelihood near or above the cutoff. It then only appears in the normalization term, but, as NIFTy uses log-likelihoods the normalization is a negligible constant, which hence does not have to be specified.

We now have a model for the DM sky constrained by two data sets $d_{\mathrm{DM,lower}}$ and $d_{\mathrm{DM,edge}}$, which could be used to infer the sky on their own. If combined with the Faraday rotation sky inference as illustrated in the graph in Fig. 5.5, the addition of pulsars allows for a separation of the Faraday depth sky into DM and magnetic field average. The precision mainly relies on the density of pulsars on the sky, specifically the ones lying in the outskirts of the Milky Way. We will refer to this model as Model 1 in the further course of the text.

MODEL 1

$$
\begin{aligned}
\phi &= 0.812\, e^{\rho}\, \chi \frac{\text{rad}}{\text{m}^2}, \\
\text{DM} &= e^{\rho} \frac{\text{pc}}{\text{cm}^3},
\end{aligned}
\tag{5.17}
$$

5.3.3 Model 2 - Adding the EM data

In order to increase the precision of the DM sky inference, we include the *Planck* EM data in the second model. For this, we need to relate the EM to the DM sky or more general to the p-th moment of n_{th} in Eq. (5.11). For that, we will make the generic assumption that the electron distribution along the LOS can be modeled via a log-normal process

$$
n_{\text{th}}(l) = n_{\text{th},0} e^{s(l)}, \tag{5.18}
$$

where $s(l)$ is a Gaussian process with unknown correlation structure along the LOS. The mean of the process can be completely absorbed in the pre-factor $n_{\text{th},0}$, it is therefore sufficient to assume s to have zero mean. Using this, we can relate the EM to the DM along the LOS via

$$
\text{EM} = \frac{\text{DM}^2}{\text{L}_\text{P}} \frac{\langle e^{2s(l)} \rangle_{\text{L}_\text{P}}}{\langle e^{s(l)} \rangle^2_{\text{L}_\text{P}}} = \frac{\text{DM}^2}{\text{L}_\text{P}\, f_{\text{EM,DM}}} \tag{5.19}
$$

The filling factor $f_{\text{EM,DM}}$ is strictly positive and smaller than one. It is generally viewed as a measure of clumpiness of the ISM (Pynzar' 1993; Gaensler et al. 2008), as in the limit of $s(l) \approx$ const. it approaches unity and EM and DM become directly translatable up to the distance factor. In the other extreme, when $s(l)$ is extremely small scaled $f_{\text{EM,DM}}$ approaches 0.

If we assume $p = 0$ in Eq. 5.11, we easily integrate the EM into the model, under the assumption that Faraday rotation and emission measure probe the same length of the LOS (i.e. $\text{L}_\text{ff} = \text{L}_\phi$),

MODEL 2

$$
\begin{aligned}
\phi &= 0.812\, e^{\rho}\, \chi \frac{\text{rad}}{\text{m}^2}, \\
\text{DM} &= e^{\rho} \frac{\text{pc}}{\text{cm}^3}, \\
\text{EM} &= e^{2\rho+\psi} \frac{\text{pc}}{\text{cm}^6},
\end{aligned}
\tag{5.20}
$$

where

$$
e^{\psi} = \frac{1}{f_{\text{EM,DM}} \text{L}_\text{P}}. \tag{5.21}
$$

In order to build a bridge to the phenomenological model of Hutschenreuter & Enßlin (2020a), we consider potential variations in the $p-$factor, the equation relating the amplitude of the Faraday sky and e.g. the EM is:

$$\mathrm{EM} = \mathrm{L_P} \left\langle n_{\mathrm{th}}^{p+1} \right\rangle_{\mathrm{L}}^{\frac{2}{p+1}} f_{\mathrm{EM},p}^{-1}, \tag{5.22}$$

where a new filling factor $f_{\mathrm{EM},p}$ is introduced. To model this, at least two additional degrees of freedom have to be introduced, one catching the variable p factor and the other the new filling factor. A viable model would be

$$\mathrm{EM} \equiv e^{\rho\gamma+\psi}, \tag{5.23}$$

where γ models the p-variations and ψ the new filling factor.

To make things complicated, a similar equation as Eq. (5.22) holds for the relationship between DM and $\left\langle n_{\mathrm{th}}^{p+1} \right\rangle_{\mathrm{L}}$, which implies that at least one other field (for yet another filling factor, $f_{p,\mathrm{DM}}$) would need to be introduced in order to combine ϕ, DM and EM data under the assumption of p deviating from 0. Given the sparsity of pulsars on the sky, the problem is now vastly under-constrained, making a reliable inference in this case very hard.

Not using the DM data eases the problem numerically, however, in this cases the model components become degenerate again, implying that if no further prior assumptions or additional data are provided,they can not be mapped uniquely to the physical components. One can, however, revert to a phenomenological model by introducing further degrees of freedom, e.g.

$$\begin{aligned} \phi &= e^{\rho}\chi\frac{\mathrm{rad}}{\mathrm{m}^2}, \\ \mathrm{EM} &\equiv e^{\rho\gamma+\epsilon} + e^{\delta}\frac{\mathrm{pc}}{\mathrm{cm}^6} \end{aligned} \tag{5.24}$$

were the additional δ field allows the qualitative absorption of specific structures on the sky. This model is exactly the one implemented in HE19 which revealed the signature of the Orion Arm, where however the above derivation was lacking. As we are focusing on the extraction of the dispersion measure and magnetic field skies in this work, it is not reimplemented here.

5.4 The results

5.4.1 Magnetic field sky

In the following we present the results on the magnetic field sky of Model 1 (Eq. 5.5) and Model 2 (see Eq. 5.6). We see that both estimates widely agree on the large scale scale structure on the sky. Mid-latitude regions are generally the most pronounced, with magnetic field strengths reaching between 2.5μG in Model 1 and 1.5μG in Model 2. The disc shows small averaged field strengths, consistent with a picture of many field reversals

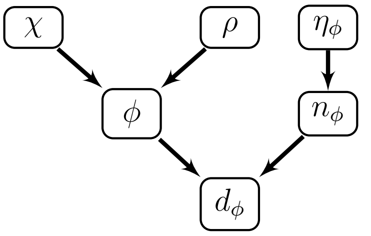
χ
ρ
η_ϕ
ϕ
n_ϕ
d_ϕ

Figure 5.4: Graph illustrating the hierarchical Bayesian model used for the Faraday sky inference by HE19 and HE20. This is the base model that all further models derive from.

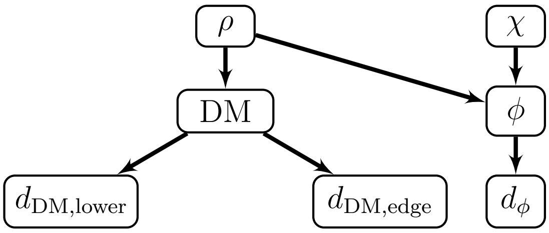
ρ
χ
DM
ϕ
$d_{\mathrm{DM,lower}}$
$d_{\mathrm{DM,edge}}$
d_ϕ

Figure 5.5: Graph illustrating the hierarchical Bayesian model described in Eqs. (5.17).

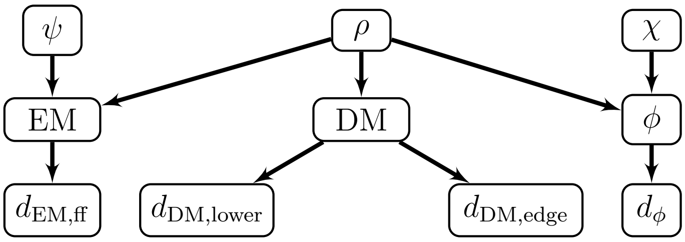
ψ
ρ
χ
EM
DM
ϕ
$d_{\mathrm{EM,ff}}$
$d_{\mathrm{DM,lower}}$
$d_{\mathrm{DM,edge}}$
d_ϕ

Figure 5.6: Graph illustrating the hierarchical Bayesian model described in Eqs. (5.20).

and a rather small scaled (e.g. turbulent) magnetic field in the disc. It should be noted, that above the overall variations in magnetic field strength between the models do not necessarily imply that the inclusion free-free data leads to a significant difference, but may also be a result of convergence issues of the numerical model. Nonetheless, both obtained magnetic field strengths are consistent with measurements of the local large scale magnetic field (Haverkorn 2015).

5.4.2 Dispersion measure sky

In Figs. 5.8a and 5.8b we show the results on the logarithmic Galactic dispersion measure sky. The profile of both maps agrees rather well with each other on large scales. The results of Model 1 are significantly smoother as the ones of the Model 2, while the latter has a very pronounced disc. The smoothness of 5.8a may result from the limited information of the scattered pulsars on the small scale structure of the map. In Fig 5.10, we show the log-DM calculated from the Yao et al. (2017) electron model. The map here is somewhat more pronounced in the disc, more akin to 5.8b. The slice plots in Fig. 5.9 reveal that the 5.8a fits better to the (Yao et al. 2017) model. It should be noted that Yao et al. (2017) had to enforce strong modelling assumptions on the thermal electron density, as their results are only based on the few existing pulsar DMs with associated distances. The strong loop feature at about 300° latitude is easily discernible in both our results and the Yao et al. (2017) model.

5.4.3 The filling factor

In Fig. 5.11a, we show the results on the ψ field as defined in Eq. (5.21). This field traces the logarithm of the inverse EM-DM filling factor times the LOS length. A direct comparison with the literature values on the filling factor is difficult, as in our case we cannot disentangle it form the length of the LOS, $\mathrm{L}_{\mathrm{LOS}}$. Nonetheless, a few qualitative statements can be made. Since we find values of ψ between 2 and 6, this implies approximately that $0.1 > f_{\mathrm{EM,DM}}\,\mathrm{L}_{\mathrm{LOS}} > 0.002$. As the length of the LOS should almost always be on the order of several kiloparsecs, $f_{\mathrm{EM,DM}}$ must be extremely small for most LOS. On first sight, this is in contrast to e.g. Gaensler et al. (2008), where they find the filling factor to be between 0.04 and 0.3. Their method, however, relies on local measurements using close by pulsars. The filling factor however is dependent on the length of the LOS, as it is essentially a measure of the variance of the cumulative electron density. We can give some further evidence that the map shows real structures by comparing it with the logarithmic integrated dust density as derived by Leike & Enßlin (2019). This demonstrates a rather strong anti-correlation of the two maps. This may indicate that the effective LOS lengths in direction of local dust clouds are rather short and that hence the EM and DM skies (and potentially the Faraday depth sky) have strong local features in these directions.

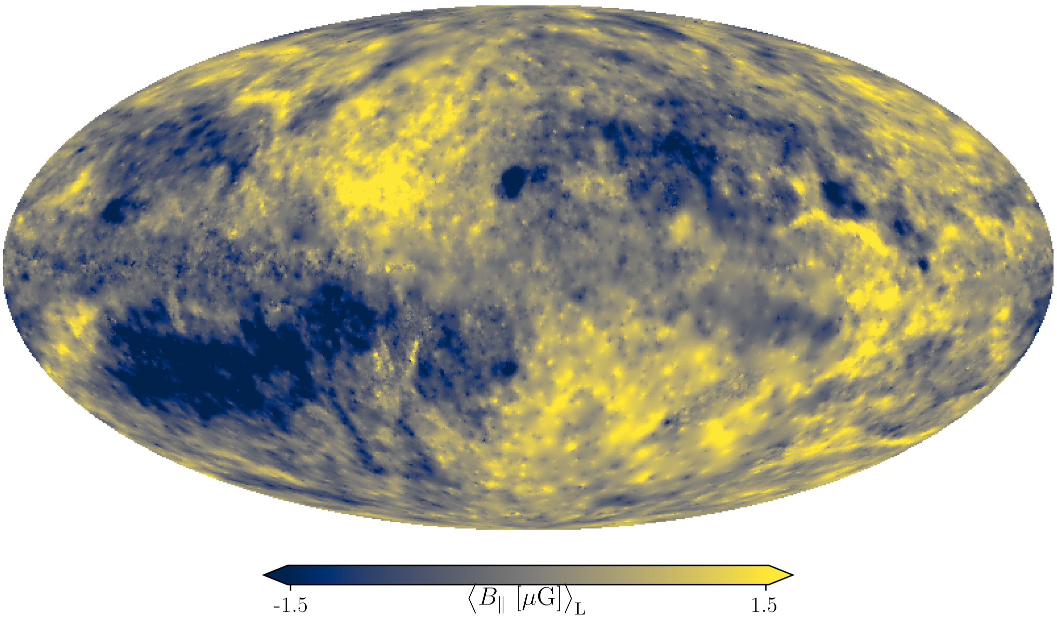
-1.5
$\langle B_\parallel\ [\mu\mathrm{G}]\rangle_\mathrm{L}$
1.5

(a)

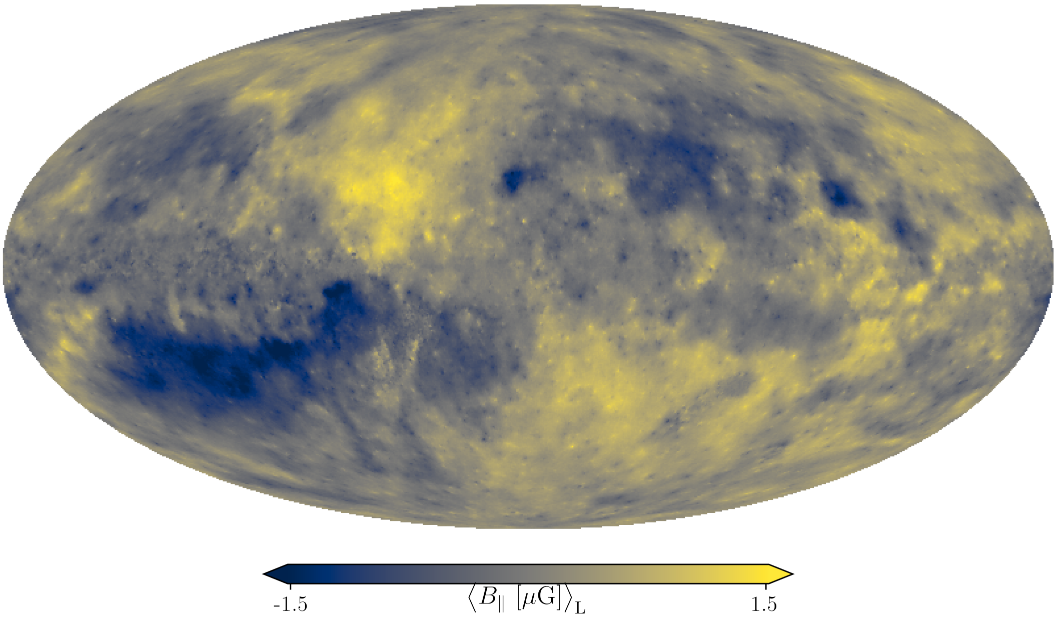
-1.5
$\langle B_\parallel\ [\mu\mathrm{G}]\rangle_\mathrm{L}$
1.5

(b)

Figure 5.7: The LOS parallel and LOS averaged magnetic field, Fig. (a) shows the posterior mean of Model 1, Fig. (b) the corresponding results of Model 2. In both cases the color scale is saturated at ±1.5 μG.

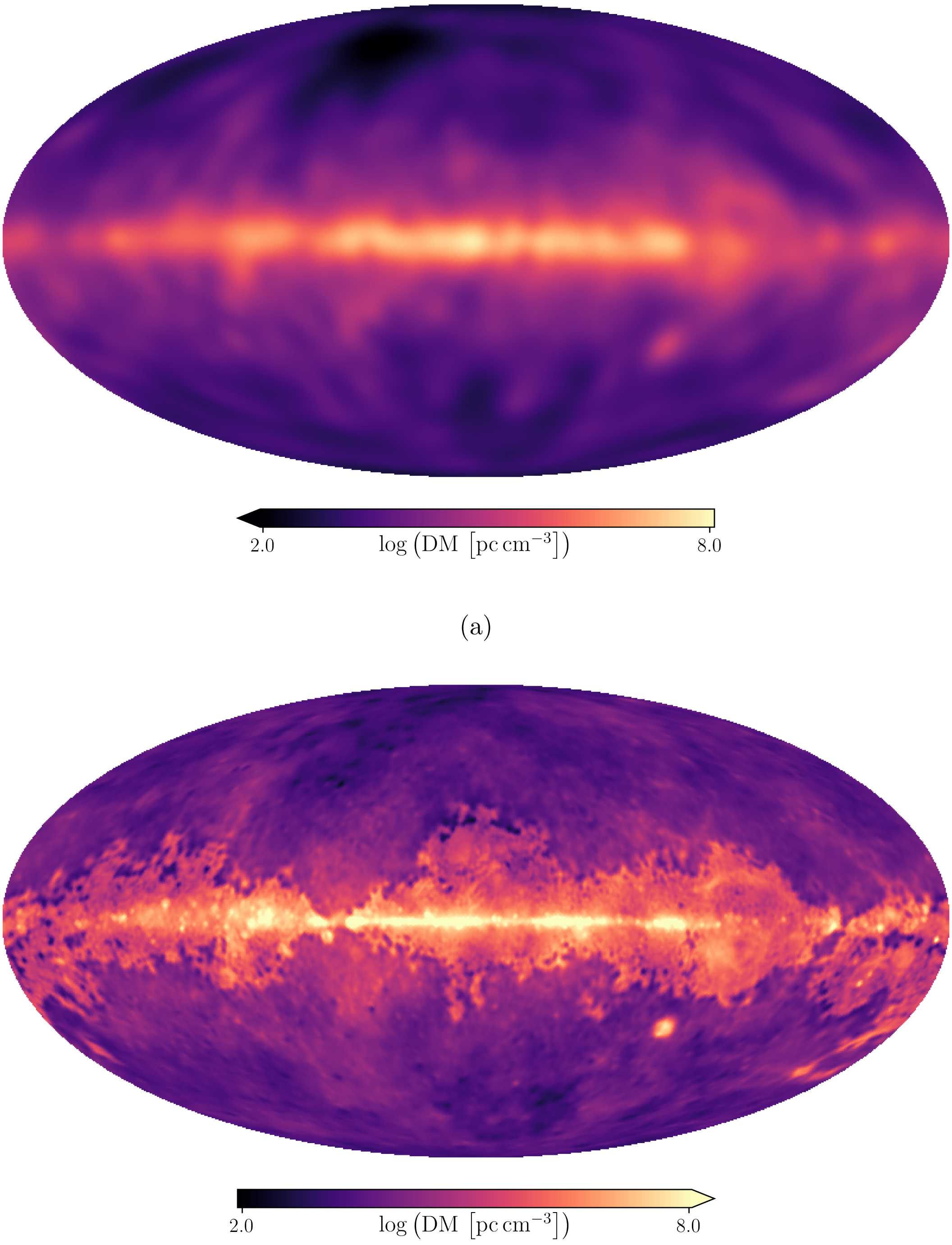
2.0
log (DM [pc cm^{-3}])
8.0
2.0
log (DM [pc cm^{-3}])
8.0

(a)

(b)

Figure 5.8: Inference results for the logarithmic Galactic DM sky. Fig. (a) shows the posterior mean of Model 1, Fig. (b) the corresponding results of Model 2.

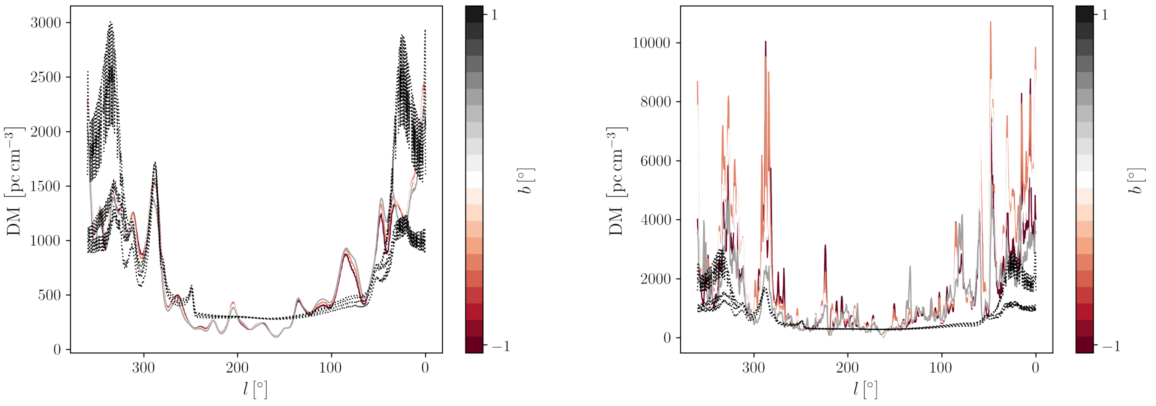

(a) (b)

Figure 5.9: Slices through the Galactic DM sky. Fig. (a) shows the posterior mean resulting from Model 1 (5.5), while Fig. (b) shows the posterior mean resulting from Model 2 (5.6). The black dots indicate the corresponding results of Yao et al. (2017).

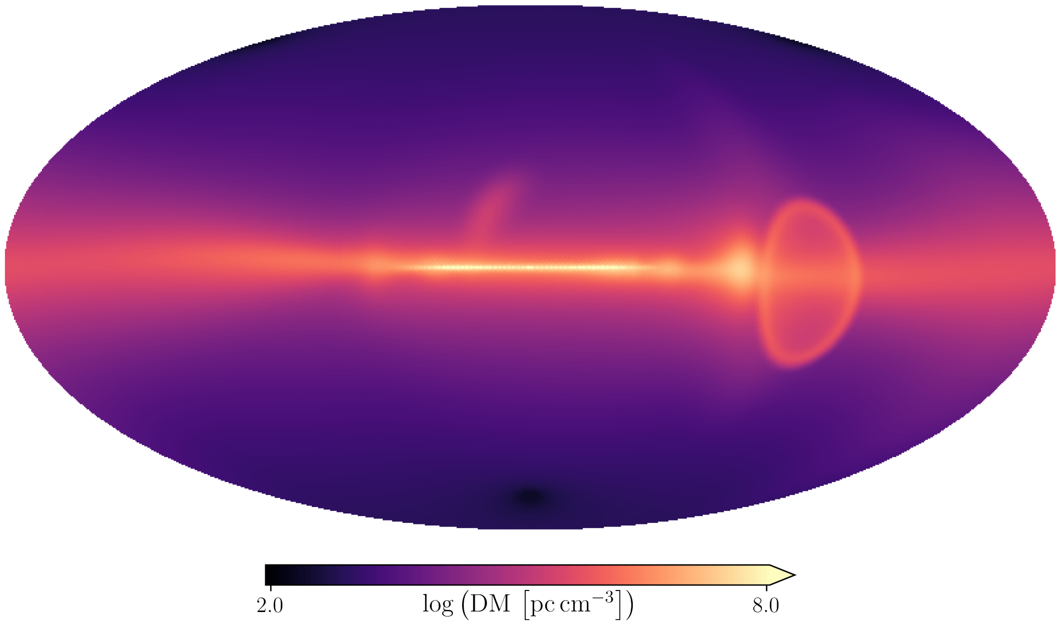

Figure 5.10: The logarithmic integrated electron density profile of Yao et al. (2017) in log dispersion measure units.

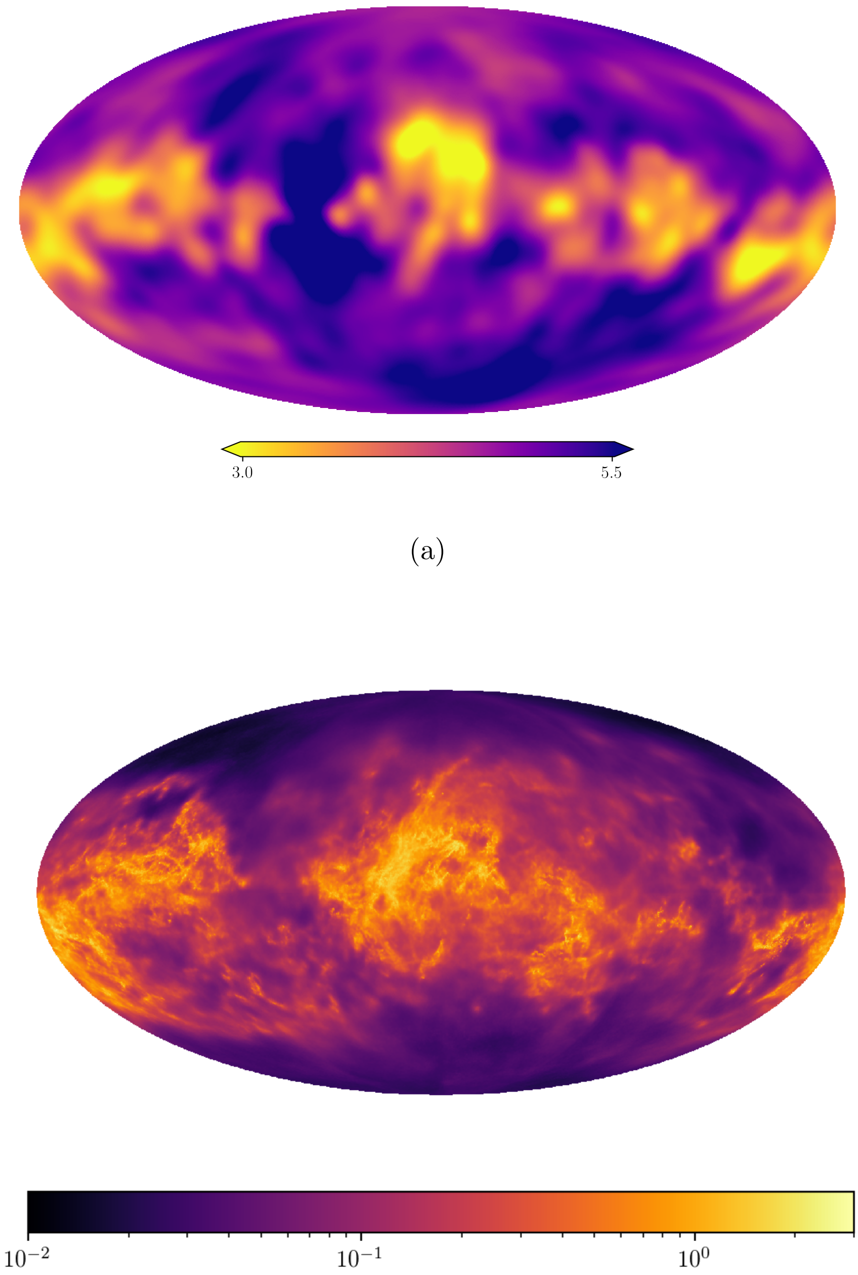

(a)

(b)

Figure 5.11: Inference results for the EM-DM filling factor (see Eq. (5.21)). Fig. (a) shows the posterior mean of the *psi* field from Model 2 (5.5), while Fig. (b) shows the log integrated dust density as derived by (Leike & Enßlin 2019). It should be noted that the colorbars are reversed in the two plots to highlight the anti-correlation of the two fields.

5.4.4 Faraday sky

For completeness, we show the results of the Faraday depth sky in Fig. 5.12. The general agreement with the results obtained by HE20 is good, which gives an important validity check for our method. Fig. 5.12b shows evidence of an amplified disc feature, in line with the results of HE20.

5.5 Discussions

In this work, we use three different data sets in order to disentangle the Galactic Faraday rotation sky into a its physical components, namely the averaged LOS parallel magnetic field component and the DM sky. For this, we developed two models based on Faraday rotation measure, pulsar dispersion measure and free-free emission measure data.

We find magnetic field values of around $2\,\mu$G, consistent with local measurements. The morphology of the magnetic field maps in Fig. 5.7 indicated the strongest field averages in mid-latitude regions outside the turbulent Galactic disc.

In terms of large scale morphology, the DM skies shows good agreement with results stemming from a methodologically independent analysis, but show significantly more small scaled structures.

In our second model, we implement a joint analysis of Faraday rotation, EM and DM sky. This allows us to constrain the filling factor that connects EM and DM skies, which we find to be strongly correlated with the integrated local dust densities. This indicates that many LOS are strongly influenced by these structures. Significant differences in the results between the two models indicate the need for further inspection of the methods implemented in this work.

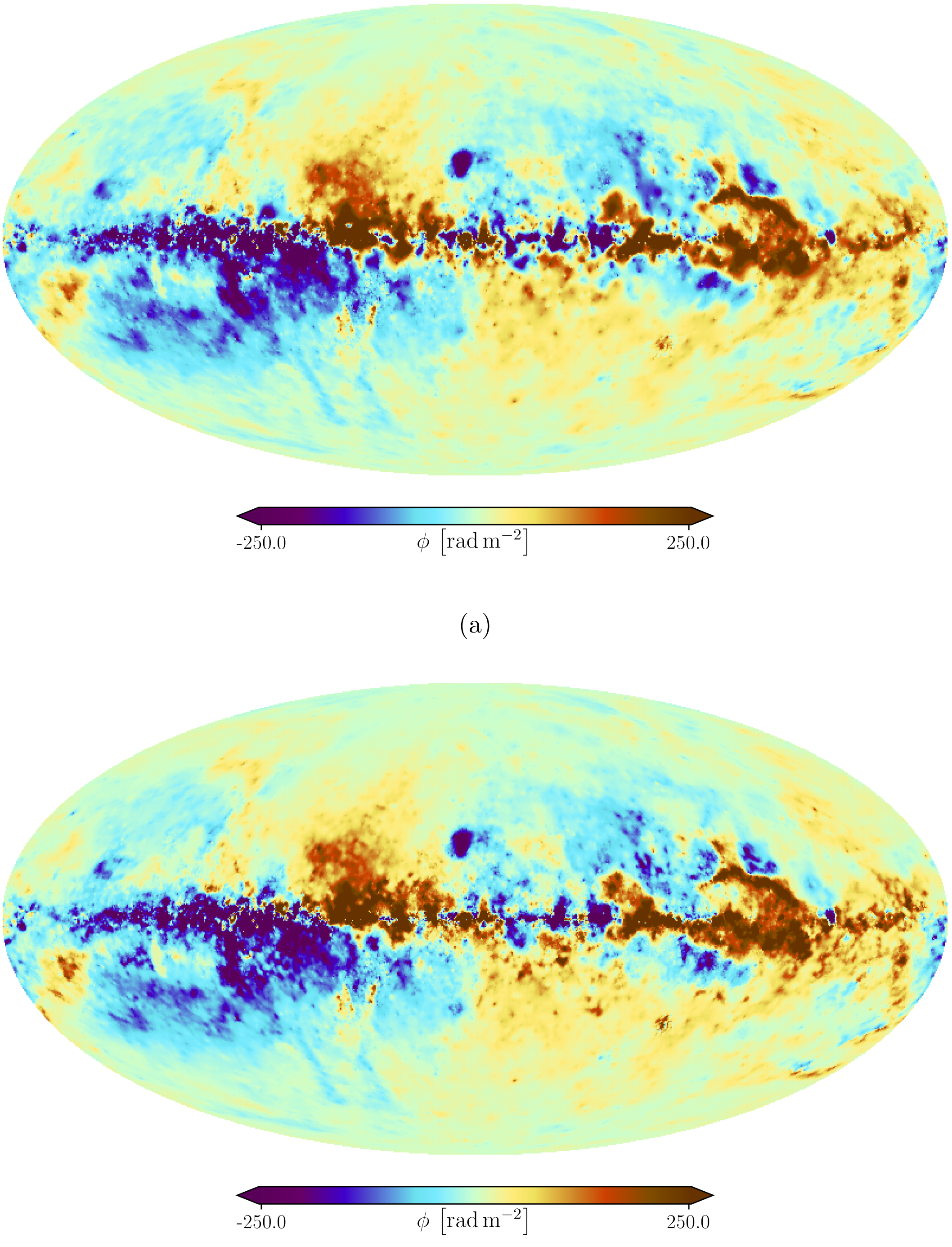
-250.0
ϕ [rad m^{-2}]
250.0
-250.0
ϕ [rad m^{-2}]
250.0

(a)

(b)

Figure 5.12: Inference results for the Galactic Faraday depth sky. Fig. (a) shows the posterior mean resulting from Model 1 (5.5), while Fig. (b) shows the posterior mean resulting from Model 2 (5.6).

Chapter 6

Circular polarization in the radio sky

References and Acknowledgment

This chapter summarizes work related to circular polarization. This has lead to two publications (Enßlin et al. 2017a, 2019), in each of which Torsten Enßlin is the main author. In both cases, I contributed to the analytical derivations, implemented the numerical calculations and took part in writing of the manuscripts.

6.1 Introduction

Radio synchrotron emission of astrophysical magnetized plasmas should be circularly polarized due to the circular motions of relativistic charged particles in magnetic fields. Because of the relativistic beaming effect of the particle's motion on the emitted radiation we see mostly the electrons that spiral around fields oriented perpendicular to the line-of-sight (LOS) and therefore predominantly linearly polarized emission. The magnetic fields that point towards us could be a source of circular polarization (CP), reflecting the circular motions of the relativistic particles visible in this geometry. However, the aforementioned beaming effect diminishes any radiation parallel to the magnetic field. The largest CP emission should therefore result from magnetic fields with an inclination in between parallel and perpendicular to the LOS. The field component parallel to the LOS, $B_{\|}$, ensures that a circular component of the electron gyration is visible to the observer, and determines thereby the sign of Stokes-V. The field component perpendicular to the LOS, $B_{\perp}$, enables the gyrating charged particles to send some beamed flux into the direction of the observer and therefore largely determines the strength of the CP. The rotational sense of the CP is entirely determined by the charge of the emitter, a property that is not shared by the (usually much easier) linear polarized synchrotron emission. Hence, CP provides an excellent tracer of the charge content of astrophysical plasmas, a property that is exploited in the next chapter.

6.1.1 Testing the charge composition of the emitters

In the following, we highlight specifically how the sensitivity of the sign of CP on the charge of the emitting plasma can be used to determine the nature of astrophysical plasmas in different environments. The first case will be concerned with the Milky Way and the second case with relativistic jets ejected of Active Galactic Nuclei (AGNs).

The case of the Milky Way

The rotational sense of the CP flux should typically have the opposite sign of that of the Faraday rotation if both are measured with the same convention and if the relativistic and thermal particles involved have the same charge sign, e.g. are both electrons. The reason is that the CP sense should directly reflect the gyro-motion of the relativistic particles emitting the radio emission. Faraday rotation is caused by the different phase speeds of left and right polarised electromagnetic waves in a magnetized plasma. The waves that co-rotates with the lightest thermal charge carriers – usually the electrons – can interact most strongly with them and gets the largest delay. Consequently, a linear wave that can be regarded as a superposition of left and right circular waves gets rotated in the sense of the faster wave, and therefore counter rotates with respect to the gyro-motion of the light charge carriers. Thus, if the involved thermal and relativistic particles have the same charge sign, CP and Faraday rotation produced in the same magnetic field counter rotate. This opens the possibility to test for the existence of regions with positrons dominating the radio synchrotron emission. The circular polarization sky of the Milky Way will be the topic of Sect. 6.2.1.

The case of the Cygnus A Hotspots

In the case of hot-spots, the radiation of relativistic electrons and positrons is beamed in the direction of their instantaneous motion and for this reason very little of the circular motion of an ensemble of relativistic leptons gets imprinted onto their radiation as circular polarization. Nevertheless, an asymmetry in the charge distribution of particles contributing to a given observational frequency should leave a weak CP signal. Such an asymmetry should exist if the radio plasma is mainly an electron-proton plasma, as one might expect in case the radio jets consist of material launched magnetically from accretion discs around super-massive black holes. On the other hand, no CP signal should arise in case radio plasma is composed of electrons and positrons created in similar amounts and with identical spectra by pair production events from hard photons in the vicinity of such black holes. Thereafter, acceleration and energy loss mechanism should not distinguish between electrons and positrons in case the radio plasma stays purely leptonic in its subsequent evolution. Then the dynamics of electrons and positrons is (mirror) symmetric and they should aquire similar energy spectra, which leads to cancellation of their individual CP contributions.

Therefore, the detection of CP intrinsically emitted from radio plasma would indicate that the charge symmetry of the synchrotron radiation arising from the plasma constituents is broken, and therefore either an electron proton plasma is dominant, or alternatively, the particle acceleration mechanism favours electrons or positrons for a yet unknown reason.

More interesting, therefore, would be a reliable observational upper bound on the CP flux from radio plasma, which is distinctly below the expected level for an electron-proton plasma. That would be a strong evidence against emission from an electron-proton plasma and therefore favor an electron-positron plasma.

Other sources of CP should be excluded before accepting the electron-proton plasma scenario via CP detection. The primary candidates for this are Faraday conversion and instrumental polarization.

Faraday conversion is the transformation of linearly polarized emission into CP by the different dispersion a linear polarized wave experiences depending on whether its polarization is parallel or perpendicular to the magnetic field. It is believed to be the main cause of the highly variable CP observed in compact objects (Jones & Odell 1977a,b; Hodge 1982; Valtaoja 1984; Komesaroff et al. 1984; Bjornsson 1990; Beckert & Falcke 2002; Ruszkowski & Begelman 2002; Enßlin 2003) like Sagrittarius A*, GRS 1915, SS 433 (Bower et al. 1999; Sault & Macquart 1999; Fender et al. 2000, 2002). Faraday conversion can be identified via its characteristic dependence on wavelength to the third power, as long one does not probe the extreme regimes like in AGNs (Vitrishchak & Gabuzda 2008). It operates most efficiently in the strong magnetic fields and dense plasma present near these objects. Thus, if we wish to minimise the contamination to CP on account of Faraday conversion, we should investigate regions with weaker magnetic field strengths and lower particle densities. As we still need a high brightness, the hot spots of radio galaxies seem to be ideal, and the brightest of those are the ones seen at the tips of the radio lobes of Cygnus A, which will therefore be the focus of Sect. 6.3

6.1.2 Circularly polarized synchrotron emission

In the following, we derive the necessary framework to give estimates on the strength and sign of CP. The synchrotron emissivity of relativistic electrons with density n_{rel} is dependent on their energy spectrum, which we here assume to follow a power law spectrum as

$$\frac{dn(\gamma)}{d\gamma} = \frac{n_{\mathrm{e}}\gamma^{-p}}{\gamma_{\mathrm{min}}^{1-p} - \gamma_{\mathrm{max}}^{1-p}} \tag{6.1}$$

between γ_{min} and γ_{max} with energy spectral index p. The synchrotron emissivity is (Pandya et al. 2016)

$$j = \begin{pmatrix} j_I \\ j_Q \\ j_U \\ j_V \end{pmatrix} = \underbrace{j_0 n_{n_{\mathrm{rel}}} B_{\perp}^{\frac{p+1}{2}}\, \nu^{\frac{1-p}{2}}}_{j_I} \begin{pmatrix} 1 \\ q \\ u \\ v \end{pmatrix}, \tag{6.2}$$

where

$$
\begin{aligned}
j_0 &= \frac{\mathrm{e}^2}{c}\left(\frac{\mathrm{e}}{2\pi m_\mathrm{e} c}\right)^{\frac{p+1}{2}} \frac{3^{\frac{p}{2}}(p-1)\,\Gamma\left(\frac{3p-1}{12}\right)\,\Gamma\left(\frac{3p+19}{12}\right)}{2\,(p+1)\,(\gamma_\mathrm{min}^{1-p}-\gamma_\mathrm{max}^{1-p})} && (6.3)\\
q &= -\frac{p+1}{p+{}^7\!/\!_3}\cos\left(2\varphi\right) && (6.4)\\
u &= +\frac{p+1}{p+{}^7\!/\!_3}\sin\left(2\varphi\right) && (6.5)\\
v &= -\frac{j_1\,B_{||}}{\left(\nu\,B_\perp\right)^{1/2}} && (6.6)\\
j_1 &= \frac{171}{250}\left(\frac{3\,\mathrm{e}\,p}{2\pi m_\mathrm{e} c}\right)^{1/2} = 0.06268\left(\frac{p\,\mathrm{GHz}}{\mathrm{Gauss}}\right)^{1/2}. && (6.7)
\end{aligned}
$$

The symbols e, m_e and c denote the elementary charge, the electron mass, and the speed of light, respectively. The magnetic field is

$$
\mathbf{B} = \begin{pmatrix} B_\perp\cos\left(\varphi\right) \\ B_\perp\sin\left(\varphi\right) \\ B_{||} \end{pmatrix} = \begin{pmatrix} \sin(\theta)\,\cos\left(\varphi\right) \\ \sin(\theta)\,\sin\left(\varphi\right) \\ \cos(\theta) \end{pmatrix} B,
$$

with the z-axis being parallel to the LOS and φ the angle between the x-axis and the field component in the plane of the sky, $\mathbf{B}_\perp$(Pandya et al. 2016).
The CP intensity as characterized by Stokes V for a given LOS is then approximately given by

$$
V = \alpha_V \int dl\, n_\mathrm{rel} B_{||}\, B_\perp^{p/2}, \tag{6.8}
$$

where

$$
\alpha_V = -j_0 j_1 \nu^{-\frac{p}{2}} \tag{6.9}
$$

is a constant, which depends only on natural constants, model parameters and the CP-observational frequency ν. Analogously, total intensity can be written as

$$
I = \alpha_I \int dl\, n_\mathrm{rel} B_\perp^2, \tag{6.10}
$$

$$
\tag{6.11}
$$

with

$$
\alpha_I = j_0 \nu^{\frac{1-p}{2}} \tag{6.12}
$$

.

6.2 The Galaxy in circular polarization: all-sky radio prediction and the charge of leptonic cosmic rays

6.2.1 Circular polarization in the Milky Way

So far only linear polarization has been detected and imaged in the diffuse radio-synchtron emission of the Milky Way (Wolleben et al. 2006; Page et al. 2007; Pandya et al. 2016).[1] CP should be much weaker and therefore harder to be detected and charted. Nevertheless, Galactic CP emission should exist and therefore should in principle be observable. Since the CP signal is weak, and has to be discriminated from instrumental polarization leakage effects, it would be very helpful to have a prediction not only on the magnitude of this emission, but also on its detailed morphology on the sky. This work provides such a prediction.

To predict the CP emission accurately knowledge of the Galactic magnetic field (GMF) strength and orientation is necessary throughout the Galactic volume, as well on the number density and the energy spectrum of the relativistic electron population. Currently we are lacking this information, despite substantial efforts to model the GMF (Sun et al. 2008; Waelkens et al. 2009b; Jansson et al. 2009; Jaffe et al. 2010; Sun & Reich 2010; Fauvet et al. 2011; Jaffe et al. 2011; Jansson & Farrar 2012a,b; Planck Collaboration 2016d), the Galactic thermal electrons (Cordes & Lazio 2002; Greiner et al. 2016b), and relativistic electrons (Strong & Moskalenko 2001; Strong et al. 2004; Vladimirov et al. 2011; Oppermann et al. 2012b; Orlando et al. 2015; Mazziotta et al. 2016; Evoli et al. 2017) from various observables. The observables informing us about the perpendicular GMF component (times the relativistic electron density) are the linear polarization and total emission of the synchrotron emission. The parallel GMF component imprints onto the Galactic Faraday rotation measures of extra-galactic sources, however modulated by the thermal electron density. Instead of using these observables to construct a 3D GMF model from which CP can be predicted (King & Lubin 2016), here we exploit that a certain combination of these observables should be linearly correlated with the CP signal. Exploiting this correlation without the detour of building a simplified 3D GMF model should permit to predict more small-scale structures of the Galactic CP signal than by usage of a coarse 3D GMF model.

The pieces of information that are put together, the Faraday signal as a tracer of $B_{\|}$ and the total synchrotron intensity as a tracer of $B_{\perp}$, might report about different locations along the LOS, whereas the combination of both components at the locations of CP emission would be needed. The former signal results predominately from locations of high thermal and the latter of high relativistic electron density, and these do not need to coincide spatially.

---

[1] CP from compact Galactic objects like Sagrittarius A*, GRS 1915, SS 433 has been detected (Bower et al. 1999; Sault & Macquart 1999; Fender et al. 2000, 2002), which seems to result from a different process as discussed here, namely Faraday conversion operating in the much stronger magnetic fields of these objects (Jones & Odell 1977a,b; Hodge 1982; Valtaoja 1984; Komesaroff et al. 1984; Bjornsson 1990; Beckert & Falcke 2002; Ruszkowski & Begelman 2002; Enßlin 2003).

Fortunately, the GMF exhibits some spatial correlation as the observables are correlated as a function of sky direction and this correlation should also hold in the LOS direction. Therefore, information on field components resulting from slightly different locations might still provide a good guess at a position. Some of the structures imprinted onto the observables are caused by structures in the underlying thermal or – to a lesser degree – relativistic electron population and might, however, be misleading and lead to spurious structures in a CP sky predicted this way.

Anyhow, a CP prediction constructed directly form such observables will be mostly model independent and therefore ideal for template-based CP detection efforts. It will have small angular scale structures that should also permit the usage of interferometer data that usually lack large angular scale sensitivity. While using this CP template map, it should just be kept in mind that it resembles an educated guess for the galactic CP morphology, and is certainly not accurate in all details. It should, however, be a very helpful template for the extraction of a detectable signal out of the probably noisy CP data and help to verify the detection of the Galactic CP signal by discriminating this from instrumental systematics that plague the measurement of weak polarization signals.

6.2.2 Model

The core insight for modeling the CP sky is that the building blocks of the CP signal n_{rel}, $B_{||}$, and $B_{\perp}$ (see Eq. (6.8)) appear in nearly the same combination in the Galactic total synchrotron intensity I (see Eq. (6.10)) and the Faraday depth ϕ defined in previous chapters. In particular, the data combination

$$d = \phi\, I = \alpha_{\phi} \alpha_I \int dl \int dl'\, n_{\mathrm{th}}(l)\, n_{\mathrm{rel}}(l')\, B_{||}(l)\, B_{\perp}^2(l') \tag{6.13}$$

contains the same magnetic field components as $V = \alpha_V \int dl\, n_{\mathrm{rel}}(l)\, B_{||}(l)\, B_{\perp}^{3/2}(l)$, although with slightly different spatial dependence and a slightly different $B_{\perp}$ dependence. Again, a index of $p = 2$ was assumed for the spectrum in Eq. (6.1). The constant $\alpha_{\phi} = \frac{e^3}{2\pi m_e^2 c^4}$ entails the constant terms stemming from Faraday rotation. If the magnetic field would be spatially constant along a LOS, d and V would be correlated according to

$$\frac{V}{d} = \frac{\alpha_V}{\alpha_{\phi}\alpha_I} \frac{1}{\int dl\, n_{\mathrm{th}}\, B_{\perp}^{1/2}}\ , \tag{6.14}$$

so that knowing d would allow us to predict V ap art from the weak $B_{\perp}$ dependence, assuming we know the LOS integrated thermal electron density from other measurements like pulsar dispersions. In reality, d and V will not be perfectly correlated as there are unknown magnetic structures on the LOS. The ratio

$$\frac{V}{d} = \frac{\alpha_V}{\alpha_{\phi}\alpha_I} \frac{\int dl\, n_{\mathrm{rel}} B_{||}\, B_{\perp}^{3/2}}{\left(\int dl\, n_{\mathrm{th}} B_{||}\right)\left(\int dl\, n_{\mathrm{rel}} B_{\perp}^2\right)} \tag{6.15}$$

therefore encodes information on magnetic structures along the LOS, in particular on the co-spatiality of Faraday rotating and synchrotron emitting regions. This information would be interesting to obtain in order to improve our GMF models.

Before CP observations can be exploited for studying Galactic magnetism, the CP signal has to be detected. For this, a rough model of the CP sky would be extremely helpful, as it can be used to build optimal detection templates to be applied to the noisy CP data. In the following, we construct such a predictive CP-polarization all sky map for this purpose. As d is already an observable today, it can be used to predict V to some degree.

V and d will in general be correlated. The production of CP is inevitably associated with total intensity emission and the sign of the produced V is determined by the sign of $B_{||}$, which always also imprints into the Faraday depth (for emission locations with thermal electrons). This correlation might be weak, in case the synchrotron emission and Faraday depth signals are mostly created at distinct locations with mostly uncorrelated magnetic LOS component $B_{||}$. If, on the other hand, synchrotron emissions and Faraday rotation are mainly co-spatial, a strong correlation between V and d can be expected. The fact that the Galactic radio emission exhibits strong signatures of Faraday depolarization (Wolleben et al. 2006) supports the idea of an intermixed Faraday rotating and synchrotron emitting medium, which promises a large cross-correlation of d and V. Thus the prospects for predicting the CP sky signal to some degree are good.

All three observables under consideration here, I, ϕ, and V, could be predicted for a given Galactic model in $n = (n_{\mathrm{th}}, n_{\mathrm{rel}})$ and $\vec{B} = (B_{||}, \vec{B}_{\perp})$, where we have chosen the LOS direction to be always our first coordinate. Although we have rough models for the 3D Galactic electron distributions n, the full 3D GMF configuration is currently poorly known. The existing GMF models (Sun et al. 2008; Waelkens et al. 2009b; Jansson et al. 2009; Jaffe et al. 2010; Sun & Reich 2010; Fauvet et al. 2011; Jaffe et al. 2011; Jansson & Farrar 2012a,b; Planck Collaboration 2016d) largely exploit the available Faraday and synchrotron data and therefore do not contain too much in addition to what these datasets have to offer. The additional information of these models is due to the usage of parametric models of the GMF spiral structure, which are inspired from the observations of other galaxies. Although this is certainly helpful information, the price to be paid for it is a loss of small-scale structure in the model prediction as the parametric models do not capture all complexity of the data sets they are fitted to. These small-scale structures are, however, extremely important for detecting the Galactic CP signal, as many radio telescopes and in particular radio interferometers are insensitive to large-scale angular structures. Furthermore, a GMF model based prediction is only superior on large scales if the included additional assumptions were correct. Although, this might well be the case, to have a more model independent prediction is certainly healthy.

For these reasons, we will try to predict the CP sky from existing I and ϕ sky maps directly, using only a minimal set of absolutely necessary model assumptions, which we describe now. The inclusion of more information and assumptions is in principle possible and would to lead more sophisticated V-map predictions as we are aiming for here.

As the fluctuations in our observables are mainly caused by magnetic field structures and to a lesser degree by structures in the electron densities $n = (n_{\rm th},\, n_{\rm rel})$, for which rough, but sufficiently accurate models exist, we will assume n to be known along any given LOS. For $n_{\rm th}$ we adopt the large-scale structure of the popular NE2001 model (Cordes & Lazio 2002) and $n_{\rm rel}$ is modeled as a thick exponential discs, with parameters as specified in detail in Sec. 6.2.4. Adapting a simplistic model for the electron densities means that any structure in the RM sky, which is a consequence of not modeled structures in the thermal electron density, will be attributed to magnetic field structures and imprints on the resulting CP sky. Thus, the predicted CP sky will show some features not being present in the real CP sky. Not modeled structures in the relativistic electron density will imprint to both, the total intensity map and the CP map. Therefore, those will imprint on the CP prediction despite the fact that the inference model assigns them to magnetic sub-structures internally.

Although the detailed GMF is still a matter of research, reasonable guesses for how the magnetic energy density scales typically with Galactic locations as expressed through n exist and will be adopted here. This means, we assume that the GMF energy density is largely a function of the electron density. We therefore need an expression for

$$\overline{B}^2(n) = \langle \vec{B}^2 \rangle_{(\vec{B}|n)} \tag{6.16}$$

with $\langle f(x,y) \rangle_{(x|y)} = \int dx\, \mathcal{P}(x|y)\, f(x,y)$ expressing the probabilistic expectation value of a function $f(x,y)$ (here $\vec{B}^2$) averaged over the conditional probability $\mathcal{P}(x|y)$ of an unknown variable x (here $\vec{B}$) given a known variable y (here n to characterize the different typical environments in the Galaxy).

In this work, a simple parametrization of the form

$$\overline{B}^2(n) = \frac{B_0^2}{n_{\rm th0}^{\beta_{\rm th}} n_{\rm rel0}^{\beta_{\rm rel}}} n_{\rm th}^{\beta_{\rm th}} n_{\rm rel}^{\beta_{\rm rel}} = B_0^2\, x_{\rm th}^{\beta_{\rm th}} x_{\rm rel}^{\beta_{\rm rel}} \tag{6.17}$$

will be used, with $x_i \equiv \frac{n_i}{n_{i0}}$ and plausible scaling indices of $\beta = (\beta_{\rm th}, \beta_{\rm rel}) \in [0,1]^2$. To be definitive, we adopt $\beta_{\rm th} = 0$ and $\beta_{\rm rel} = 1$ to model our intuition that the observed thick synchrotron disk of the Milky Way and other galaxies probably require magnetic fields which have a thick disk as well as the relativistic electrons causing this thick disk emission. This is in line with the expectation that the relativistic fluid in galaxies, consisting of mainly of relativistic protons, other ions, and electrons, drags magnetic fields with it when it streams out of galactic disks.

In order to show to which degree our CP sky prediction depends on this assumption we also show results for the complementary case $\beta = (1,0)$. It will turn out that β has only a marginal effect on our prediction, indicating also that the 3D modeling of the electron distributions is not the most essential input to our calculation. The exact normalization of the scaling relation Eq. 6.17 is given by the parameters $B_0^2, n_{\rm th0}^{\beta_{th}}$ and $n_{\rm rel0}^{\beta_{rel}}$. In the explicit calculation later on we use $B_0 \approx 6\,\mu$G and $n_{\rm th0} \approx 5 \cdot 10^{-2}{\rm cm}^{-3}$. The parameter for the relativistic electron density $n_{\rm rel0}$ drops out later on in the course of the calculation and is therefore left unspecified. The reason for this is that it affects the observable I in exactly the same way as the predicted quantity V, and therefore becomes irrelevant when conditioning our prediction on the observable I, which contains the necessary information on n_{rel0} .

We will exploit the correlation of V with the quantity $d = \phi I$ to predict the former. These quantities depend on the magnetic field structure along a LOS in different ways. Their cross-correlation depends on the magnetic field correlation tensor

$$M_{ij}(\vec{x}, \vec{y}) = \langle B_i(\vec{x})\, B_j(\vec{y})\rangle_{(\vec{B})} \tag{6.18}$$

as well as on higher correlations functions. A priori, we have no reason to assume that within a roughly homogeneous Galactic environment (as defined by roughly constant n) any direction or location to be singled out. Thus, a statistical homogeneous, isotropic, and mirror-symmetric correlation tensor should model our a priori knowledge about the field, which then is of the form (Subramanian 1999)

$$\begin{aligned} M_{ij}(\vec{x}, \vec{y}) &= M_{ij}(\vec{r}) \\ &= M_{\mathrm{N}}(r)\, \delta_{ij} + (M_{\mathrm{L}}(r) - M_{\mathrm{N}}(r))\ \hat{r}_i \hat{r}_j, \end{aligned} \tag{6.19}$$

with $M_{\mathrm{N}}(r)$ and $M_{\mathrm{L}}(r)$ normal and longitudinal scalar correlation functions, which depend only on the magnitude r of the distance vector $\vec{r} = \vec{x} - \vec{y}$ with normalized components $\hat{r}_i = r_i/r$. These functions describe the correlation of the field at one location with that at another location shifted in a normal or longitudinal direction with respect to the local magnetic field orientation. These correlation functions are connected due to $\vec{\nabla} \cdot \vec{B} = 0$ via

$$M_{\mathrm{N}}(r) = \frac{1}{2r} \frac{d}{dr} \left[r^2\, M_{\mathrm{L}}(r) \right] \tag{6.20}$$

and can be combined into the magnetic scalar correlation $w(r) = \langle \vec{B}(\vec{x}) \cdot \vec{B}(\vec{x} + \vec{r}) \rangle_{(\vec{B})} = 2M_{\mathrm{N}}(r) + M_{\mathrm{L}}(r)$ so that $\overline{B}^2 = w(0) = 2M_{\mathrm{N}}(0) + M_{\mathrm{L}}(0)$ (Subramanian 1999).

In our calculations, only correlations along of LOSs are needed, leading to the restriction $\vec{r} = (r, 0, 0)$ if we identify the LOS direction with the first coordinate axis. This implies a component-wise diagonal correlation structure

$$\begin{aligned} M_{ij}(\vec{r})|_{\vec{r}=(r,0,0)} &= [M_{\mathrm{N}}(r) + (M_{\mathrm{L}}(r) - M_{\mathrm{N}}(r))\ \delta_{i1}]\ \delta_{ij} \\ &= \begin{pmatrix} M_{\mathrm{L}} & 0 & 0 \\ 0 & M_{\mathrm{N}} & 0 \\ 0 & 0 & M_{\mathrm{N}} \end{pmatrix}_{ij} (r) \end{aligned} \tag{6.21}$$

and therefore no a priori expectation of any cross-correlation of $B_{||}$ and $B_{\perp}$ along a given LOS. This simplifies the calculation of higher order magnetic correlation functions. For such we will use the Wick theorem, e.g.

$$\langle B_i B_j B_k B_l \rangle_{(\vec{B})} = M_{ij} M_{kl} + M_{ik} M_{jl} + M_{il} M_{jk},$$

and therefore implicitly a Gaussian probability for the magnetic field components. The real magnetic field statistics is most likely non-Gaussian, leading to differences between our estimated higher order correlates and the real ones. However, since we do not know how to model this non-Gaussianity correctly as we do not know even the sign of its effect on higher order correlations, and as we also like to keep the complexity of our calculations moderate we accept this simplification. We expect only a moderate and global multiplicative change of order unity on our predicted CP sky if the nature of non-Gaussianity would be known and taken into account in the prediction, as non-Gaussianity corrections would roughly affect all LOSs more or less similarly.

Furthermore, we assume the longitudinal and normal magnetic correlation lengths (defined here differently to match our later needs)

$$\begin{aligned}\lambda_{\mathrm{L}} &= \int dr\, M_{\mathrm{L}}(r)/M_{\mathrm{L}}(0) \text{ and} \\ \lambda_{\mathrm{N}} &= \int dr\, M_{\mathrm{N}}^2(r)/M_{\mathrm{N}}^2(0) \qquad (6.22)\end{aligned}$$

to be much smaller than typical variations in the underlying electron density profiles, so that e.g. the expected Farday dispersion can be calculated via

$$\begin{aligned}\langle \phi^2 \rangle_{(\vec{B}|n)} &= \alpha_\phi^2 \int_0^\infty dl \int_0^\infty dl'\, n_{\mathrm{th}}(l)\, n_{\mathrm{th}}(l') \langle B_{||}(l)\, B_{||}(l') \rangle_{(\vec{B}|n)} \\ &\approx \alpha_\phi^2 \int_0^\infty dl \int_{-\infty}^\infty dr\, n_{\mathrm{th}}(l)\, n_{\mathrm{th}}(l+r)\, M_{\mathrm{L}}(r) \\ &\approx \frac{1}{3} \alpha_\phi^2 \lambda_{\mathrm{L}} \int_0^\infty dl\, n_{\mathrm{th}}^2\, \overline{B}^2(n). \qquad (6.23)\end{aligned}$$

We introduced the notation $f(l) = f(l\,\widehat{r}_{\mathrm{LOS}})$ for the value of the 3D field $f(\vec{r})$ along the LOS coordinate l in direction $\widehat{r}_{\mathrm{LOS}}$. Here, and in the following we will treat the individual LOSs separately. Furthermore, we assumed that magnetic structures are smaller than the part of the LOS that resides in the Galaxy as expressed in terms of the structure of the adopted thermal electron model, so that a negligible error is implied by extending the integration over the relative distances $r = l' - l$ from minus to plus infinity or by using the same thermal electron density for both locations, l and $l + r$. Furthermore, we used $M_{\mathrm{L}}(0) = M_{\mathrm{N}}(0) = \frac{1}{3}\overline{B}^2$, which follows from isotropy and Eq. 6.21.

Finally, we assume the observed Faraday and total intensity skies to be noiseless. This approximation will simplify the CP sky estimator and make it independent of the normalization of the scaling relation Eq. 6.17 and the actual value of the correlation length λ_{L} as long this does not vary (strongly) along a given LOS. The assumed correlations length λ_{N} will have some small impact on our result, however, of sub-dominant order and therefore it is also not necessary to specify it if only a rough CP sky prediction is required.

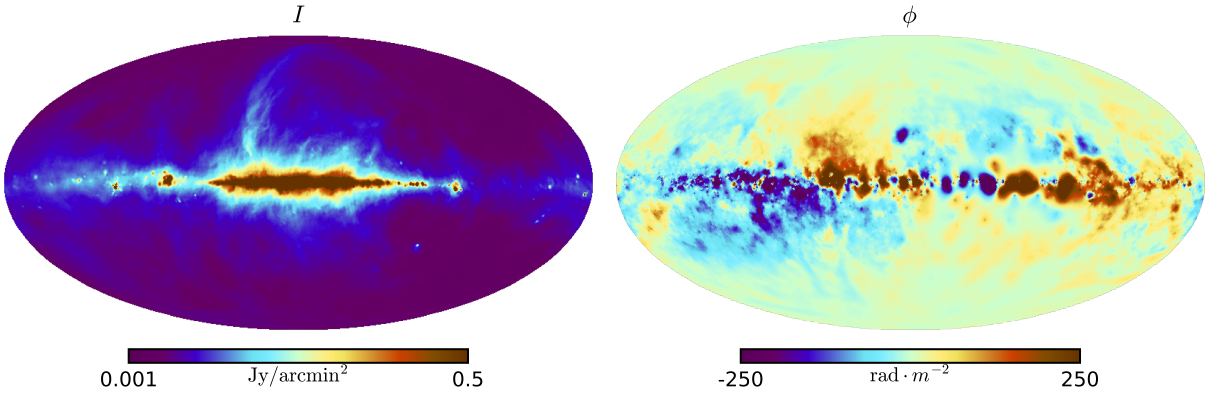
I
ϕ
0.001
Jy/arcmin^2
0.5
-250
$\mathrm{rad}\cdot m^{-2}$
250

Figure 6.1: Left: Synchrotron intensity at 408 MHz as provided by (Remazeilles et al. 2015a). Right: Faraday rotation map as constructed by (Oppermann et al. 2012b). Red indicates magnetic fields predominantly pointing towards the observer and clockwise rotation of the received linear polarisation. This is according to the IAU convention for measuring angles and is therefore opposite to the mathematical convention.

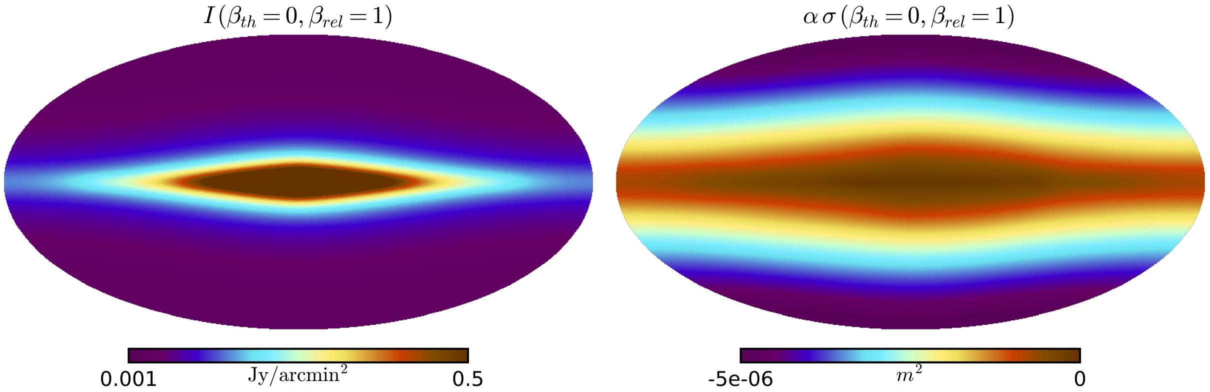
$I\,(\beta_{th}=0, \beta_{rel}=1)$
$\alpha\,\sigma\,(\beta_{th}=0, \beta_{rel}=1)$
0.001
Jy/arcmin^2
0.5
-5e-06
m^2
0

Figure 6.2: Left: Synchrotron emission intensity at 408 MHz of the simplistic 3D model. Right: Map of the resulting conversion factor $\alpha\sigma$, which translates the Faraday rotation map ϕ into the fractional CP map V/I at 408 MHz. For both the relativistic electron profile of Eq. 6.33 and $\beta = (0, 1)$ were assumed.

6.2.3 Estimator

We want to exploit the correlation of V with $d = \phi\, I$ to construct an optimal linear estimator for V given d. This is given by

$$\overline{V} = \langle V\, d\rangle_{(\vec{B}|n)} \langle d^2\rangle^{-1}_{(\vec{B}|n)} d \tag{6.24}$$

irrespectively the underlying statistics, since one can easily show that the quadratic error expectation $\epsilon^2 = \langle \left[V - \overline{V}(d)\right]^2\rangle_{(\vec{B}|n)}$ is always minimized for linear estimators of the form $\overline{V}(d) = v\, d$ for $v = \langle V\, d\rangle_{(\vec{B}|n)} \langle d^2\rangle^{-1}_{(\vec{B}|n)}$:

$$\begin{aligned} \frac{d\epsilon^2}{dv} &= -2\langle [V - v\, d]\; d\rangle_{(\vec{B}|n)} \\ &= 2\, \left[v\langle d^2\rangle_{(\vec{B}|n)} - \langle V\, d\rangle_{(\vec{B}|n)}\right] = 0. \end{aligned} \tag{6.25}$$

All remaining analytical work is to calculate the correlates which compose v. The simpler one is

$$\begin{aligned} \langle d^2\rangle_{(\vec{B}|n)} &= \langle \phi^2 I^2\rangle_{(\vec{B}|n)} \\ &= \alpha_\phi^2 \alpha_I^2 \int dl_1 \ldots \int dl_4\, n_{\mathrm{th}1}\, n_{\mathrm{th}2}\, n_{\mathrm{rel}3}\, n_{\mathrm{rel}4} \times \\ &\quad \langle B_{||1} B_{||2} B_{\perp 3}^2 B_{\perp 4}^2\rangle_{(B|n)} \\ &= \alpha_\phi^2 \alpha_I^2 \int dl_1 \ldots \int dl_4\, n_{\mathrm{th}1}\, n_{\mathrm{th}2}\, n_{\mathrm{rel}3}\, n_{\mathrm{rel}4} \times \\ &\quad M_{\mathrm{L}12}\, \left[M_{\mathrm{N}33}\, M_{\mathrm{N}44} + 2\, M_{\mathrm{N}34}^2\right] \\ &\approx \frac{1}{27}\, \lambda_{\mathrm{L}} \alpha_\phi^2 \alpha_I^2\, \left[\int dl\, n_{\mathrm{th}}^2 \overline{B}^2\right] \times \\ &\quad \left[\left(\int dl\, n_{\mathrm{rel}}\, \overline{B}^2\right)^2 + 2\lambda_{\mathrm{N}} \int dl\, n_{\mathrm{rel}}^2\, \overline{B}^4\right]. \end{aligned} \tag{6.26}$$

Here, we used the abbreviations $n_{\mathrm{th}1} = n_{\mathrm{th}}(l_1)$, $B_{||2} = B_{||}(l_2)$, $M_{\mathrm{N}34} = M_{\mathrm{N}}(l_3 - l_4)$, and the like, exploited the diagonal structure of the magnetic correlations along the LOS as expressed by Eq. 6.21 while applying the Wick theorem, and inserted the correlation lengths λ_{L} and λ_{N} as defined in Eq. 6.22 while applying the short correlation length approximation as previously used in Eq. 6.23.

The calculation of $\langle V\, d\rangle_{(\vec{B}|n)}$ is slightly more complicated. To handle the $B_\perp^{3/2}$ dependence of V, we Taylor expand it in terms of $B_\perp^2$ around $B_{\perp 0}^2 = \frac{2}{3} B_0^2$ via

$$\begin{aligned}
B_\perp^{3/2} = (B_\perp^2)^{3/4} = \sum_{n=0}^{\infty} \binom{3/4}{n} B_{\perp 0}^{2(\frac{3}{4}-n)} \left(B_\perp^2 - B_{\perp 0}^2\right)^n \\
= \binom{3/4}{0} B_{\perp 0}^{3/2} + \binom{3/4}{1} B_{\perp 0}^{-\frac{1}{2}} \left(B_\perp^2 - B_{\perp 0}^2\right) + \mathcal{O}\left(B_\perp^4\right) \\
\approx \frac{1}{4} B_{\perp 0}^{3/2} + \frac{3}{4} B_{\perp 0}^{-1/2} B_\perp^2 .
\end{aligned} \tag{6.27}$$

We choose to expand in $B_\perp^2$ rather than $B_\perp$, as the linear terms would vanish anyway during the application of the Wick theorem.

We then find:

$$\begin{aligned}
\langle V\, d\rangle_{(\vec{B}|n)} &= \langle V\, \phi\, I\rangle_{(\vec{B}|n)} \\
&= \alpha_V \alpha_\phi \alpha_I \int dl_1 \ldots \int dl_3\, n_{\mathrm{th}1}\, n_{\mathrm{rel}2}\, n_{\mathrm{rel}3} \times \\
&\quad \langle B_{||1} B_{||2} B_{\perp 2}^{\frac{3}{2}} B_{\perp 3}^2 \rangle_{(B|n)} \\
&\approx \alpha_V \alpha_\phi \alpha_I \int dl_1 \ldots \int dl_3\, n_{\mathrm{th}1}\, n_{\mathrm{rel}2}\, n_{\mathrm{rel}3} \times \\
&\quad \left\langle B_{||1} B_{||2} \left(\frac{1}{4} B_{\perp 0}^{3/2} + \frac{3}{4} B_{\perp 0}^{-1/2} B_{\perp 2}^2 \right) B_{\perp 3}^2 \right\rangle_{(B|n)} \\
&= \alpha_V \alpha_\phi \alpha_I \int dl_1 \ldots \int dl_3\, n_{\mathrm{th}1}\, n_{\mathrm{rel}2}\, n_{\mathrm{rel}3} \times \\
&\quad \frac{B_{\perp 0}^{-1/2}}{4} M_{\mathrm{L}12} \Bigg(B_{\perp 0}^2 M_{\mathrm{N}33} + \\
&\quad + 3 \left[M_{\mathrm{N}22}\, M_{\mathrm{N}33} + 2\, M_{\mathrm{N}23}^2 \right] \Bigg) \\
&\approx \frac{B_{\perp 0}^{-\frac{1}{2}}}{36} \lambda_{\mathrm{L}} \alpha_V \alpha_\phi \alpha_I \times \\
&\quad \left[B_{\perp 0}^2 \left(\int dl\, n_{\mathrm{th}} n_{\mathrm{rel}}\, \overline{B}^2 \right) \left(\int dl\, n_{\mathrm{rel}}\, \overline{B}^2 \right) \right. \\
&\quad + \left(\int dl\, n_{\mathrm{th}}\, n_{\mathrm{rel}}\, \overline{B}^4 \right) \left(\int dl\, n_{\mathrm{rel}}\, \overline{B}^2 \right) + \\
&\quad \left. 2\lambda_{\mathrm{N}} \int dl\, n_{\mathrm{th}}\, n_{\mathrm{rel}}^2\, \overline{B}^6 \right] .
\end{aligned} \tag{6.28}$$

Again we used $M_{\mathrm{L}}(0) = M_{\mathrm{N}}(0) = \frac{1}{3}\overline{B}^2$ and λ_{L} and λ_{N} as defined in Eq. 6.22. This gives us in Gaussian units

$$
\begin{aligned}
\overline{V} &= \alpha\,\sigma\,\phi\,I, \text{ with} \qquad (6.29)\\
\alpha &= \frac{3\,\alpha_V}{4\,\alpha_\phi\,\alpha_I\,B_{\perp 0}^{1/2}}\\
&\approx -4.269\cdot\sqrt{\frac{m_{\mathrm{e}}^3\,c^7}{\mathrm{e}^5\,\nu\,B_0}}\\
&\approx \text{-}2.189\cdot 10^{18}\left(\frac{\nu}{408\,\mathrm{MHz}}\right)^{-1/2}\left(\frac{B_0}{6\,\mu\mathrm{G}}\right)^{-1/2} \qquad (6.30)
\end{aligned}
$$

being a LOS-independent dimensionless quantity and

$$
\begin{aligned}
\sigma = &\left(\int dl\, n_{\mathrm{th}}^2 \overline{B}^2\right)^{-1} \times\\
&\left[\left(\int dl\, n_{\mathrm{rel}}\,\overline{B}^2\right)^2 + 2\lambda_{\mathrm{N}}\int dl\, n_{\mathrm{rel}}^2\,\overline{B}^4\right]^{-1} \times\\
&\left[\frac{2}{3}B_0^2\left(\int dl\, n_{\mathrm{rel}}\,\overline{B}^2\right)\left(\int \ dl\, n_{\mathrm{th}} n_{\mathrm{rel}}\,\overline{B}^2\right)\right.\\
&\quad + \left(\int dl\, n_{\mathrm{rel}}\,\overline{B}^2\right)\left(\int dl\, n_{\mathrm{th}}\, n_{\mathrm{rel}}\,\overline{B}^4\right)\\
&\quad \left. + \ 2\lambda_{\mathrm{N}}\int dl\, n_{\mathrm{th}}\, n_{\mathrm{rel}}^2\,\overline{B}^6\right] \qquad (6.31)
\end{aligned}
$$

a LOS-dependent constant with dimension of an area. The unknown λ_{L} canceled out and the unknown λ_{N} affects only sub-dominant terms, as it is e.g. compared in the denominator to the Galactic dimension $L = \left(\int dl\, n_{\mathrm{rel}}\,\overline{B}^2\right)^2 / \left(\int dl\, n_{\mathrm{rel}}^2\,\overline{B}^4\right) \gg \lambda_{\mathrm{N}}$. We therefore neglect terms proportional to λ_{N} in the following and calculate

$$
\begin{aligned}
\sigma &\approx \frac{\frac{2}{3}\,B_0^2 \int \ dl\, n_{\mathrm{th}} n_{\mathrm{rel}}\,\overline{B}^2 + \int dl\, n_{\mathrm{th}}\, n_{\mathrm{rel}}\,\overline{B}^4}{\left(\int dl\, n_{\mathrm{th}}^2 \overline{B}^2\right)\left(\int dl\, n_{\mathrm{rel}}\,\overline{B}^2\right)}\\
&\approx \frac{\frac{2}{3}\int \ dl\, x_{\mathrm{th}}^{1+\beta_{th}} x_{\mathrm{rel}}^{1+\beta_{rel}} + \int dl\, x_{\mathrm{th}}^{1+2\beta_{\mathrm{th}}}\, x_{\mathrm{rel}}^{1+2\beta_{rel}}}{n_{\mathrm{th}0}\left(\int dl\, x_{\mathrm{th}}^{2+\beta_{\mathrm{th}}} x_{\mathrm{rel}}^{\beta_{rel}}\right)\left(\int dl\, x_{\mathrm{th}}^{\beta_{\mathrm{th}}} x_{\mathrm{rel}}^{1+\beta_{rel}}\right)}
\end{aligned}
\qquad (6.32)
$$

for each LOS to translate $d = \phi\, I$ into $\overline{V}$ there.

6.2.4 Prediction

To give an estimate for the CP sky, we need maps of the total synchrotron intensity and the Faraday rotation of the Milky Way. We use the 408 MHz map provided by (Remazeilles

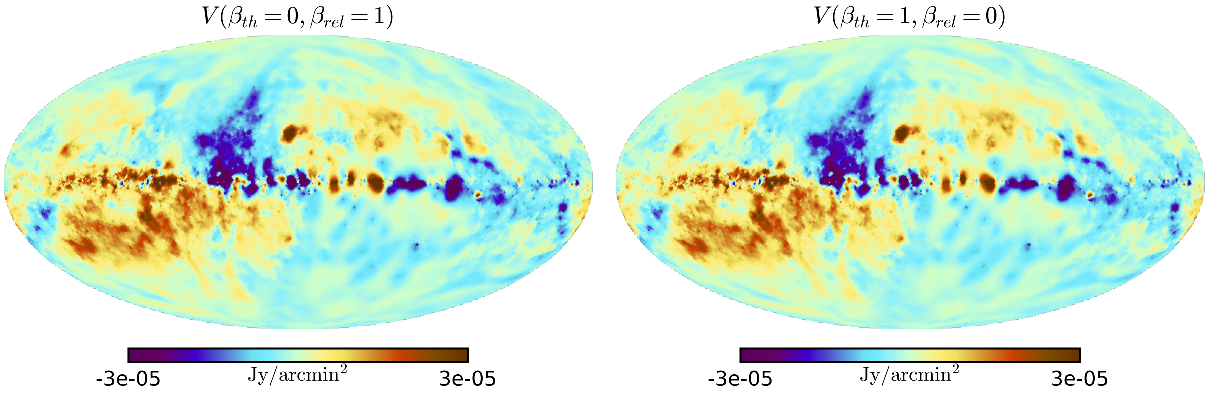
$V(\beta_{th}=0,\beta_{rel}=1)$
$V(\beta_{th}=1,\beta_{rel}=0)$
-3e-05
Jy/arcmin^2
3e-05
-3e-05
Jy/arcmin^2
3e-05

Figure 6.3: Predicted circular polarisation intensity at 408 MHz for $\beta = (0,1)$ (left) and $\beta = (1,0)$. Red indicates clockwise rotation, according to the IAU convention for measuring angles that is opposite to the mathematical convention.

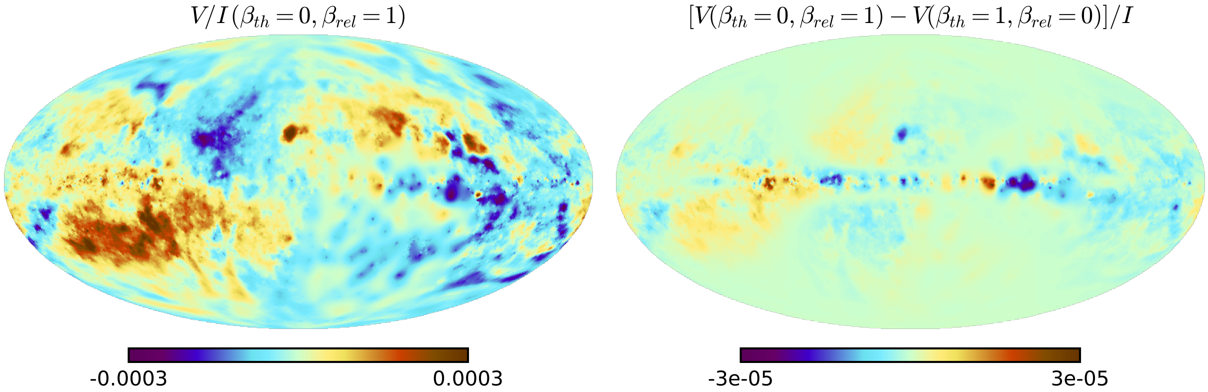
$V/I\,(\beta_{th}=0,\beta_{rel}=1)$
$[V(\beta_{th}=0,\beta_{rel}=1)-V(\beta_{th}=1,\beta_{rel}=0)]/I$
-0.0003
0.0003
-3e-05
3e-05

Figure 6.4: Predicted V/I ratio at 408 MHz for $\beta = (0,1)$ (left) and the difference of the $\beta = (0,1)$ and $\beta = (1,0)$ ratios (right) .

et al. 2015a), which is based on the data of (Haslam et al. 1970, 1974, 1981, 1982b), and the Faraday rotation map provided by (Oppermann et al. 2012b), which is largely based on the data of (Taylor et al. 2009). These are shown in Fig. 6.1

We further need to quantify the σ parameter given in Eq. 6.32. For this we need the thermal and relativistic electron distribution of the galaxy and thereby x_{rel} and x_{th}. For the 3D distribution of the thermal electron density in the Milky Way we use the NE2001 model (Cordes & Lazio 2002) without its local features. The spatial and the energy distribution of relativistic electrons in the Galaxy are more uncertain as we have only direct measurements of the cosmic ray electrons near the Earth. Considerable effort to infer these distributions have been made (Strong & Moskalenko 2001; Strong et al. 2004; Vladimirov et al. 2011; Oppermann et al. 2012b; Orlando et al. 2015; Mazziotta et al. 2016; Evoli et al. 2017). As we have shown in Eq. 6.32, we only need the spatial dependence and not the actual normalisation of n_{rel}, which means that this quantity only effects the relative strength of different structures in the CP map and not the overall strength of the predicted CP intensity itself. For this reason, and since we only aim for a rough estimate, we are content with a simplistic large-scale relativistic electron model. Given the distribution of matter in the galaxy, a exponential model for the spatial structure of cosmic ray electrons may make sense, as already adopted by other authors ((Drimmel & Spergel 2001; Page et al. 2007; Sun et al. 2008; Sun & Reich 2010)), at least in a similar way. In our case, we can use Eqs. 6.10 and 6.17 to give an estimate of the of total synchrotron map given our relativistic electron model and the scaling parameters of Eq. 6.17, where we adopt $\beta = (0, 1)$ and try to reproduce the large scale pattern of the 408 MHz map shown in Fig. 6.1. We thereby choose the following model for the spatial dependence of the relativistic electrons:

$$x_{\mathrm{rel}} = e^{-|\vec{r}|/r_0} \cdot \cosh^{-2}(|\vec{z}|/z_0) \tag{6.33}$$

The vector $\vec{r}$ points in the radial direction in the galactic plane, the vector $\vec{z}$ points out of the plane. As mentioned before, the parameters r_0 and z_0 are estimated via a naive comparison of the observed and estimated synchrotron maps at 408 MHz shown in Figs. 6.1 and 6.2, respectively. The parameters adapted in this work are $r_0 = 12\,\mathrm{kpc}$ and $z_0 = 1.5\,\mathrm{kpc}$. Given the morphological complexity of the map in relation to the simplicity of the model and the poorly understood nature of the origin and evolution of electron cosmic rays we acknowledge that the parameters of this model are highly uncertain. Also completely different parametrization of x_{rel} might lead to the same estimate for I because of the projection involved. The conversion factor $\alpha\,\sigma$ implied by our rough 3D model at 408 MHz is also shown in 6.2 for $\beta = (0, 1)$.

The resulting estimate of the circular polarisation intensity of the Milky Way is depicted in Figs. 6.3 for the two cases $\beta = (0, 1)$ and $\beta = (1, 0)$. The morphology of the resulting maps is dominated by the morphology of the Faraday and the synchrotron map, what seems natural given our formalism. The influence of the dependence of the magnetic field on the different electron densities seems to be small, as the difference between between the two complementary cases is negligible, as we show for the predicted V/I ratio in Fig. 6.4. We predict a signal of up to $5 \cdot 10^{-4}$ Jansky per square arcminute at 408 MHz and more

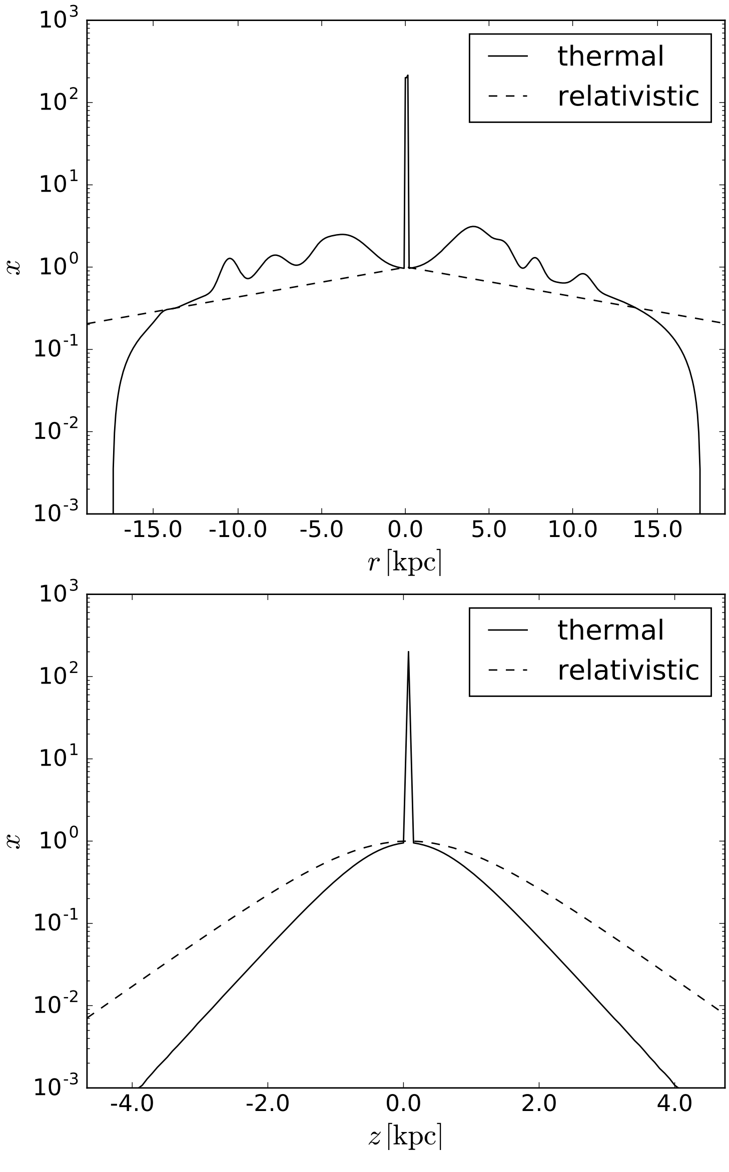

Figure 6.5: Profiles of the thermal and relativistic electron density used in this work in terms of the dimensionless quantities x_{th} and x_{rel} as defined in the context of Eq. 6.17.

at lower frequencies. The CP is strongest in the center plane of the Galaxy. The relative strength of the CP intensity to the total synchrotron intensity up to $V/I \sim 3 \cdot 10^{-4}$ as depicted in Fig. 6.4. The V/I ratio is largest just above and below the disc, as well as in some spots in the outer disc. We expect this ratio to increase with $\nu^{-0.5}$, approaching 10^{-3} at 40 MHz, which might be a detectable level for current instrumentation(Myserlis et al. 2018). The frequency scaling of $V/I \propto \nu^{-0.5}$ was already predicted by (King & Lubin 2016) for the GHz range.

The diffusion length of relativistic electrons depends on energy, therefore, the radio sky at different frequencies is not just a rescaled version of the 408 MHz map used as a template here. The V/I map provided by this work, however, should – within its own limitations – be valid at others frequencies as well. Therefore, it can be used after scaling by $(\nu/408\text{ MHz})^{-0.5}$ to translate total intensity templates at other frequencies into CP expectation maps at the same frequency, which then incorporate any difference of the radio sky due to spatially varying relativistic electron spectra.

Anyhow, even if a total intensity template is not available at the measurement frequency, the main structure of the CP prediction, which are the sign changes induced by the sign changes of the Faraday sky, will be robust with respect to a change in frequency. Therefore, the CP template should be used as a structure expected on the sky, while allowing the real sky to deviate by some factor from it due to errors induced by the assumed frequency scaling and other simplifications. A template search method that is robust in this respect, is discussed below.

The assumed scaling of the magnetic field energy density with the electron densities, β has only a minor impact on the result. The difference between the $\beta = (0, 1)$ and the $\beta = (1, 0)$ scenarios is less than 10%, as Fig. 6.4 shows. Together with Fig. 6.5 this is indeed evidence for the robustness of our results, as the profiles of relativistic and thermal electrons used in this work are quite different, nonetheless the different scaling does not lead to significantly different CP maps.

6.3 Determining the composition of radio plasma via circular polarization: the prospects of the Cygnus A hot spots

6.3.1 Previous studies on the composition of hot spots

Previous proposals to settle the question of the composition of radio plasma were usually based on energetic arguments. More importantly, from an observational standpoint, the composition of the relativistic nonthermal plasma radiating in the jets and lobes of radio galaxies continues to be a long-standing issue (e.g.,(Wardle et al. 1998; Sikora & Madejski 2000; Noerdlinger 1978; De Young 2006)). This question is crucial also because the acceleration and deceleration of the jet near a supermassive black hole depends on the composition of its plasma (e.g.,(Blandford & Znajek 1977; Blandford & Payne 1982; Phinney 1982)).

Over the years, a number of authors have argued in favour of the dominance of relativistic electron-positron pair-plasma in the jets ejected by the central engines of radio galaxies, both from observational and theoretical perspectives (e.g.,(Kundt & Gopal-Krishna 1980; Reynolds et al. 1996; Wardle et al. 1998; Hirotani et al. 2000)). More recent arguments for a significant, if not dominant, presence of relativistic pair plasma in the radio lobes include those put forward by Kawakatu et al. (2016) and Potter (2018) who also provide a summary of the observational and theoretical work done on this topic.

According to a currently popular scenario, the generation of relativistic pair-plasma begins with photon-photon pair production in the spark gap of the magnetosphere surrounding a supermassive black-hole ((Blandford & Znajek 1977; Goldreich & Julian 1969)) and the process continues along the length of the jet, e.g. via dissipation of magnetic energy by reconnection (see, e.g., (Potter 2018)). Although, at large distances from the black-hole, some hadronic plasma may gradually get entrained in the jet flow, this process is unlikely to be efficient at least in Fanaroff-Riley type II (FR II) radio galaxies, since their jets remain effectively shielded by the cocoon of relativistic lobe plasma (Potter 2018; Mizuta et al. 2004; Scheuer 1974). For FR I radio galaxies, the need for non-radiating pressure support of the radio plasma hints at an efficient entrainment of protons into the jet (Croston et al. 2018).

A hadronic jet model was proposed by Mannheim and collaborators (Mannheim 1996, 1998; Mannheim et al. 1991; Mannheim & Biermann 1992) to explain the TeV gamma-ray emission of blazars. The same emission can, however, also be explained in terms of leptonic models, which invoke synchrotron self-Compton (SSC) emission to produce TeV photons.

In the case of FR II radio sources, hadronic jets have been considered to explain their X-ray emission in terms of proton synchrotron radiation, rather than as the inverse-Compton boosted cosmic-microwave background photons (e.g., Aharonian 2002; Honda & Honda 2004; Uchiyama et al. 2006; Bhattacharyya & Gupta 2016; Breiding et al. 2017). The needed high energy protons could even be injected into the jet via turbulent acceleration in the shear layer of the jet (Ostrowski 2000). Alternatively, the x-ray jets could be synchrotron radiation produced by the secondary electrons arising from photo-hadronic interactions like the Bethe-Heitler process or photopion production (see Petropoulou et al. 2017; Kusunose & Takahara 2017; Bhattacharyya & Gupta 2016). In all such scenarios of hadronic jets, one would expect neutrino emission from charged pion or neutron decay resulting from interactions between high energy protons and photons (Mannheim & Biermann 1989). The recent observation of a high energetic neutrino from the Blazar TXS 0506+056, is best explained by a hadronic emission process (IceCube Collaboration et al. 2018). A similar signal has not yet been observed from FR II radio galaxies, which may constrain the hadronic jet model (Neronov et al. 2017).

Lepto-hadronic model for high-energy emission from FR I radio galaxies are consistent with their observed high energy radiation (Reynoso et al. 2011).

Over the years, significant observational evidence has in fact emerged in support of a dominant leptonic relativistic plasma component in the extended radio lobes of FR II sources. The evidence has come mainly from balancing the observationally estimated pressure of the external X-ray emitting thermal plasma and the internal lobe pressure due to the nonthermal plasma estimated by modeling of the combined synchrotron/inverse-Compton spectrum of the lobe, as constrained by measurements at radio and X-ray energies, respectively (e.g.,(Ineson et al. 2017; Hardcastle et al. 2002; Croston et al. 2004; Konar & Hardcastle 2013)). This concurs with the conclusion reached indpendently for the lobes of several FR II sources, including Cygnus A, based on modeling of the observed shapes of the radio lobes (see (Kawakatu et al. 2016)). The X-ray emission from hotspots of powerful FR II sources is often consistently explained in terms of the SSC mechanism, when the magnetic field is close to the equipartition value and under the assumption of an energetically significant, if not a dominant, pair-plasma (vis a vis the electron-proton plasma) (Hardcastle et al. 2004; Kataoka & Stawarz 2005), which is in accord with the findings for powerful radio lobes of FRII sources (see above). Specifically, for the well studied case of Cygnus A, the analysis of the X-ray emission from its hotspots has lent strong support to such an interpretation (Hardcastle et al. 2004; Wilson et al. 2000). Clearly, pair-plasma dominated powerful hotspots would be entirely in tune with the dominance of pair-plasma inferred for FR II lobes (see above), since the latter are fed by the hotspots. Nonetheless, given the various uncertainties involved, such as spatial inhomogeneities in the radiating plasma and beaming of the radiation, independent observational constraints on the presence of an energetic proton population in the hotspots would be very desirable. A population of energetic protons in hot spots could be the origin of the ultra-high energetic cosmic rays observed, as the hot spots of FR II radio galaxies are potential acceleration sites (see e.g. (Eichmann et al. 2018) and reference therein). They would also be in line with the recent detection of neutrinos from the Blazar TXS 0506+056 (IceCube Collaboration et al. 2018).

There is a long history of circular polarization measurements aiming to determine the relativistic plasma composition near the jet's base itself. More recently, VLBI imaging of both circular and linear polarization have been carried out for a few blazars on sub-parsec scale, sometimes at multiple radio frequencies (Homan et al. 2009; Gabuzda et al. 2008). For the blazar 3C 279, Homan et al. (Homan et al. 2009) have reported a particularly detailed observational study which also includes simulations of their sensitive VLBI results in Stokes I, linear polarization, and circular polarization at 6 frequencies in the range 8 to 25 GHz. The significant detection of CP is thus interpreted by them primarily in terms of Faraday conversion of the linear polarization within the nuclear jet. Their main conclusion is that the jet is kinetically dominated by electron-proton plasma, though a significant presence of pair-plasma may still contribute to the radiation. Clearly, even this detailed analysis is vulnerable to uncertainties in the jet's physical parameters, like bulk speed and the minimum Lorenz factor of the relativistic plasma ($\gamma_{\min}$). Interestingly, these uncertainties are largely obviated in the case of Cygnus A hotspots since not only is their motion non-relativistic (like all hotspots on kiloparsec-scale) but estimates of $\gamma_{\min} \sim 600$ are also available, based on recent spectral turnover measurements made with the LOFAR telescope (McKean et al. 2016).

The energy of the leptons that are visible within the observationally accessible radio wavebands is usually not sufficient to explain the rough pressure balance between radio lobes and their surrounding thermal plasma. Additional relativistic protons could fill in the deficit. However, a large population of leptons with lower than observable energies could as well bridge the gap, as would deviations from the usually invoked equipartition assumption between particles and magnetic fields. For these reasons, a more direct determination of the composition of radio plasma via CP measurements as proposed here would be very important.

6.3.2 Estimation

In the following we estimate the expected fractional CP emission arising from the hotspots of Cygnus A, in the case of a pure relativistic electron-proton plasma. A volume element of a hotspot along a line of sight (LOS) may harbor n_e relativistic electrons with a power law spectrum following Eq.6.1. The emissivities for relativistic electrons is given by eqs , relativistic positrons have exactly the same emissivities, with the only difference of an opposite Stokes V sign. For this reason, there is no CP synchrotron emission in case the electron and positron spectra are identical in slope and normalization. The total polarized emission of our electron-proton plasma is then the volume integrated emissivity,

$$J = \int_\mathcal{V} dx\, j(x) \approx \sum_{i=1}^{N_\mathrm{cell}} \mathcal{V}_i\, j_i, \tag{6.34}$$

which we assume to be made of N_cell similar sized cells with spatially constant emissivity j_i within the cell volume $\mathcal{V}_i \approx \mathcal{V}_\mathrm{cell}$.

For simplicity, we assume only the magnetic field orientation to vary from cell to cell, whereas the field strength B and the electron spectrum $\frac{dn(\gamma)}{d\gamma}$ are taken to be approximately the same within the entire emitting volume $\mathcal{V} = N_\mathrm{cell}\mathcal{V}_\mathrm{cell}$. As no magnetic field direction is a priori preferred, we assume a random distribution of field orientations from cell to cell and therefore get for the average, dispersion, and root mean square (rms) of a quantity X

$$\begin{aligned} \overline{X} &= \frac{1}{4\pi}\int_0^{2\pi} d\varphi \int_0^{\pi} d\theta\, \sin\theta\, X(\theta,\varphi), && (6.35)\\ \sigma_X^2 &= \frac{\overline{(X-\overline{X})^2}}{N_\mathrm{cell}}, \text{ and} && (6.36)\\ X_\mathrm{rms} &= \sqrt{\overline{X^2}} = \sqrt{\overline{X}^2 + \sigma_X^2}. && (6.37) \end{aligned}$$

The expected mean of the emission is $\overline{J} = (\overline{I},\, 0,\, 0,\, 0)^\mathrm{t}$, with $\overline{I} = \overline{j_I}\mathcal{V}$ and $\overline{j_I} \approx 0.719 j_0 n_\mathrm{e} B^{\frac{3}{2}}\, \nu^{\frac{-1}{2}}$ for $p = 2$. For an individual emission region like a hot spot, the different Stokes parameters show nonzero variance:

$$\begin{pmatrix} \sigma_I \\ \sigma_Q \\ \sigma_U \\ \sigma_V \end{pmatrix} = \begin{pmatrix} 0.190 \\ 0.106 \\ 0.106 \\ 0.0229\, B_\mathrm{Gauss}^{1/2}\, \nu_\mathrm{GHz}^{-1/2} \end{pmatrix} \frac{j_0 n_\mathrm{e} B^{\frac{3}{2}}\, \nu^{\frac{-1}{2}} \mathcal{V}}{\sqrt{N_\mathrm{cell}}} \tag{6.38}$$

One should note that the assumption of randomness in the directional distribution is related to the cell sizes and the typical coherence length of the magnetic field, which may be rather large in Cygnus A due to the presence of shocks. In the most extreme limit of a completely coherent magnetic field one may set $N_{\rm cell} = 1$, in order to get a intuition for this effect.

In any case, the cell model is just a simplification, which may be dropped for a more elaborate calculation based on a physical model. It should, however, provide the right order of magnitude of the expected effect in a statistical sense.

If we investigate the vector $J' = (I,\, P, V)^{\rm t}$ with $P = \sqrt{Q^2+U^2}$ being the total linear polarization, we find $\overline{J'} = (1, \frac{p+1}{p+7/3}\frac{1}{N_{\rm cell}}, 0)^{\rm t}\overline{I}$, since each cell has a fractional polarization of $\frac{p+1}{p+7/3} \approx 0.69$. Thus, we expect

$$\frac{\sigma_V}{\sigma_P} = \frac{\sigma_V}{\sqrt{\sigma_Q^2+\sigma_U^2}} = 0.153\, B_{\rm Gauss}^{1/2}\, \nu_{\rm GHz}^{-1/2}. \tag{6.39}$$

Given that the fractional linear polarization of the Cygnus A hot spots is about $f_P = \sigma_P/\overline{I} \approx 0.7$ (Carilli et al. 1999) and and the field strength is $B \approx 1.5\,10^{-4}$ Gauss (Wilson et al. 2000), we expect a fractional circular polarization of about $f_V = \sigma_V/\overline{I} \approx 1.31 \cdot 10^{-3}\,\nu_{\rm GHz}^{-1/2}$.

In order to be able to correctly assess the expeced CP emission, we must also consider the Faraday conversion effect of the foreground, which translates linear into circular polarized emission.

From the generic radiative transfer equations we know that

$$j_{V,\rm conv} = \phi_{\rm c}\lambda^3 j_Q,$$

where $\phi_{\rm c}$ is called the conversion measure in analogy to the Faraday rotation measure $\phi_{\rm r}$. In the thermal regime it can be sufficiently fitted via (Huang & Shcherbakov 2011)

$$\phi_{\rm c} \approx \frac{{\rm e}^4}{4\pi^2 m_{\rm e}^3 c^6}\int_{\rm LOS} dr\; n_{\rm th}\; B_\perp^2,$$

under the assumption that the j_Q emission takes place only in the hotspots. The thermal electron density $n_{\rm th}$ poses a problem, as we do not have precise information on the electron column density of the Cygnus cluster in the vicinity of the hotspots, where most of the conversion is likely to take place. We do, however, have precise measurements on the Faraday rotation $\phi_{\rm r}$, which contains the same $n_{\rm th}$-dependence. We can write

$$\phi_{\rm c} \approx \frac{{\rm e}B_{\rm ICM}}{2\pi m_{\rm e}c^2}\int_{\rm LOS} dr \frac{{\rm e}^3}{2\pi m_{\rm e}^2 c^4} n_{\rm th} B_{\rm ICM} \approx \frac{{\rm e}cB_{\rm ICM}}{2\pi m_{\rm e}c^2}\phi_{\rm r}$$

under the assumption of a similar strength and correlation structure of the intracluster magnetic field in both the parallel and perpendicular component of the line of sight. We choose $B_{\rm ICM} = 8\cdot 10^{-6}$G as a typical value of the intracluster magnetic field (Carilli et al. 1988). Cygnus A has very high values of rotation measures with around $|\phi_{\rm r}| \approx \frac{\rho_\phi}{\lambda^2} \approx 1000\,\frac{\rm rad}{\rm m^2}$ (Dreher et al. 1987a), which we will choose for our estimate. Therefore we arrive at $\phi_c\lambda^3 \approx 2.013\cdot 10^{-6}\nu_{\rm GHz}^{-3}$.

The mean $\overline{V_\mathrm{c}}$ is again zero. For the variance we find

$$\sigma_{V_\mathrm{c}} = \phi_\mathrm{c} \lambda^3 \sigma_Q \approx 2.133 \cdot 10^{-7} \frac{\overline{I}}{\nu_\mathrm{GHz}^3 \sqrt{N_\mathrm{cell}}}$$

and for the ratio

$$\frac{\sigma_{V_\mathrm{c}}}{\sigma_V} \approx 9.32 \cdot 10^{-6} \frac{1}{B_\mathrm{Gauss}^{1/2} \nu_\mathrm{GHz}^{2.5}}.$$

Although small in the GHz regime, the above ratio reaches unity rather fast for smaller frequencies. We expect $\sigma_{V_\mathrm{c}}/\sigma_V \approx 1$ for $\nu \approx 57$ MHz and the aforementioned hotspot magnetic field strength of $B \approx 1.5\,10^{-4}$ Gauss. Therefore, observations well above 56 MHz should not be significantly affected by Faraday conversion.

6.3.3 Conclusions

An electron-proton jet is expected to give rise to a fractional CP at a level of $10^{-3}(\nu/\mathrm{GHz})^{-1/2}$. Clearly, this is very challenging to measure, given the faintness of the signal and the systematic cross talk of polarized radio receivers. Nevertheless, systematic effects change from receiver to receiver, and even as a function of time as the relative orientation of sky and the telescope changes with the Earth's rotation. This engenders some hope that genuine CP detection might become technically feasible.

Due to the effect of Faraday conversion of LP into CP, we expect the optimal frequency window for the detection of CP to be around 70 MHz. This renders low frequency radio telescopes like LOFAR most suitable. However, an excellent polarimetry is important as well, so that the the JVLA and in future the Square Kilometer Array as well as its precursors, the MeerKAT and ASKAP telescopes, are promising. The necessary polarimetric accuracies have already been achieved in observations (Rayner et al. 2000).

A detection of the CP signal and thereby a confirmation of the electron-proton jet scenario might therefore be in reach soon. This would be very exciting, as it would contradict the prevailing majoritarian view in the radio galaxy community on jet composition in FR II radio galaxies. At the same time, it would make it more plausible that such galaxies are the acceleration sites of ultra high energy cosmic rays and it would also be in line with the recent detection of neutrinos from the Blazar TXS 0506+056 (IceCube Collaboration et al. 2018). The exclusion of electron-positron jets would, however, not be absolute. A possible scenario in which such jets can produce CP is the case of differing electron and positron energy spectra. These could be caused by their acceleration in a charge asymmetric environment, for example due to the entrainment of thermal electron-proton plasma into the particle acceleration sites, so that plasma physical effects might engender different acceleration efficiencies of electrons and positrons.

A non-detection with a sensitivity well below the CP flux level estimated here for the hotspots of Cygnus A would also be very interesting, as it would argue strongly in favour of an electron-positron pair plasma, where both electrons and positrons have similar energy spectra, indicating a charge symmetric genesis and acceleration history for both species.

The exclusion of the electron-proton jet scenario would be relatively firm in this case, as the only remaining way to avoid predicting detectable CP emission would be that the magnetic field in the hotspots points in a highly matched fashion towards and away from the observer, such that the CP emission of those volumes cancel. Given the high linear polarisation of the Cygnus A hotspots, and therefore an imbalance of the field orientations projected on the plane of the sky, a symmetry along the line of sights seems unlikely. Spatially resolved CP observations, or the study of a larger sample of hotspots of FR II galaxies could negate such an explanation.

To conclude, we have shown that sensitive CP observations of radio galaxy hotspots are a promising way to determine the composition of synchrotron plasma in radio galaxies in a way which is independent of many of the assumptions made in other lines of investigation probing this question.

Bibliography

Aharonian, F. A. 2002, MNRAS, 332, 215

Anderson, C. S., Gaensler, B. M., Feain, I. J., & Franzen, T. M. O. 2015, ApJ, 815, 49

Arras, P., Frank, P., Haim, P., et al. 2020, arXiv e-prints, arXiv:2002.05218

Arras, P., Frank, P., Leike, R., Westermann, R., & Enßlin, T. A. 2019, A&A, 627, A134

Battye, R. A., Browne, I. W. A., Peel, M. W., Jackson, N. J., & Dickinson, C. 2011, MNRAS, 413, 132

Beck, A. M., Hanasz, M., Lesch, H., Remus, R.-S., & Stasyszyn, F. A. 2013, MNRAS, 429, L60

Beck, M. C., Beck, A. M., Beck, R., et al. 2016, J. Cosmology Astropart. Phys., 5, 056

Beck, R., Shukurov, A., Sokoloff, D., & Wielebinski, R. 2003, A&A, 411, 99

Beck, R. & Wielebinski, R. 2013, Magnetic Fields in Galaxies, Vol. 5, 641

Beckert, T. & Falcke, H. 2002, A&A, 388, 1106

Bell, M. R. & Enßlin, T. A. 2012, A&A, 540, A80

Belsole, E., Worrall, D. M., Hardcastle, M. J., & Croston, J. H. 2007, MNRAS, 381, 1109

Bennett, C. L., Larson, D., Weiland, J. L., et al. 2013, ApJS, 208, 20

Beresnyak, A. & Miniati, F. 2016, ApJ, 817, 127

Betti, S. K., Hill, A. S., Mao, S. A., et al. 2019, ApJ, 871, 215

Bhattacharyya, W. & Gupta, N. 2016, ApJ, 817, 121

BICEP2 Collaboration. 2014, Physical Review Letters, 112, 241101

Bjornsson, C.-I. 1990, MNRAS, 242, 158

Blandford, R. D. & Payne, D. G. 1982, MNRAS, 199, 883

Blandford, R. D. & Znajek, R. L. 1977, MNRAS, 179, 433

Blas, D., Lesgourgues, J., & Tram, T. 2011, J. Cosmology Astropart. Phys., 2011, 034

Bonafede, A., Feretti, L., Murgia, M., et al. 2010a, A&A, 513, A30

Bonafede, A., Feretti, L., Murgia, M., et al. 2010b, A&A, 513, A30

Bonafede, A., Vazza, F., Brüggen, M., et al. 2013, MNRAS, 433, 3208

Boudjada, M. Y. & Lecacheux, A. 1991, A&A, 247, 235

Bower, G. C., Falcke, H., & Backer, D. C. 1999, ApJ, 523, L29

Bower, G. C., Falcke, H., Sault, R. J., & Backer, D. C. 2002, ApJ, 571, 843

Bracco, A., Candelaresi, S., Del Sordo, F., & Brand enburg, A. 2019, A&A, 621, A97

Brandenburg, A., Kahniashvili, T., & Tevzadze, A. G. 2015, Physical Review Letters, 114, 075001

Braun, R., Oosterloo, T. A., Morganti, R., Klein, U., & Beck, R. 2007, A&A, 461, 455

Breiding, P., Meyer, E. T., Georganopoulos, M., et al. 2017, ApJ, 849, 95

Brentjens, M. A. & de Bruyn, A. G. 2005a, A&A, 441, 1217

Brentjens, M. A. & de Bruyn, A. G. 2005b, A&A, 441, 1217

Broten, N. W., MacLeod, J. M., & Vallee, J. P. 1988, Ap&SS, 141, 303

Brown, J. C., Haverkorn, M., Gaensler, B. M., et al. 2007, ApJ, 663, 258

Brown, J. C., Taylor, A. R., & Jackel, B. J. 2003, ApJS, 145, 213

Bryan, G. L., Norman, M. L., O'Shea, B. W., et al. 2014, ApJS, 211, 19

Burn, B. J. 1966, MNRAS, 133, 67

Cabral, B. & Leedom, L. C. 1993, in Proceedings of the 20th Annual Conference on Computer Graphics and Interactive Techniques, SIGGRAPH '93 (New York, NY, USA: ACM), 263–270

Carilli, C. L. & Barthel, P. D. 1996, A&A Rev., 7, 1

Carilli, C. L., Kurk, J. D., van der Werf, P. P., Perley, R. A., & Miley, G. K. 1999, AJ, 118, 2581

Carilli, C. L., Perley, R. A., & Dreher, J. H. 1988, ApJ, 334, L73

Celotti, A., Kuncic, Z., Rees, M. J., & Wardle, J. F. C. 1998, MNRAS, 293, 288

Christopherson, A. J., Malik, K. A., & Matravers, D. R. 2011, Phys. Rev. D, 83, 123512

Clarke, T. E. 2004, Journal of Korean Astronomical Society, 37, 337

Clarke, T. E., Kronberg, P. P., & Böhringer, H. 2001, ApJ, 547, L111

Clarke, T. E., Kronberg, P. P., & Bhringer, H. 2001, The Astrophysical Journal Letters, 547, L111

Clegg, A. W., Cordes, J. M., Simonetti, J. M., & Kulkarni, S. R. 1992, ApJ, 386, 143

Condon, J. J., Cotton, W. D., Greisen, E. W., et al. 1998, AJ, 115, 1693

Cordes, J. M. & Lazio, T. J. W. 2002, arXiv e-prints, astro

Costa, A. H. & Spangler, S. R. 2018, ApJ, 865, 65

Costa, A. H., Spangler, S. R., Sink, J. R., Brown, S., & Mao, S. A. 2016, ApJ, 821, 92

Croston, J. H., Birkinshaw, M., Hardcastle, M. J., & Worrall, D. M. 2004, MNRAS, 353, 879

Croston, J. H., Hardcastle, M. J., Harris, D. E., et al. 2005, ApJ, 626, 733

Croston, J. H., Ineson, J., & Hardcastle, M. J. 2018, MNRAS, 476, 1614

Crutcher, R. M., Wandelt, B., Heiles, C., Falgarone, E., & Troland, T. H. 2010, The Astrophysical Journal, 725, 466

Davis, A.-C., Lilley, M., & Törnkvist, O. 1999, Phys. Rev. D, 60, 021301

de Gouveia Dal Pino, E. M. 2006, in American Institute of Physics Conference Series, Vol. 875, Plasma and Fusion Science: 16th IAEA Technical Meeting on Research using Small Fusion Devices, ed. J. J. E. Herrera-Velázquez, 289–295

De Young, D. S. 2006, ApJ, 648, 200

Dedner, A., Kemm, F., Kröner, D., et al. 2002, Journal of Computational Physics, 175, 645

Dennison, B. 1979, AJ, 84, 725

Dennison, B., Simonetti, J. H., & Topasna, G. A. 1998, PASA, 15, 147

Dickinson, C., Davies, R. D., & Davis, R. J. 2003, MNRAS, 341, 369

Dineen, P. & Coles, P. 2005, MNRAS, 362, 403

Dodelson, S. 2003, Modern cosmology (San Diego, CA: Academic Press)

Dolag, K., Kachelriess, M., Ostapchenko, S., & Tomàs, R. 2011, ApJ, 727, L4

Dorn, S. 2016

Draine, B. T. 2011, Physics of the Interstellar and Intergalactic Medium

Dreher, J. W., Carilli, C. L., & Perley, R. A. 1987a, ApJ, 316, 611

Dreher, J. W., Carilli, C. L., & Perley, R. A. 1987b, ApJ, 316, 611

Drimmel, R. & Spergel, D. N. 2001, The Astrophysical Journal, 556, 181

Durrer, R. & Caprini, C. 2003, J. Cosmology Astropart. Phys., 2003, 010

Durrer, R. & Neronov, A. 2013, A&A Rev., 21, 62

Eichmann, B., Rachen, J. P., Merten, L., van Vliet, A., & Becker Tjus, J. 2018, J. Cosmology Astropart. Phys., 2, 036

Enßlin, T. A. 2003, A&A, 401, 499

Enßlin, T. A. 2019, Annalen der Physik, 531, 1800127

Enßlin, T. A. & Frommert, M. 2011, Phys. Rev. D, 83, 105014

Enßlin, T. A., Frommert, M., & Kitaura, F. S. 2009, Phys. Rev. D, 80, 105005

Enßlin, T. A., Hutschenreuter, S., & Gopal-Krishna. 2019, J. Cosmology Astropart. Phys., 2019, 035

Enßlin, T. A., Hutschenreuter, S., Vacca, V., & Oppermann, N. 2017, Phys. Rev. D, 96, 043021

Enßlin, T. A., Hutschenreuter, S., Vacca, V., & Oppermann, N. 2017a, Phys. Rev. D, 96, 043021

Enßlin, T. A., Hutschenreuter, S., Vacca, V., & Oppermann, N. 2017b, Phys. Rev. D, 96, 043021

Enßlin, T. A. & Weig, C. 2010, Phys. Rev. E, 82, 051112

Eriksen, H. K., Jewell, J. B., Dickinson, C., et al. 2008, ApJ, 676, 10

Evoli, C., Gaggero, D., Vittino, A., et al. 2017, J. Cosmology Astropart. Phys., 2, 015

Fauvet, L., Macías-Pérez, J. F., Aumont, J., et al. 2011, A&A, 526, A145

Feain, I. J., Cornwell, T. J., Ekers, R. D., et al. 2011, ApJ, 740, 17

Feain, I. J., Ekers, R. D., Murphy, T., et al. 2009, ApJ, 707, 114

Fender, R., Rayner, D., Norris, R., Sault, R. J., & Pooley, G. 2000, ApJ, 530, L29

Fender, R. P., Rayner, D., McCormick, D. G., et al. 2002, MNRAS, 336, 39

Fenu, E., Pitrou, C., & Maartens, R. 2011, MNRAS, 414, 2354

Fidler, C., Pettinari, G., & Pitrou, C. 2016, Phys. Rev. D, 93, 103536

Finkbeiner, D. P. 2003, ApJS, 146, 407

Frick, P., Stepanov, R., Shukurov, A., & Sokoloff, D. 2001, MNRAS, 325, 649

Gabuzda, D. C., Vitrishchak, V. M., Mahmud, M., & O'Sullivan, S. P. 2008, MNRAS, 384, 1003

Gaensler, B. M., Dickey, J. M., McClure-Griffiths, N. M., et al. 2001a, ApJ, 549, 959

Gaensler, B. M., Dickey, J. M., McClure-Griffiths, N. M., et al. 2001b, ApJ, 549, 959

Gaensler, B. M., Haverkorn, M., Staveley-Smith, L., et al. 2005, Science, 307, 1610

Gaensler, B. M., Landecker, T. L., Taylor, A. R., & POSSUM Collaboration. 2010, in Bulletin of the American Astronomical Society, Vol. 42, American Astronomical Society Meeting Abstracts #215, 515

Gaensler, B. M., Madsen, G. J., Chatterjee, S., & Mao, S. A. 2008, PASA, 25, 184

Gaia Collaboration et al. 2018, A&A, 616, A1

Gaustad, J. E., McCullough, P. R., Rosing, W., & Van Buren, D. 2001, PASP, 113, 1326

Gießübel, R., Heald, G., Beck, R., & Arshakian, T. G. 2013, A&A, 559, A27

Goldreich, P. & Julian, W. H. 1969, ApJ, 157, 869

Gopal, R. & Sethi, S. K. 2005, MNRAS, 363, 521

Govoni, F., Orrù, E., Bonafede, A., et al. 2019, Science, 364, 981

Grasso, D. & Rubinstein, H. R. 2001, Phys. Rep., 348, 163

Gregorini, L., Vigotti, M., Mack, K. H., Zoennchen, J., & Klein, U. 1998, Astronomy and Astrophysics Supplement Series, 133, 129

Greiner, M., Schnitzeler, D. H. F. M., & Enßlin, T. A. 2016a, A&A, 590, A59

Greiner, M., Schnitzeler, D. H. F. M., & Enßlin, T. A. 2016b, A&A, 590, A59

Haffner, L. M., Reynolds, R. J., Tufte, S. L., et al. 2003, ApJS, 149, 405

Hammond, A. 2011, Private Communication

Han, J. L., Manchester, R. N., Lyne, A. G., Qiao, G. J., & van Straten, W. 2006, ApJ, 642, 868

Hardcastle, M. J., Birkinshaw, M., Cameron, R. A., et al. 2002, ApJ, 581, 948

Hardcastle, M. J., Harris, D. E., Worrall, D. M., & Birkinshaw, M. 2004, ApJ, 612, 729

Harris, D. E., Leighly, K. M., & Leahy, J. P. 1998, ApJ, 499, L149

Harrison, E. R. 1970, Phys. Rev. D, 1, 2726

Harrison, E. R. 1970, MNRAS, 147, 279

Harvey-Smith, L., Madsen, G. J., & Gaensler, B. M. 2011, ApJ, 736, 83

Haslam, C. G. T., Klein, U., Salter, C. J., et al. 1981, A&A, 100, 209

Haslam, C. G. T., Quigley, M. J. S., & Salter, C. J. 1970, MNRAS, 147, 405

Haslam, C. G. T., Salter, C. J., Stoffel, H., & Wilson, W. E. 1982a, A&AS, 47, 1

Haslam, C. G. T., Salter, C. J., Stoffel, H., & Wilson, W. E. 1982b, A&AS, 47, 1

Haslam, C. G. T., Wilson, W. E., Graham, D. A., & Hunt, G. C. 1974, A&AS, 13, 359

Haverkorn, M. 2015, Astrophysics and Space Science Library, Vol. 407, Magnetic Fields in the Milky Way, 483

Haverkorn, M., Gaensler, B. M., McClure-Griffiths, N. M., Dickey, J. M., & Green, A. J. 2004, ApJ, 609, 776

Haverkorn, M., Gaensler, B. M., McClure-Griffiths, N. M., Dickey, J. M., & Green, A. J. 2006, The Astrophysical Journal Supplement Series, 167, 230

Heald, G., Braun, R., & Edmonds, R. 2009, A&A, 503, 409

Hennessy, G. S., Owen, F. N., & Eilek, J. A. 1989, ApJ, 347, 144

Hirotani, K., Iguchi, S., Kimura, M., & Wajima, K. 2000, ApJ, 545, 100

Hodge, P. E. 1982, ApJ, 263, 595

Homan, D. C., Lister, M. L., Aller, H. D., Aller, M. F., & Wardle, J. F. C. 2009, ApJ, 696, 328

Honda, Y. S. & Honda, M. 2004, ApJ, 613, L25

Hou, L. G., Han, J. L., & Shi, W. B. 2009, A&A, 499, 473

Huang, L. & Shcherbakov, R. V. 2011, MNRAS, 416, 2574

Hutschenreuter, S., Dorn, S., Jasche, J., et al. 2018, Classical and Quantum Gravity, 35, 154001

Hutschenreuter, S. & Enßlin, T. A. 2020a, A&A, 633, A150

Hutschenreuter, S. & Enßlin, T. A. 2020b, A&A, 633, A150

Hutschenreuter et al., S. in prep.

IceCube Collaboration et al. 2018, ApJ, 863, L10

Ineson, J., Croston, J. H., Hardcastle, M. J., & Mingo, B. 2017, MNRAS, 467, 1586

Jaffe, T., Waelkens, A., Reinecke, M., Kitaura, F. S., & Enßlin, T. A. 2012, Hammurabi: Simulating polarized Galactic synchrotron emission, Astrophysics Source Code Library

Jaffe, T. R., Banday, A. J., Leahy, J. P., Leach, S., & Strong, A. W. 2011, MNRAS, 416, 1152

Jaffe, T. R., Leahy, J. P., Banday, A. J., et al. 2010, MNRAS, 401, 1013

Jansson, R. & Farrar, G. R. 2012a, ApJ, 757, 14

Jansson, R. & Farrar, G. R. 2012b, ApJ, 761, L11

Jansson, R., Farrar, G. R., Waelkens, A. H., & Enßlin, T. A. 2009, J. Cosmology Astropart. Phys., 7, 021

Jasche, J., Leclercq, F., & Wandelt, B. D. 2015, J. Cosmology Astropart. Phys., 1, 036

Jasche, J. & Wandelt, B. D. 2013, MNRAS, 432, 894

Johnson, S. G. 2011, Notes on FFT-based differentiation

Johnston-Hollitt, M. 2003a, PhD thesis, University of Adelaide

Johnston-Hollitt, M. 2003b, PhD thesis, University of Adelaide

Johnston-Hollitt, M. 2003, Detection of magnetic fields and diffuse radio emission in Abell 3667 and other rich southern clusters of galaxies / Melanie Johnston-Hollitt.

Johnston-Hollitt, M. 2011, Private Communication

Johnston-Hollitt, M. & Ekers, R. D. 2004, arXiv e-prints, astro

Johnston-Hollitt, M., Hollitt, C. P., & Ekers, R. D. 2004, in The Magnetized Interstellar Medium, ed. B. Uyaniker, W. Reich, & R. Wielebinski, 13–18

Jones, B. 1870, The Life And Letters of Faraday (Philadelphia: Lippincott)

Jones, T. W. & Odell, S. L. 1977a, ApJ, 214, 522

Jones, T. W. & Odell, S. L. 1977b, ApJ, 215, 236

Kaczmarek, J. F., Purcell, C. R., Gaensler, B. M., McClure-Griffiths, N. M., & Stevens, J. 2017, MNRAS, 467, 1776

Kandus, A., Kunze, K. E., & Tsagas, C. G. 2011, Phys. Rep., 505, 1

Kataoka, J. & Stawarz, Ł. 2005, ApJ, 622, 797

Kato, T., Tabara, H., Inoue, M., & Aizu, K. 1987, Nature, 329, 223

Kawakatu, N., Kino, M., & Takahara, F. 2016, MNRAS, 457, 1124

Kim, K. S., Lilly, S. J., Miniati, F., et al. 2016, ApJ, 829, 133

Kim, K.-T., Tribble, P. C., & Kronberg, P. P. 1991, ApJ, 379, 80

King, S. & Lubin, P. 2016, Phys. Rev. D, 94, 023501

Klein, U., Mack, K. H., Gregorini, L., & Vigotti, M. 2003, A&A, 406, 579

Knollmüller, J. & Enßlin, T. A. 2017, Phys. Rev. E, 96, 042114

Knollmüller, J. & Enßlin, T. A. 2019, arXiv e-prints, arXiv:1901.11033

Knollmüller, J., Steininger, T., & Enßlin, T. A. 2017a, arXiv e-prints, arXiv:1711.02955

Knollmüller, J., Steininger, T., & Enßlin, T. A. 2017b, arXiv e-prints, arXiv:1711.02955

Komesaroff, M. M., Roberts, J. A., Milne, D. K., Rayner, P. T., & Cooke, D. J. 1984, MNRAS, 208, 409

Konar, C. & Hardcastle, M. J. 2013, MNRAS, 436, 1595

Kooi, J. E., Fischer, P. D., Buffo, J. J., & Spangler, S. R. 2017, Sol. Phys., 292, 56

Kuchar, P. & Enßlin, T. A. 2011, A&A, 529, A13

Kundt, W. & Gopal-Krishna. 1980, Nature, 288, 149

Kusunose, M. & Takahara, F. 2017, ApJ, 835, 20

Lallement, R., Capitanio, L., Ruiz-Dern, L., et al. 2018, A&A, 616, A132

Langer, M. & Durrive, J.-B. 2018, arXiv e-prints, arXiv:1811.09717

Lavaux, G. & Hudson, M. J. 2011, MNRAS, 416, 2840

Lavaux, G. & Jasche, J. 2016, MNRAS, 455, 3169

Law, C. J., Gaensler, B. M., Bower, G. C., et al. 2011, ApJ, 728, 57

Lawler, J. M. & Dennison, B. 1982, ApJ, 252, 81

Leike, R. H. & Enßlin, T. A. 2019, A&A, 631, A32

Lewis, A. & Bridle, S. 2002, Phys. Rev. D, 66, 103511

Lorimer, D. R. 2008, Living Reviews in Relativity, 11, 8

Ma, C.-P. & Bertschinger, E. 1995, ApJ, 455, 7

Ma, Y. K., Mao, S. A., Stil, J., et al. 2019, MNRAS, 1401

Macquart, J.-P., Kedziora-Chudczer, L., Rayner, D. P., & Jauncey, D. L. 2000, ApJ, 538, 623

Manchester, R. N., Hobbs, G. B., Teoh, A., & Hobbs, M. 2005, AJ, 129, 1993

Mannheim, K. 1996, Space Sci. Rev., 75, 331

Mannheim, K. 1998, Science, 279, 684

Mannheim, K. & Biermann, P. L. 1989, A&A, 221, 211

Mannheim, K. & Biermann, P. L. 1992, A&A, 253, L21

Mannheim, K., Biermann, P. L., & Kruells, W. M. 1991, A&A, 251, 723

Mao, S. A., Carilli, C., Gaensler, B. M., et al. 2017, Nature Astronomy, 1, 621

Mao, S. A., Gaensler, B. M., Haverkorn, M., et al. 2010, ApJ, 714, 1170

Mao, S. A., Gaensler, B. M., Stanimirović, S., et al. 2008, ApJ, 688, 1029

Mao, S. A., McClure-Griffiths, N. M., Gaensler, B. M., et al. 2012a, ApJ, 755, 21

Mao, S. A., McClure-Griffiths, N. M., Gaensler, B. M., et al. 2012b, ApJ, 759, 25

Matarrese, S., Mollerach, S., Notari, A., & Riotto, A. 2005, Phys. Rev. D, 71, 043502

Mazziotta, M. N., Cerutti, F., Ferrari, A., et al. 2016, Astroparticle Physics, 81, 21

McClure-Griffiths, N. M., Dickey, J. M., Gaensler, B. M., et al. 2005, The Astrophysical Journal Supplement Series, 158, 178

McKean, J. P., Godfrey, L. E. H., Vegetti, S., et al. 2016, MNRAS, 463, 3143

Mestel, L. 1966, MNRAS, 133, 265

Minter, A. H. & Spangler, S. R. 1996, ApJ, 458, 194

Mizuta, A., Yamada, S., & Takabe, H. 2004, ApJ, 606, 804

Mouschovias, T. C. 1976, ApJ, 207, 141

Murgia, M., Govoni, F., Carretti, E., et al. 2016, MNRAS, 461, 3516

Myserlis, I., Angelakis, E., Kraus, A., et al. 2018, A&A, 609, A68

Naab, T. & Ostriker, J. P. 2017, ARA&A, 55, 59

Nalson, E., Christopherson, A. J., & Malik, K. A. 2014, Journal of Cosmology and Astroparticle Physics, 2014, 023

Neronov, A. & Semikoz, D. V. 2009, Phys. Rev. D, 80, 123012

Neronov, A., Semikoz, D. V., & Ptitsyna, K. 2017, A&A, 603, A135

Neronov, A. & Vovk, I. 2010, Science, 328, 73

Noerdlinger, P. D. 1978, Physical Review Letters, 41, 135

Norman, M. L., Bryan, G. L., Harkness, R., et al. 2007, arXiv e-prints, arXiv:0705.1556

Oppermann, N., Junklewitz, H., Greiner, M., et al. 2015, A&A, 575, A118

Oppermann, N., Junklewitz, H., Robbers, G., et al. 2012a, A&A, 542, A93

Oppermann, N., Junklewitz, H., Robbers, G., et al. 2012b, A&A, 542, A93

Oppermann, N., Junklewitz, H., Robbers, G., et al. 2012c, A&A, 542, A93

Ordog, A., Brown, J. C., Kothes, R., & Landecker, T. L. 2017, A&A, 603, A15

Oren, A. L. & Wolfe, A. M. 1995, ApJ, 445, 624

Orlando, E., Strong, A. W., Moskalenko, I. V., et al. 2015, arXiv e-prints, arXiv:1507.05958

Ostrowski, M. 2000, MNRAS, 312, 579

O'Sullivan, S. P. 2011, Private Communication

O'Sullivan, S. P., Purcell, C. R., Anderson, C. S., et al. 2017, MNRAS, 469, 4034

Page, L., Hinshaw, G., Komatsu, E., et al. 2007, ApJS, 170, 335

Pandya, A., Zhang, Z., Chandra, M., & Gammie, C. F. 2016, ApJ, 822, 34

Passot, T. & Vázquez-Semadeni, E. 2003, A&A, 398, 845

Perley, R. A. & Butler, B. J. 2013, ApJS, 206, 16

Petropoulou, M., Vasilopoulos, G., & Giannios, D. 2017, MNRAS, 464, 2213

Pfrommer, C., Broderick, A. E., Chang, P., Puchwein, E., & Springel, V. 2013, arXiv e-prints, arXiv:1308.6284

Phinney, E. S. 1982, MNRAS, 198, 1109

Planck Collaboration. 2016a, A&A, 594, A10

Planck Collaboration. 2016b, A&A, 594, A25

Planck Collaboration. 2016c, A&A, 594, A25

Planck Collaboration. 2016d, A&A, 596, A103

Planck Collaboration, Ade, P. A. R., Aghanim, N., et al. 2016, A&A, 594, A20

Planck Collaboration et al. 2016a, A&A, 594, A13

Planck Collaboration et al. 2016b, A&A, 594, A19

Polderman, I. M., Haverkorn, M., & Jaffe, T. R. 2020, arXiv e-prints, arXiv:2002.09204

Potter, W. J. 2018, MNRAS, 473, 4107

Prandoni, I., Murgia, M., Tarchi, A., et al. 2017, A&A, 608, A40

Pumpe, D., Gabler, M., Steininger, T., & Enßlin, T. A. 2018, A&A, 610, A61

Purcell, C. R., Gaensler, B. M., Sun, X. H., et al. 2015, ApJ, 804, 22

Pynzar', A. V. 1993, Astronomy Reports, 37, 245

Rayner, D. P., Norris, R. P., & Sault, R. J. 2000, Monthly Notices of the Royal Astronomical Society, 319, 484

Remazeilles, M., Dickinson, C., Banday, A. J., Bigot-Sazy, M.-A., & Ghosh, T. 2015a, MNRAS, 451, 4311

Remazeilles, M., Dickinson, C., Banday, A. J., Bigot-Sazy, M. A., & Ghosh, T. 2015b, MNRAS, 451, 4311

Reppin, J. & Banerjee, R. 2017, Phys. Rev. E, 96, 053105

Reynolds, C. S., Fabian, A. C., Celotti, A., & Rees, M. J. 1996, MNRAS, 283, 873

Reynoso, M., Medina, C., & Romero, G. 2011, 531, A30

Riseley, C. J., Lenc, E., Van Eck, C. L., et al. 2018, PASA, 35, 43

Rossetti, A., Dallacasa, D., Fanti, C., Fanti, R., & Mack, K. H. 2008, A&A, 487, 865

Roy, S., Rao, A. P., & Subrahmanyan, R. 2005, MNRAS, 360, 1305

Rudnick, L. & Jones, T. W. 1983, AJ, 88, 518

Ruszkowski, M. & Begelman, M. C. 2002, ApJ, 573, 485

Saga, S., Ichiki, K., Takahashi, K., & Sugiyama, N. 2015, Phys. Rev. D, 91, 123510

Sault, R. J. & Macquart, J.-P. 1999, ApJ, 526, L85

Saveliev, A., Jedamzik, K., & Sigl, G. 2012, Phys. Rev. D, 86, 103010

Saveliev, A., Jedamzik, K., & Sigl, G. 2013, Phys. Rev. D, 87, 123001

Scheck, L., Aloy, M. A., Martí, J. M., Gómez, J. L., & Müller, E. 2002, MNRAS, 331, 615

Scheuer, P. A. G. 1974, MNRAS, 166, 513

Schnitzeler, D. H. F. M. 2011, Private Communication

Schnitzeler, D. H. F. M., Carretti, E., Wieringa, M. H., et al. 2019, MNRAS, 485, 1293

Selig, M., Bell, M. R., Junklewitz, H., et al. 2013, A&A, 554, A26

Selig, M., Vacca, V., Oppermann, N., & Enßlin, T. A. 2015, A&A, 581, A126

Shanahan, R., Lemmer, S. J., Stil, J. M., et al. 2019a, ApJ, 887, L7

Shanahan, R., Lemmer, S. J., Stil, J. M., et al. 2019b, ApJ, 887, L7

Sikora, M. & Madejski, G. 2000, ApJ, 534, 109

Simard-Normandin, M., Kronberg, P. P., & Button, S. 1981, ApJS, 45, 97

Smoot, G. F. 1998, arXiv e-prints, 9801121

Stawarz, Ł., Tanaka, Y. T., Madejski, G., et al. 2013, ApJ, 766, 48

Steininger, T., Dixit, J., Frank, P., et al. 2017, arXiv e-prints, arXiv:1708.01073

Stil, J. M., Taylor, A. R., & Sunstrum, C. 2011, ApJ, 726, 4

Strong, A. W. & Moskalenko, I. V. 2001, Advances in Space Research, 27, 717

Strong, A. W., Moskalenko, I. V., & Reimer, O. 2004, ApJ, 613, 962

Subramanian, K. 1999, Physical Review Letters, 83, 2957

Subramanian, K. 2016, Reports on Progress in Physics, 79, 076901

Subramanian, K. 2019, Galaxies, 7, 47

Subramanian, K., Narasimha, D., & Chitre, S. M. 1994, MNRAS, 271

Subramanian, K., Shukurov, A., & Haugen, N. E. L. 2006, MNRAS, 366, 1437

Sun, X.-H. & Reich, W. 2010, Research in Astronomy and Astrophysics, 10, 1287

Sun, X. H., Reich, W., Waelkens, A., & Enßlin, T. A. 2008, A&A, 477, 573

Tabara, H. & Inoue, M. 1980a, A&AS, 39, 379

Tabara, H. & Inoue, M. 1980b, A&AS, 39, 379

Tanuma, S., Yokoyama, T., Kudoh, T., & Shibata, K. 1999, Two-Dimensional Numerical MHD Simulation of Magnetic Reconnection in Galaxy, ed. S. M. Miyama, K. Tomisaka, & T. Hanawa (Dordrecht: Springer Netherlands), 119–120

Tashiro, H., Chen, W., Ferrer, F., & Vachaspati, T. 2014, MNRAS, 445, L41

Tavecchio, F., Ghisellini, G., Foschini, L., et al. 2010, MNRAS, 406, L70

Taylor, A. R., Gibson, S. J., Peracaula, M., et al. 2003, The Astronomical Journal, 125, 3145

Taylor, A. R., Stil, J. M., & Sunstrum, C. 2009, ApJ, 702, 1230

The NIFTy5 team, Arras, Philipp snd Baltac, M., Enßlin, T. A., et al. 2019, In preparation

Turner, M. S. & Widrow, L. M. 1988, Phys. Rev. D, 37, 2743

Uchiyama, Y., Urry, C. M., Cheung, C. C., et al. 2006, ApJ, 648, 910

Vallée, J. P. 2017, The Astronomical Review, 13, 113

Vallée, J. P. 2018, Ap&SS, 363, 243

Valtaoja, E. 1984, Ap&SS, 100, 227

van Eck, C. & Brown, J. in prep.

Van Eck, C. L., Brown, J. C., Stil, J. M., et al. 2011, ApJ, 728, 97

Van Eck, C. L., Haverkorn, M., Alves, M. I. R., et al. 2018, A&A, 613, A58 van Eck et al., C. in prep.

Vázquez, R. A., May, J., Carraro, G., et al. 2008, ApJ, 672, 930

Vázquez-Semadeni, E. 2015, in Astrophysics and Space Science Library, Vol. 407, Magnetic Fields in Diffuse Media, ed. A. Lazarian, E. M. de Gouveia Dal Pino, & C. Melioli, 401

Vazza, F., Brüggen, M., Gheller, C., et al. 2017, Classical and Quantum Gravity, 34, 234001

Vazza, F., Brüggen, M., Gheller, C., & Wang, P. 2014, MNRAS, 445, 3706

Vernstrom, T., Gaensler, B. M., Rudnick, L., & Andernach, H. 2019, ApJ, 878, 92

Vernstrom, T., Gaensler, B. M., Vacca, V., et al. 2018, MNRAS, 475, 1736

Vigotti, M., Gregorini, L., Klein, U., & Mack, K. H. 1999, Astronomy and Astrophysics Supplement Series, 139, 359

Vitrishchak, V. M. & Gabuzda, D. C. 2008, International Journal of Modern Physics D, 17, 1531

Vladimirov, A. E., Digel, S. W., Jóhannesson, G., et al. 2011, Computer Physics Communications, 182, 1156

Waelkens, A., Jaffe, T., Reinecke, M., Kitaura, F. S., & Enßlin, T. A. 2009a, A&A, 495, 697

Waelkens, A., Jaffe, T., Reinecke, M., Kitaura, F. S., & Enßlin, T. A. 2009b, A&A, 495, 697

Wagstaff, J. M., Banerjee, R., Schleicher, D., & Sigl, G. 2014, Phys. Rev. D, 89, 103001

Wang, P. & Abel, T. 2009, ApJ, 696, 96

Wardle, J. F. C., Homan, D. C., Ojha, R., & Roberts, D. H. 1998, Nature, 395, 457

Wiener, N. 1966, Extrapolation, Interpolation, and Smoothing of Stationary Time Series (Cambridge, Mass. : Technology Press of the Massachusetts Institute of Technology,)

Wilson, A. S., Young, A. J., & Shopbell, P. L. 2000, ApJ, 544, L27

Wilson, A. S., Young, A. J., & Shopbell, P. L. 2000, The Astrophysical Journal Letters, 544, L27

Wolleben, M., Landecker, T. L., Reich, W., & Wielebinski, R. 2006, A&A, 448, 411

Wright, M. & Birkinshaw, M. 1984, ApJ, 281, 135

Wrobel, J. M. 1993, AJ, 106, 444

Xu, J. & Han, J.-L. 2014, Research in Astronomy and Astrophysics, 14, 942

Xu, Y., Kronberg, P. P., Habib, S., & Dufton, Q. W. 2006, ApJ, 637, 19

Xu, Y., Reid, M. J., Menten, K. M., et al. 2009, ApJ, 693, 413

Yamazaki, D. G., Kajino, T., Mathews, G. J., & Ichiki, K. 2012, Phys. Rep., 517, 141

Yao, J. M., Manchester, R. N., & Wang, N. 2017, ApJ, 835, 29

Zeldovich, Y. B. 1972, MNRAS, 160, 1P

Danksagung

Diese Arbeit wäre nicht möglich gewesen ohne die Hilfe einer Vielzahl von Personen, denen ich hier meinen Dank aussprechen möchte.

Dies gilt zunächst meinem Doktorvater Torsten Enßlin für dessen Betreung und insbesondere für seinen Rückhalt, seine Unterstützung und seine Begeisterungfähigkeit. Auch das MPA und insbeondere die Information Field Theory Gruppe haben mir den letzten Jahren eine wunderbare Umgebung geboten. Ich möchte daher meinen Mitdoktoranden Phillip Arras, Vanessa Böhm, Phillip Frank, Johannes Harth-Kitzerow, Maksim Greiner, Jakob Knollmüller, Ivan Kostyuk, Reimar Leike, Daniel Pumpe, Natalia Porqueres, Theo Steininger und außerdem Martin Reinecke und Sebastian Dorn für ihren Ideenreichtum, ihre Hilfe und Diskussionen danken. Dies gilt natürlich auch den vielen PostDocs, Master- und Bachelorstudenten unserer Gruppe, die ich nur aufgrund ihrer großen Zahl hier nicht namentlich aufzähle.

Zuletzt gilt mein Dank im besonderen Maße meiner Familie und Alexandra, deren Unterstützung in diesen manchmal stressigen Jahren mir vieles erleichtert hat.